

© 2020 by Kuo-Pin Tseng. All rights reserved.

CHEMICAL SELECTION RULES OF SINGLE-PHASE HIGH-ENTROPY OXIDES

BY

KUO-PIN TSENG

DISSERTATION

Submitted in partial fulfillment of the requirements  
for the degree of Doctor of Philosophy in Materials Science and Engineering  
in the Graduate College of the  
University of Illinois at Urbana-Champaign, 2020

Urbana, Illinois

Doctoral Committee:

Professor Waltraud M. Kriven, Chair and Director of Research

Professor Jian-Min Zuo

Assistant Professor Daniel Philip Shoemaker

Assistant Professor Robert Maaß

## ABSTRACT

High-entropy oxides, as a novel research field in ceramics, have been found to present state-of-the-art improvement in various properties. These contributions could be achieved by multiple cations homogeneously occupying the same polyhedral sites, introducing severe lattice distortion throughout a structure. However, the mechanism of chemical selection rules for designing new high-entropy oxides was still unclear. Randomly mixed, multi-components usually form composites instead of a single-phase, solid solution. In this research, twenty high-entropy lanthanide candidates were synthesized and examined to explore the function of two potential parameters: (1) cation size mismatch, and (2) preferred valence states.

The oxide candidates were synthesized by the polymeric steric entrapment method to ensure homogeneous mixing among the cations. The evolution of phase transformation and structural stability from room temperature up to  $\sim 2000^{\circ}\text{C}$  were examined in a quadrupole lamp furnace and conical nozzle levitator at synchrotron X-ray facilities. The thermal expansion behaviors of single-phase, high-entropy, lanthanide oxides were measured.

Cation size mismatch and preferred valence configurations have significant influences on the formation of high-entropy oxides. In most of circumstances, mixing cations with excess threshold in size mismatch ( $\delta > 7$ ) caused the formation of secondary phase(s), leading to failure in forming stable, single-phase, high-entropy oxides. By choosing cations with different preferences in valence configurations, the final structure could be constructed for a prototype with a similar combination of oxidation states. Furthermore, merging cations with different valence states could trigger phase transformations/separations during heat treatments. However, in high-entropy oxides, the contribution from configurational mixing entropy was thought to be negligible. Understanding the function of cation size mismatch and preferred valence configurations can benefit the ceramic community in the future when designing high-entropy oxides.

## ACKNOWLEDGMENTS

First, I would like to thank my advisor, Professor Waltraud M. Kriven, for giving me the opportunity to join her research group. During my Ph.D. study, she gave me the great opportunity to learn problem-solving skills, data analysis techniques, and the art of experimental design and planning. Her complete support in both funding of chemicals, and collaborations with other research groups and national labs facilitated this research.

I am greatly thankful to Professors Jian-Min Zuo, Professor Daniel Philip Shoemaker, and Professor Robert Maaß for their kindness to serve on my thesis committee. Their knowledge and academic experience give me very helpful guidance and suggestion to improve my Ph.D. research.

I would like to acknowledge the members of Professor Kriven's research group. Many thanks to the synchrotron beamline team: Dr. Daniel Ribero Rodriguez, Dr. Scott McCormack, Dr. Andrew Steveson, and Benjamin Hulbert. I also want to thank Dr. Daniel Ribero Rodriguez for his kindly patience while training me in my early Ph.D. study. Benjamin Hulbert gave me plenty of helpful support and guidance on data analysis and beamline experiment improvements. Meanwhile, I would like to thank Dr. Yan Qun for sharing her experiences and generous support in electron microscopy work. I thank Ms. Dana Yun for synthesizing materials for my study during my internship at Pacific Northwest National Laboratory.

I am very thankful to Dr. Theva Thevuthasan for giving me the great opportunity to join his research group. Many thanks to Dr. Swarup China for his training in experimental design and data organization/analysis. I also would like to thank Dr. Eric Bylaska and Dr. Duo Song for the thermodynamics discussions.

Furthermore, I would like to thank my undergraduate thesis advisor, Professor Fu-Su Yen, and Dr. Chen-Tsung Hung; Master's thesis advisor, Professor William Carty, in providing me

essential scientific training on experimental design and organization. I am also thankful to Professor Hao-Chih Liu for sharing his experience in his Ph.D. study.

This work could not be done without the support of beamline scientists at Argonne National Lab, Advanced Photon Source, 33-BM-C, Dr. Jenia Karapetrova for her help on X-ray beam alignment, 6ID-D, Dr. Chris Benmore for his help on the conical nozzle levitator apparatus and 17-BM-B, Dr. Wenqian Xu and Dr. Andrey Yakovenko for their passion in mounting the quadrupole lamp furnace at their beamline.

Especially, I would like to thank my wife, Yan Yang, for her endless support during every failure I encountered during my Ph.D. study. Her encouragement in my study was important for the completion of this research. I also want to thank my family, Shu-Chen Chao (Mother), Wei-Ming Tseng (Father), Yung-Fang Tseng (Sister), and Chi-Chang Tseng (Brother) for always being there for me.

Throughout my Ph.D. study, my friends, Dr. Cheng-Wei Lee, Dr. Hsuan-Chin Jonathan Wang, Dr. Yu-Tsun Shao, Dr. Chun-Ming Lai, Haw-Wen Hsiao, Ching-Yu Tsai, SyeMay Chau, Yen-Bo Lin, M.D. MPH, Fang-Chi Liang, Ting-Kai Fan, and Ya-Hsuan Wu gave me enormous help with challenges in either scientific or daily life. We will continue supporting each other to overcome any obstacles in the future.

Last but not least, I would like to acknowledge my friends at UIUC Kendo Club, Dr. Donald Edward McLawhorn Jr., Daniel Sang-Baek Kim, Youngjun Choi, Khoi-Nguyen Mac, Junhao Pan, Jennifer Kusumah, Ewan Yulun Bohannon, Doris Jung-Lin Lee, Younghwan Lee. You all taught me how to reach the goals and never give up.

*To Yan Yang (my wife), Shu-Chen Chao (my Mother), Wei-Ming Tseng (my Father),  
Yung-Fang Tseng (my Sister), Chi-Chang Tseng (my Brother), and my childhood dream*

## TABLE OF CONTENTS

<b>LIST OF FIGURES</b> .....	ix
<b>LIST OF TABLES</b> .....	xvi
<b>CHAPTER 1: INTRODUCTION</b> .....	1
1.1. Motivation .....	1
1.2. Definition of High-Entropy Materials.....	2
1.3. Objectives and Scope of Research .....	3
<b>CHAPTER 2: LITERATURE REVIEW</b> .....	5
2.1. Core Effects of High-Entropy Materials .....	5
2.1.1. High-entropy effect .....	5
2.1.2. Lattice distortion effect .....	7
2.1.3. Sluggish diffusion effect .....	8
2.1.4. Cocktail effect .....	9
2.2. Chemical Selection Rules for High-Entropy Alloys .....	10
2.3. Current Status of High-Entropy Oxides .....	12
2.4. Binary Lanthanide Oxide Materials .....	17
2.5. Ternary Lanthanide Oxide Materials.....	23
<b>CHAPTER 3: EXPERIMENTAL PROCEDURES</b> .....	28
3.1. Modified Thermodynamic Definition of High-Entropy Ceramics .....	28
3.2. Materials Design—High-Entropy Lanthanide Oxides (HELOs).....	30
3.3. Materials Synthesis .....	37
3.4. Characterizations .....	40
3.4.1. Powder X-ray diffraction .....	40
3.4.2. Microstructure characterization .....	46
<b>CHAPTER 4: PHASE IDENTIFICATION AND STABILITY OF MIDDLE LANTHANIDE HELO— (Gd<sub>0.4</sub>Tb<sub>0.4</sub>Dy<sub>0.4</sub>Ho<sub>0.4</sub>Er<sub>0.4</sub>)O<sub>3</sub></b> .....	48

4.1. Crystal Structure and High-Temperature Stability of $(\text{Gd}_{0.4}\text{Tb}_{0.4}\text{Dy}_{0.4}\text{Ho}_{0.4}\text{Er}_{0.4})\text{O}_3$ (GTDHEO) .....	48
4.2. Characterization of GTDHEO.....	55
4.2.1. Coefficient of thermal expansion of GTDHEO .....	55
4.2.2. Elemental distribution in GTDHEO crystal structure.....	58
4.2.3. Valence configuration of GTDHEO.....	61
4.2.4. Magnetic property of GTDHEO .....	63
4.3. Conclusions .....	65
CHAPTER 5: CRYSTAL STRUCTURE IDENTIFICATION OF MULTI-COMPONENT OXIDES AT AMBIENT CONDITIONS.....	67
5.1. Crystal Structure of a System with Small Based Lanthanides (Lu, Yb, Tm, Er) (LYTE).....	67
5.2. Crystal Structure of the System with Large Based Lanthanides (La, Ce, Pr, Nd) (LCPN).....	77
5.3. Homogeneity of High-Entropy Lanthanide Oxide Systems .....	82
5.4. Conclusions .....	87
CHAPTER 6: STRUCTURAL STABILITY AND TRANSFORMATIONS IN MULTI-COMPONENT OXIDES BELOW 2000°C.....	89
6.1. Phase Evolution and Lattice Parameters of the LYTE System .....	89
6.2. Phase Evolution and Lattice Parameters of the LCPN System.....	105
6.3. The Hypothesis of Stability with respect to LCPN Phase Transformations .....	122
6.4. Thermal Expansions of Single-Phase High-Entropy Lanthanide Oxides .....	129
CHAPTER 7: KEY PARAMETERS OF THE SINGLE-PHASE HIGH-ENTROPY LANTHANIDE OXIDES.....	143
7.1. Size Mismatch ( $\delta$ ) of Constituent Lanthanide Cations .....	143
7.2. Valence Configurations and High-Temperature Stability .....	149
7.3. Mixing Enthalpy and Mixing Entropy .....	155
CHAPTER 8: MINOR PROJECT .....	161
8.1. High-Temperature Behavior of $(\text{Mg}_{0.2}\text{Co}_{0.2}\text{Ni}_{0.2}\text{Cu}_{0.2}\text{Zn}_{0.2})\text{O}$ .....	161



CHAPTER 9: CONCLUSIONS .....	165
CHAPTER 10: SUGGESTIONS FOR FUTURE RESEARCH.....	168
REFERENCES .....	170

## LIST OF FIGURES

Figure 1. The value of mixing entropy increases with the number of constituent components. The increment of entropy becomes less significant as the number of components increase. Based on the definition of high-entropy materials, the value of mixing entropy should be equal to or more than  $1.61R$ , which value results from five components mixing in an equal molar ratio.  $R$ : gas constant  $8.314 \text{ J/mol}\cdot\text{K}$  ..... 6

Figure 2. The lattice distortion effect of high-entropy materials is due to the size difference of constituent elements. In HECs, the different sizes in polyhedral sites can induce lattice distortion throughout the crystal structure. Figure taken from ref. [36] ..... 8

Figure 3. Constituent elements in high-entropy materials are surrounded by different types of constituent components. The sluggish diffusion effect can prevent the segregation of cations in HEC. Figure taken from ref. [37]..... 9

Figure 4. Correlations between Vickers hardness and yield strength in HEAs, composites, conventional alloys, ceramics, and glass. Figure taken from ref. [39] ..... 10

Figure 5. Statistical analysis of multi-component ( $n>5$ ) alloys as a function of mixing enthalpy,  $\Delta H_{\text{mix}}$ , and atomic size mismatch,  $\delta$ . The solid solution HEAs were constrained in the region when the value of  $\Delta H_{\text{mix}}$  is either slightly positive or negative, and the atomic size mismatch is small. Figure taken from ref. [25]..... 12

Figure 6. The phase diagram of lanthanide sesquioxides,  $M_2O_3$ , as a function of temperature. Structures including: A-type: hexagonal structure, B-type: monoclinic structure, C-type: cubic-bixbyite structure, H-type: tilted hexagonal structure, X-type: tilted cubic structure. Figure taken from ref. [58]..... 18

Figure 7. The C-type cubic-bixbyite structures can be derived from eight fluorite structures with oxygen vacancies involved. The bixbyite structure can be naturally found in the middle and heavy lanthanide (Sm-Lu) sesquioxides as well as yttrium sesquioxides. Figure taken from ref. [64] ..... 19

Figure 8. The structure of lanthanide oxide  $Ce_{1-x}Nd_xO_{2-y}$ . The fraction of fluorite (F-phase) and C-type cubic-bixbyite (C phase) phases coexist in the region  $0.4 \leq x \leq 0.7$ . The fluorite phase dominates in the cerium-rich sample, and vice versa. Figure taken from ref. [93] ..... 26

Figure 9. Ternary lanthanide oxides, with perovskite structures, have been observed as metastable phases at high temperatures ( $>1000^\circ\text{C}$ ). Those phases can be found when the size mismatch between two lanthanides is large, with  $t_{\text{IR}}$  values exceeding 0.847. Other ternary oxides exhibiting C-type cubic-bixbyite structures experience similar phase transformations as the middle lanthanide sesquioxides ( $Gd_2O_3\text{-}Ho_2O_3$ )..... 27

Figure 10. The configurational entropy ( $\Delta S_{\text{conf}}$ ) parameter varies for different stoichiometries between cations and anions as a function of the number of constituent cations. The mixing entropy contribution from anions is significant and should be considered. R: gas constant 8.314 J/mol·K.....29

Figure 11. Room-temperature structures and high-temperature structural transformations of chosen lanthanide sesquioxides. The systems were selected from either the four largest cations (La, Ce, Pr, Nd) or the smallest cations (Lu, Yb, Tm, Er) as the base, and adding the fifth cation in equimolar ratios to form the five-component oxides, respectively.....36

Figure 12. The process of polymeric steric entrapment. The long-chain polymer can entrap cations in the solution to prevent cation segregation; in other words, ensure that the configurational entropy is maximized. After drying out water at 200°C, the added cations are homogeneously entrapped in the long-chain polymer. ....38

Figure 13. Schematic diagram of sample preparation for powder X-ray diffraction experiment in the quadrupole lamp furnace capable of reaching 2000°C in air.....41

Figure 14. The quadrupole lamp furnace installed at APS 33BM-C. The bottom-right schematic is modified from ref. [150].....42

Figure 15. Schematic of conical nozzle levitator at 6ID-D. (a) The bead sample was heated by a CO<sub>2</sub> laser, up to 3000°C. The X-ray beam was focused on the top of the vertically spinning bead. (b) The spherical beads were prepared by the vibration method, where the major ingredients of the tested sample and additives bounce in a constraint area.[152] The edges of a sample were smoothed over time and became a spherical bead. ....43

Figure 16. The process of integrating a 2D area diffraction pattern to 1D data. (a) The data obtained from a 2D detector plate. (b) The diffractions emitted from sapphire capillary were masked out (red circle). The section of the diffraction ring was chosen for integration. (c) Final 1D diffraction data after integration, without the interference of sapphire diffractions .....45

Figure 17. Schematic of powder sample preparation process for microstructure analysis. After passing through the cascade impactor, small powder particles (<0.18μm) were collected on 400 mesh copper grids. ....47

Figure 18. In situ high-temperature X-ray diffraction patterns of 600°C/2h-calcined, multi-component precursor in the temperature range of 600°C to 1514°C (multiple phases were formed below 1149°C). Above 1149°C, the high-entropy, lanthanide sesquioxide, Gd<sub>0.4</sub>Tb<sub>0.4</sub>Dy<sub>0.4</sub>Ho<sub>0.4</sub>Er<sub>0.4</sub>O<sub>3</sub>, having a bixbyite structure became single-phase and remained stable up to 1514°C. The temperatures of in situ experiments were determined via a platinum standard. Representative data were selected from 15 powder diffraction patterns. ....49

Figure 19. Refinement results of the in-situ cooling X-ray diffraction. No transformation was observed from 1487°C to room-temperature. ....	52
Figure 20. Schematic of the heat treatments for the stability study. The single-phase, solid solution GTDHEO was prepared at 1200°C and then annealed at 600°C, 800°C, and 1000°C for 10 hours, respectively.....	54
Figure 21. Phase transformation reversibility of $Gd_{0.4}Tb_{0.4}Dy_{0.4}Ho_{0.4}Er_{0.4}O_3$ (GTDHEO) upon cooling. X-ray powder diffraction patterns of the samples experiencing the cooling treatments were identical. The cubic-bixbyite structure remained stable after 10 hours of annealing. ....	54
Figure 22. The cubic lattice parameter (a) as a function of temperature (T) for the bixbyite GTDHEO structure. The lattice parameters were analyzed from in situ heating X-ray diffraction patterns obtained from room temperature to 1639°C. The lattice expanded as temperature increased. The polynomial curve fitted the trend of the lattice parameter with an R-squared value of 0.9994. ....	57
Figure 23. The evolution of the coefficient of linear thermal expansion in the GTDHEO sample, from room temperature to about 1600°C .....	58
Figure 24. TEM diffraction of the high-entropy, lanthanide sesquioxide. (a) Selected area electron diffraction (SAED) pattern of the single-phase, solid solution GTDHEO taken down the $\langle 111 \rangle$ direction matches with the simulated pattern (b) of a bixbyite structure containing five lanthanide cations. The simulated pattern was constructed from the high precision, synchrotron-sourced, X-ray diffraction results. The cross marks in the simulated pattern represent electron double diffraction reflections. ....	59
Figure 25. HAADF and ABF images were taken from the $\langle 110 \rangle$ direction and atomic resolution elemental mappings of GTDHEO. It is seen that five constituent cations were homogeneously distributed in the elemental maps. The anion/cation positions, obtained via the CIF file generated by XRD results, are overlaid on the ABF image. ....	60
Figure 26. The color of the crystallized GTDHEO powder sample. Based on the yellowish-brown color, trivalent and tetravalent terbium might have coexisted in the bixbyite structure. ....	62
Figure 27. XPS spectra of 4d orbital electrons in selected lanthanides. Compared to terbium sesquioxide, the terbium oxides are composed of a mixture of trivalent and tetravalent, $Tb_7O_{12}$ and $Tb_{11}O_{20}$ , involving additional peaks in binding energy at 155-170eV. The binding energy of lanthanide elements (Er, Ho, Dy) in $Gd_{0.4}Tb_{0.4}Dy_{0.4}Ho_{0.4}Er_{0.4}O_3$ overlap with the tetravalent terbium element. ....	63
Figure 28. Magnetic susceptibility of the high-entropy, lanthanide sesquioxide, GTDHEO from 5-400K. This oxide has paramagnetic susceptibility. The inverse magnetic molar susceptibility	

has a linear relationship with temperature. The molar susceptibility ( $\chi_m$ ) at room temperature follows the rule of mixtures (ROM) of mono-cation sesquioxides. .... 65

Figure 29. X-ray diffraction patterns of the candidates in the LYTE system at room temperature. The LYTELa sample exhibits the coexistence of bixbyite and perovskite structures. Other LYTE samples have identical single-phase bixbyite structure. .... 69

Figure 30. Intensity maps of crystallized LYTE samples ..... 70

Figure 31. The cations (yellow-green) in fluorite structure (a) have a similar arrangement with the cations in the cubic-bixbyite structure (b) in all observable planes as seen by X-ray diffraction (c). .... 73

Figure 32. The color of crystallized powder samples in the LYTE system ..... 75

Figure 33. The size mismatch ( $\delta$ ) as a function of the lattice parameter obtained via the X-ray diffraction patterns. The mismatch parameters were calculated under the circumstances that (a) all trivalent states are in 6-fold coordination, and (b) Ce and Pr in tetravalent states are in 8-fold coordination. The lattice parameters increase as a larger fifth cation (larger  $\delta$ ) is incorporated in the bixbyite crystal structure. .... 76

Figure 34. X-ray diffraction patterns of candidates in LCPN system at room temperature. All synthesized samples became single-phase solid solutions after crystallization..... 78

Figure 35. Intensity maps of crystallized LCPN samples..... 79

Figure 36. The colors of crystallized powder samples in the LCPN system ..... 80

Figure 37. The size mismatch ( $\delta$ ) as a function of the lattice parameter in the LCPN system obtained via X-ray diffraction patterns. The lattice parameters of HELOs decreased as the smaller fifth cations (larger  $\delta$ ) were added to the structure. .... 82

Figure 38. TEM diffraction of the LYTECe sample. The selected area electron diffraction (SAED) patterns were taken down different zone axes in different crystals. The measured SAD patterns matched with corresponding simulated patterns based on crystallographic information files (CIF) generated by XRD Rietveld refinement. .... 84

Figure 39. HAADF, ABF images, and atomic resolution elemental mappings were taken from the  $\langle 110 \rangle$  direction of LCPN<sub>Lu</sub>. It is seen that five constituent cations were homogeneously distributed in the elemental maps. The anion/cation positions, obtained via the CIF file generated by XRD results, perfectly matched with the TEM microscopy maps. .... 86

Figure 40. Rietveld refinement of the LYTEO powder ..... 91

Figure 41. Rietveld refinement of the LYTEY powder ..... 92

Figure 42. Rietveld refinement of the LYTEDy powder ..... 93

Figure 43. Rietveld refinement of the LYTETb powder..... 94

Figure 44. Rietveld refinement of the LYTEGd powder ..... 95

Figure 45. Rietveld refinement of the LYTESm powder .....	96
Figure 46. Rietveld refinement of the LYTEND powder .....	97
Figure 47. Rietveld refinement of the LYTEPr powder.....	98
Figure 48. Rietveld refinement of the LYTECe powder.....	99
Figure 49. Rietveld refinement of the LYTELa powder .....	100
Figure 50. XRD patterns of LYTE candidates (LYTEY-LYTEGd) obtained with the conical nozzle levitator. The droplet symbol indicates melting during the in-situ experiment.....	102
Figure 51. XRD patterns of LYTE candidates (LYTESm-LYTECe) obtained with the conical nozzle levitator. The droplet symbol indicates melting during the in-situ experiment.....	103
Figure 52. The zoomed-in view of XRD patterns obtained from the LYTECe sample. The CeO <sub>2</sub> having the fluorite structure became distinguishable from the bixbyite structure above 1300°C.....	104
Figure 53. Rietveld refinement of the LCPNO powder .....	108
Figure 54. Rietveld refinement of the LCPNSm powder .....	109
Figure 55. Rietveld refinement of the LCPNGd powder .....	110
Figure 56. Rietveld refinement of the LCPNTb powder .....	111
Figure 57. Rietveld refinement of the LCPNDy powder .....	112
Figure 58. Rietveld refinement of the LCPNY powder .....	113
Figure 59. Rietveld refinement of the LCPNEr powder .....	114
Figure 60. Rietveld refinement of the LCPNTm powder .....	115
Figure 61. Rietveld refinement of the LCPNYb powder .....	116
Figure 62. Rietveld refinement of the LCPNLu powder .....	117
Figure 63. XRD patterns of LCPN candidates (LCPNSm-LCPNDy) obtained in the conical nozzle levitator. The droplet symbol indicates melting during the in-situ experiment.....	120
Figure 64. XRD patterns of LCPN candidates (LCPNY-LCPNLu) obtained in the conical nozzle levitator. The droplet symbol indicates melting during the in-situ experiment. ....	121
Figure 65. XRD patterns of LCPNEr under three different heat treatments. The orange lines indicate the D-type phase. Secondary phases were found in the powder sample after fast-cooling from 1673°C by in-situ measurements. The annealed sample had approximately identical phase to the single-phase HELO synthesized at 1150°C. ....	123
Figure 66. Possible routes for phase transformations involved in most of the LCPN candidates.....	125
Figure 67. XRD patterns of LCPNLu and LCPNTb samples. The orange and purple lines were diffraction peaks from F-type and D-type structures, respectively. LCPNTb exhibited approximately identical patterns in the annealed sample (blue) and single-phase sample (black).	

A coexistence of perovskite structure and D-type structure were observed in the annealed LCPN <sub>Lu</sub> sample.....	127
Figure 68. Possible routes for phase transformations involved in the LCPN <sub>Tb</sub> sample. The rapid, reversible transformation between F-type fluorite and D-type bixbyite structures occurred at ~790°C, followed by similar high-temperature behavior observed in other LCPN candidates.	128
Figure 69. The evolution of lattice parameters of LYTE HELOs obtained in-situ in the quadrupole lamp furnace.....	130
Figure 70. Evolution of the coefficients of thermal expansion among the LYTE systems. All candidates exhibited positive thermal expansions in their cubic structures. ....	135
Figure 71. The evolution of lattice parameters in LCPN HELOs obtained in-situ in the quadrupole lamp furnace.....	137
Figure 72. The evolution of the coefficients of thermal expansion among the LCPN system (except for LCPN <sub>Tb</sub> ). All candidates exhibited positive thermal expansions in their cubic structures. ....	141
Figure 73. The evolution of thermal expansion coefficients in LCPN <sub>Tb</sub> . The tendency changed after the phase transformation from the F-type fluorite structure to the D-type tilted fluorite structure.....	142
Figure 74. Summary of high-entropy oxides (HEOs) as a function of configurational entropy and size mismatch ( $\delta$ ). In this research, most of the designed high-entropy lanthanide oxides became a single-phase solid solution (red circle), while two of them formed secondary phases (blue “X” cross). The contribution from configurational entropy was not significant, due to the cation-anion arrangements in ceramics. For most of the single-phase HEOs, the threshold of $\delta$ was determined to be around 7.0. R: gas constant 8.314 J/mol·K .....	147
Figure 75. XRD patterns obtained from different levels of lanthanum contained in the LYTEL <sub>a</sub> candidates. The amount of secondary phase(s) was dominated by the lanthanum content. ..	149
Figure 76. XRD patterns obtained from LCPN <sub>Tb</sub> candidate materials having varying terbium compositions. The structure remained fluorite within the composition of 11 mol% terbium involved in the cations. The bixbyite structure showed up with a further decrease ( $x=0.059$ ) of terbium cations. The diffraction intensity was expressed as a log scale for better differentiation between these two structures. ....	153
Figure 77. The relationship between the valence states and the final crystal structures. In the LYTE system, the maximum non-trivalent cations came from one constituent cation (20 mol%). As the non-trivalent cation (Ce, Pr, Tb) content in HELOs increases, the structure can be modified from C-type bixbyite ( $M_2O_3$ ), tilted fluorite ( $M_2O_{3.5}$ ) to fluorite ( $MO_2$ ) structures.	155

Figure 78. Rietveld refinement of the MCCZN sample, obtained by the conical nozzle levitator ..... 162

Figure 79. The MCCZN sample became volatile as the temperature reached above 2000°C, under the exposure to the CO<sub>2</sub> laser. .... 163

Figure 80. SEM/EDS analyses of the deformed MCCZN bead after heat treatment at >2000°C. The remnant phase was dominated by the presence of magnesium and oxygen. .... 164



## LIST OF TABLES

Table 1. The structure, configurational mixing entropy ( $\Delta S_{\text{conf}}$ ), and size mismatch ( $\delta$ ) of reported high-entropy oxides .....	15
Table 2. The common binary oxide structures of lanthanides and yttrium in descending order of cation radii in trivalent and six-fold coordinates. Data obtained from the International Center for Diffraction Data (ICDD) database and literature [58-60, 62, 65, 66].....	20
Table 3. Oxidation energies in electron volts between lanthanide sesquioxides and dioxides. The negative energy indicates that the material prefers to exist in the dioxide form. Table taken from ref. [67] .....	22
Table 4. Color of the trivalent lanthanide, yttrium ions and tetravalent cerium, praseodymium, and terbium [82, 84].....	23
Table 5. Ternary oxides structures of the lanthanides and yttrium. Data obtained from the International Center for Diffraction Data (ICDD) database and literature [91-93, 97] .....	25
Table 6. Reported cation radii with respect to valence configuration and coordination number [49].....	32
Table 7. Crystal structures, cation coordination numbers (CN), cation radii ( $R_c$ ), and magnetic molar susceptibilities ( $\chi_m$ ) of mono-cation lanthanide oxides .....	34
Table 8. The chemical information, abbreviation, and cation size mismatch ( $\delta$ ) of chosen candidates. The value of $\delta$ is calculated in the single-phase situation. ....	37
Table 9. Detailed information of synchrotron sourced X-ray diffraction beamline.....	45
Table 10. The evolution of HELO sample $\text{Gd}_{0.4}\text{Tb}_{0.4}\text{Dy}_{0.4}\text{Ho}_{0.4}\text{Er}_{0.4}\text{O}_3$ . The temperatures were identified by the platinum standard.....	50
Table 11. The evolution of lattice parameters in the single-phase GTDHEO.....	56
Table 12. Room-temperature structures of LYTE candidates and phase identification reference.....	71
Table 13. Room-temperature structures of LCPN candidates and phase identification references .....	81
Table 14. The atomic percentage of each cation in the LYTE and LCPN systems .....	87
Table 15. Transition temperatures identified by the in-situ heating X-ray diffractions .....	118
Table 16. Lattice parameters ( $a$ ) of cubic-bixbyite structures in LYTE HELOs corresponding to temperature (T) .....	132
Table 17. Coefficients of the second-order polynomial fitting curves ( $y = a + bT + cT^2$ ) in LYTE HELOs .....	133
Table 18. The detail values of the coefficients of thermal expansion ( $y = a + bT$ ) in LYTE HELOs .....	134

Table 19. Cubic lattice parameters ( $a$ ) of single-phase structures in LCPN HELOs corresponding to temperature (T) .....	139
Table 20. Coefficient of the second-order polynomial fitting curves ( $y = a + bT + cT^2$ ) in LCPN HELOs .....	140
Table 21. The detailed equations for the coefficients of thermal expansion ( $y = a + bT$ ) in LCPN HELOs .....	142
Table 22. Configurational entropy and size mismatches ( $\delta$ ) of synthesized candidates.....	145
Table 23. The molcular composition (mol %) of tetravalent cations (Bold, Red) among constituent cations.....	151
Table 24. Formation enthalpy ( $\Delta H_{f(298K)}$ , kJ/mol), transition enthalpy ( $\Delta H_{trso}$ , kJ/mol),, and standard entropy (J/mol·K) in mono-cation lanthanide oxides [62] .....	159
Table 25. Melting points of binary oxides [146].....	164

# CHAPTER 1: INTRODUCTION

## 1.1. Motivation

In general, research in materials science is mainly focused on a single, binary, or ternary system. Due to the complex reactions and thermodynamics in constituent compounds, materials with multiple components usually form composites instead of a single-phase solid solution. In 2004, high-entropy alloys (**HEAs**) were first reported where the definition of a single-phase alloy describes at least five equimolar mixed metals in a concentration range of 5-35 atomic percent.[1-3] HEAs have been found to exhibit advanced mechanical properties due to four effects: (1) a high-entropy effect, (2) a lattice distortion effect, (3) a sluggish diffusion effect, and (4) a “cocktail” effect.[3-6] Compared to metal alloy systems, research in high-entropy oxides (**HEOs**) started only recently in 2015.[7] Even though in a very early stage, the reported HEO ( $\text{Co}_{0.2}\text{Cu}_{0.2}\text{Mg}_{0.2}\text{Ni}_{0.2}\text{Zn}_{0.2}\text{O}$ ) containing aliovalent dopants ( $\text{Li}^+$ ), had exhibited an astonishing tailorable electrochemical property, which had a promising application in all-solid-state battery cells.[8] Moreover, other works of literature presented improvements in mechanical [9, 10], magnetic [11], and optical properties [12]. Beyond oxide systems, the research into high-entropy ceramics (**HECs**) has been extended to carbides, borides, nitrides, sulfides, and fluorides.[13-18] However, limited fundamental and systematic studies in this field have been reported. The current studies on developing novel high-entropy ceramics were time-consuming and material-wasting through the “trial and error” method. Moreover, designing a new single-phase, high-entropy material is challenging without the knowledge of the formation mechanism. The formation of a multi-component system often suffers from phase separation during synthesis, resulting in multiple phases instead of single-phase materials. Here, this research provided a protocol for cation

selection in order to synthesize high-entropy ceramics and explore the next generation of structure-stabilized ceramics.

## 1.2. Definition of High-Entropy Materials

The field of high-entropy materials includes high-entropy alloys (**HEAs**) and high-entropy ceramics (**HECs**). The definition of these high-entropy materials is based on the value of configurational mixing entropy ( $\Delta S_{conf}$ ):

$$\Delta S_{conf} = -R \sum_{i=1}^N x_i \ln x_i \quad \{1\}$$

Where  $x$  represents the mole fraction of elements in the crystal structure, and  $R$  is the universal gas constant  $8.314 \text{ J/mol}\cdot\text{K}$ . Yeh et al. proposed that HEAs are materials with  $\Delta S_{conf} \geq 1.61R$ , which is the value for five equimolar elements in an alloy system.[19] In HECs, the configurational entropy can reach  $1.61R$  when cations are solely considered in equation {1}. In general, this number  $1.61R$  was initially defined by the five-component system in a high-entropy alloy system. As a result, the value is less significant compared to the effect in stabilizing crystal structure, which can be explained via thermodynamic calculations. According to the following equation, the Gibbs free energy decreases as the entropy term increases:

$$\Delta G_{mix} = \Delta H_{mix} - T\Delta S_{mix} \quad \{2\}$$

Where  $\Delta G_{mix}$ : Gibbs free energy of mixing ( $\text{kJ mol}^{-1}$ )

$\Delta H_{mix}$ : enthalpy of mixing ( $\text{kJ mol}^{-1}$ )

$\Delta S_{mix}$ : entropy of mixing ( $\text{kJ K}^{-1}\text{mol}^{-1}$ )

$T$ : temperature (K)

Assuming the enthalpy value is constant in a crystal structure, the entropy value dominates, especially under a high-temperature environment, leading to lower the free energy. The entropy of

mixing ( $\Delta S_{mix}$ ) is contributed from multiple factors, such as configurational mixing entropy ( $\Delta S_{conf}$ ), vibrational mixing entropy ( $\Delta S_{vib}$ ), electric mixing entropy ( $\Delta S_{elec}$ ), and magnetic mixing entropy ( $\Delta S_{mag}$ ). If the single-phase structure has the lowest free energy, compared to other multi-component secondary structures, a single-phase, high-entropy material can be synthesized. The critical effects of high-entropy materials are introduced in the next chapter.

At this point, the definition of high-entropy materials is controversial. Different concepts in describing what factors those materials should follow are still unclear.[20] Some research proposed that the multi-phase materials should be included in the high-entropy materials by calculating the configurational entropy of the whole composites system.[3, 5, 19] Besides, new technical terms, including multi-principal element alloys [21, 22], complex concentrated alloys [23], were found to define the materials which were not fulfilled in the requirements of high-entropy materials. Those ideas could confuse the research in this research field. *In this research, the term “high-entropy material” is defined as a single-phase, solid solution containing at least five elements, in alloys, or five cations sitting in one polyhedral site, in ceramics.* The detailed explanation of thermodynamics calculations is introduced in Section 2.1.

### 1.3. Objectives and Scope of Research

This work aims to provide an initial protocol for cation selection in synthesizing high-entropy oxides, as well as to explore the effects of different parameters in structural stability. The candidates were designed via considering all binary oxides in the online-sourced Materials Project [24] and International Center for Diffraction Data. The main questions initially posed were:

1. What are the possible parameters controlling the formation of HEOs?
2. Which systems of candidates are appropriate in materials design?
3. Which synthesis method would be ideal for synthesizing HEOs?

4. What is the possible limit of chosen parameters, such as cation radii mismatch and configurational entropy?
5. Would a single-phase, high-entropy structure be stable from room temperature to extreme conditions (up to 2000°C)?
6. If phase transformation(s) are involved, are they reversible or not?

This work reveals essential design criteria and proposes an ideal synthesis method in this novel field of ceramic-HEOs. By understanding the effects of different combinations of cations in HEOs, the concepts can be transferred to other HEC systems, such as carbides, borides, nitrides, and sulfides. Furthermore, controlling the final, high-entropy structures was still unclear due to the limit of HEC reported. This systematic research produces a variety of novel HEOs involving lanthanide elements. Different phases in these HEOs can benefit the ceramic community in future HEOs design. Furthermore, the properties, such as thermal expansion, can be found in this research, through the in-situ experimentation at synchrotron-sourced, X-ray diffraction.

## CHAPTER 2: LITERATURE REVIEW

In this chapter, studies of up-to-date research, including the mechanism of high-entropy materials, as well as current research on HEAs and HEOs, are reviewed. Next, since the candidates chosen for this research are lanthanides, the crystallographic background of both binary and ternary lanthanide oxides are introduced.

### 2.1. Core Effects of High-Entropy Materials

Yet et al. proposed four high-entropy effects: (1) high-entropy effect, (2) lattice distortion effect, (3) sluggish diffusion effect, and (4) cocktail effect.[4, 5, 19, 20] These effects were used to explain the potential for single-phase formation and promising applications of high-entropy materials.

#### 2.1.1. High-entropy effect

As mentioned in Section 1.2, multi-component arrangements in high-entropy materials can increase the configurational entropy in equation {1}, leading to lower Gibbs free energy in equation {2}. Compared to conventional materials, the configurational mixing entropies in HEAs are relatively high, due to the large number ( $\geq 5$ ) of constituent elements. Figure 1 represents the relationship between configurational entropy and the number of component(s) in the HEAs system. The configurational entropy increases with the number of constituent components. However, the increments of configurational entropy become less significant as the number of constituent elements increase. Yet et al. proposed that one system could reach the “high-entropy” level when  $\Delta S_{conf} \geq 1.61R$ , the value of five elements upon equal molar mixing.[4, 19] According to equation {2}, the contribution from the entropy effect becomes more significant as temperature increases.

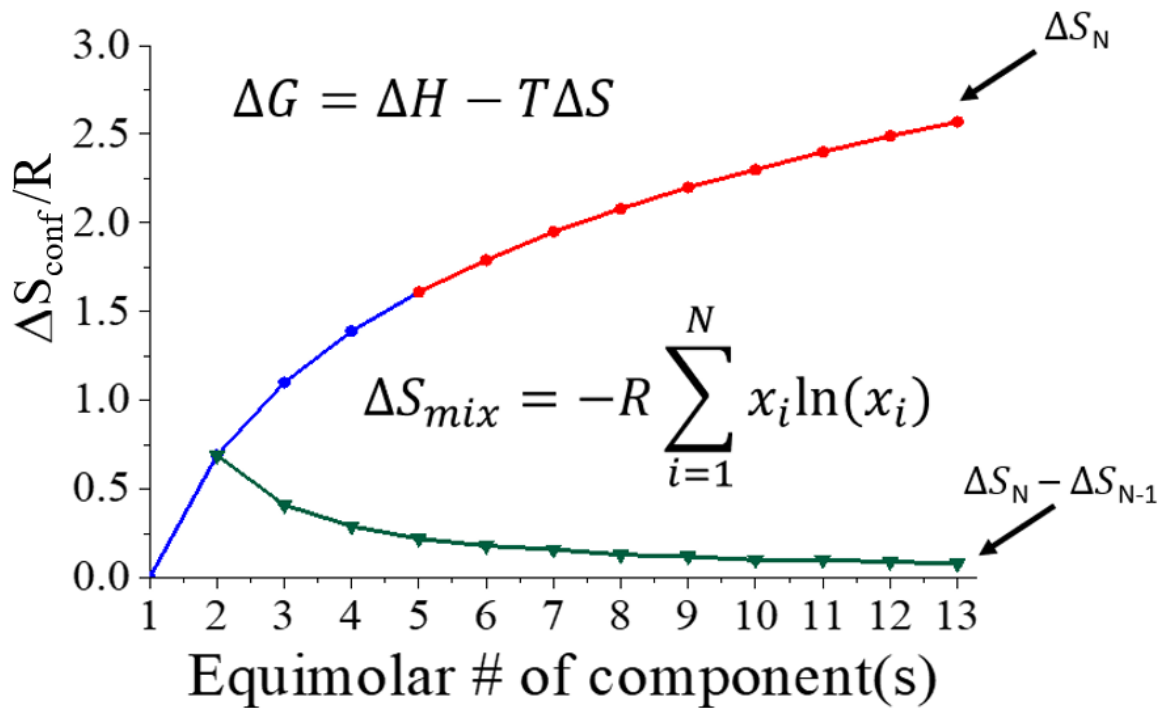


Figure 1. The value of mixing entropy increases with the number of constituent components. The increment of entropy becomes less significant as the number of components increase. Based on the definition of high-entropy materials, the value of mixing entropy should be equal to or more than 1.61R, which value results from five components mixing in an equal molar ratio. R: gas constant 8.314 J/mol·K

In current HEAs research, the concept of high-entropy effects is also applied to the materials with intermetallic phases involved.[1, 25-28] A recent paper has reported that actually more than 80% of discovered HEAs were related to multi-phases, instead of single-phase solid solutions.[29] The concept of those multi-phase materials, the so-called “complex ordering phase,” might confuse this community due to the ambiguous limitation for the thermodynamic calculation. For example, a recently reported alloy containing five metals, CoCrCuMnNi, exhibited two different face-centered cubic (FCC) phases in the final products.[30] Each FCC phase has at least one element with <7% or >35% in chemical composition. In addition, the configurational mixing



entropy did not reach 1.61R for each FCC phase. These materials disobey the definition of high-entropy alloys. In the HECs system, both anions and cations are involved in the crystal sites which further complicates the high-entropy system. So far, current research only considers cations, neglecting the contribution from anions, in the thermodynamics calculations.[9, 31-33] In order to clarify the concept of HECs, a new thermodynamic definition for HECs is proposed in Section 3.1.

#### 2.1.2. Lattice distortion effect

Severe lattice distortion of high-entropy materials is hypothesized from the size difference of multi-constituent components. Elements with different sizes randomly located in the same crystal sites can generate lattice distortions throughout the structure, leading to defects, which may enhance their mechanical properties.[6, 34] A schematic of lattice distortion is shown in Figure 2. Recently, the evidence of lattice distortion in HEAs has been observed by the direct imaging method using electron nano-diffraction.[35] In HEC, different constituent cations are surrounded by the same type of anions, such as oxygens or carbons. Larger cations sitting in a crystal site can expand the size of a polyhedron; on the other hand, smaller cations shrink the size of the polyhedron. In this case, different sizes of polyhedra also cause severe lattice distortion in the HECs system.

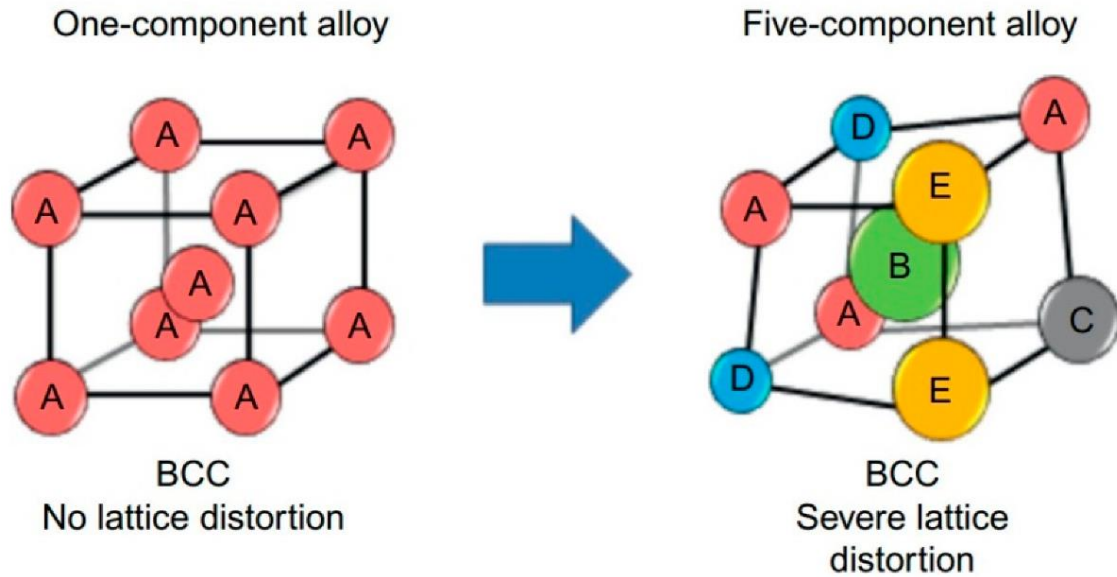


Figure 2. The lattice distortion effect of high-entropy materials is due to the size difference of constituent elements. In HECs, the different sizes in polyhedral sites can induce lattice distortion throughout the crystal structure. Figure taken from ref. [36]

### 2.1.3. Sluggish diffusion effect

The sluggish diffusion effect is also derived from the variation of constituent elements in high-entropy materials. The metals in HEAs system, or cations in HECs system, are homogeneously, randomly distributed in the crystal. One specific metallic element is surrounded by different kinds of components, as shown in Figure 2. In the HECs system, by neglecting anions in a crystal structure, the environment of cations is similar to elements in HEAs. This sluggish diffusion effect can constrain the substitutional diffusion and prevent the aggregation of the same type of cations (Figure 3). In other words, forming secondary phases from high-entropy materials might require considerable input energy and longer reaction times.

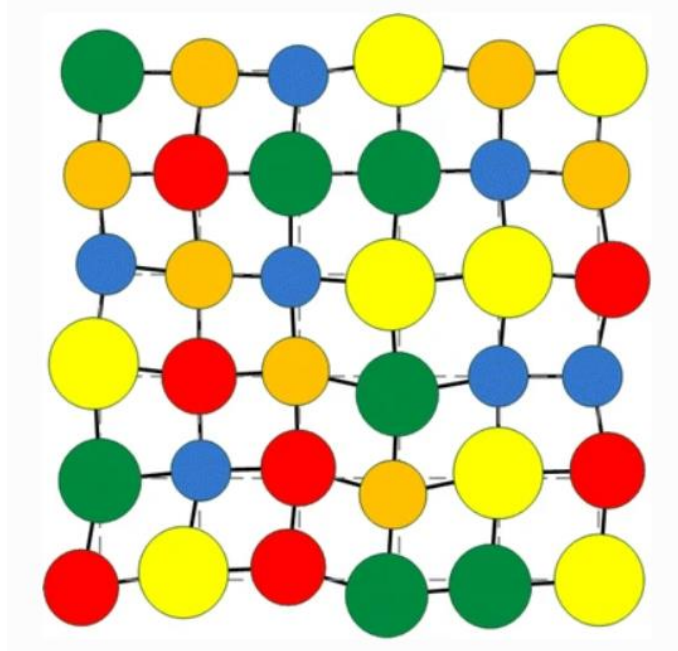


Figure 3. Constituent elements in high-entropy materials are surrounded by different types of constituent components. The sluggish diffusion effect can prevent the segregation of cations in HEC. Figure taken from ref. [37]

#### 2.1.4. Cocktail effect

This colorful phrase is firstly proposed by Ranganathan.[38] The Cocktail effect represents the observation that the physical properties of high-entropy materials might not follow the rule-of-mixtures. Figure 4 illustrates that HEAs tend to have higher mechanical properties, such as hardness and yield strength, compared to conventional alloys.[39, 40] In addition, by altering the composition of aluminum in  $Al_xCoCrCuFeNi$  alloy, the crystal can transform from an FCC structure to a base-centered cubic (BCC) structure.[4] Furthermore, each constituent element in the system can contribute their intrinsic physico-chemical properties to the high-entropy materials. The HEO, Pt/Ru-(NiMgCuZnCo)O, has been found to produce high temperature stability and good catalytic activity in transforming atmospheric  $CO_2$  to CO.[41, 42]

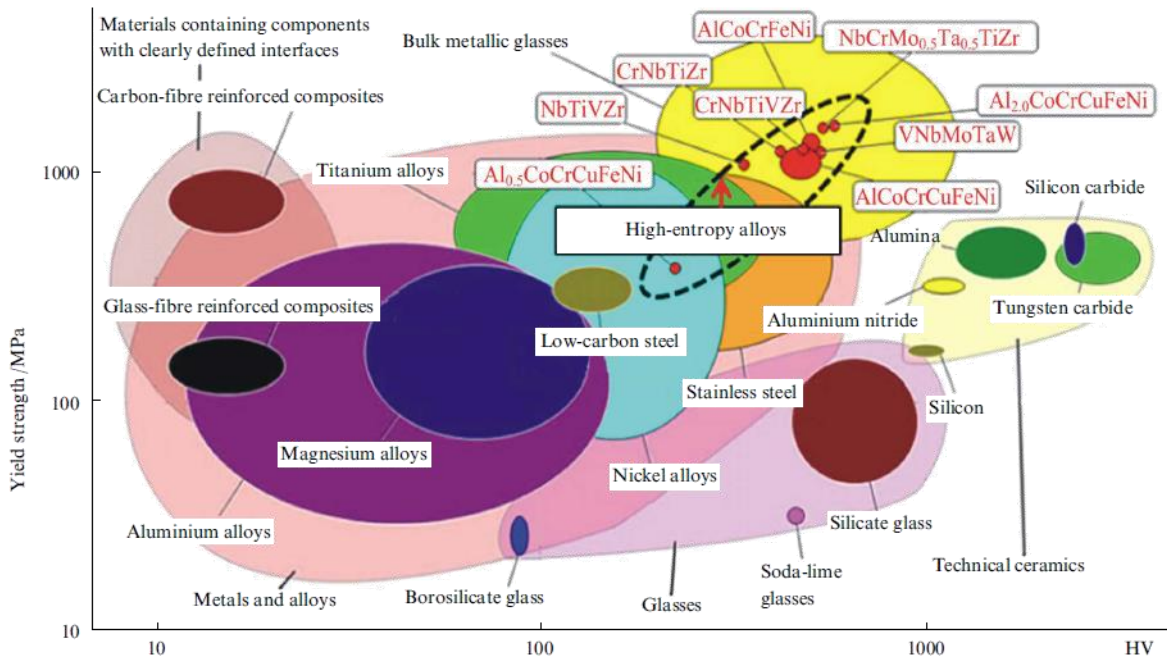


Figure 4. Correlations between Vickers hardness and yield strength in HEAs, composites, conventional alloys, ceramics, and glass. Figure taken from ref. [39]

## 2.2. Chemical Selection Rules for High-Entropy Alloys

In HEAs, five concepts have been popularly accepted as roles in dominating single-phase solid solution and crystal structures: (1) mixing enthalpy,  $\Delta H_{mix}$ , (2) mixing entropy,  $\Delta S_{mix}$ , (3) atomic size mismatch,  $\delta$ , (4) valence electron concentration, and (5) electronegativity.[28, 43-46] Recently, it has been shown that the fourth and fifth parameters only determine the alloy structure, with limited impacts on solid solution predictions.[44] Hence, these two factors would not be addressed here, considering their small inherent effects in ceramic systems. In thermodynamics, the phase stability is dominated by Gibbs free energy, which can be calculated as a function of enthalpy and entropy, as previously mentioned, in equation {2}:

$$\Delta G_{mix} = \Delta H_{mix} - T\Delta S_{mix} \quad \{2\}$$

where  $\Delta G_{mix}$ : Gibbs free energy of mixing ( $\text{kJ mol}^{-1}$ )

$\Delta H_{mix}$ : enthalpy of mixing ( $\text{kJ mol}^{-1}$ )

$\Delta S_{mix}$ : entropy of mixing ( $\text{kJ K}^{-1}\text{mol}^{-1}$ )

$T$ : temperature (K)

In high-entropy materials, the growth of  $\Delta S_{mix}$  decreases as the number of constituent elements increases. Comparing with  $\Delta H_{mix}$ , the influence of  $\Delta S_{mix}$  in HEAs can be neglected since the  $\Delta S_{mix}$  of high-entropy alloys are similar ( $\geq 1.61R$ ). The large number of  $|\Delta H_{mix}|$ , either as a positive or negative value, would lead to phase separations or intermetallic compounds, which are not preferable in formation of single-phase HEAs.[47] The other important parameter is the size mismatch of metallic atoms, which controls the formation of single-phase HEAs.[28] The size mismatch of metallic atoms, denoted as  $\delta$ , is defined as:

$$\delta = \sqrt{\sum_{i=1}^n C_i \left(1 - \frac{r_i}{\bar{r}}\right)^2} \quad \{3\}$$

where  $C_i$  is the atomic fraction of atom (i),  $r_i$  is the atomic radius of an atom (i), and  $\bar{r}$  is the average of atomic radii. Increasing  $\delta$  causes more local distortion in the crystal system, leading to an unstable crystal structure. As shown in Figure 5, the statistical results concluded that the single-phase solid solution HEAs could be synthesized when  $\Delta H_{mix}$  is in the range of  $-11.6 \text{ kJ mol}^{-1} < \Delta H_{mix} < 3.2 \text{ kJ mol}^{-1}$  with a low  $\delta (< 0.066)$ . [25]

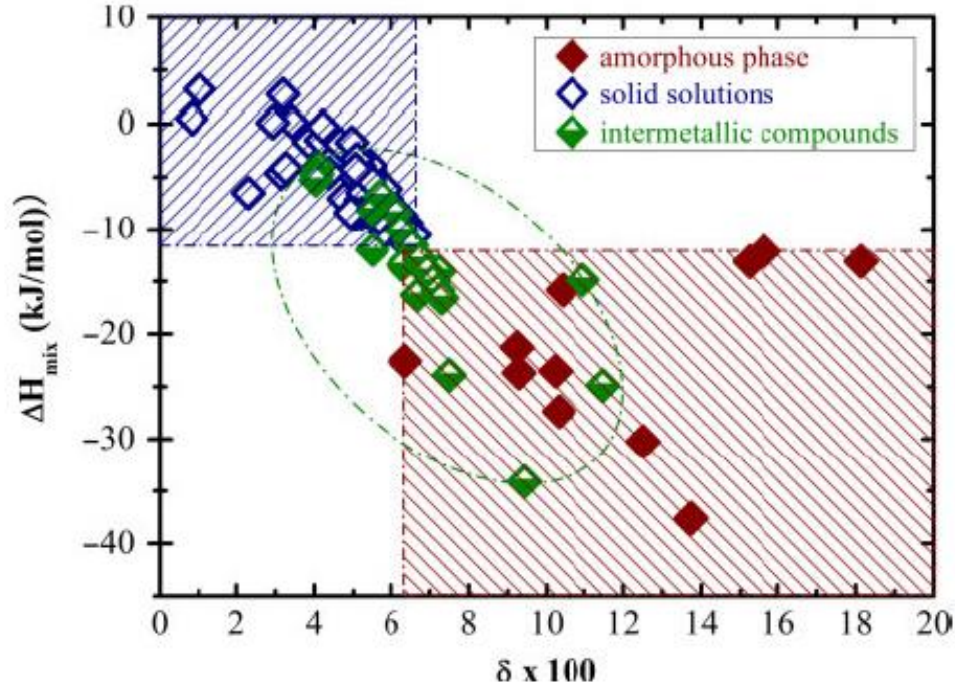


Figure 5. Statistical analysis of multi-component ( $n > 5$ ) alloys as a function of mixing enthalpy,  $\Delta H_{mix}$ , and atomic size mismatch,  $\delta$ . The solid solution HEAs were constrained in the region when the value of  $\Delta H_{mix}$  is either slightly positive or negative, and the atomic size mismatch is small. Figure taken from ref. [25]

### 2.3. Current Status of High-Entropy Oxides

In HEAs, metal atoms are surrounded by other metallic atoms. However, in HEOs, the metallic cations are located at polyhedral sites surrounded by oxygens. The coordinates vary in different types of crystal structures. The  $\Delta H_{mix}$  of a system is only determined by metallic cations, which distribute randomly at different polyhedral sites in a unit cell. The ratio of cation to anion varies with different crystallographic chemistry. The up-to-date, reported HEOs are summarized in Table 1. In this research, HEOs are defined as a single-phase structure consisting of at least five metallic cations randomly located in the same structural sites with the atomic percentage of 5-35%. For example, the sample  $(\text{Co}_{0.2}\text{Cr}_{0.2}\text{Fe}_{0.2}\text{Mn}_{0.2}\text{Ni}_{0.2})_3\text{O}_4$  with a spinel structure, which contains five cations, is not considered to be a HEO for the reason that not all the five constituent cations were

distributed in the same polyhedral sites.[48] In the reported spinel system, five (or six) cations were randomly distributed in two different cation sites. In this case, one of the key effects — “severe lattice distortion” might be compensated by those polyhedral sites with a large size range. The radius of oxygen is constant throughout a ceramic structure. Therefore, the difference in crystallography between HEAs and HEOs leads to the equation for  $\Delta S_{conf}$  in HEAs (Equation {1}) is not applicable to the systems of HEOs. Furthermore, the cation radii in HECs vary with different valence configurations, cation-anion coordination geometries, and sometimes, spin states.[49]

In Table 1, two parameters, configurational entropy ( $\Delta S_{conf}$ ) and size mismatch ( $\delta$ ), were calculated with consideration of the relationship between cations and anions, and cation radii in their specific crystal structures. In the calculation of configurational entropy, both cations and anions are considered in the modified thermodynamics calculations. The calculation detail, as listed in Equation {5}, {6}, and {7}, is introduced in Section 3.1. So far, different types of oxides have been synthesized in the literature. The modified configurational entropies of reported HEOs are at least half compared to the HEAs criteria ( $\Delta S_{conf} \geq 1.61R$ ). Those result is due to oxygen  $\geq 50\%$  occupancy in the HEOs composition, with zero contribution to configurational entropy. In perovskite  $ABO_3$  chemistry, the contribution from both tetrahedral and octahedral sites were weighed to be 50% in the calculation of size mismatch ( $\delta$ ). In this structure, if only one polyhedral site is occupied by the multi-cations, the value in configurational entropy would be significantly low ( $\sim 0.3$ ). The criteria of HEOs, or its larger category HECs, is still unclear and requires a universal definition. A wide range of size mismatch can be found in the HEOs systems, compared to HEAs. In particular, in yttrium-stabilized zirconia (YSZ) based HEOs, all the values exceed 8.0 in size mismatch. This result is caused by the prototype of YSZ, where  $Y^{3+}$  ( $1.019\text{\AA}$ ) is located on the same site as  $Zr^{4+}$  ( $0.84\text{\AA}$ ). Higher tolerance in size mismatch in a prototype structure could

increase the tolerance in fitting a variety of cations. However, the preferred valence configuration might be one of the main factors dominating the cation radii and structural stability, which has not been studied yet. This research provides a brief study of the contribution of oxidation states amongst the constituent cations.



Table 1. The structure, configurational mixing entropy ( $\Delta S_{conf}$ ), and size mismatch ( $\delta$ ) of reported high-entropy oxides

Composition	Structure	$\Delta S_{conf}/R$	$\delta \times 100$	Ref.
<b>MO</b>				
(Co <sub>0.2</sub> Cu <sub>0.2</sub> Mg <sub>0.2</sub> Ni <sub>0.2</sub> Zn <sub>0.2</sub> )O	Rocksalt (NaCl)	0.805	2.6888	[7]
<b>MO<sub>2</sub></b>				
(Ce <sub>0.2</sub> La <sub>0.2</sub> Pr <sub>0.2</sub> Sm <sub>0.2</sub> Y <sub>0.2</sub> )O <sub>2-x</sub>		0.536	7.1647 <sup>^</sup>	
(Ce <sub>0.16</sub> La <sub>0.16</sub> Pr <sub>0.16</sub> Sm <sub>0.16</sub> Y <sub>0.16</sub> Nd <sub>0.16</sub> )O <sub>2-x</sub>	Fluorite	0.597	6.9456 <sup>^</sup>	[50]
(Ce <sub>0.14</sub> La <sub>0.14</sub> Pr <sub>0.14</sub> Sm <sub>0.14</sub> Y <sub>0.14</sub> Nd <sub>0.14</sub> Gd <sub>0.14</sub> )O <sub>2-x</sub>	(CeO <sub>2</sub> )	0.649	6.4284 <sup>^</sup>	
(Ce <sub>0.2</sub> Zr <sub>0.2</sub> Hf <sub>0.2</sub> Ti <sub>0.2</sub> Sn <sub>0.2</sub> )O <sub>2</sub>		0.536	8.9108	[51]
<b>M<sub>2</sub>O<sub>3</sub></b>				
(Ce <sub>0.16</sub> La <sub>0.16</sub> Pr <sub>0.16</sub> Sm <sub>0.16</sub> Y <sub>0.16</sub> Nd <sub>0.16</sub> )O <sub>2-x</sub>		0.717	4.2918 <sup>^</sup>	
(Ce <sub>0.14</sub> La <sub>0.14</sub> Pr <sub>0.14</sub> Sm <sub>0.14</sub> Y <sub>0.14</sub> Nd <sub>0.14</sub> Gd <sub>0.14</sub> )O <sub>2-x</sub>	Bixbyite (Er <sub>2</sub> O <sub>3</sub> )	0.778	4.2585 <sup>^</sup>	[50]
(Gd <sub>0.2</sub> Tb <sub>0.2</sub> Dy <sub>0.2</sub> Ho <sub>0.2</sub> Er <sub>0.2</sub> ) <sub>2</sub> O <sub>3</sub>		0.644	1.8324	[52]
<b>M<sub>5</sub>O<sub>9</sub> (3MO<sub>2</sub>·M<sub>2</sub>O<sub>3</sub>)</b>				
(Hf <sub>0.2</sub> Zr <sub>0.2</sub> Ce <sub>0.2</sub> Y <sub>0.2</sub> Yb <sub>0.2</sub> )O <sub>2-x</sub>		0.557	8.4281	
(Hf <sub>0.2</sub> Zr <sub>0.2</sub> Ce <sub>0.2</sub> Y <sub>0.2</sub> Gd <sub>0.2</sub> )O <sub>2-x</sub>	Fluorite (YSZ)	0.557	9.9736	[9]
(Hf <sub>0.2</sub> Zr <sub>0.2</sub> Ce <sub>0.2</sub> Yb <sub>0.2</sub> Gd <sub>0.2</sub> )O <sub>2-x</sub>		0.557	9.3772	
<b>M<sub>8</sub>O<sub>15</sub> (6MO<sub>2</sub>·M<sub>2</sub>O<sub>3</sub>)</b>				
(Hf <sub>0.25</sub> Zr <sub>0.25</sub> Ce <sub>0.25</sub> )(Y <sub>0.125</sub> Yb <sub>0.125</sub> )O <sub>2-x</sub>		0.560	8.5103	
(Hf <sub>0.25</sub> Zr <sub>0.25</sub> Ce <sub>0.25</sub> )(Y <sub>0.125</sub> Ca <sub>0.125</sub> )O <sub>2-x</sub>	Fluorite	0.560	11.0866	
(Hf <sub>0.25</sub> Zr <sub>0.25</sub> Ce <sub>0.25</sub> )(Y <sub>0.125</sub> Gd <sub>0.125</sub> )O <sub>2-x</sub>	(YSZ)	0.560	9.6281	[9]
(Hf <sub>0.25</sub> Zr <sub>0.25</sub> Ce <sub>0.25</sub> )(Yb <sub>0.125</sub> Gd <sub>0.125</sub> )O <sub>2-x</sub>		0.560	9.1922	
<b>ABO<sub>3</sub></b>				
Sr(Zr <sub>0.2</sub> Sn <sub>0.2</sub> Ti <sub>0.2</sub> Hf <sub>0.2</sub> Mn <sub>0.2</sub> )O <sub>3</sub>	Perovskite	0.322	5.5936 <sup>*</sup>	
Sr(Zr <sub>0.2</sub> Sn <sub>0.2</sub> Ti <sub>0.2</sub> Hf <sub>0.2</sub> Nb <sub>0.2</sub> )O <sub>3</sub>	(SrTiO <sub>3</sub> )	0.322	2.9770 <sup>*</sup>	
Ba(Zr <sub>0.2</sub> Sn <sub>0.2</sub> Ti <sub>0.2</sub> Hf <sub>0.2</sub> Ce <sub>0.2</sub> )O <sub>3</sub>		0.322	5.9595 <sup>*</sup>	
Ba(Zr <sub>0.2</sub> Sn <sub>0.2</sub> Ti <sub>0.2</sub> Hf <sub>0.2</sub> Y <sub>0.2</sub> )O <sub>3-x</sub>	Perovskite	0.322	6.6508 <sup>**</sup>	
Ba(Zr <sub>0.2</sub> Sn <sub>0.2</sub> Ti <sub>0.2</sub> Hf <sub>0.2</sub> Nb <sub>0.2</sub> )O <sub>3</sub>	(BaTiO <sub>3</sub> )	0.322	2.9770 <sup>*</sup>	[53]
(Sr <sub>0.5</sub> Ba <sub>0.5</sub> )(Zr <sub>0.2</sub> Sn <sub>0.2</sub> Ti <sub>0.2</sub> Hf <sub>0.2</sub> Nb <sub>0.2</sub> )O <sub>3</sub>	Perovskite (SrTiO <sub>3</sub> , BaTiO <sub>3</sub> )	0.461 (0.139+ 0.322)	5.7639 <sup>*</sup> (2.7869+ 2.9770)	

\* Cation site in perovskite structure is calculated individually, with a weighting of 50% on each site.

<sup>^</sup> The oxidation states and coordination numbers are normalized based on the base structure (if applicable)

R: gas constant 8.314 J/mol·K

Table 1 (continued). The structure, configurational mixing entropy ( $\Delta S_{conf}$ ), and size mismatch ( $\delta$ ) of reported high-entropy oxides

Composition	Structure	$\Delta S_{conf}/R$	$\delta \times 100$	Ref.
<b>ABO<sub>3</sub></b>				
(Gd <sub>0.2</sub> La <sub>0.2</sub> Nd <sub>0.2</sub> Sm <sub>0.2</sub> Y <sub>0.2</sub> )CoO <sub>3</sub>		0.322	2.2228	
(Gd <sub>0.2</sub> La <sub>0.2</sub> Nd <sub>0.2</sub> Sm <sub>0.2</sub> Y <sub>0.2</sub> )FeO <sub>3</sub>		0.322	2.2228	
(Gd <sub>0.2</sub> La <sub>0.2</sub> Nd <sub>0.2</sub> Sm <sub>0.2</sub> Y <sub>0.2</sub> )MnO <sub>3</sub>		0.322	2.2228	
Gd(Co <sub>0.2</sub> Cr <sub>0.2</sub> Fe <sub>0.2</sub> Mn <sub>0.2</sub> Ni <sub>0.2</sub> )O <sub>3</sub>	Perovskite (GdFeO <sub>3</sub> )	0.322	1.4929-4.7202*~	[32]
La(Co <sub>0.2</sub> Cr <sub>0.2</sub> Fe <sub>0.2</sub> Mn <sub>0.2</sub> Ni <sub>0.2</sub> )O <sub>3</sub>		0.322	1.4929-4.7202*~	
Nd(Co <sub>0.2</sub> Cr <sub>0.2</sub> Fe <sub>0.2</sub> Mn <sub>0.2</sub> Ni <sub>0.2</sub> )O <sub>3</sub>		0.322	1.4929-4.7202*~	
(Gd <sub>0.2</sub> La <sub>0.2</sub> Nd <sub>0.2</sub> Sm <sub>0.2</sub> Y <sub>0.2</sub> ) (Co <sub>0.2</sub> Cr <sub>0.2</sub> Fe <sub>0.2</sub> Mn <sub>0.2</sub> Ni <sub>0.2</sub> )O <sub>3</sub>		0.644 (0.322+ 0.322)	3.7157-6.9430*~	
<b>M<sub>3</sub>O<sub>4</sub></b>				
(Co <sub>0.2</sub> Cr <sub>0.2</sub> Fe <sub>0.2</sub> Mn <sub>0.2</sub> Ni <sub>0.2</sub> ) <sub>3</sub> O <sub>4</sub> <sup>§</sup>	Spinel (Ni <sub>1.43</sub> Fe <sub>1.7</sub> O <sub>4</sub> , NiCr <sub>1.5</sub> Mn <sub>0.5</sub> O <sub>4</sub> , FeCr <sub>2</sub> O <sub>4</sub> , CoFe <sub>2</sub> O <sub>4</sub> )	0.440 (0.220+ 0.220)		[48]
(Co <sub>0.2</sub> Cr <sub>0.2</sub> Fe <sub>0.2</sub> Mn <sub>0.2</sub> Zn <sub>0.2</sub> ) <sub>3</sub> O <sub>4</sub> <sup>§</sup> (Ni <sub>0.2</sub> Cr <sub>0.2</sub> Fe <sub>0.2</sub> Mn <sub>0.2</sub> Zn <sub>0.2</sub> ) <sub>3</sub> O <sub>4</sub> <sup>§</sup>	Same as above (Zn <sup>2+</sup> substitute Co <sup>2+</sup> )	0.440		[54]
(Al <sub>0.167</sub> Co <sub>0.167</sub> Cr <sub>0.167</sub> Fe <sub>0.167</sub> Mn <sub>0.167</sub> Ni <sub>0.167</sub> ) <sub>3</sub> O <sub>4</sub> <sup>§</sup>	Spinel (AB <sub>2</sub> O <sub>4</sub> , A: Mn, Co; B: Fe, Cr, Al, Ni)	0.416 (0.139+ 0.277)	Not HEO <sup>§</sup> (2 sites)	[55]
(Mg <sub>0.2</sub> Ti <sub>0.2</sub> Zn <sub>0.2</sub> Cu <sub>0.2</sub> Fe <sub>0.2</sub> ) <sub>3</sub> O <sub>4</sub> <sup>§</sup>	Spinel (AB <sub>2</sub> O <sub>4</sub> , A: Mg, Ti, Zn, Cu; B: Fe)	0.277		[56]
<b>Amorphous</b>				
10% La <sub>2</sub> O <sub>3</sub> -20% TiO <sub>2</sub> -10% Nb <sub>2</sub> O <sub>5</sub> - 20% WO <sub>3</sub> -20% ZrO <sub>2</sub>	Glass	NA	NA	[57]

\* Cation site in perovskite structure is calculated individually, with a weighting of 50% on each site.

~ Ranging from high spin states to low spin states of constituent cations

§ The spinel structure has two cation sites, where Co and Ni are located at one cation site, Cr and Mn sites are located at the other sites; Fe can be arranged in both sites. In this case, this material did not fulfill the criteria of a HEO.

R: gas constant 8.314 J/mol·K

The term “entropy stabilized oxide” was firstly reported by Rost et al.[7] in the HEO  $\text{Mg}_{0.2}\text{Cu}_{0.2}\text{Ni}_{0.2}\text{Co}_{0.2}\text{Zn}_{0.2}\text{O}$ . The material exhibited a reversible solid-state transformation between multi-phase oxides and a single-phase oxide. The single-phase HEO phase could only be obtained as the temperature reached above 1100°C. Rost et al.[7] claimed that this reversible phase separation was driven by entropy, based on Equation {2}. In this case, a quenching process above the transformation temperature was required for the synthesis of this high entropy oxide. However, quenching could induce thermal shock and cause cracking in a bulk ceramic, which is not favorable in materials production. Djenedic et al.[50] proposed that multi-component, equiatomic, rare-earth oxides can be synthesized without quenching. In their research, lanthanide cations were chosen in the designed HEOs. The author reported that cerium cation played a critical role in the formation of high-entropy, rare-earth oxides. Without cerium, secondary phases formed after the thermal treatments of the multi-component oxides. In addition, the crystal structures are different between HEOs obtained through quenching versus furnace-cooled processes. The HEO,  $(\text{Ce}_{0.16}\text{La}_{0.16}\text{Pr}_{0.16}\text{Sm}_{0.16}\text{Y}_{0.16}\text{Nd}_{0.16})\text{O}_{2-x}$ , exhibit fluorite structure (space group  $\text{Fm}\bar{3}\text{m}$ ) at 750°C, and transform to cubic-bixbyite structure (space group  $\text{Ia}\bar{3}$ ) after air-cooling to room temperature. The structure is characterized by a Cu-sourced X-ray diffractometer (Bruker D8, Bruker AXS Inc., Madison, WI, USA).

#### 2.4. Binary Lanthanide Oxide Materials

The detailed review of common lanthanide oxides is summarized in Table 2, listed in order of decreasing radii under trivalent cation charge and six-fold coordination. As shown in Figure 6, at room temperature ( $\sim 300\text{K}$ ), lanthanide sesquioxides ( $\text{M}_2\text{O}_3$ ) can be separated into either A-type hexagonal structures in the light lanthanides (La-Nd) or the C-type cubic-bixbyite structures in middle and heavy lanthanides (Sm-Lu).[58] As temperature increases, the middle-lanthanide

sesquioxides ( $\text{Sm}_2\text{O}_3\text{-Dy}_2\text{O}_3$ ), can experience the structural transformation from cubic to B-type monoclinic. Above  $2000^\circ\text{C}$ , most of the lanthanide sesquioxides can transform to H-type (tilted hexagonal) and X-type (tilted cubic) structures, before melting.[59] Several researcher have worked to determine the accurate phase transformation temperatures involved in lanthanide sesquioxides.[58-63] Those properties make lanthanides a promising candidate in our formation study of high-entropy oxides.

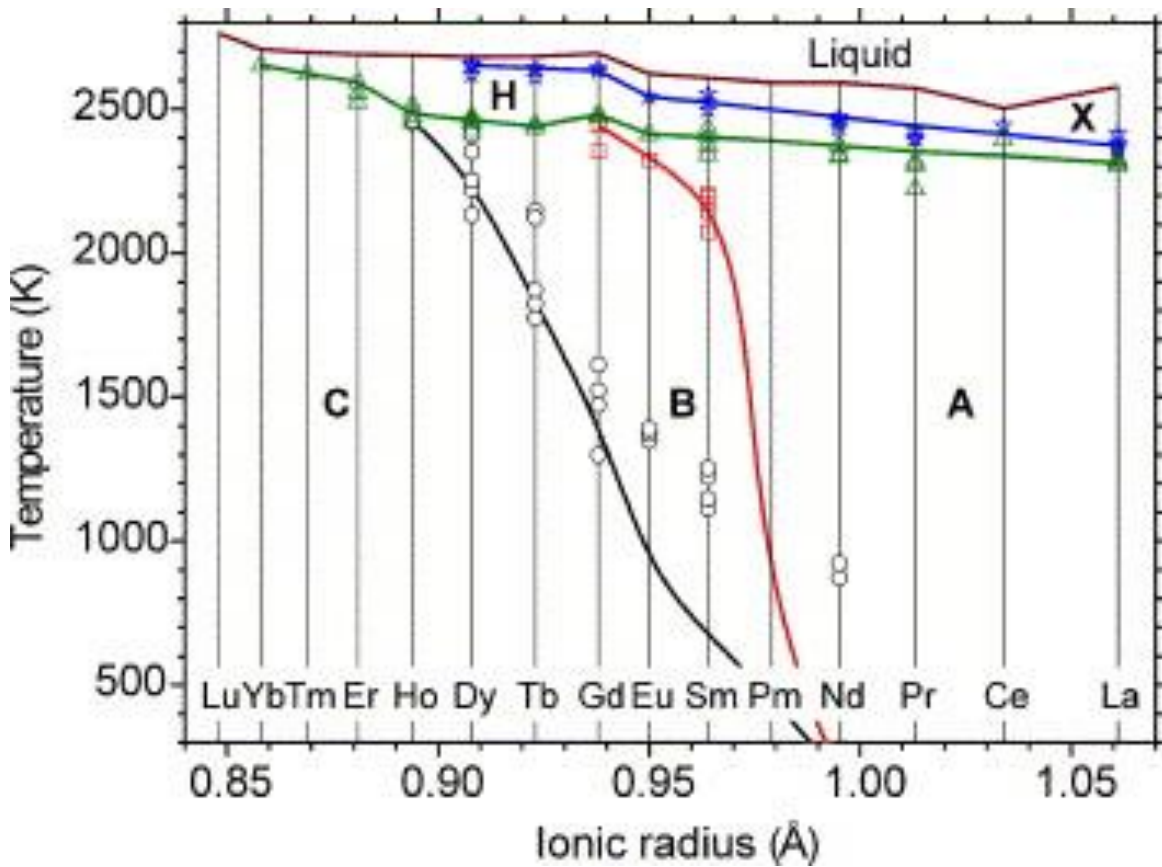


Figure 6. The phase diagram of lanthanide sesquioxides,  $\text{M}_2\text{O}_3$ , as a function of temperature. Structures including: A-type: hexagonal structure, B-type: monoclinic structure, C-type: cubic-bixbyite structure, H-type: tilted hexagonal structure, X-type: tilted cubic structure. Figure taken from ref. [58]

The C-type cubic bixbyite structure (space group  $Ia\bar{3}$ , Pearson symbol cI80) contains 32 cations (occupying the 8a and 24d equipoints) and 48 anions (occupying the 48e equipoints) in this relatively large unit cell. This structure can be derived from eight fluorite crystals with oxygen vacancies sitting in two tetrahedral sites, as shown in Figure 7.

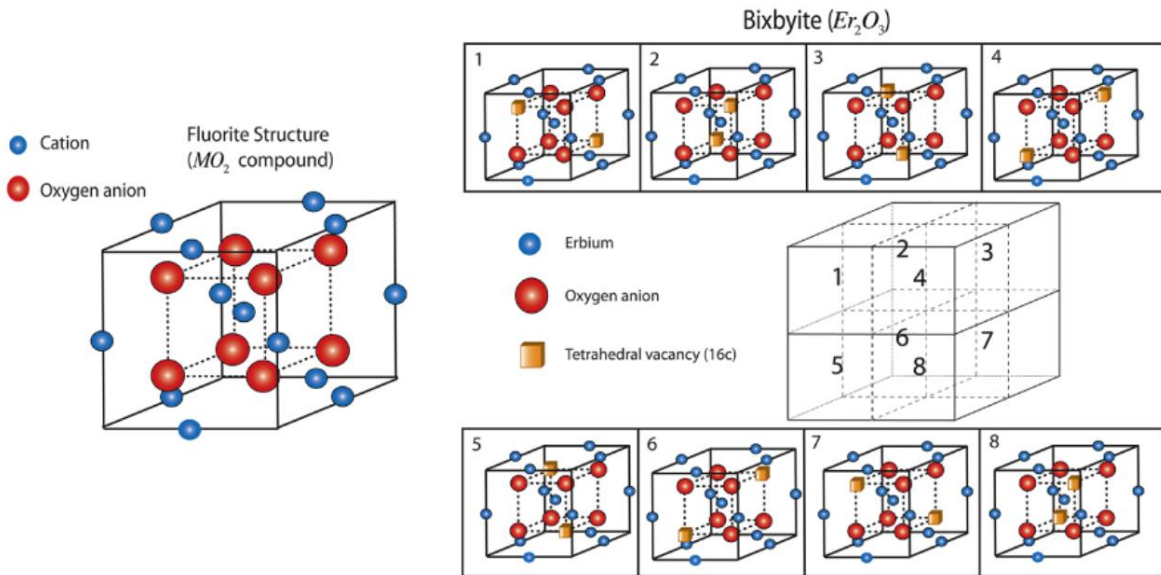


Figure 7. The C-type cubic-bixbyite structures can be derived from eight fluorite structures with oxygen vacancies involved. The bixbyite structure can be naturally found in the middle and heavy lanthanide (Sm-Lu) sesquioxides as well as yttrium sesquioxides. Figure taken from ref. [64]

Table 2. The common binary oxide structures of lanthanides and yttrium in descending order of cation radii in trivalent and six-fold coordinates. Data obtained from the International Center for Diffraction Data (ICDD) database and literature [58-60, 62, 65, 66]

Cation	Mono-oxide	Structure	Space Group	Pearson Symbol	Valency	CN	$r_c$ (Å)
La	La <sub>2</sub> O <sub>3</sub>	Hexagonal	$P\bar{3}m1$	hP5 (La <sub>2</sub> O <sub>3</sub> )	3+	VII	
	-	-	-	-	3+	VI	1.032
Ce	CeO <sub>2</sub>	Fluorite	$Fm\bar{3}m$	cF12 (CaF <sub>2</sub> )	4+	VIII	
	Ce <sub>2</sub> O <sub>3</sub> *	Hexagonal	$P\bar{3}m1$	hP5 (La <sub>2</sub> O <sub>3</sub> )	3+	VII	
Pr	-	-	-	-	3+	VI	1.01
	Pr <sub>6</sub> O <sub>11</sub>	Monoclinic	$P2_1/c$		3+, 4+	VII, VIII	
	Pr <sub>2</sub> O <sub>3</sub> *	Hexagonal	$P\bar{3}m1$	hP5 (La <sub>2</sub> O <sub>3</sub> )	3+	VII	
Nd	-	-	-	-	3+	VI	0.99
	Nd <sub>2</sub> O <sub>3</sub>	Hexagonal	$P\bar{3}m1$	hP5 (La <sub>2</sub> O <sub>3</sub> )	3+	VII	
Sm	-	-	-	-	3+	VI	0.983
	Sm <sub>2</sub> O <sub>3</sub>	Bixbyite	$Ia\bar{3}$	cI80 (Mn <sub>2</sub> O <sub>3</sub> )	3+	VI	0.958
Eu	Eu <sub>2</sub> O <sub>3</sub>	Bixbyite	$Ia\bar{3}$	cI80 (Mn <sub>2</sub> O <sub>3</sub> )	3+	VI	0.947
Gd	Gd <sub>2</sub> O <sub>3</sub>	Bixbyite	$Ia\bar{3}$	cI80 (Mn <sub>2</sub> O <sub>3</sub> )	3+	VI	0.938
Tb	Tb <sub>7</sub> O <sub>12</sub>	Trigonal	$R\bar{3}$	hR19 (Tb <sub>7</sub> O <sub>12</sub> )	3+, 4+	VI, VII	
	Tb <sub>11</sub> O <sub>20</sub>	Triclinic	$P\bar{1}$	aP31 (Tb <sub>11</sub> O <sub>20</sub> )	3+, 4+	VI, VII, VIII	
	Tb <sub>2</sub> O <sub>3</sub> *	Bixbyite	$Ia\bar{3}$	cI80 (Mn <sub>2</sub> O <sub>3</sub> )	3+	VI	0.923
Dy	Dy <sub>2</sub> O <sub>3</sub>	Bixbyite	$Ia\bar{3}$	cI80 (Mn <sub>2</sub> O <sub>3</sub> )	3+	VI	0.912
Y	Y <sub>2</sub> O <sub>3</sub>	Bixbyite	$Ia\bar{3}$	cI80 (Mn <sub>2</sub> O <sub>3</sub> )	3+	VI	0.9
Ho	Ho <sub>2</sub> O <sub>3</sub>	Bixbyite	$Ia\bar{3}$	cI80 (Mn <sub>2</sub> O <sub>3</sub> )	3+	VI	0.901
Er	Er <sub>2</sub> O <sub>3</sub>	Bixbyite	$Ia\bar{3}$	cI80 (Mn <sub>2</sub> O <sub>3</sub> )	3+	VI	0.89
Tm	Tm <sub>2</sub> O <sub>3</sub>	Bixbyite	$Ia\bar{3}$	cI80 (Mn <sub>2</sub> O <sub>3</sub> )	3+	VI	0.88
Yb	Yb <sub>2</sub> O <sub>3</sub>	Bixbyite	$Ia\bar{3}$	cI80 (Mn <sub>2</sub> O <sub>3</sub> )	3+	VI	0.868
Lu	Lu <sub>2</sub> O <sub>3</sub>	Bixbyite	$Ia\bar{3}$	cI80 (Mn <sub>2</sub> O <sub>3</sub> )	3+	VI	0.861

\*metastable phase under ambient conditions

In Table 2, most of the chosen cations are stable in their trivalent states under ambient conditions. In contrast, cerium, praseodymium, and terbium are thermodynamically unstable in their trivalent states. Petit et al. [67] performed systematic research between lanthanide sesquioxides and lanthanide dioxides. In Table 3, the oxidation energy between lanthanide dioxides and A-type hexagonal sesquioxides, and between lanthanide dioxide and C-type bixbyite sesquioxides were calculated. If the oxidation energy is negative, the cation is preferably in the

tetravalent state instead of the trivalent state. Taking dysprosium oxide as an example, the oxidation energy between  $\text{DyO}_2$  and A-type  $\text{Dy}_2\text{O}_3$  is negative, meaning that the tetravalent phase  $\text{DyO}_2$  is thermodynamically stable, compared to the A-type  $\text{Dy}_2\text{O}_3$ . By comparing C-type  $\text{Dy}_2\text{O}_3$  to  $\text{DyO}_2$ , the energy value is positive, indicating that trivalent, C-type  $\text{Dy}_2\text{O}_3$  is more favorable in the dysprosium oxide system. The calculations indicate that the stable sesquioxide phases agree with the research from experimental studies.[58, 60, 62, 65, 68, 69]. The results proved that cerium, praseodymium, and terbium prefer to be in their tetravalent states, compared to in their trivalent states.

In addition to the cations with stable trivalent states, some lanthanide cations— cerium, praseodymium, and terbium, have stable tetravalent configurations due to their electronic configurations.[70] Under ambient conditions, cerium oxide behaves in a tetravalent state, having a dioxide composition and a fluorite crystal structure.[58, 61] On the other hand, crystallographic studies on terbium and praseodymium are more complicated. Even the related research agrees with that terbium and praseodymium occur as coexisting trivalent and tetravalent oxidation states; the room-temperature oxide structures were controversial. The chemistry of terbium oxide was believed to be the single-phase  $\text{Tb}_4\text{O}_7$  ( $\text{Tb}_2\text{O}_3 \cdot 2\text{TbO}_2$ ).[71-73] Recent research has updated that the room-temperature structure of terbium oxide is not a single phase but a two-phase mixture of  $\text{Tb}_7\text{O}_{12}$  ( $2\text{Tb}_2\text{O}_3 \cdot 3\text{TbO}_2$ , rhombohedral structure) and  $\text{Tb}_{11}\text{O}_{20}$  ( $2\text{Tb}_2\text{O}_3 \cdot 7\text{TbO}_2$ , triclinic structure, respectively).[60, 74, 75] However, some research indicated that this two-phase mixture is an intermediate phase instead of a stable phase.[76] Despite on-going discussion of the crystal structures of terbium oxide, all reports claim that terbium acts as a mixture of tetravalent and trivalent states under ambient temperature. Via calcination under an inert or reducing atmosphere, the structure can become C-type bixbyite sesquioxide,  $\text{Tb}_2\text{O}_3$ , with only a trivalent oxidation state. However, above  $280^\circ\text{C}$  in air, the sesquioxide transforms back to  $\text{Tb}_7\text{O}_{12}$  and  $\text{Tb}_{11}\text{O}_{20}$  with

corresponding mixtures of +3 and +4 valence states, respectively.[77] This transition involves a change in the terbium cation radii from 0.923Å to 0.88Å and 0.98Å, caused by a variation in both the oxidation states and coordination geometry.[49] Praseodymium oxide occurs as Pr<sub>6</sub>O<sub>11</sub> (Pr<sub>2</sub>O<sub>3</sub>•4PrO<sub>2</sub>) at room temperature.[78-80] The fluorite structured phase PrO<sub>2</sub>, with tetravalent praseodymium, can be obtained through calcination under positive oxygen pressure. Overall, all lanthanides can occur in sesquioxide stoichiometry, either as stable or metastable forms, under ambient conditions.[81]

Table 3. Oxidation energies in electron volts between lanthanide sesquioxides and dioxides. The negative energy indicates that the material prefers to exist in the dioxide form. Table taken from ref. [67]

MO <sub>2</sub> /M <sub>2</sub> O <sub>3</sub>	E <sub>ox</sub> (A-M <sub>2</sub> O <sub>3</sub> )	E <sub>ox</sub> (C-M <sub>2</sub> O <sub>3</sub> )
CeO <sub>2</sub> /Ce <sub>2</sub> O <sub>3</sub>	-1.90	-3.54
PrO <sub>2</sub> /Pr <sub>2</sub> O <sub>3</sub>	-0.14	-1.90
NdO <sub>2</sub> /Nd <sub>2</sub> O <sub>3</sub>	0.54	-0.54
PmO <sub>2</sub> /Pm <sub>2</sub> O <sub>3</sub>	0.00	0.27
SmO <sub>2</sub> /Sm <sub>2</sub> O <sub>3</sub>	-0.82	0.68
GdO <sub>2</sub> /Gd <sub>2</sub> O <sub>3</sub>	-10.88	0.14
TbO <sub>2</sub> /Tb <sub>2</sub> O <sub>3</sub>	-8.16	-0.27
DyO <sub>2</sub> /Dy <sub>2</sub> O <sub>3</sub>	-4.08	0.27
HoO <sub>2</sub> /Ho <sub>2</sub> O <sub>3</sub>	-0.68	0.00

A basic method to identify the valence configurations of lanthanide cations is through the color of the powder sample (Table 4).[59, 76, 82-84] Cerium and terbium are both colorless in their trivalent states. The yellowish or brownish color can be observed from a sample containing tetravalent cerium or tetravalent terbium, respectively. For praseodymium, the color becomes darker in the tetravalent sample, compared to the trivalent state. Most of the trivalent lanthanide cations are colorless or exhibit a light color in their oxide powder form.



Table 4. Color of the trivalent lanthanide, yttrium ions and tetravalent cerium, praseodymium, and terbium [82, 84]

Z	Lanthanides		Color
39	Yttrium	$Y^{3+}$	Colorless
57	Lanthanum	$La^{3+}$	Colorless
58	Cerium	$Ce^{3+}$	Colorless
		$Ce^{4+}$	Yellow
59	Praseodymium	$Pr^{3+}$	Yellow
		$Pr^{4+}$	Brown
60	Neodymium	$Nd^{3+}$	Violet-blue
62	Samarium	$Sm^{3+}$	Pale yellow
64	Gadolinium	$Gd^{3+}$	Colorless
65	Terbium	$Tb^{3+}$	Colorless
		$Tb^{4+}$	Brown
66	Dysprosium	$Dy^{3+}$	Pale yellow
67	Holmium	$Ho^{3+}$	Brownish pink
68	Erbium	$Er^{3+}$	Pink
69	Thulium	$Tm^{3+}$	Pale green
70	Ytterbium	$Yb^{3+}$	Colorless
71	Lutetium	$Lu^{3+}$	Colorless

## 2.5. Ternary Lanthanide Oxide Materials

Considering equimolar mixtures of two candidate cations, there are 78 types (through the combination equation,  $C_2^{13}$ ) of possible ternary lanthanide oxides. However, not every combination has been investigated in previous research. Table 5 lists some of the reported ternary oxide structures, including lanthanides and yttrium cations. Aliovalent doped- $CeO_2$  has been widely used in oxygen concentration cells and in solid oxide fuel cells.[85-88] Below 800°C, some doped- $CeO_2$  materials have been found to exhibit high ionic conductivity coupled with low activation energy for ionic conduction. In addition, as mentioned in the previous Section 2.4, cerium is stable in tetravalent states under ambient conditions. Mixing cerium with other lanthanide cations, which corresponds to a trivalent configuration or the mixture of trivalent and

tetravalent states, could form a tilted fluorite solid solution with oxygen vacancies.[89] Yamamura et al.[90] reported that the dopant vacancy in these materials could suppress oxide-ion conductivity. By altering the composition of lanthanides in trivalent and tetravalent states, the crystal structure can change between tilted fluorite versus C-type cubic-bixbyite structures.[91] Consider  $Ce_{1-x}Nd_xO_{2-y}$  as an example: when the compositions between two oxidation states are an equimolar fraction ( $x=0.5$ ), the structure behaves as the tilted fluorite structure. Under the trivalent cation depletion situation ( $x=0.25$ ), the  $CeO_2$ -type fluorite structure is the only structure observed from neutron diffraction.[92] However, Hagiwara et al. [93] claimed that these two structures coexist in the  $Ce_{1-x}Nd_xO_{2-y}$  sample (in the range of  $0.4 \leq x \leq 0.7$ ). As presented in Figure 8, the crystal structures behave as a tilted fluorite structure or a  $CeO_2$ -type fluorite structure in the trivalent cation dominated ( $x > 0.7$ ) or depletion ( $x < 0.4$ ) cases, respectively. In the region where two phases coexist, the composition of fluorite structure decreases as the fraction of cerium, the cation preferred in tetravalent states, and vice versa. This behavior has been reported in other Ce-M (M=Gd, Yb, Y) oxide solid solutions.[94, 95]

Comparing this tilted fluorite structure to the C-type bixbyite structure, they both are in the bixbyite category having the same space group  $Ia\bar{3}$ . One way to distinguish them via the crystallographic naming method is the Pearson symbol.[96] The tilted fluorite and C-type cubic-bixbyite structures are designated as cI88 and cI80 in the Pearson system, respectively. The first and second letters are indicating that they are classified in the cubic family (c) and body-centered type (I). The number at the end indicates the number of the atoms in the conventional unit cell.

Table 5. Ternary oxides structures of the lanthanides and yttrium. Data obtained from the International Center for Diffraction Data (ICDD) database and literature [91-93, 97]

Composition	Structure	Space Group	Pearson Symbol
CeLaO <sub>3.5</sub>	Fluorite	<i>Fm</i> $\bar{3}$ <i>m</i>	cF12 (CaF <sub>2</sub> )
CeNdO <sub>3.5</sub>	Fluorite	<i>Fm</i> $\bar{3}$ <i>m</i>	cF12 (CaF <sub>2</sub> )
	Tilted Fluorite	<i>Ia</i> $\bar{3}$	cI88 (Mn <sub>2</sub> O <sub>3</sub> )
CeSmO <sub>3.5</sub>	Tilted Fluorite	<i>Ia</i> $\bar{3}$	cI88 (Mn <sub>2</sub> O <sub>3</sub> )
CeGdO <sub>3.5</sub>	Tilted Fluorite	<i>Ia</i> $\bar{3}$	cI88 (Mn <sub>2</sub> O <sub>3</sub> )
CeDyO <sub>3.5</sub>	Tilted Fluorite	<i>Ia</i> $\bar{3}$	cI88 (Mn <sub>2</sub> O <sub>3</sub> )
CeHoO <sub>3.5</sub>	Tilted Fluorite	<i>Ia</i> $\bar{3}$	cI88 (Mn <sub>2</sub> O <sub>3</sub> )
CeErO <sub>3.5</sub>	Tilted Fluorite	<i>Ia</i> $\bar{3}$	cI88 (Mn <sub>2</sub> O <sub>3</sub> )
	Cubic-Bixbyite*	<i>Ia</i> $\bar{3}$	cI80 (Mn <sub>2</sub> O <sub>3</sub> )
CeYbO <sub>3.5</sub>	Tilted Fluorite	<i>Ia</i> $\bar{3}$	cI88 (Mn <sub>2</sub> O <sub>3</sub> )
	Cubic-Bixbyite*	<i>Ia</i> $\bar{3}$	cI80 (Mn <sub>2</sub> O <sub>3</sub> )
CeLuO <sub>3.5</sub>	Tilted Fluorite	<i>Ia</i> $\bar{3}$	cI88 (Mn <sub>2</sub> O <sub>3</sub> )
	Cubic-Bixbyite*	<i>Ia</i> $\bar{3}$	cI80 (Mn <sub>2</sub> O <sub>3</sub> )
CeYO <sub>3.5</sub>	Tilted Fluorite	<i>Ia</i> $\bar{3}$	cI88 (Mn <sub>2</sub> O <sub>3</sub> )
	Cubic-Bixbyite*	<i>Ia</i> $\bar{3}$	cI80 (Mn <sub>2</sub> O <sub>3</sub> )
LaLn <sup>1</sup> O <sub>3</sub>	Perovskite	<i>Pnma</i>	oP20 (GdFeO <sub>3</sub> )
Ln <sup>1</sup> : (Lu, Yb, Tm, Er, Ho, Y)			
CeLn <sup>2</sup> O <sub>3</sub>	Perovskite	<i>Pnma</i>	oP20 (GdFeO <sub>3</sub> )
Ln <sup>2</sup> : (Lu, Yb, Tm)			

\*Minor secondary peaks with low diffraction intensity.

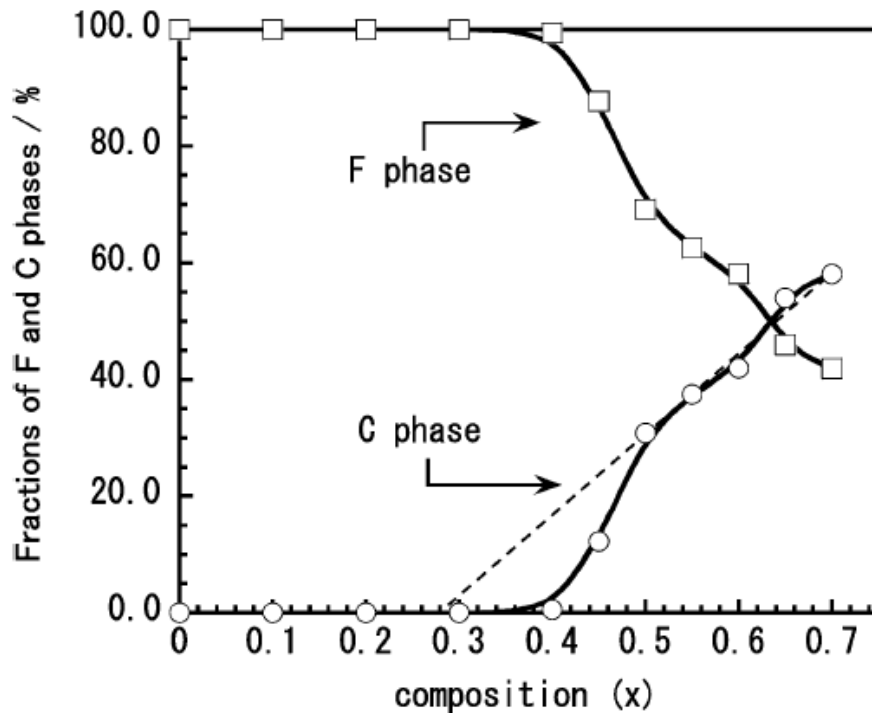


Figure 8. The structure of lanthanide oxide  $Ce_{1-x}Nd_xO_{2-y}$ . The fraction of fluorite (F-phase) and C-type cubic-bixbyite (C phase) phases coexist in the region  $0.4 \leq x \leq 0.7$ . The fluorite phase dominates in the cerium-rich sample, and vice versa. Figure taken from ref. [93]

Another typical structure type usually found in the ternary lanthanide oxides is  $ABO_3$  perovskite, where A and B sites represent the cation with larger and smaller radii, respectively. Materials within a perovskite structure have been investigated for decades due to their promising and useful electrical properties, such as superconductivity, ferroelectricity, photoluminescence, and catalytic activity.[98-101] Due to the wide radii range in lanthanide cations (0.861 to 1.032Å), the light lanthanides, with larger cations, can occupy the corners of the unit cell, and the heavy lanthanide sits in the center position to form a perovskite structure. Several ternary lanthanide oxides with perovskite materials have been found in the literature, as shown in Figure 9.[102-105] The symbol  $t_{IR}$  is used in expressing the level of size mismatch in A and B cations in a perovskite structure.

$$t_{IR} = (R_A + R_O)/\sqrt{2}(R_B + R_O) \quad \{4\}$$

Where R represents the radius of ion in the perovskite structure. When  $t_{IR}$  exceed 0.847, the ternary oxide oxides could transform into perovskite structures, such as  $\text{LaYbO}_3$ , and  $\text{CeLuO}_3$ . During the cooling process, the ternary lanthanide oxide could slowly convert back to the C-type bixbyite structure. For other ternary oxides in the C-type structure at ambient conditions, they follow the similar high-temperature phase transformation trends as in the sesquioxides system between oxygen and middle lanthanides ( $\text{Gd}_2\text{O}_3$ - $\text{Ho}_2\text{O}_3$ ).

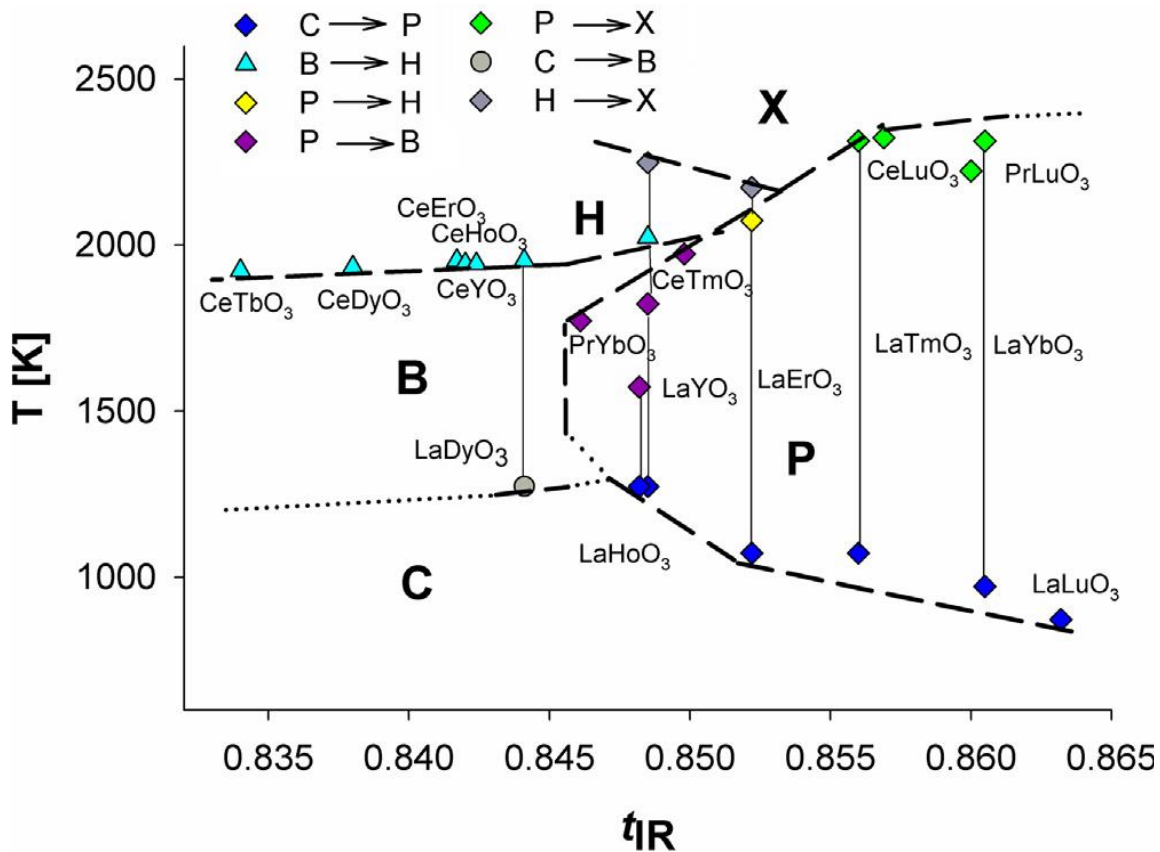


Figure 9. Ternary lanthanide oxides, with perovskite structures, have been observed as metastable phases at high temperatures ( $>1000^\circ\text{C}$ ). Those phases can be found when the size mismatch between two lanthanides is large, with  $t_{IR}$  values exceeding 0.847. Other ternary oxides exhibiting C-type cubic-bixbyite structures experience similar phase transformations as the middle lanthanide sesquioxides ( $\text{Gd}_2\text{O}_3$ - $\text{Ho}_2\text{O}_3$ ).

## CHAPTER 3: EXPERIMENTAL PROCEDURES

### 3.1. Modified Thermodynamic Definition of High-Entropy Ceramics

In ceramics, cations and anions are distributed in a crystal structure, occupying different sites. Previously, the calculation of configurational entropy ( $\Delta S_{conf}$ ) took cations solely into consideration because the value of the mono-anion is zero.[7, 33] This calculation neglected the contribution from anions in the ceramic chemistry. We propose that the contribution from both cation and anion should be considered based on their molar ratios. For example, the contribution of  $\Delta S_{conf}$  from a  $M_2O_3$  stoichiometry consists of 40% from cations and 60% from anions. Even though the values would be significantly lower than in the HEAs systems, the difference in chemical configuration should be included in a ceramic structure. Hence, the calculation results of  $\Delta S_{conf}$  in different oxide stoichiometries are illustrated in Figure 10. Compared with HEAs, using a specific range of configurational entropy as a definition of HEOs may not be appropriate. The basic concept of high-entropy materials is that a variety of atoms sitting on the same sites, inducing severe lattice distortion. Having five cations lying in two different sites may compensate for the local strength in the system. The overall  $\Delta S_{conf}$  can still be calculated from different sites with their weighting levels, but it might not meet the definition of high-entropy materials. As a result, the definition of HEC should depend on whether there are an equal number or more than five cations sitting on the same site, so that the equation of  $\Delta S_{conf}$  should be modified according to:

$$\Delta S_{conf} = C_{cation,mole} \times \Delta S_{conf,cation} + C_{anion,mole} \times \Delta S_{conf,anion} \quad \{5\}$$

$$\Delta S_{conf,cation} = -R \sum_{i1=1}^N x_{i1} \ln x_{i1} + R \sum_{i2=1}^N x_{i2} \ln x_{i2} \dots \quad \{6\}$$

$$\Delta S_{mix,anion} = -R \sum_{j=1}^M x_j \ln x_j \quad (vacancy \text{ should be included}) \quad \{7\}$$

where  $C$  is the mole fraction of cation or anion,  $x$  represents the mole fraction of elements located in each cation (i) or anion (j) site, and  $R$  is the universal gas constant 8.314 J/mol·K.

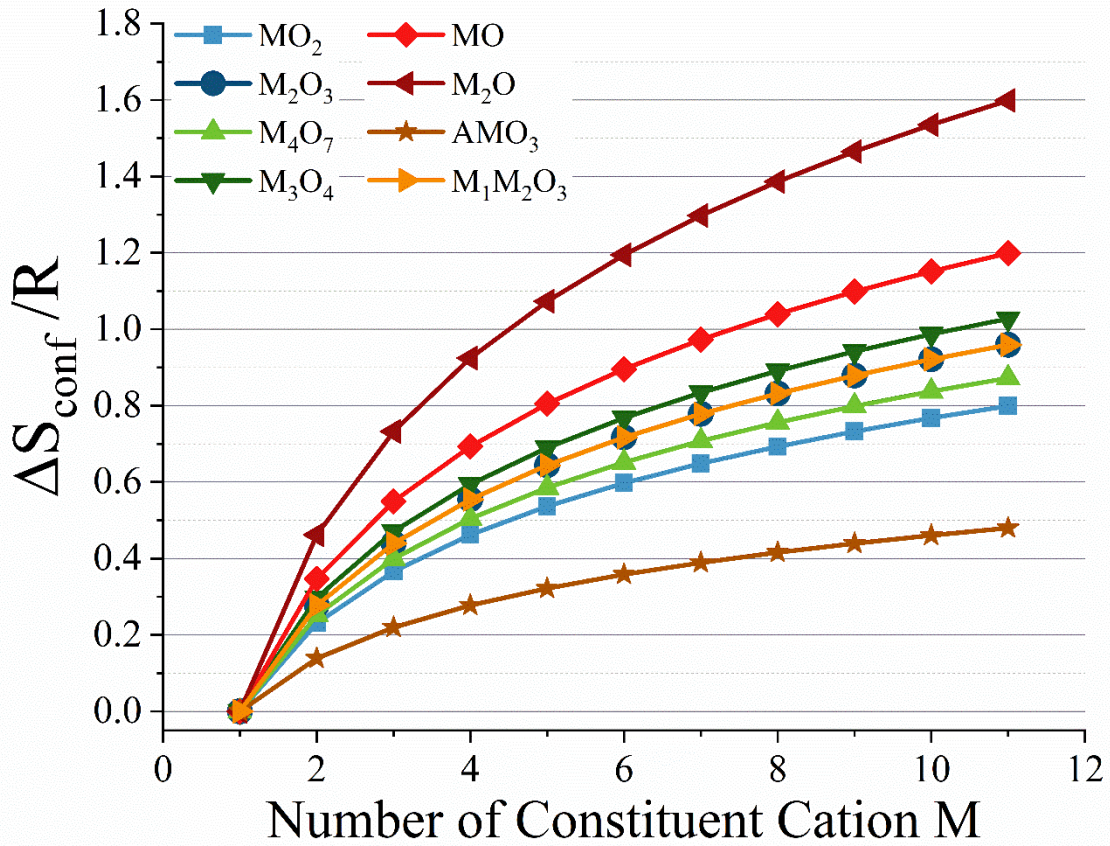


Figure 10. The configurational entropy ( $\Delta S_{conf}$ ) parameter varies for different stoichiometries between cations and anions as a function of the number of constituent cations. The mixing entropy contribution from anions is significant and should be considered. R: gas constant 8.314 J/mol·K

With this novel HEOs definition, the value of  $\Delta S_{conf}$  changes with different chemical stoichiometries. Therefore, setting a value, such as 1.61R in the HEAs system, is not ideal for the HEOs field. However, for each structure, having five or more cations located in the same site does introduce higher configurational entropy, compared to the binary or low concentration doping arrangement. Even though the value of  $\Delta S_{conf}$  is smaller in HEOs, these materials still follow the four effects of high-entropy materials.

### 3.2. Materials Design—High-Entropy Lanthanide Oxides (HELOs)

As mentioned in Section 2.2, the size mismatch is a critical parameter in evaluating whether the structures in HEAs are stable or not. In the ceramic field, the size of a cation could vary with both oxidation states and coordination geometry. For example, in one of the most well-studied transformation—zirconia ( $\text{ZrO}_2$ ), the radius of the zirconium cation changes from  $0.78\text{\AA}$  to  $0.72\text{\AA}$ , while the structure reconstructs from monoclinic to tetragonal symmetry.[49, 106, 107] During this transition, the stoichiometry remains the same ( $\text{ZrO}_2$ ). However, the coordination number shifts from seven-fold to eight-fold coordination, leading to the change in cation radii. The radius of cation can shift significantly, even in a similar crystal structure. The element chromium reduces by almost 50% in  $\text{CrO}_3$  ( $0.26\text{\AA}$ ,  $\text{Cr}^{6+}$ , 4-fold coordination), in the orthorhombic crystal structure, compared to in  $\text{CrO}_2$  ( $0.55\text{\AA}$ ,  $\text{Cr}^{4+}$ , 6-fold coordination) within the same orthorhombic symmetry.[49, 108] Furthermore, like the example of zirconia, phase transformations are commonly involved in ceramic materials. As a result, the three key parameters: (1) cationic radii, (2) oxidation states, and (3) high-temperature phase transformations need to be taken into account while designing the candidates for this research.

Table 6 lists cation radii having a combination of valence states and coordination numbers that have been reported in oxide materials.[49] Some cations could behave in multiple valence states, such as vanadium or iron. However, if the valence state is not stable under ambient conditions (marked as “\*” in Table 6), those states exist only under high pressure or other particular environments. The following rules were applied to narrow the selection of candidates:

- 1) No radioactive elements involved (excluded in Table 6)
- 2) For polymeric steric entrapment synthesis, nitrate, chloride, iso-propoxide products of targeted cation should be available in the market.



- 3) The ratio between a small cation to a large cation should be more than 0.9 in order to avoid a large gap contributed from two cations.
- 4) The high cost of some novel precursors (>\$100/g) was not considered.

The large ratio mismatch between two elements (ratio <0.9) could cause phase separation, especially when the oxidation state in one of them is usually unstable. In this research, one sample was synthesized to prove this hypothesis.

After an in-depth investigation of oxides, the lanthanide elements were chosen as our candidates because of the following criteria: (1) an ideal range of cation radii, (2) similar electron configurations, (3) different valence states, and (4) high-temperature phase transformations being involved. Firstly, trivalent cations have small gaps between adjacent ions in an octahedral interstitial site, where the selected cations have a wide radius range from 0.861Å (lutetium) to 1.032Å (lanthanum).[49] Yttrium was added into the system for its similarity to its cation radius (0.9 Å). In oxides, most of the chosen cations are stable in trivalent states. In contrast, cerium, praseodymium, and terbium prefer to exist in either tetravalent states (e.g., CeO<sub>2</sub>) or mixed states (such as Pr<sub>6</sub>O<sub>11</sub>, Tb<sub>7</sub>O<sub>12</sub>, Tb<sub>11</sub>O<sub>20</sub>).[60, 74] Under ambient conditions, the light lanthanide oxides exist in an A-type hexagonal structure, while heavy lanthanide oxides, including yttrium, adopt a C-type, cubic-bixbyite structure. Furthermore, as mentioned in Section 2.4, complicated phase transformations are involved in most of the binary lanthanide oxides. As temperature increases, the middle lanthanide oxides can experience structural transformations from a C-type cubic to a B-type monoclinic phase on heating. Lanthanides are ideal components in building candidates for the study of chemical selection criteria of HEOs.

Table 6. Reported cation radii with respect to valence configuration and coordination number [49]

M <sup>3+</sup> , VI	Radius (Å)			M <sup>4+</sup> , VI	Radius (Å)		
Al	0.535	Sb	0.76	Ni*	0.48	Sn	0.69
Cu*	0.54	Au	0.85	Se	0.5	Hf	0.71
Co	0.545	<b>Lu</b>	0.861	Co*	0.53	Zr	0.72
Ni*	0.56	<b>Yb</b>	0.868	Ge	0.53	Pr*	0.85
As	0.58	<b>Tm</b>	0.88	Mn	0.53	Ce	0.87
Mn*	0.58	Tl	0.885	Cr*	0.55		
Cr	0.615	<b>Er</b>	0.89	V*	0.58		
Ga	0.62	<b>Y</b>	0.9	Fe*	0.585		
V*	0.64	<b>Ho</b>	0.901	Rh*	0.6		
Fe	0.645	<b>Dy</b>	0.912	Ti	0.605		
Rh	0.665	<b>Tb*</b>	0.923	Pd	0.615		
Ti*	0.67	<b>Gd</b>	0.938	Ru	0.62		
Ir	0.68	<b>Eu</b>	0.947	Ir	0.625		
Ru	0.68	<b>Sm</b>	0.958	Pt	0.625		
Mo*	0.69	<b>Nd</b>	0.983	Os	0.63		
Nb*	0.72	<b>Pr*</b>	0.99	Re	0.63		
Ta*	0.72	<b>Ce*</b>	1.01	Mo	0.65		
Sc	0.745	Bi	1.03	W	0.66		
Ag*	0.75	<b>La</b>	1.032	Nb*	0.68		
Pd*	0.76			Ta*	0.68		
M <sup>2+</sup> , VI	Radius (Å)			M <sup>3+</sup> , VIII	Radius (Å)		
Fe	0.61	Ti*	0.86	Lu	0.977	Nd	1.109
Mn	0.67	Ag*	0.94	Tl	0.98	Pr*	1.126
Ni	0.69	Cd	0.95	Yb	0.985	Ce	1.143
Mg	0.72	Ca	1	Tm	0.994	La	1.16
Cu	0.73	Hg	1.02	Er	1.004	Bi	1.17
Ge	0.73	Yb*	1.02	Ho	1.015		
Zn	0.74	Tm*	1.03	Y	1.019		
Co	0.745	Dy*	1.07	Dy	1.027		
V*	0.79	Eu*	1.17	Tb*	1.04		
Cr*	0.8	Sr	1.18	Gd	1.053		
Pt	0.8	Pb	1.19	Eu	1.066		
Pd	0.86			Sm	1.079		

\*naturally not stable in this oxidation state

Three systems were designed in this research and the following questions were considered here:

- 1) Whether the HELOs formation is dominated by cerium as a stabilizer
- 2) With four lanthanide cations fixed, the size limitation of the fifth cation (larger or smaller cation)
- 3) Other than the cation size, whether the preferred oxidation states affect the final crystal structure
- 4) For single-phase HELOs, whether the phase transformations of constituent cations could break the high-entropy arrangement and trigger phase separation(s) as temperature increases

To answer the first question, we chose five elements: gadolinium (Gd), terbium (Tb), dysprosium (Dy), holmium (Ho), and erbium (Er), as our candidate cations. The combination of these five elements tends to form a single-phase HELO due to their similarity in cation radii, preferred trivalent oxidation state, and cubic-bixbyite oxide structure under ambient conditions.[49, 59, 67] The only exception here is terbium. At room temperature, trivalent and tetravalent states coexist in its structures,  $Tb_7O_{12}$  and  $Tb_{11}O_{20}$ . [60, 74] Terbium sesquioxide,  $Tb_2O_3$ , can be obtained in an inert or reducing atmosphere. However, the trivalent state transforms back to the mixed oxidation states under heat treatments, along with crystal structural changes.[77] Furthermore, another important reason for choosing these five candidates was due to their promising magnetic properties.[109-113] Even though their sesquioxides exist as paramagnetic materials, these materials have the highest magnetic susceptibility values in oxides and constitute the top 15 rankings in all reported inorganic materials.[114] The detailed information of those five cations was listed in Table 7. The initial results showed that a single-phase HELO was successfully formed by those five middle lanthanides, proving that certain specific elements, such as cerium in the lanthanides, were not a restricting factor in single-phase HELOs formation. The next step was to

systematically design candidates for understanding the questions regarding cation size mismatch, valence configurations, and structural stability under high temperature.

Table 7. Crystal structures, cation coordination numbers (CN), cation radii ( $R_c$ ), and magnetic molar susceptibilities ( $\chi_m$ ) of mono-cation lanthanide oxides

<b>Chemical formula</b>	<b>Crystal structure (space group)</b> Ref.[58, 60, 66, 115]	<b>CN</b>	<b><math>R_c</math> (Å)</b> Ref.[49]	<b><math>\chi_m</math>, 285K (cm<sup>3</sup>/mol)</b> Ref.[114]
<b>Gd<sub>2</sub>O<sub>3</sub></b>	Cubic (Ia $\bar{3}$ )	VI	0.938	5.32 x 10 <sup>-2</sup>
<b>Tb<sub>2</sub>O<sub>3</sub>*</b>	Cubic (Ia $\bar{3}$ )	VI	0.923	7.83 x 10 <sup>-2</sup>
<b>Dy<sub>2</sub>O<sub>3</sub></b>	Cubic (Ia $\bar{3}$ )	VI	0.912	8.96 x 10 <sup>-2</sup>
<b>Ho<sub>2</sub>O<sub>3</sub></b>	Cubic (Ia $\bar{3}$ )	VI	0.901	8.81 x 10 <sup>-2</sup>
<b>Er<sub>2</sub>O<sub>3</sub></b>	Cubic (Ia $\bar{3}$ )	VI	0.89	7.39 x 10 <sup>-2</sup>

\*Metastable phase at ambient conditions.

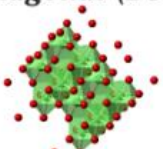
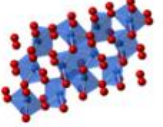
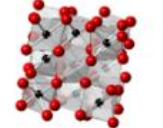
Two different systems were designed for discerning the limitation of cation radii:

System (1): larger cations which expanded the polyhedral sites,

System (2) smaller cations which fit into the more significant interstitial sites.

In the system (1), each of nine larger cation candidates (La, Ce, Pr, Nd, Sm, Gd, Tb, Dy, Y) was included with the four smallest lanthanides (Lu, Yb, Tm, Er), while, europium and holmium were excluded from the list due to their cost and similarity in cation radii. At ambient conditions, every base cation (Lu, Yb, Tm, Er) was stable in trivalent oxidation states in the mono-cation oxide with bixbyite structures having six-fold coordination. In the system (2), the four largest cations (La, Ce, Pr, Nd) were fixed with the fifth cation candidate chosen from nine smaller cations. However, the room-temperature structures of these larger-radius, mono-cation oxide were complicated. Cerium prefers to exist in a tetravalent state (CeO<sub>2</sub>), and praseodymium tends to have a mixture of both trivalent and tetravalent states (Pr<sub>6</sub>O<sub>11</sub> corresponding to Pr<sub>2</sub>O<sub>3</sub>•4PrO<sub>2</sub>). The sesquioxides (M<sub>2</sub>O<sub>3</sub>) of these four base candidates exist in the same A-type hexagonal structure. In the valence state

prospective, the system (1) is less influenced by different preferred oxidation states compared to the system (2). The precursors of these thirteen (4+9) lanthanides were chosen from the lanthanide nitrates having cations in trivalent oxidation states. The structures of our candidates at room temperature and high temperature are shown in Figure 11. The room-temperature phase identification of these five-component oxides was studied. Furthermore, in situ X-ray diffraction data were collected up to a maximum temperature  $\sim 2000^{\circ}\text{C}$ . The chosen candidates and their abbreviations are listed in Table 8.

$M_2O_3$	$M^{3+}$	Structure
<b>A-type</b> Hexagonal ( $P\bar{3}m1$ ) 	La	● A-type → H → X
	Ce*	● A-type → H → X
	Pr*	● A-type → H → X
	Nd	● A-type → H → X
<b>B-type</b> Monoclinic ( $C2/m$ ) 	Sm	● C-type → B → A → H → X
	Gd	● C-type → B → A → H → X
<b>C-type</b> Cubic-Bixbyite ( $Ia\bar{3}$ ) 	Tb*	● C-type → B → H → X
	Dy	● C-type → B → H → X
	Y	● C-type → H
<b>High-T structure</b> >2100°C distorted octahedra <b>H-type</b> Hexagonal ( $P\bar{3}m1$ )	Er	● C-type → H
	Tm	● C-type → H
<b>X-type</b> Cubic ( $Im\bar{3}m$ )	Yb	● C-type → H
	Lu	● C-type

\*Naturally not in  $M_2O_3$  chemical form

Figure 11. Room-temperature structures and high-temperature structural transformations of chosen lanthanide sesquioxides. The systems were selected from either the four largest cations (La, Ce, Pr, Nd) or the smallest cations (Lu, Yb, Tm, Er) as the base, and adding the fifth cation in equimolar ratios to form the five-component oxides, respectively.

Table 8. The chemical information, abbreviation, and cation size mismatch ( $\delta$ ) of chosen candidates. The value of  $\delta$  is calculated in the single-phase situation.

Chemistry	Abbreviation	$\delta \times 100$
(Gd <sub>0.4</sub> Tb <sub>0.4</sub> Dy <sub>0.4</sub> Ho <sub>0.4</sub> Er <sub>0.4</sub> )O <sub>x1</sub>	GTDHEO	1.8324
(Lu <sub>0.5</sub> Yb <sub>0.5</sub> Tm <sub>0.5</sub> Er <sub>0.5</sub> )O <sub>x2</sub>	LYTEO	1.2714
(Lu <sub>0.4</sub> Yb <sub>0.4</sub> Tm <sub>0.4</sub> Er <sub>0.4</sub> Y <sub>0.4</sub> )O <sub>x3</sub>	LYTEY	1.6113
(Lu <sub>0.4</sub> Yb <sub>0.4</sub> Tm <sub>0.4</sub> Er <sub>0.4</sub> Dy <sub>0.4</sub> )O <sub>x4</sub>	LYTEDy	2.0308
(Lu <sub>0.4</sub> Yb <sub>0.4</sub> Tm <sub>0.4</sub> Er <sub>0.4</sub> Tb <sub>0.4</sub> )O <sub>x5</sub>	LYTETb	2.4551
(Lu <sub>0.4</sub> Yb <sub>0.4</sub> Tm <sub>0.4</sub> Er <sub>0.4</sub> Gd <sub>0.4</sub> )O <sub>x6</sub>	LYTEGd	3.0635
(Lu <sub>0.4</sub> Yb <sub>0.4</sub> Tm <sub>0.4</sub> Er <sub>0.4</sub> Sm <sub>0.4</sub> )O <sub>x7</sub>	LYTESm	3.8988
(Lu <sub>0.4</sub> Yb <sub>0.4</sub> Tm <sub>0.4</sub> Er <sub>0.4</sub> Nd <sub>0.4</sub> )O <sub>x8</sub>	LYTENd	4.9563
(Lu <sub>0.4</sub> Yb <sub>0.4</sub> Tm <sub>0.4</sub> Er <sub>0.4</sub> Pr <sub>0.4</sub> )O <sub>x9</sub>	LYTEPr	5.2530
(Lu <sub>0.4</sub> Yb <sub>0.4</sub> Tm <sub>0.4</sub> Er <sub>0.4</sub> Ce <sub>0.4</sub> )O <sub>x10</sub>	LYTECe	6.0997
(Lu <sub>0.4</sub> Yb <sub>0.4</sub> Tm <sub>0.4</sub> Er <sub>0.4</sub> La <sub>0.4</sub> )O <sub>x11</sub>	LYTELa	7.0273
(La <sub>0.5</sub> Ce <sub>0.5</sub> Pr <sub>0.5</sub> Nd <sub>0.5</sub> )O <sub>x12</sub>	LCPNO	2.8029
(La <sub>0.4</sub> Ce <sub>0.4</sub> Pr <sub>0.4</sub> Nd <sub>0.4</sub> Sm <sub>0.4</sub> )O <sub>x13</sub>	LCPNSm	2.5161
(La <sub>0.4</sub> Ce <sub>0.4</sub> Pr <sub>0.4</sub> Nd <sub>0.4</sub> Gd <sub>0.4</sub> )O <sub>x14</sub>	LCPNGd	3.1651
(La <sub>0.4</sub> Ce <sub>0.4</sub> Pr <sub>0.4</sub> Nd <sub>0.4</sub> Tb <sub>0.4</sub> )O <sub>x15</sub>	LCPNTb	3.6991
(La <sub>0.4</sub> Ce <sub>0.4</sub> Pr <sub>0.4</sub> Nd <sub>0.4</sub> Dy <sub>0.4</sub> )O <sub>x16</sub>	LCPNDy	4.1075
(La <sub>0.4</sub> Ce <sub>0.4</sub> Pr <sub>0.4</sub> Nd <sub>0.4</sub> Y <sub>0.4</sub> )O <sub>x17</sub>	LCPNY	4.5649
(La <sub>0.4</sub> Ce <sub>0.4</sub> Pr <sub>0.4</sub> Nd <sub>0.4</sub> Er <sub>0.4</sub> )O <sub>x18</sub>	LCPNEr	4.9536
(La <sub>0.4</sub> Ce <sub>0.4</sub> Pr <sub>0.4</sub> Nd <sub>0.4</sub> Tm <sub>0.4</sub> )O <sub>x19</sub>	LCPNTm	5.3483
(La <sub>0.4</sub> Ce <sub>0.4</sub> Pr <sub>0.4</sub> Nd <sub>0.4</sub> Yb <sub>0.4</sub> )O <sub>x20</sub>	LCPNYb	5.8283
(La <sub>0.4</sub> Ce <sub>0.4</sub> Pr <sub>0.4</sub> Nd <sub>0.4</sub> Lu <sub>0.4</sub> )O <sub>x21</sub>	LCPNLu	6.1112
(La <sub>0.4</sub> Ce <sub>0.4</sub> Pr <sub>0.4</sub> Nd <sub>0.4</sub> Ag <sub>0.4</sub> )O <sub>x23</sub>	LCPNAg	10.8001

The compositions of oxygens were unknown during the process of materials designs.

### 3.3. Materials Synthesis

Precursors were synthesized by the polymeric steric entrapment method. This process has an advantage in synthesizing homogeneous solid solutions, which is critical in preparing high-entropy materials.[116-141] High-entropy alloys have typically been prepared by conventional melting and casting methods.[25, 28, 43, 47, 142] Due to the relatively high melting temperature and thermal shock behavior in ceramics, oxide materials were usually synthesized through solid

or wet chemical methods. However, homogeneously mixing multiple cations in solid-state reaction or conventional liquid solution method is challenging. Aggregation of one of the constituent cations in the solution can lower the configurational entropy, leading to the formation of secondary phases. The polymeric steric entrapment method, a versatile technique developed by our research group, is an ideal method for synthesizing high-entropy ceramics. As shown in Figure 12, This method uses long-chain polymers, such as polyvinyl alcohol (PVA) or polyethylene glycol (PEG), to entrap cations dissolved in a water-based or isopropanol-based solution. In addition to forming a homogeneous solution, this method has advantages in controlling synthesized materials having a desired crystal structure, chemical homogeneity, shape, and particle size distribution at lower temperatures and higher time efficiency.[116, 117, 127-129, 143, 144]

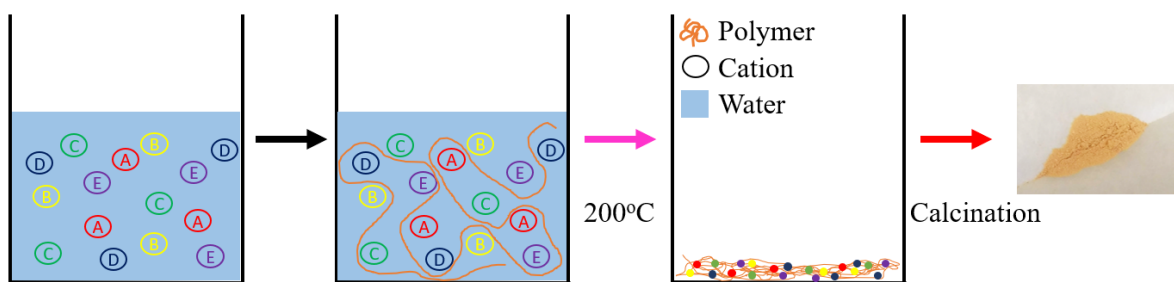


Figure 12. The process of polymeric steric entrapment. The long-chain polymer can entrap cations in the solution to prevent cation segregation; in other words, ensure that the configurational entropy is maximized. After drying out water at 200°C, the added cations are homogeneously entrapped in the long-chain polymer.

The nitrate precursors, with good water-solubility and having cations in trivalent states, were purchased from Millipore Sigma (Burlington, MA,  $\geq 99.5\%$  purity) and Alfa Aesar (Haverhill, MA,  $\geq 99.5\%$  purity). Firstly, each nitrate salt was dissolved in water in an equimolar ratio. Then 5 wt% of polyvinyl alcohol solution (99% PVA; Millipore Sigma) was added into the mother solution such that the ratio of cation valence charges : monomer ( $-\text{OH}^-$ ) charge = 4:1. The solution



was then mixed by stirring on a hot plate for two hours at room temperature, to ensure the homogeneous distribution of metallic cations in the solution. The mother solution was further heated at 200°C to remove all the water. During this process, long-chain PVA would entrap the cations to form a homogeneous, amorphous, organic-inorganic mixture. During the calcination process, the decomposition of a dry precursor was calcined in the temperature range of 550°C to 600°C. The heat treatments of the powder obtained were designed differently in the designed candidate mixtures:

- (1) The middle lanthanide cation system (Gd, Tb, Dy, Ho, Er): As the first attempt in this research, the ex situ heating experiments were performed from 600°C/2h to 1200°C/2h, with 100°C interval, to understand the optimum condition for crystallization. For the stability study, the amorphous samples were crystallized at 1200°C and further annealed at three different temperatures (600°C, 800°C, and 1000°C), with a dwell time of 10 hours. The densified pellets were finally sintered at 1400°C for microstructural and elemental analysis.
- (2) For system (1) and (2), small base lanthanides (Lu, Yb, Tm, Er, Ln) and large base lanthanides (La, Ce, Pr, Nd, Ln), experienced similar pre-calcining conditions to those described above, being heated to a temperature of 550°C at a ramp rate of 10°C/min, dwelling for 2 hours, followed by a hold time at 1150°C/2h, at a ramp rate of 5°C/min to allow for crystallization. The nano-sized particles were collected by a 10-stage cascade Multi Orifice Uniform Deposition Impactor (MSP Corporation MOUDI-110) for microstructure analysis.

### 3.4. Characterizations

#### 3.4.1. Powder X-ray diffraction

The structures of synthesized powder candidates were analyzed by the X-ray diffraction method. The calcined materials were first studied using a Cu K $\alpha$  radiation diffractometer (Siemens-Bruker D5000, Bruker AXS Inc., Madison, WI, USA). The diffraction results provided information on rough structural identification and crystallinity of powder samples. The high-resolution, in-situ high-temperature, X-ray powder diffraction patterns were collected at:

- (1) Advanced Photon Source (APS) at Argonne National Laboratory: synchrotron-generated X-rays at Beamlines 11-BM-B, 33-BM-C, 17-BM-B, and 6-ID-D.
- (2) National Synchrotron Light Source II (NSLS II) at Brookhaven National Laboratory: synchrotron-generated X-ray at Beamline 28-ID-2.

For all the in situ, high-temperature XRD studies, except for beamline 6 ID-D, the tested samples consisted of 90 wt% multicomponent lanthanide oxide and approximately 10 wt% platinum powder as a temperature standard.[145] The powders were mixed by a mortar and pestle with a small amount of isopropyl alcohol. After drying the solute in air, the tested powder samples were mounted in a sapphire capillary, sealed by an alumina stopper and zirconia paste, as shown in Figure 13. Mixing platinum with the tested sample powder had two functions:

- (1) Platinum, the stable metal with low heat capacity, can assist the temperature inside a sapphire capillary to reach the target temperature.[146, 147]
- (2) The thermal expansion trend of platinum has been well-studied.[147-149] The precise sample temperature could be obtained from the lattice parameters of platinum. In addition, the platinum powder did not react with the candidates under our testing environments (25-2000°C).

Furthermore, the platinum paste was painted between the scanning region in order to assist the heat transformation inside the sapphire capillary. The sapphire capillary usually softened or reacted with tested samples at around 1750°C.

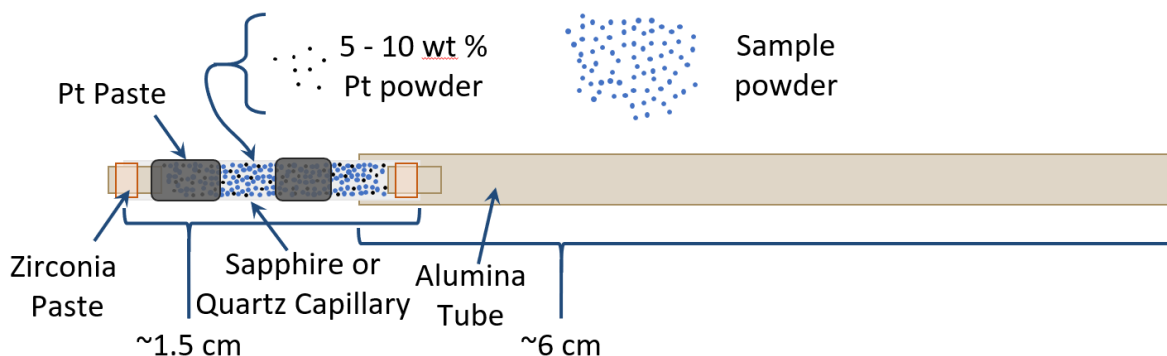


Figure 13. Schematic diagram of sample preparation for powder X-ray diffraction experiment in the quadrupole lamp furnace capable of reaching 2000°C in air

The quadrupole lamp furnace (4 x 150W bulbs) was equipped as a source to heat the mixture samples at the following three beamlines— 33-BM-C, 17-BM-B, and 28-ID-2.[145] The quadrupole furnace has the ability to heat the sample in the center hot zone, shown in Figure 14, from 200°C to about 2000°C. The water-cooling system was arranged around the furnace to either cool down the furnace and prevent damage to the wires and furnace body at high temperatures. A proportional-integral-derivative (PID) controller (Omega Engineering, Inc) was used to control the output power to the furnace. A type-B thermocouple was located on the top of the capillary, slightly outside of the middle hot zone. By receiving the temperature information from a thermocouple, the PID controller automatically adjusted the output power to make sure of the stability at the target temperature ( $\pm 10^\circ\text{C}$ ). The capillary was rotating during the experiment to avoid the influence of possible preferred orientations.

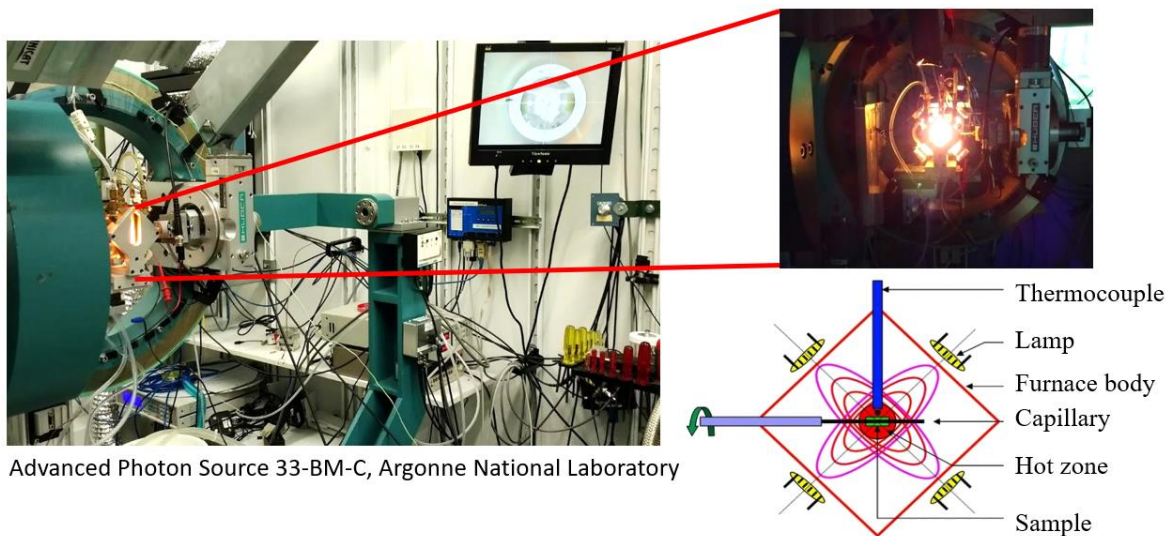


Figure 14. The quadrupole lamp furnace installed at APS 33BM-C. The bottom-right schematic is modified from ref. [150].

For the diffraction experiment performed at 6ID-D, a 400W CO<sub>2</sub> laser was equipped to achieve a high-temperature environment, under air gas, from 800°C to 3000°C.[151] In this conical nozzle levitator (CNL) system, schematically presented in Figure 15, a bead sample was placed on an air-streaming nozzle.

The bead samples were prepared by mixing 87 vol% of 1150°C calcined oxide powder with approximately 5 vol% methylcellulose binder (Millipore Sigma), 1 vol% Darvan C<sup>®</sup> dispersant (Vanderbilt Company, Inc., Norwalk, CT, USA), and a balanced vol% of deionized water. The slurry was pre-shaped into a spherical shape and dropped into the vibrating table at a frequency of about 70 Hz. The edges of the sample were smoothed by vibrating in a constrained 1 inch square volume and formed a spherically-shaped bead, as shown in Figure 15(b).[152] The samples were then calcined at 1100°C for 2 hours at a 10°C heating/cooling rate to burn out the organic additives.

During the in-situ heating experiments, the top of a tested bead was under exposure to a CO<sub>2</sub> laser (hot zone), while the bottom of a bead was close to room temperature. In this case, the X-ray

needed to be adjusted to focus on the top  $\sim 100\mu\text{m}$  of the bead. This process was to avoid obtaining diffraction patterns of our candidates with large temperature gradients. Unlike in the quadrupole lamp furnace, no platinum was added to the sample, due to the low melting point of platinum ( $1768.2^\circ\text{C}$ ). [146] The real temperature was identified by the infrared radiation on the top of the bead. The air flowing through the nozzle assisted the bead to spin vertically, which increased the homogeneity of heating on the top. Compared with the quadrupole lamp furnace ( $\pm 10^\circ\text{C}$ ),  $\text{CO}_2$  laser furnaces have a higher temperature deviation of  $\pm 100^\circ\text{C}$ . [153, 154] The large deviation in the latter system was caused by multiple issues: (1) no temperature standard (platinum) involved, (2) temperature gradient on the top of a tested sample, and (3) the calibration of the pyrometer. [145, 148, 154, 155]

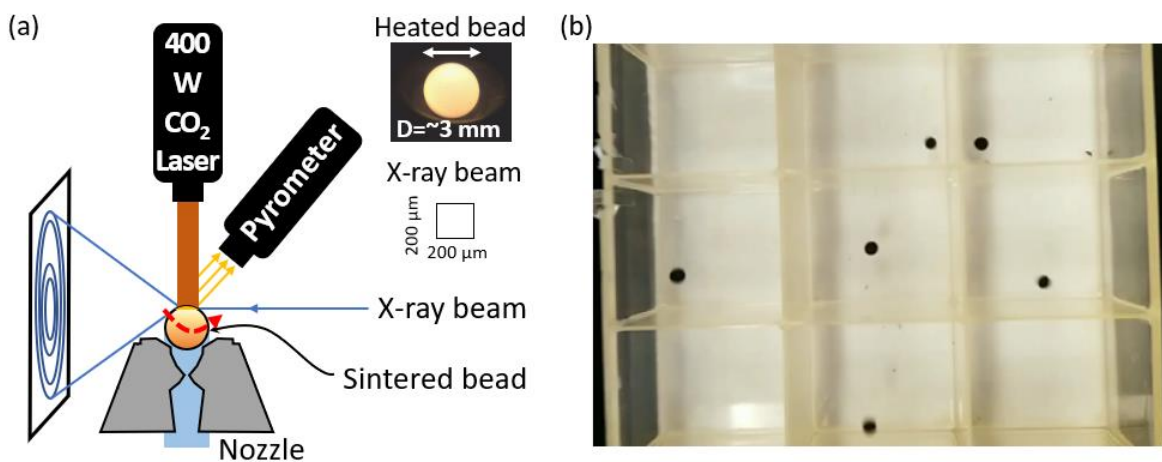


Figure 15. Schematic of conical nozzle levitator at 6ID-D. (a) The bead sample was heated by a  $\text{CO}_2$  laser, up to  $3000^\circ\text{C}$ . The X-ray beam was focused on the top of the vertically spinning bead. (b) The spherical beads were prepared by the vibration method, where the major ingredients of the tested sample and additives bounce in a constraint area. [152] The edges of a sample were smoothed over time and became a spherical bead.

The powder X-ray diffraction data were collected at five synchrotron-sourced beamlines. Detailed information is listed in Table 9. The sample to detector distance was determined by either

LaB<sub>6</sub> or CeO<sub>2</sub> standards. The area detectors were equipped at beamline 17-BM-B, 6-ID-D (APS), and 28-ID-2 (NSLS II). Figure 16(a) represents the diffraction pattern obtained from the LCPNTb sample at room temperature. The noise on both sides of the detector was due to the diffraction path being blocked by the quadrupole furnace. In an area detector, the high-intensity diffraction emitted from single-crystal sapphire can be observed (in red circles). The intensities of the sapphire capillary sometimes overlap with some of the diffraction peaks from the test sample and platinum. This situation could pose obstacles to phase identifications and refinement processes. One advantage of obtaining diffraction results via a 2D area detector is that the troublesome sapphire diffractions can be masked before integration. Because the final 1D diffraction data was obtained by integrating the section of diffraction rings generated by the tested sample, masking a small portion of the integrated diffraction ring merely affects the final diffraction pattern, as shown in Figure 16(c).

In the analysis process, firstly, the diffraction patterns were fitted by the JADE software, version 9.5, Materials Data, Livermore, CA, 2019. The crystalline phase identification database was obtained from the PDF-4+ 2017 database, from the International Center for Diffraction Data. The crystallographic information files (CIF) with similar crystal structures were modified to the correct chemical compositions. For example, during the analysis of GTDHEO, the best fitting CIF was Er<sub>2</sub>O<sub>3</sub> (PDF #04-008-8242).[156] This bixbyite crystal seemed to be the structure of our candidates; however, in the origin CIF, only erbium cation occupied in the octahedral sites. The CIF was modified by adding five constituent cations (Gd, Tb, Dy, Ho, Er) in the cation sites, with 20% occupancy each. Then the CIF was used as the input file for the Rietveld refinement analysis using TOPAS 5 software.[157, 158]

Table 9. Detailed information of synchrotron sourced X-ray diffraction beamline

Beamline	Wavelength	Calibration Standard	Detector	Temperature Ranges
11-BM-B (APS)	0.4127 Å	LaB <sub>6</sub>	Multiple Scintillators (LaCl <sub>3</sub> )	25°C
33-BM-C (APS)	0.5902 Å	LaB <sub>6</sub>	Pilatus 70K	200-1800°C
17-BM-B (APS)	0.2416 Å	CeO <sub>2</sub>	Varex 4343CT*	200-1800°C
6-ID-D (APS)	0.1285 Å	CeO <sub>2</sub>	Amorphous silicon*	800-2500°C
28-ID-2 (NSLS II)	0.2370 Å	LaB <sub>6</sub> and CeO <sub>2</sub>	α-Si Perkin Elmer XRD1621*	200-1100°C

\*Area detector

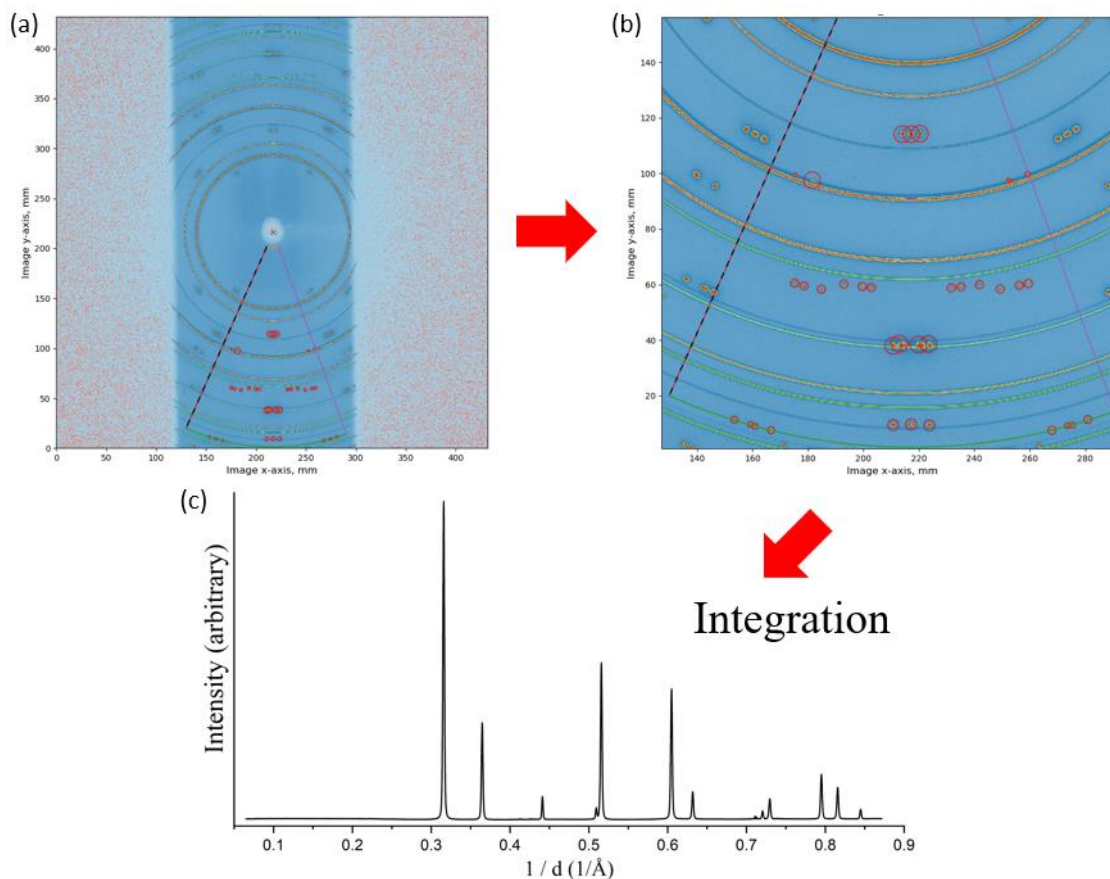


Figure 16. The process of integrating a 2D area diffraction pattern to 1D data. (a) The data obtained from a 2D detector plate. (b) The diffractions emitted from sapphire capillary were masked out (red circle). The section of the diffraction ring was chosen for integration. (c) Final 1D diffraction data after integration, without the interference of sapphire diffractions

### 3.4.2. Microstructure characterization

The microstructures and elemental compositions were examined by:

- (1) Scanning electron microscopes (SEM, model S-4700, Hitachi; Quanta 3D model, FEI, Inc.) with energy-dispersive X-ray spectroscopy (EDS).
- (2) JEOL 2010 LaB<sub>6</sub> Transmission Electron Microscopy (TEM) (voltage: 200 kV)
- (3) JEOL JEM-ARM300F Scanning Transmission Electron Microscope (STEM) (double aberration correctors and two JEOL Si drift EDS detectors), operated by Dr. Qun Yang

The high angle, annular dark-field (HAADF), annular bright-field (ABF) images, and atomic-scale STEM-EDS mapping were performed at a voltage of 300 kV using the STEM, JEOL JEM-ARM300F. The attainable resolution of the probe was 63 picometers. The collection semi-angles for HAADF and ABF were 54-220 and 14-27 mrad, respectively. The TEM diffraction patterns were compared to the simulated pattern via Java Electron Microscopy Software.[159] The simulated patterns were generated from the CIFs constituted by the Rietveld refinement method. In the sample preparation process, soft agglomerates of crystalline powder samples were broken up by a planetary mill (Planetary Micro Mill Pulverisette 7 Classic Line, Fritsch). The grinding process was performed at 350 rpm for 10 mins. The sieving process was prepared through an aerosol sample collection method, performed at the Environmental Molecular Sciences Laboratory at Pacific Northwest National Laboratory, Richland, WA, as shown in Figure 17. First, the dried powder was added to deionized water. The nitrogen gas flow created bubbles containing a mixture of water and our synthesized powder sample. The aerosol mixtures then experienced a dehydration process by passing through the diffusion dryer CaSO<sub>4</sub>. Next, the powder sample passed through a 10-stage cascade Multi Orifice Uniform Deposition Impactor (MSP Corporation MOUDI-110). The powder sample, with particle sizes <0.18μm, was collected at the top of carbon-coated 400 mesh copper grids for microstructure analysis.



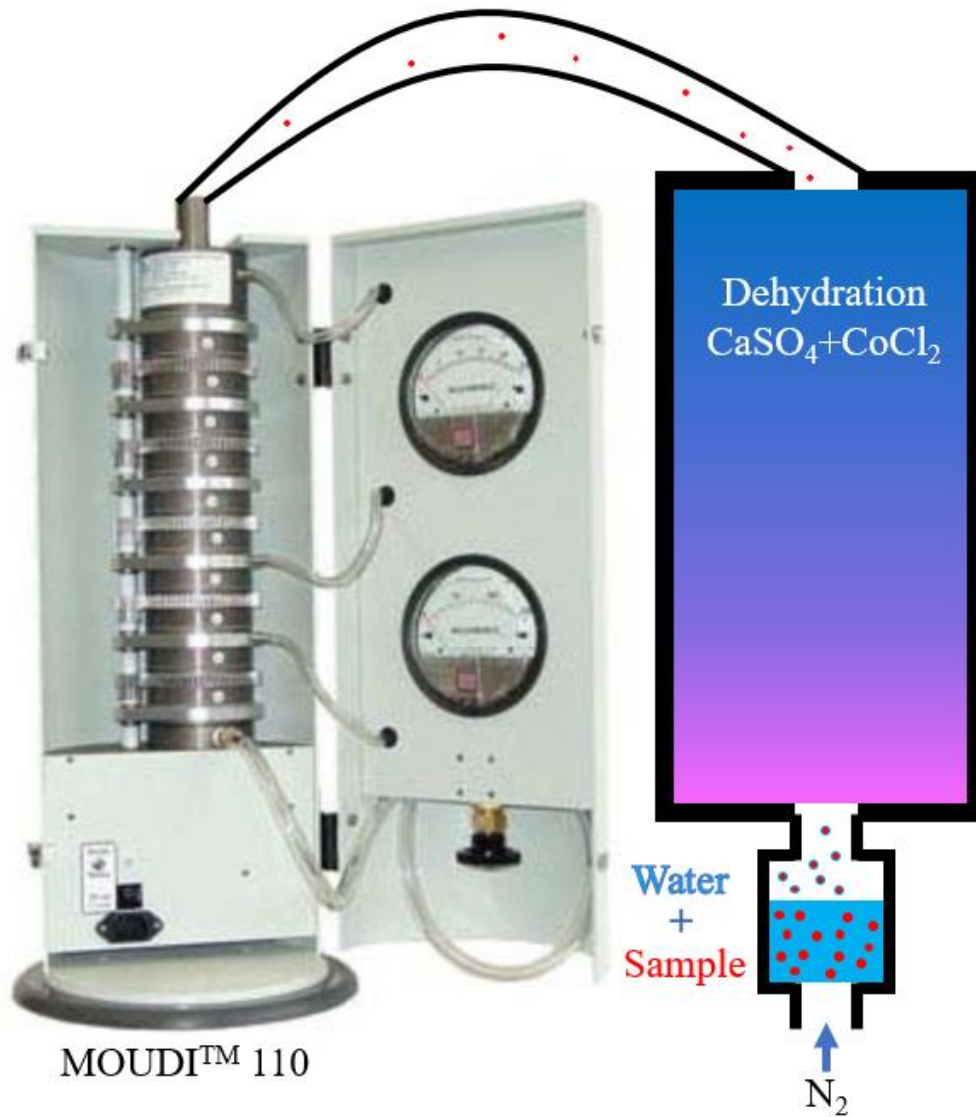


Figure 17. Schematic of powder sample preparation process for microstructure analysis. After passing through the cascade impactor, small powder particles ( $<0.18\mu\text{m}$ ) were collected on 400 mesh copper grids.

## CHAPTER 4: PHASE IDENTIFICATION AND STABILITY OF

### MIDDLE LANTHANIDE HELO— $(\text{Gd}_{0.4}\text{Tb}_{0.4}\text{Dy}_{0.4}\text{Ho}_{0.4}\text{Er}_{0.4})\text{O}_3$

#### 4.1. Crystal Structure and High-Temperature Stability of $(\text{Gd}_{0.4}\text{Tb}_{0.4}\text{Dy}_{0.4}\text{Ho}_{0.4}\text{Er}_{0.4})\text{O}_3$ (GTDHEO)

Figure 18 and Table 10 summarizes the in situ high-temperature X-ray powder diffraction patterns of  $(\text{Gd}_{0.4}\text{Tb}_{0.4}\text{Dy}_{0.4}\text{Ho}_{0.4}\text{Er}_{0.4})\text{O}_3$  (GTDHEO) as a function of temperature. At 600°C, the material was in an amorphous state, where the crystalline peaks in the diffraction patterns came from the platinum standard and the sapphire capillary. The region of diffraction emitted from the sapphire capillary was excluded in the refinement process. At a temperature just below 1126°C, the lanthanide sample started to crystallize into the bixbyite structure coexisting with secondary phases. An attempt was made to fit the secondary phase(s) using the current lanthanide crystallographic database. The lanthanide oxo-sulfates,  $\text{Ln}_2\text{O}_2\text{SO}_4$  (Ln: Ho, Er), having a monoclinic structure were the only phases that matched the secondary phase. However, no sulfates were involved in our synthesis process. Because of the limited database for lanthanide materials, the secondary phase(s) we observed may not have been reported yet or were multiple metastable phases. At 1149°C, the high-entropy, lanthanide sesquioxide became a single-phase, solid solution having the bixbyite structure, which remained stable up to 1514°C. The high-entropy GTDHEO oxide did not experience phase transformations, despite using mono-cation oxides of  $\text{Tb}_2\text{O}_3$  and  $\text{Gd}_2\text{O}_3$ , which would normally disproportionate at 280°C and 1250°C, respectively.[58, 59, 74, 76, 77]

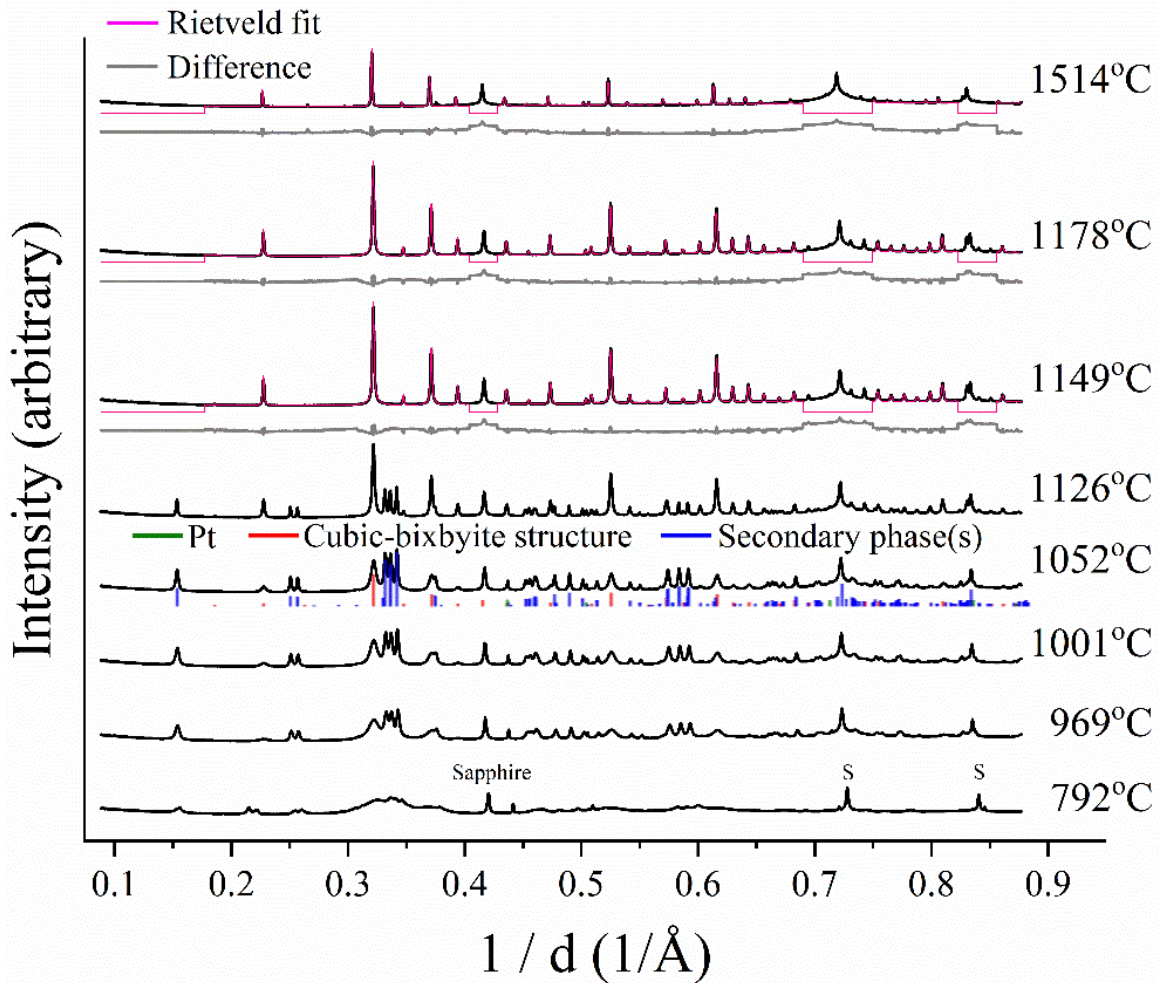


Figure 18. In situ high-temperature X-ray diffraction patterns of 600°C/2h-calcined, multi-component precursor in the temperature range of 600°C to 1514°C (multiple phases were formed below 1149°C). Above 1149°C, the high-entropy, lanthanide sesquioxide,  $\text{Gd}_{0.4}\text{Tb}_{0.4}\text{Dy}_{0.4}\text{Ho}_{0.4}\text{Er}_{0.4}\text{O}_3$ , having a bixbyite structure became single-phase and remained stable up to 1514°C. The temperatures of in situ experiments were determined via a platinum standard. Representative data were selected from 15 powder diffraction patterns.

Table 10. The evolution of HELO sample  $Gd_{0.4}Tb_{0.4}Dy_{0.4}Ho_{0.4}Er_{0.4}O_3$ . The temperatures were identified by the platinum standard.

	Real T	Lattice parameter	Bixbyite phase	Monoclinic phase
←Heating Process	25 °C		Amorphous phase	
	792 °C		Amorphous phase	
	969 °C	10.7566Å	34.35%	65.65%
	1001 °C	10.7576Å	30.49%	69.51%
	1052 °C	10.7616Å	29.24%	70.76%
	1084 °C	10.7644Å	32.20%	67.80%
	1126 °C	10.7702Å	46.72%	53.28%
	1149 °C	10.7725Å	100.00%	
	1178 °C	10.7760Å	100.00%	
	1257 °C	10.7846Å	100.00%	
	1339 °C	10.7950Å	100.00%	
	1514 °C	10.8200Å	100.00%	
←Cooling Process	1487 °C	10.8128Å	100.00%	
	1389 °C	10.8035Å	100.00%	
	1287 °C	10.7927Å	100.00%	
	1190 °C	10.7827Å	100.00%	
	1090 °C	10.7719Å	100.00%	
	984 °C	10.7611Å	100.00%	
	881 °C	10.7508Å	100.00%	
	773 °C	10.7401Å	100.00%	
	661 °C	10.7293Å	100.00%	
	562 °C	10.7196Å	100.00%	
	462 °C	10.7088Å	100.00%	
	362 °C	10.6985Å	100.00%	
	264 °C	10.6894Å	100.00%	
	26 °C	10.6694Å	100.00%	

Several HEOs have been found to experience the reversible phase transformations, which was believed to be driven by entropy.[7, 32, 33, 51] During the in-situ cooling experiments (Figure 19 and Table 10), the monoclinic phase observed before GTDHEO crystallization did not reappear.

In the Rietveld refinement process, the goodness of fit of each diffraction spectrum was identified by monitoring the quality of fit between the observed and calculated patterns. The R factor did not clearly express the good-of-fit in the powder refinement.[160] In Figure 19, the calculated pattern, red dashed lines, is overlaid on the pattern observed from X-ray diffraction, solid black lines. The difference between calculation and observation was indicated by the solid blue lines, located below the diffraction pattern. During these XRD experiments, the regions of diffraction from sapphire capillaries were excluded. The calculated patterns were virtually identical to the collected XRD patterns in the cooling process.

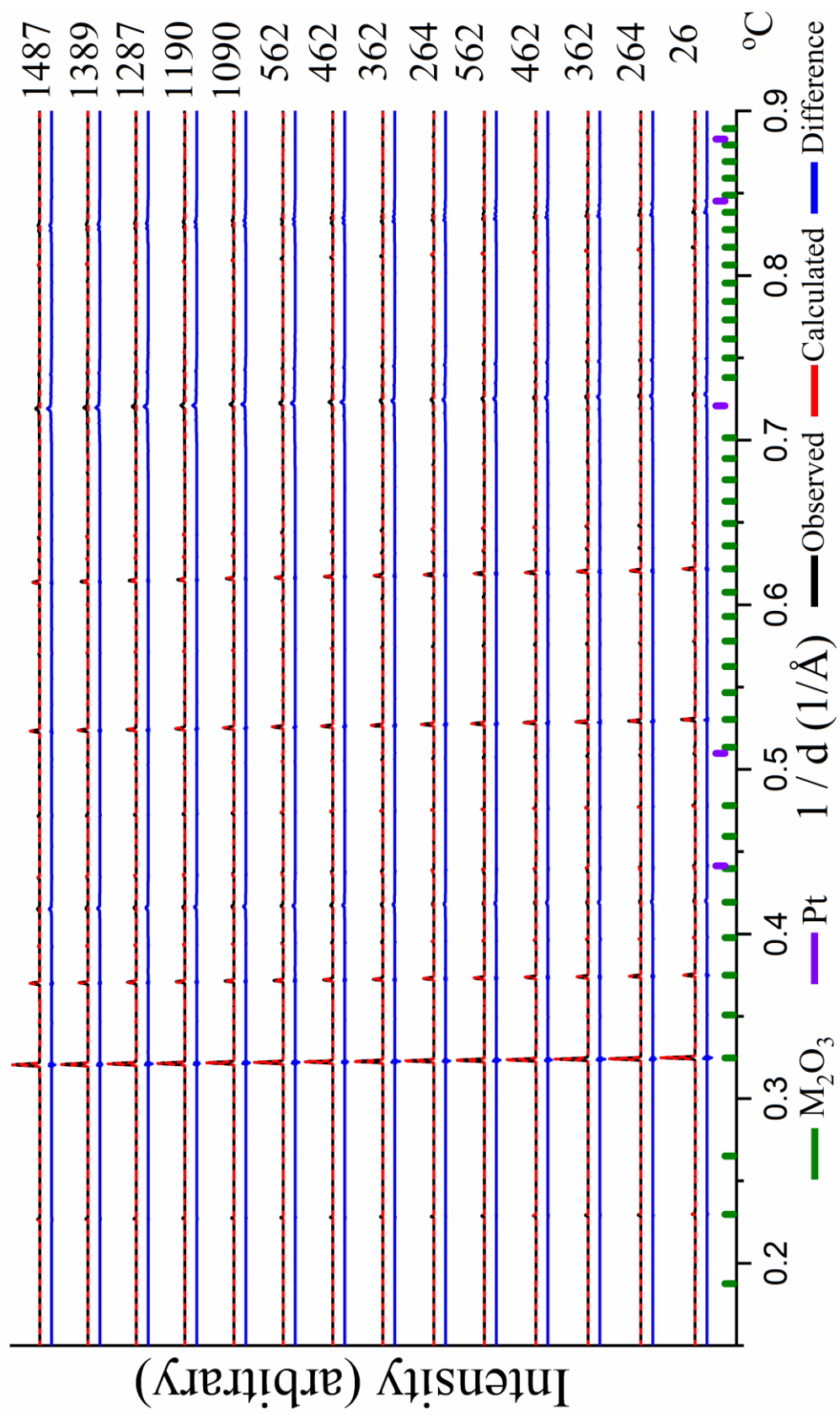


Figure 19. Refinement results of the in-situ cooling X-ray diffraction. No transformation was observed from 1487 $^{\circ}\text{C}$  to room-temperature.

In the synchrotron experiments, the cooling rate was fast ( $\sim 10^\circ\text{C}/\text{sec}$ ), and the dwell time was short ( $\sim 10$  mins), compared to the conventional furnace cooling situation. To examine the reversibility of the unknown phase(s), the single-phase GTDHEO was firstly crystallized at  $1200^\circ\text{C}$  for 2 hours, followed by annealing at three temperatures ( $600^\circ\text{C}$ ,  $800^\circ\text{C}$ , and  $1000^\circ\text{C}$ ) for 10 hours (as shown in Figure 20). The annealing temperatures were lower than the phase transition temperature, i.e.,  $1149^\circ\text{C}$ . The annealed samples were then analyzed by the high precision, synchrotron sourced, X-ray diffraction at 11BM-B at APS. In Figure 21, X-ray powder diffraction patterns indicated that the annealed samples exhibited the identical diffraction patterns with the single-phase GTDHEO, indicating no secondary phase(s) existed during the cooling process. For the GTDHEO formation, the precursor needed to reach above  $1149^\circ\text{C}$  to form the single-phase structure. Once the HEO was crystallized, the structure remained stable up to  $1514^\circ\text{C}$ . Therefore, these results provide evidence that the formation of a HELO was not dominated by a particular cation, such as cerium as reported by Djenadic et. al.[50] The next experiment was designed to study the evolution of lattice parameters of the single-phase GTDHEO, and its properties.

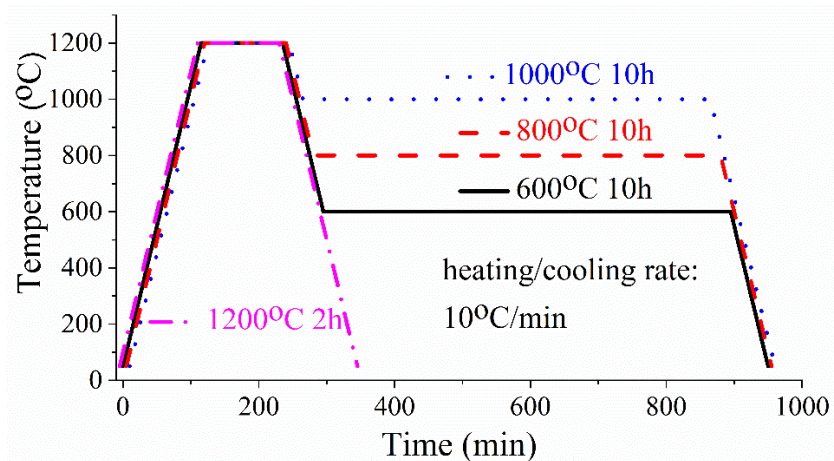


Figure 20. Schematic of the heat treatments for the stability study. The single-phase, solid solution GTDHEO was prepared at 1200°C and then annealed at 600°C, 800°C, and 1000°C for 10 hours, respectively.

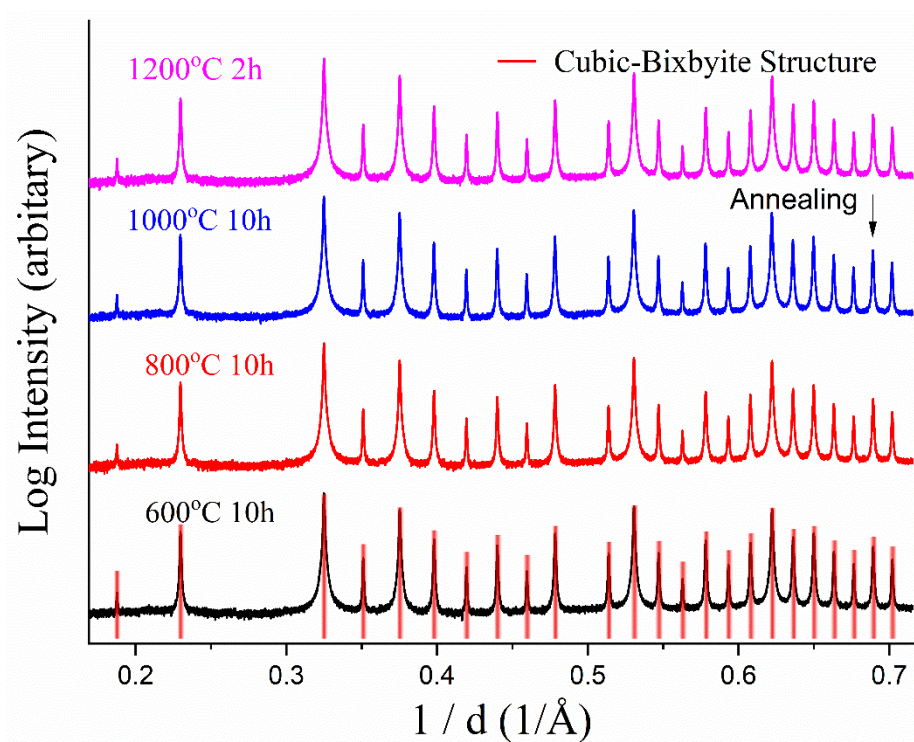


Figure 21. Phase transformation reversibility of  $\text{Gd}_{0.4}\text{Tb}_{0.4}\text{Dy}_{0.4}\text{Ho}_{0.4}\text{Er}_{0.4}\text{O}_3$  (GTDHEO) upon cooling. X-ray powder diffraction patterns of the samples experiencing the cooling treatments were identical. The cubic-bixbyite structure remained stable after 10 hours of annealing.



## 4.2. Characterization of GTDHEO

### 4.2.1. Coefficient of thermal expansion of GTDHEO

The second batch of GTDHEO powder sample was crystallized at 1200°C for 2 hours. The cubic lattice parameter of the single-phase GTDHEO having the bixbyite structure, was analyzed via in situ X-ray diffraction measured at increasing temperatures in air, from room temperature to 1639°C (Table 11). The evolution of lattice parameters with temperatures is plotted in Figure 22. The measured cubic lattice parameter at room temperature was  $10.6663 \pm 0.006$  Å. The material expanded as the temperature increased, and the change in lattice parameter followed a second-order polynomial equation having an R-squared value of 0.9994:

$$a = 10.66347 + 7.86846 \times 10^{-5} T + 1.12776 \times 10^{-8} T^2 \quad \{8\}$$

Where  $a$  is the lattice parameter in Angstroms, and  $T$  is the temperature in degrees Celsius. As a cubic structure, the bixbyite lattice expanded uniformly in all directions. The coefficient of linear thermal expansion (CTE,  $\alpha$ ) could be calculated as a function of the relationship between lattice parameter ( $L$ ), temperature ( $T$ ), and lattice parameter at room-temperature ( $L_0$ ). [148, 149, 161]

$$\alpha = \frac{1}{L_0} \frac{dL}{dT} \quad \{9\}$$

Combining equation {8} and {9}, the evolution of the coefficient of linear thermal expansion was expressed in the following equation and Figure 23.

$$\alpha = 7.37889 \times 10^{-6} + 2.11518 \times 10^{-9} T \quad \{10\}$$

Table 11. The evolution of lattice parameters in the single-phase GTDHEO

Temperature (°C)	Lattice Parameter Å	Temperature (°C)	Lattice Parameter Å
31 °C	10.6663 Å	1094 °C	10.7631 Å
335 °C	10.6908 Å	1135 °C	10.7674 Å
396 °C	10.6954 Å	1172 °C	10.7708 Å
471 °C	10.7005 Å	1215 °C	10.7751 Å
534 °C	10.7091 Å	1256 °C	10.7794 Å
606 °C	10.7161 Å	1296 °C	10.7837 Å
673 °C	10.7225 Å	1336 °C	10.7876 Å
732 °C	10.7279 Å	1384 °C	10.7930 Å
793 °C	10.7339 Å	1440 °C	10.7990 Å
845 °C	10.7389 Å	1498 °C	10.8062 Å
893 °C	10.7434 Å	1564 °C	10.8130 Å
980 °C	10.7519 Å	1602 °C	10.8199 Å
1016 °C	10.7555 Å	1639 °C	10.8250 Å
1054 °C	10.7591 Å		

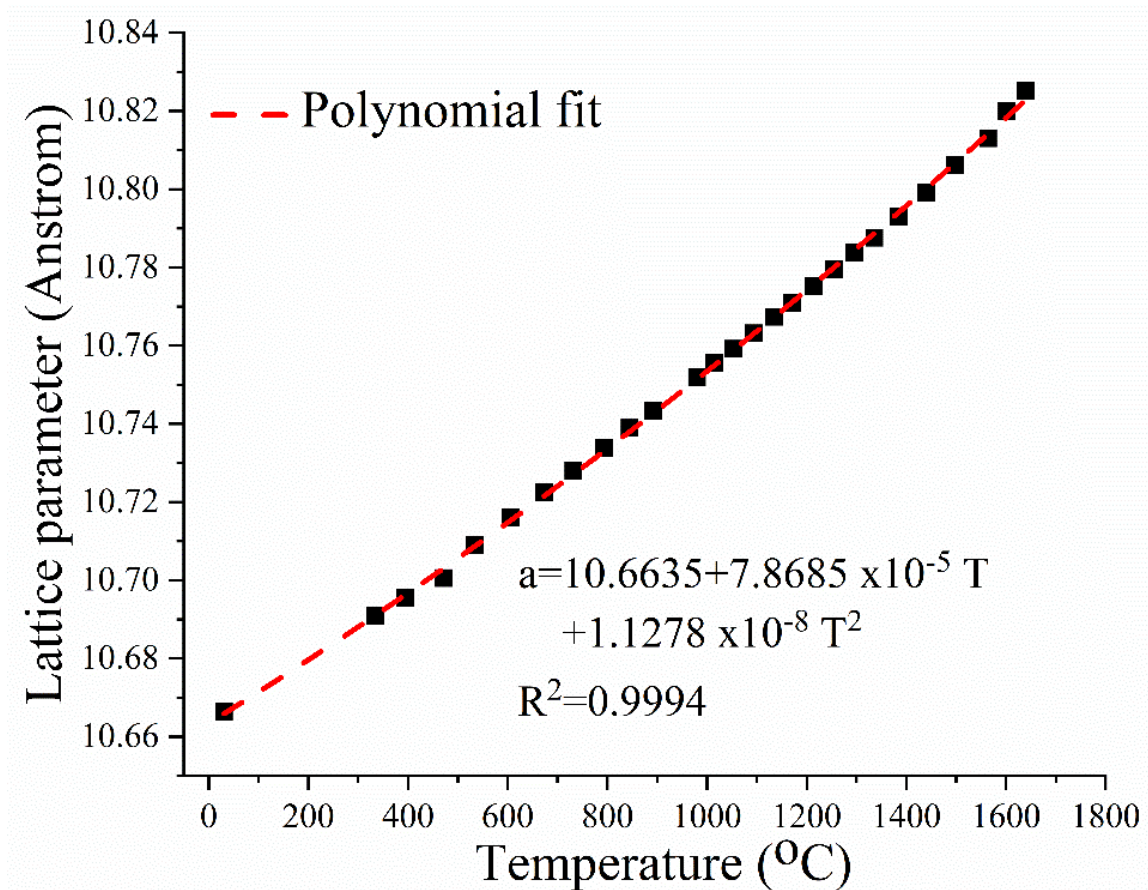


Figure 22. The cubic lattice parameter ( $a$ ) as a function of temperature ( $T$ ) for the bixbyite GTDHEO structure. The lattice parameters were analyzed from in situ heating X-ray diffraction patterns obtained from room temperature to 1639°C. The lattice expanded as temperature increased. The polynomial curve fitted the trend of the lattice parameter with an R-squared value of 0.9994.

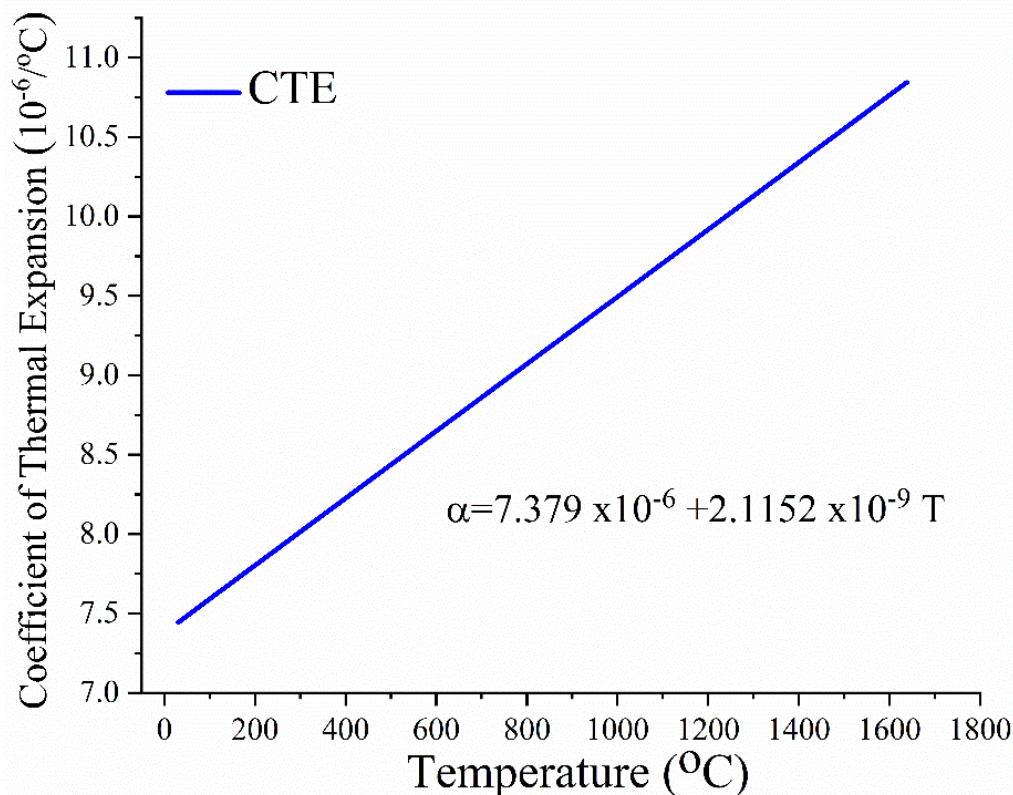


Figure 23. The evolution of the coefficient of linear thermal expansion in the GTDHEO sample, from room temperature to about 1600°C

#### 4.2.2. Elemental distribution in GTDHEO crystal structure

The single-phase, solid solution, GTDHEO bixbyite structure, was prepared by Kuo-Pin Tseng and further examined by TEM, operated by Dr. Qun Yang at the Shanghai Tech University, Shanghai, China. The selected area electron diffraction (SAED) pattern taken from the <111> direction (Figure 24(a)) matched the simulated pattern in Figure 24(b). The simulated patterns of bixbyite GTDHEO were constructed based on a high-precision crystallographic information file (CIF), which was generated by Kuo-Pin Tseng via the high-resolution X-ray powder diffraction at beamline 11-BM-B, APS, taken at room temperature, with the designation that the five-lanthanide cations occupied the same sites randomly and equally. The cross marks in the simulated pattern

represent the electron double diffraction reflections. The STEM-HAADF and ABF images taken from the  $\langle 110 \rangle$  direction were consistent with the structural model extracted from the XRD results.

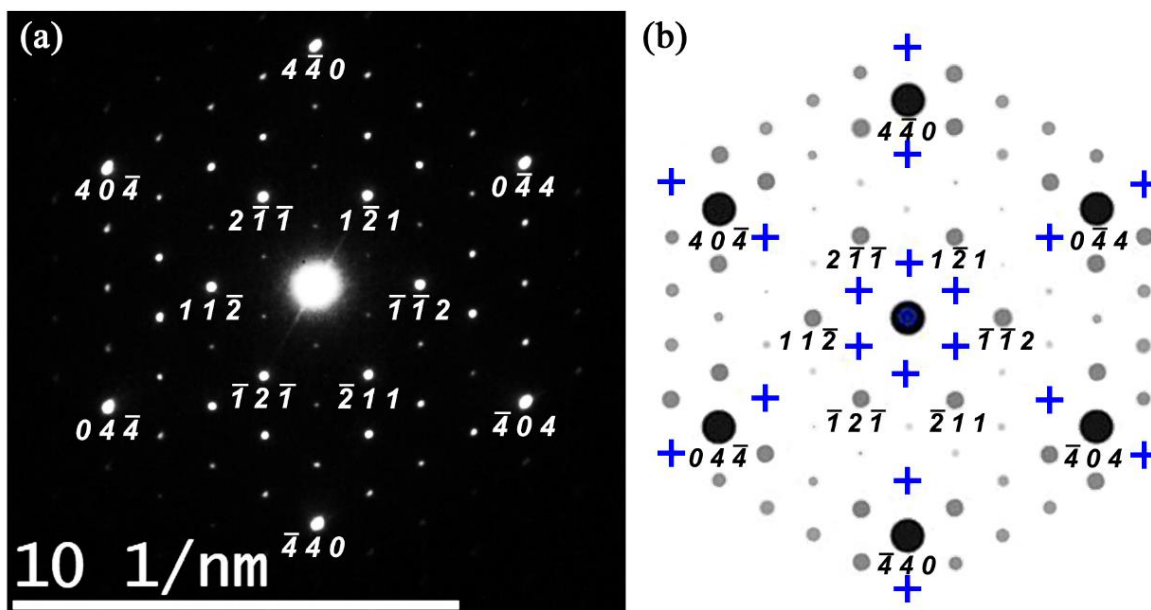
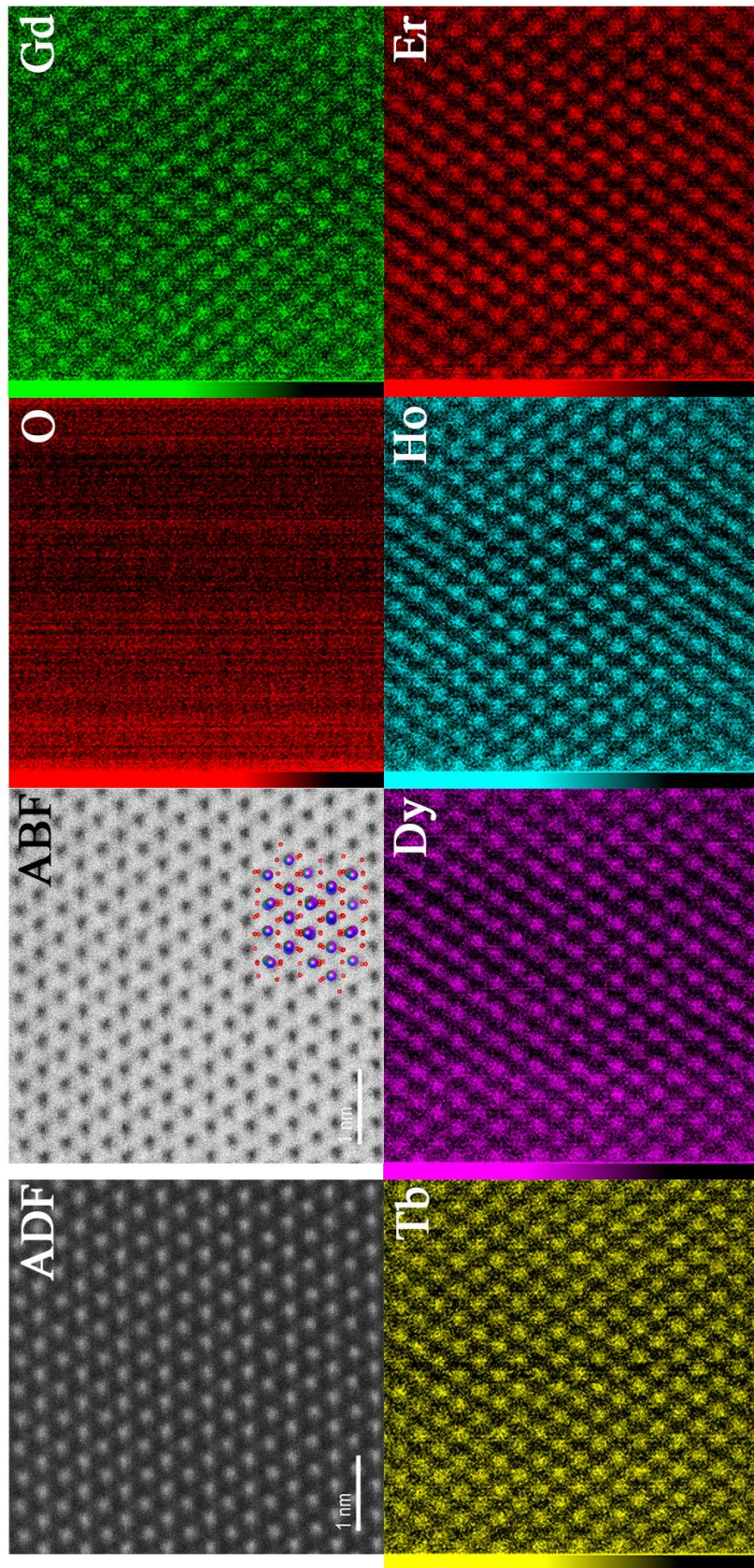


Figure 24. TEM diffraction of the high-entropy, lanthanide sesquioxide. (a) Selected area electron diffraction (SAED) pattern of the single-phase, solid solution GTDHEO taken down the  $\langle 111 \rangle$  direction matches with the simulated pattern (b) of a bixbyite structure containing five lanthanide cations. The simulated pattern was constructed from the high precision, synchrotron-sourced, X-ray diffraction results. The cross marks in the simulated pattern represent electron double diffraction reflections.

STEM-EDS mapping, Figure 25, showed that the five constituent lanthanide cations (Gd, Tb, Dy, Ho, Er) in GTDHEO were homogeneously distributed on the atomic scale. No observable segregation or aggregation of particular cation was observed. Moreover, the ion positions were constructed by the CIF file and overlaid on the ABF image. In this bright-field image, the dark region represents cations on an atomic scale, which perfectly matched the GTDHEO crystal generated by XRD. The XRD and SAED results confirmed that the obtained GTDHEO was a single-phase HELO from room temperature to 1650°C.



60

Figure 25. HAADF and ABF images were taken from the  $\langle 110 \rangle$  direction and atomic resolution elemental mappings of GTDHEO. It is seen that five constituent cations were homogeneously distributed in the elemental maps. The anion/cation positions, obtained via the CIF file generated by XRD results, are overlaid on the ABF image.

#### 4.2.3. Valence configuration of GTDHEO

In bixbyite sesquioxide,  $M_2O_3$ , the major oxidation state should be trivalent for charge balance. The powder color of GTDHEO at a glance was yellowish-brown (Figure 26). Based on the color listed in Table 4, the colors of trivalent states of constituent cations are either colorless or light colors, indicating that a terbium tetravalent (brown color) could be involved in the GTDHEO structure. In Section 4.1, XRD diffraction confirmed that there was no impurity involved after the crystallization process. In other words, both trivalent and tetravalent terbium were coerced to remain in the cubic-bixbyite structure. An attempt was made by using X-ray photoelectron spectroscopy (XPS) to determine the valence configuration of terbium. During the experiment, two terbium oxide powder samples were synthesized as the standards. In Figure 27, the characteristic signals in the range 143-154 eV were attributed to  $Tb^{3+}$ , and those in the range 153-167 eV arose from  $Tb^{4+}$ . These results obtained from two standards agreed with observations reported in the literature.[73, 162-165] The spectrum of bonding energies in GTDHEO exhibited multiple overlapping characteristic signals from 138-170 eV. In consideration of bonding energies of other constituent cations in GTDHEO: gadolinium ( $Gd^{3+}$  4d at 142eV), dysprosium ( $Dy^{3+}$  4d at 156.1eV), holmium ( $Ho^{3+}$  4d at 160eV) and erbium ( $Er^{3+}$  4d at 168eV), those characteristic signals, in or around the  $Tb^{4+}$  4d regions, increased the difficulty in identifying the presence of  $Tb^{4+}$ . Even though the evidence of trivalent terbium ( $Tb^{3+}$ ) was observed via the XPS results, the overlapping regions from the other four lanthanide cations made it difficult to obtain a reliable result.



Gd <sup>3+</sup>	Colorless
Tb <sup>3+</sup>	Colorless
Tb <sup>4+</sup>	Brown
Dy <sup>3+</sup>	Pale yellow
Ho <sup>3+</sup>	Brownish pink
Er <sup>3+</sup>	Pink

Figure 26. The color of the crystallized GTDHEO powder sample. Based on the yellowish-brown color, trivalent and tetravalent terbium might have coexisted in the bixbyite structure.



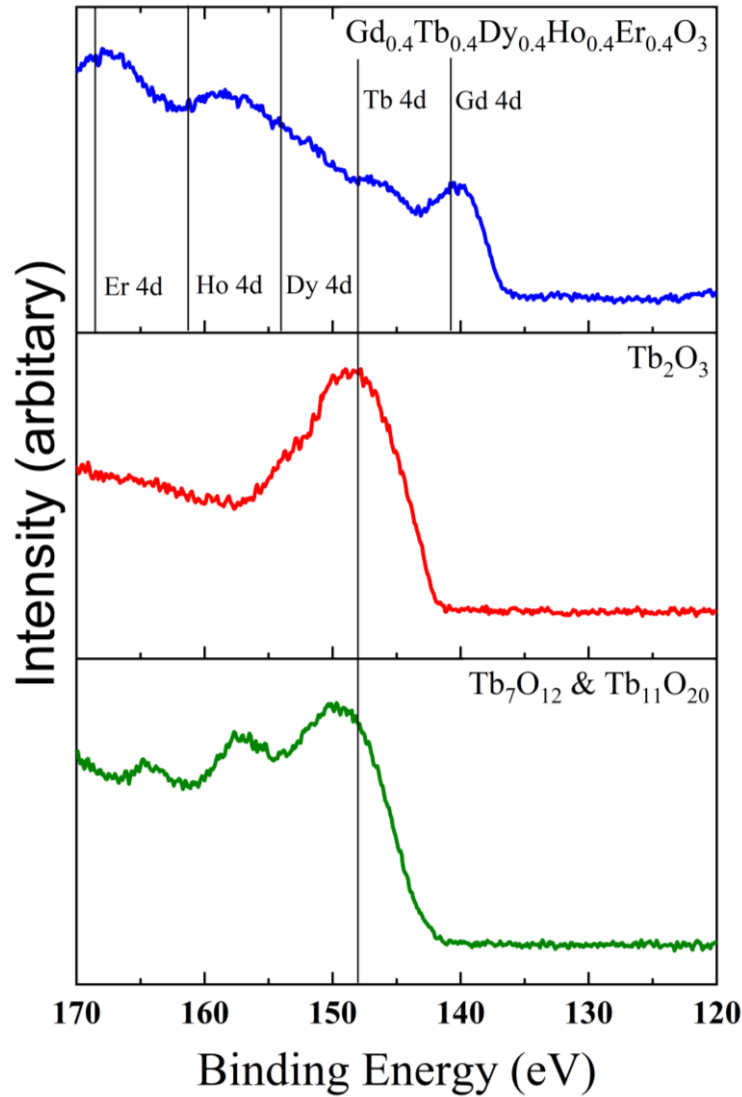


Figure 27. XPS spectra of 4d orbital electrons in selected lanthanides. Compared to terbium sesquioxide, the terbium oxides are composed of a mixture of trivalent and tetravalent,  $Tb_7O_{12}$  and  $Tb_{11}O_{20}$ , involving additional peaks in binding energy at 155-170eV. The binding energy of lanthanide elements (Er, Ho, Dy) in  $Gd_{0.4}Tb_{0.4}Dy_{0.4}Ho_{0.4}Er_{0.4}O_3$  overlap with the tetravalent terbium element.

#### 4.2.4. Magnetic property of GTDHEO

The direct current (dc) magnetic susceptibility measurements of GTDHEO in the temperature range from 5K to 400K are shown in Figure 28. They indicated that GTDHEO had paramagnetic

properties. No magnetically ordered clusters (antiferromagnetic domains) were found down to 5 K. The temperature dependence of the inverse magnetic susceptibility exhibited a linear behavior. At 285 K, the measured magnetic molar susceptibility of GTDHEO was  $7.6388 \times 10^{-2} \text{ cm}^3/\text{mol}$ , which was close to the result calculated by the rule of mixtures,  $7.6632 \times 10^{-2} \text{ cm}^3/\text{mol}$ . The calculated value was obtained from the cumulation of the magnetic molar susceptibility from each cation multiplied by its molecular percentage. Based on the measurement results, GTDHEO still exhibited relatively high magnetic susceptibility comparing to other oxide materials.[114] Normally, the rule of mixtures is applied to composites instead of to the single-phase, high-entropy materials. The homogeneous arrangement of cations in GTDHEO did not suppress or enhance the magnetic property. However, since only one HEO was analyzed for the magnetic property in this research, extrapolating this observation to be a general concept in HEOs would be hasty. Further study is required to understand the magnetic behavior in HEOs.

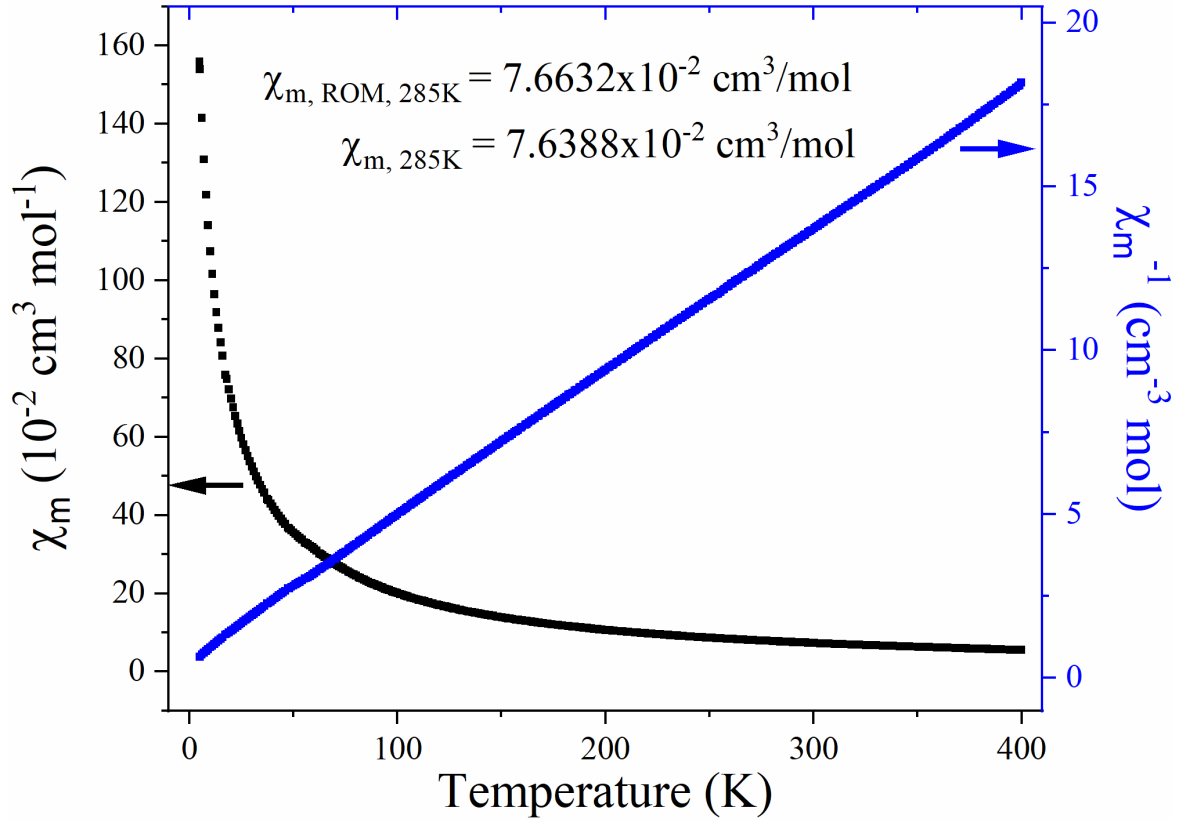


Figure 28. Magnetic susceptibility of the high-entropy, lanthanide sesquioxide, GTDHEO from 5-400K. This oxide has paramagnetic susceptibility. The inverse magnetic molar susceptibility has a linear relationship with temperature. The molar susceptibility ( $\chi_m$ ) at room temperature follows the rule of mixtures (ROM) of mono-cation sesquioxides.

#### 4.3. Conclusions

The phase stability of the high-entropy GTDHEO could be explained by the homogeneity of elements, with the support of TEM/SAED patterns and TEM/EDS mapping, presented in Figure 24 and Figure 25. Additionally, the X-ray, TEM electron diffraction, and TEM atomic resolution EDS results demonstrated that there was no clustering in GTDHEO, which fulfilled the requirement of a cation disorder, single-phase solid solution, for high-entropy oxides. In the high-entropy arrangement, individual atoms are surrounded primarily by a random distribution of the second nearest neighbor atoms.[3, 5] This arrangement of randomly distributed cations in the

oxygen polyhedron sites prevents specific elements from clustering, which would induce phase separation from a single-phase system. As a result, this arrangement was able to inhibit the phase transformations associated with individual constituent elements in this multi-component high entropy system.

Djenadic et al.[50] claimed that cerium was a crucial element for stabilizing high-entropy, rare-earth oxides. However, our high-entropy, lanthanide sesquioxide, GTDHEO, did not contain any cerium as a constituent cation. Research into high-entropy alloys stated that the atomic size plays a key role in element selection.[28, 44] In Djenadic's research, cerium may have reduced the size gap in rare-earth oxides, resulting in single-phase, solid solution formation. In our GTDHEO system, the small radii difference among the constituent cations, within a difference of 5%, could be a factor constraining constituent lanthanide cations into a single-phase structure. Further study is required to understand the mechanism of chemical selection for high-entropy oxides.

In conclusion, the high-entropy, single-phase, solid solution, lanthanide sesquioxide,  $Gd_{0.4}Tb_{0.4}Dy_{0.4}Ho_{0.4}Er_{0.4}O_3$ , exhibited non-reversible formation after 10 hours of annealing and remained stable in a bixbyite structure from room temperature to 1650°C. The homogeneous, random cation arrangement in this high-entropy oxide could inhibit the phase transformations occurring in the constituent mono-cation sesquioxides. This structural constraint of high-entropy oxides could sustain the phase stability, which could be helpful in the discovery of new refractory materials. In addition, the magnetic susceptibility of GTDHEO was not suppressed by the multi-cation arrangement and followed the rule of mixtures. The crystallographic stability of high-entropy oxides demonstrated their potential as promising heat resistant materials.

## CHAPTER 5: CRYSTAL STRUCTURE IDENTIFICATION OF MULTI-COMPONENT OXIDES AT AMBIENT CONDITIONS

Two systems were designed to understand the behavior of (1) larger cations fitted in smaller interstitial sites (LYTE system), and (2) smaller cations added in more significant interstitial sites (LCPN system). In CHAPTER 5: and CHAPTER 6:, the evolutions of crystal structures in these two systems are introduced separately. Moreover, the homogeneity of cations and thermal expansions of crystallized, single-phase, high-entropy lanthanide oxides (HELOs) are also described. The significance of size mismatch and preferred valence configurations are proposed in CHAPTER 7:.

### 5.1. Crystal Structure of a System with Small Based Lanthanides (Lu, Yb, Tm, Er) (LYTE)

In the LYTE system, larger cations were added as the fifth cation candidates. At room temperature, the X-ray diffraction results (Figure 29) indicated that all of the multi-component oxides, except LYTELa, were in the C-type cubic-bixbyite structures. According to the intensity map plotted in Figure 30, these structures exhibited an identical crystal structure. The multi-component oxide constructed by the four base constituent candidates (Lu, Yb, Tm, Er) was synthesized as a comparison. These base lanthanide sesquioxides occur in nature as C-type bixbyite structures. Obviously, the oxide material constructed by these four cations exhibited the same structure. In the LYTE system, the four largest cations (La, Ce, Pr, Nd) could be naturally stable in the A-type hexagonal sesquioxide structures. However, in these crystallized HELOs, three out of four oxides, except LYTELa, were constrained in the cubic-bixbyite, single-phase solid solution. The lattice parameters obtained through Rietveld refinement are listed in Table 12.

The coexistence of both bixbyite and perovskite phases was found in the LYTELa sample. The perovskite structure consisted of lanthanum, and a small-sized lanthanide (Lu, Yb, Tm, and Er) have been reported in the literature.[102] Previous research on phase diagrams also found that cerium and three other smaller cations (Lu, Yb, and Tm) lie in the perovskite structures.[105] However, in contrast to LYTELa, LYTECe was stabilized in a single-phase, bixbyite structure. In the meantime, based on the assumption that LYTELa formed a single-phase HELO, the radius mismatch parameter would reach 7.03, which might exceed a threshold for 6-fold geometry HEOs. The LYTE system provided clear evidence that the cation radii mismatch could obstruct the structural arrangement of high-entropy oxides.

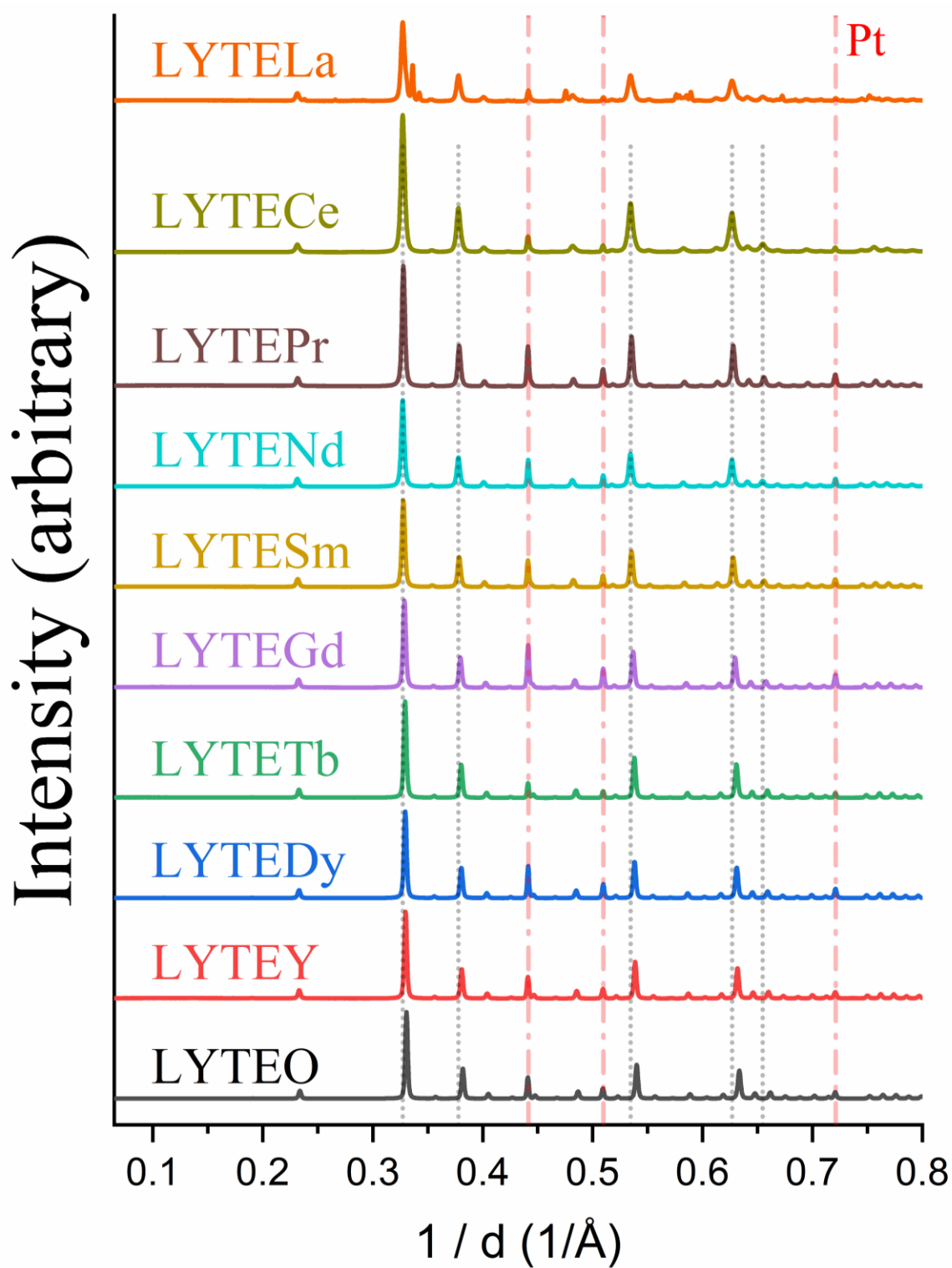


Figure 29. X-ray diffraction patterns of the candidates in the LYTE system at room temperature. The LYTELa sample exhibits the coexistence of bixbyite and perovskite structures. Other LYTE samples have identical single-phase bixbyite structure.

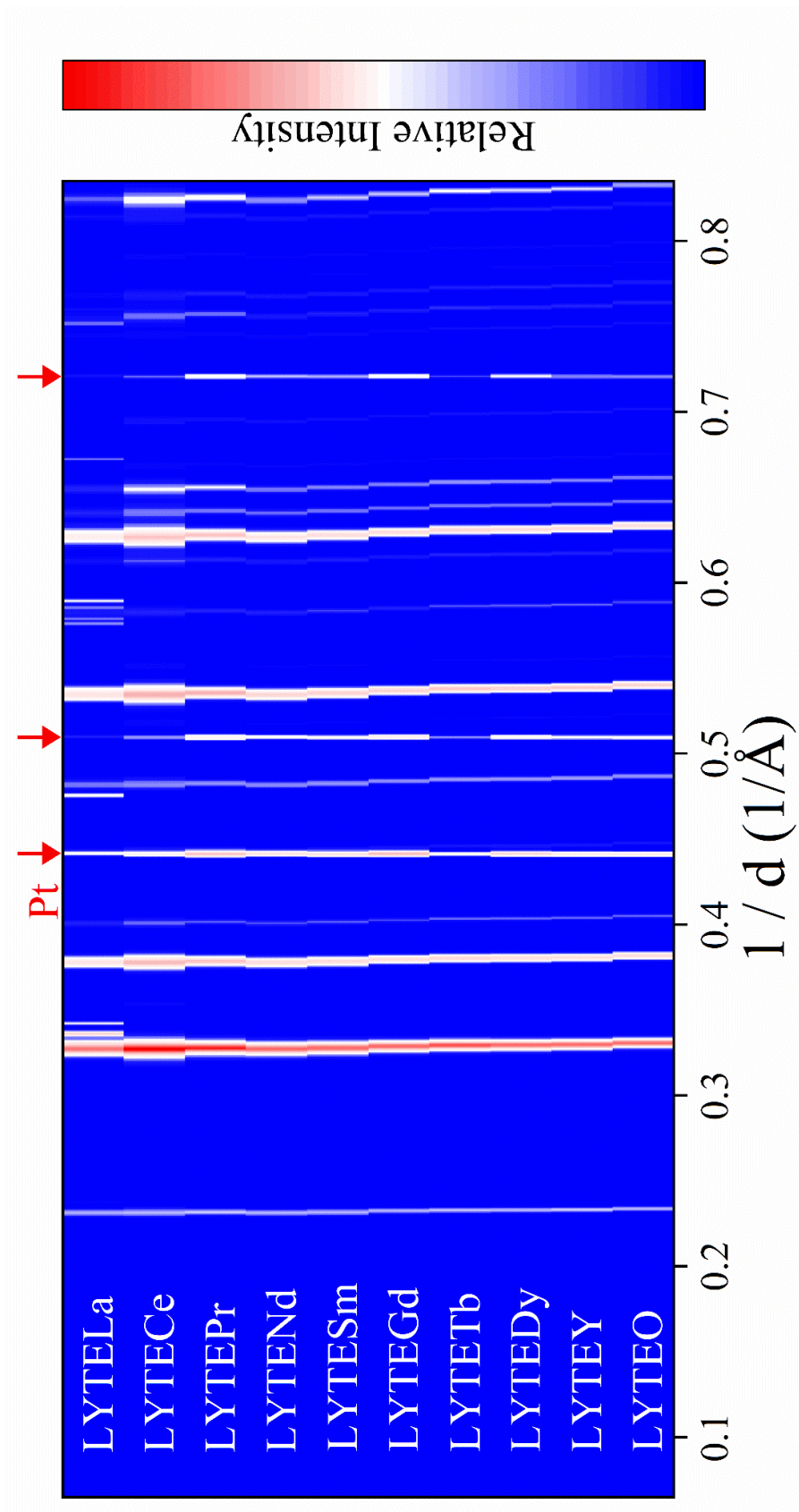


Figure 30. Intensity maps of crystallized LYTE samples



Table 12. Room-temperature structures of LYTE candidates and phase identification reference

Chemistry	Abbreviation	Structure	Space Group	Pearson Symbol	Lattice Parameter
(Lu <sub>0.5</sub> Yb <sub>0.5</sub> Tm <sub>0.5</sub> Er <sub>0.5</sub> )O <sub>3</sub>	LYTEO				10.4656
(Lu <sub>0.4</sub> Yb <sub>0.4</sub> Tm <sub>0.4</sub> Er <sub>0.4</sub> Y <sub>0.4</sub> )O <sub>3</sub>	LYTEY				10.4922
(Lu <sub>0.4</sub> Yb <sub>0.4</sub> Tm <sub>0.4</sub> Er <sub>0.4</sub> Dy <sub>0.4</sub> )O <sub>3</sub>	LYTEDy				10.5041
(Lu <sub>0.4</sub> Yb <sub>0.4</sub> Tm <sub>0.4</sub> Er <sub>0.4</sub> Tb <sub>0.4</sub> )O <sub>3</sub>	LYTETb				10.5090
(Lu <sub>0.4</sub> Yb <sub>0.4</sub> Tm <sub>0.4</sub> Er <sub>0.4</sub> Gd <sub>0.4</sub> )O <sub>3</sub>	LYTEGd	Bixbyite	<i>Ia</i> $\bar{3}$	cI80	10.5335
(Lu <sub>0.4</sub> Yb <sub>0.4</sub> Tm <sub>0.4</sub> Er <sub>0.4</sub> Sm <sub>0.4</sub> )O <sub>3</sub>	LYTESm				10.5574
(Lu <sub>0.4</sub> Yb <sub>0.4</sub> Tm <sub>0.4</sub> Er <sub>0.4</sub> Nd <sub>0.4</sub> )O <sub>3</sub>	LYTEND				10.5811
(Lu <sub>0.4</sub> Yb <sub>0.4</sub> Tm <sub>0.4</sub> Er <sub>0.4</sub> Pr <sub>0.4</sub> )O <sub>3</sub>	LYTEPr				10.5567
(Lu <sub>0.4</sub> Yb <sub>0.4</sub> Tm <sub>0.4</sub> Er <sub>0.4</sub> Ce <sub>0.4</sub> )O <sub>3</sub>	LYTECe				10.5694
		Bixbyite	<i>Ia</i> $\bar{3}$	cI80	10.5755
(Lu, Yb, Tm, Er, La)O <sub>x</sub>	LYTELa	Perovskite	<i>Pnma</i>	oP20	a=6.043 b=8.416 c=5.841

Database Structures	PDF#	Structure	Space Group	Pearson Symbol	Lattice Parameter	Prototype Structure
Er <sub>2</sub> O <sub>3</sub>	04-008-8242 [156]	Bixbyite	<i>Ia</i> $\bar{3}$	cI80	10.550	MnFeO <sub>3</sub>
CeO <sub>2</sub>	04-015-0301 [166]	Fluorite	<i>Fm</i> $\bar{3}m$	cF12	5.266 a=6.052	CaF <sub>2</sub>
LaTmO <sub>3</sub>	00-025-1061 [167]	Perovskite	<i>Pnma</i>	oP20	b=5.844 c=8.429	GdFeO <sub>3</sub>

LYTECe fitted well in the C-type bixbyite structure during the refinement process. However, the room-temperature stable oxide structure of ceria (CeO<sub>2</sub>), which exists in the fluorite structure, could possibly overlap with the bixbyite structure in X-ray diffractions. The cation arrangements are similar in both structures, leading the same X-ray diffraction peaks, under the situation of similar crystal lattices, as shown in Figure 31((a) and (b)). The slices of planes were extrapolated from the (111) plane of the fluorite structure (Figure 31(a)) and the (222) plane of the bixbyite structure (Figure 31(b)), respectively. As mentioned in Section 2.4, the C-type bixbyite structure

consists of 8 fluorite structures with ordered oxygen vacancies. Under the mono-cation circumstance, when the lattice parameter of the bixbyite structure is double that of the fluorite analogue, the diffraction peaks of the latter structure exhibit the same Q-factor (reciprocal number of d-spacing) in the collected pattern. As shown in Figure 31, it is difficult to distinguish these two structures by the XRD technique. The LYTECe powder sample was examined by TEM and SEM, with details explained in Section 5.3. These results confirmed that LYTECe is a single-phase HEO, with no cerium cation segregation or observable fluorite structure.

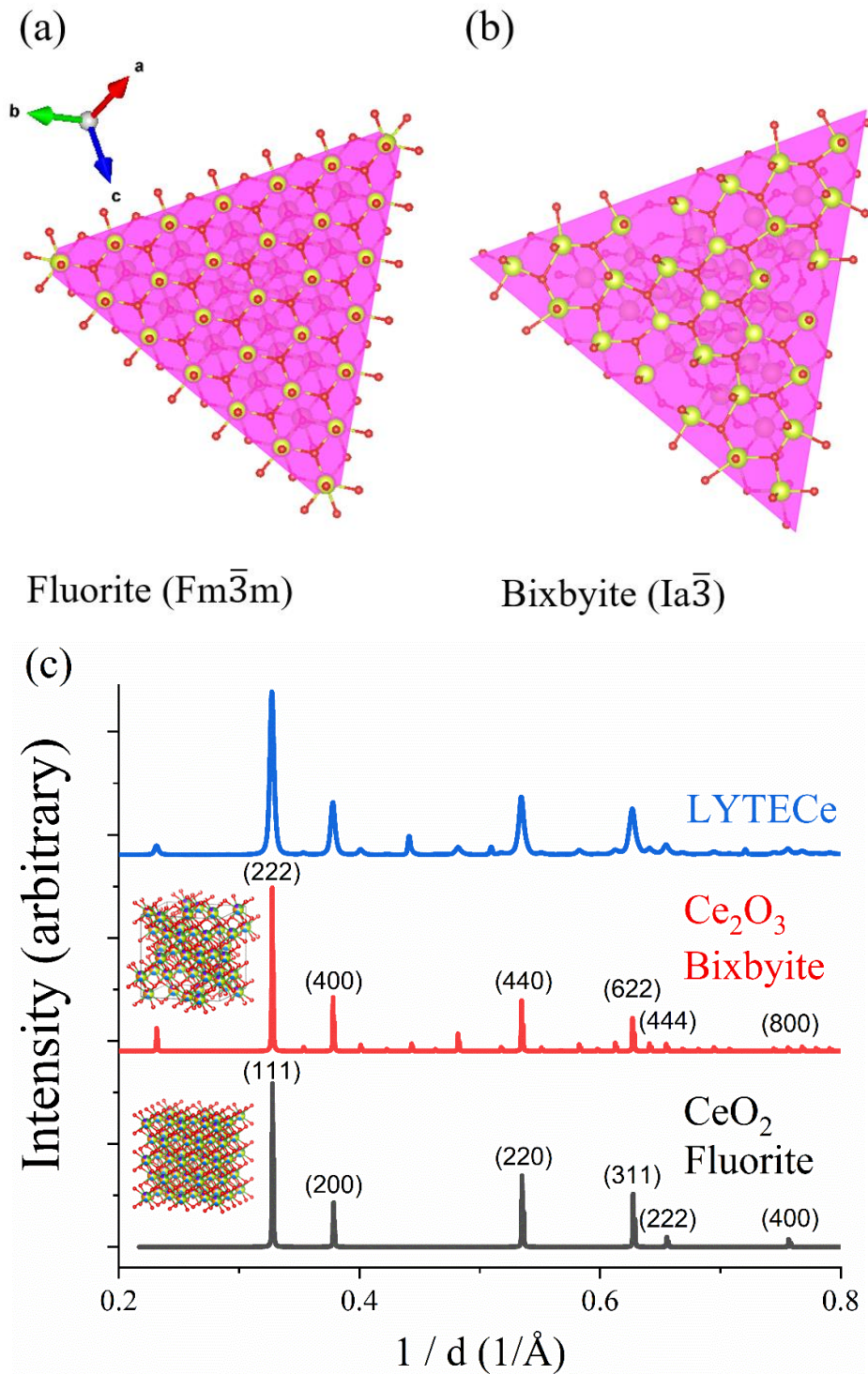
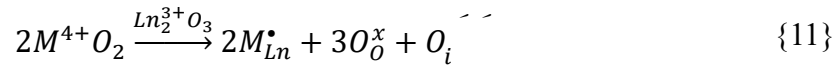


Figure 31. The cations (yellow-green) in fluorite structure (a) have a similar arrangement with the cations in the cubic-bixbyite structure (b) in all observable planes as seen by X-ray diffraction (c).

Intrinsically, cerium, praseodymium, and terbium cations have a partial preference to exist in the tetravalent states.[67] In sesquioxide chemistry, the cations of  $M_2O_3$  should exist in trivalent states for charge balance in a bixbyite structure. However, the color of the powders (pale and dark yellow, seen in Figure 32) indicated that at least some portion of these three cations were in tetravalent states.[60, 76, 82] Based on this situation, additional oxygens were randomly located in the interstitial sites, which can be addressed in the Kröger-Vink notation for defect chemistry as:[168]



where  $M$  denotes tetravalent cations, and  $Ln$  denotes trivalent cations.

The correlation between lattice parameters, extrapolated from XRD patterns, and the size mismatch ( $\delta$ ) is presented in Figure 33. In the situation when all the cations existed in trivalent states (Figure 33(a)), HELO candidates demonstrated linear increments as the cations increased from small sizes (LYTEY) to medium sizes (LYTEND). This trend proved that the crystal lattice expands as a larger cation is added into the structure. However, the linear fitting under the trivalent cation situation was poor ( $R^2=0.86$ ). The multiple-component oxide containing cerium and praseodymium showed a different trend in the linear fitting. Based on Equation {11}, the delta factor was modified with tetravalent Ce and Pr existing in 8-fold coordination ( $MO_2$ ), as presented in Figure 33(b). In this circumstance, the lattice parameter increased in a linear trend with size mismatch, and demonstrated excellent fitting  $R^2=0.99$ . This analysis, accompanied by the evidence observed from the powder color, confirmed that cerium and praseodymium existed in either tetravalent state or a mixture of trivalent and tetravalent states.

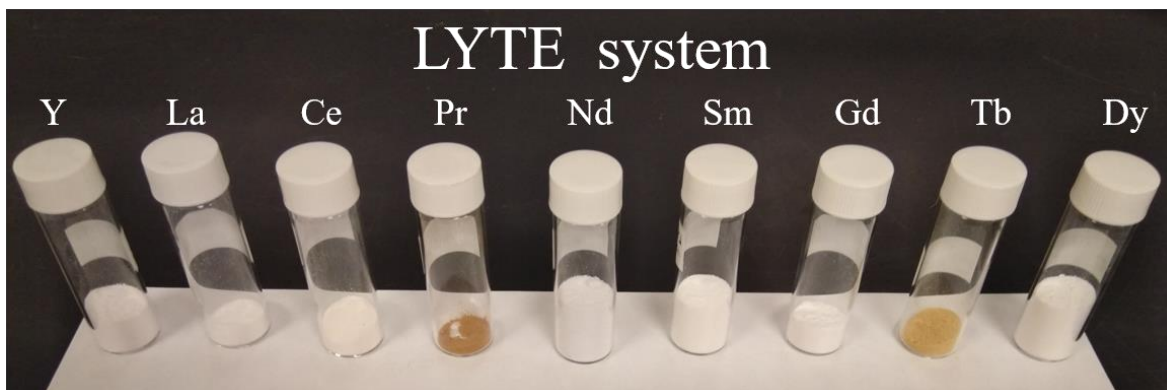
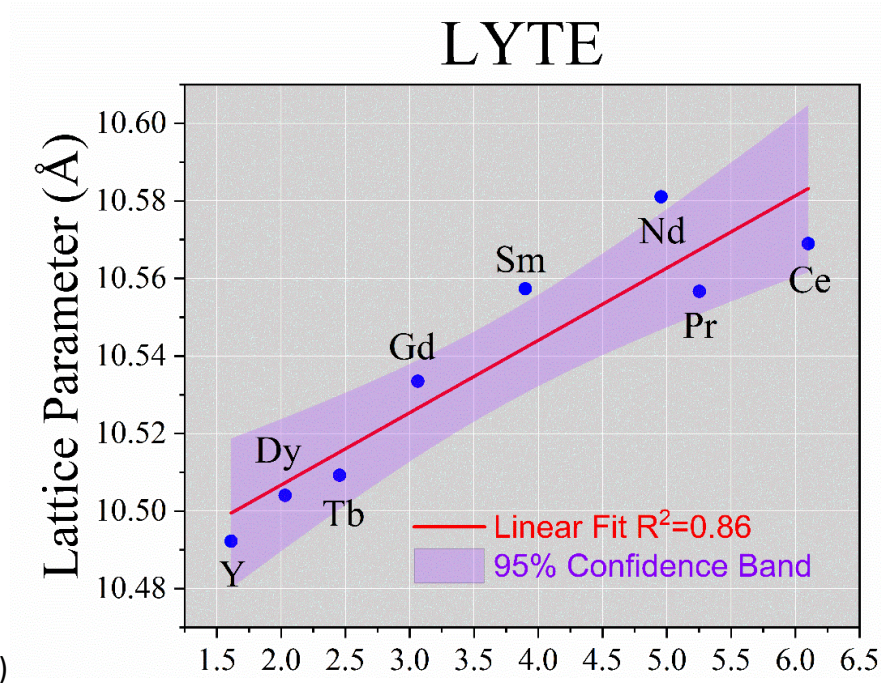


Figure 32. The color of crystallized powder samples in the LYTE system

(a)



(b)

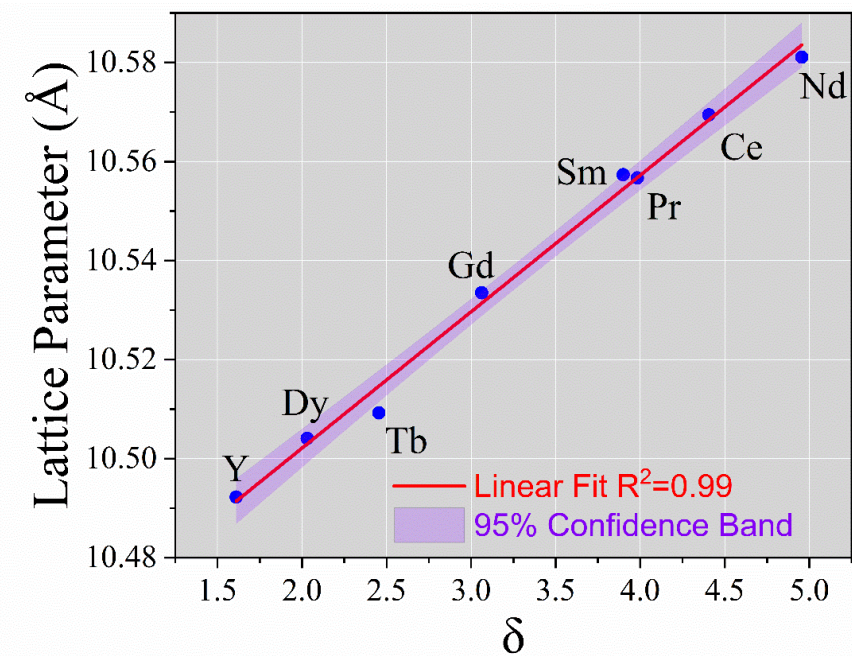
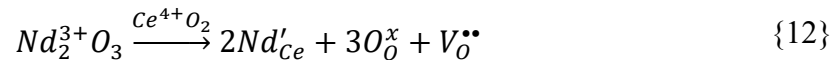


Figure 33. The size mismatch ( $\delta$ ) as a function of the lattice parameter obtained via the X-ray diffraction patterns. The mismatch parameters were calculated under the circumstances that (a) all trivalent states are in 6-fold coordination, and (b) Ce and Pr in tetravalent states are in 8-fold coordination. The lattice parameters increase as a larger fifth cation (larger  $\delta$ ) is incorporated in the bixbyite crystal structure.

## 5.2. Crystal Structure of the System with Large Based Lanthanides (La, Ce, Pr, Nd) (LCPN)

In the LCPN system, all structures became single-phase HELOs. As presented in XRD patterns (Figure 34) and maps (Figure 35), all the oxides, except LCPNTb, were crystallized in the tilted fluorite phase (Pearson symbol: cI88). LCPNTb exhibited the fluorite structure, as in the stable phase of cerium dioxide CeO<sub>2</sub>. The difference between these two structures could be easily identified by the diffraction peaks at Q~0.22 and 0.38. All the synthesized powder samples displayed brown colors. The color could be contributed to by Ce<sup>4+</sup> (yellow), Pr<sup>3+</sup> (yellow), and Pr<sup>4+</sup> (brown), as shown in Figure 36. On the other hand, lanthanum and niobium cations are thermodynamically stable in trivalent configurations. The tilted fluorite phase was similar to the cerium-niobium oxide, CeNdO<sub>3.5</sub>, where the trivalent neodymium homogeneously lies in the tetravalent cerium site. The tilted fluorite structures found in the LCPN system were constructed from trivalent and tetravalent cations located in the same polyhedral sites. This arrangement generates vacancies (*V*) at the oxygen sites for charge compensation, as shown in Equation {12}.[92]



In the LCPN system, Ce and Pr had a preference for the tetravalence states, whereas other lanthanides, except terbium, preferred the trivalent states.

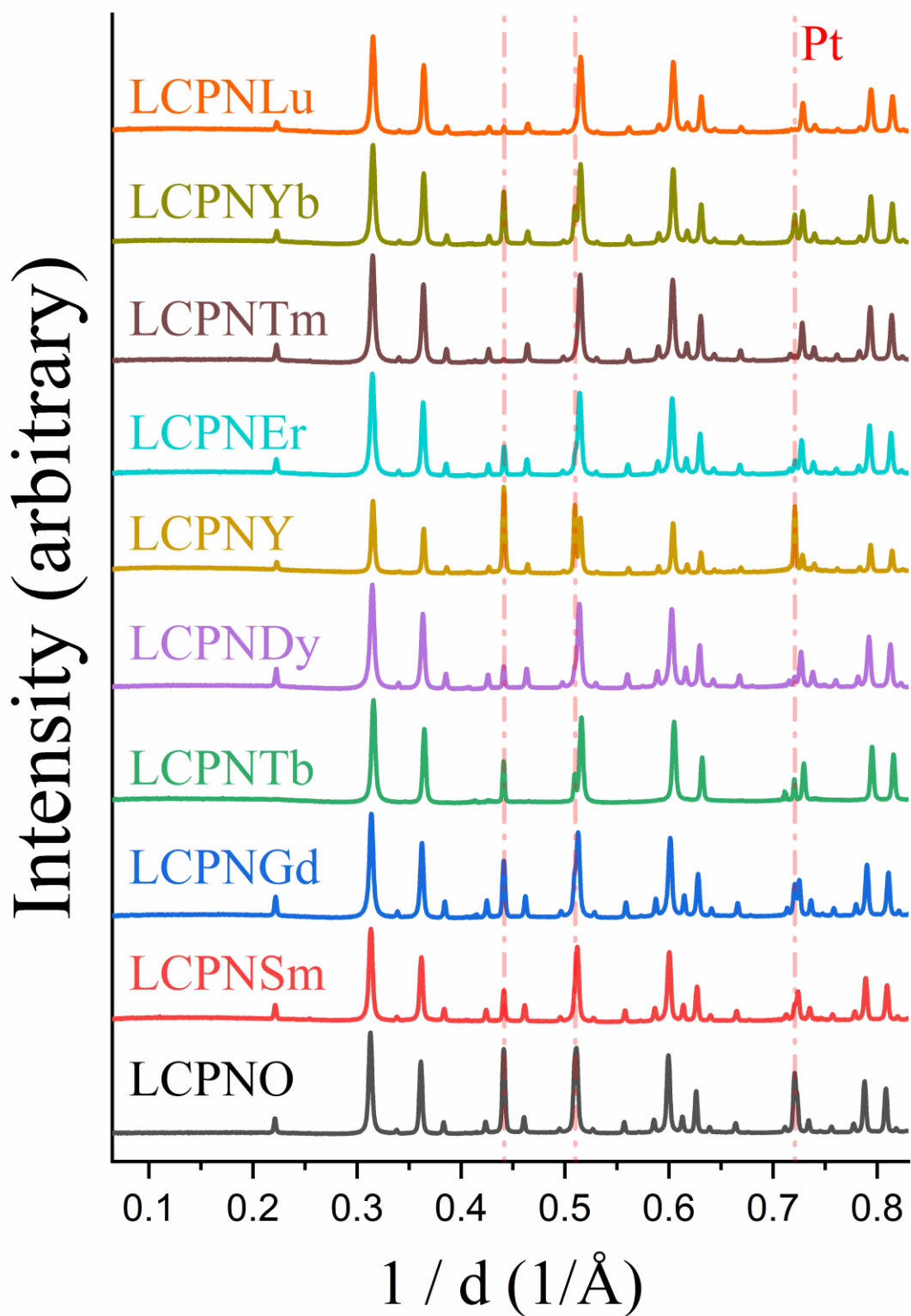


Figure 34. X-ray diffraction patterns of candidates in LCPN system at room temperature. All synthesized samples became single-phase solid solutions after crystallization.



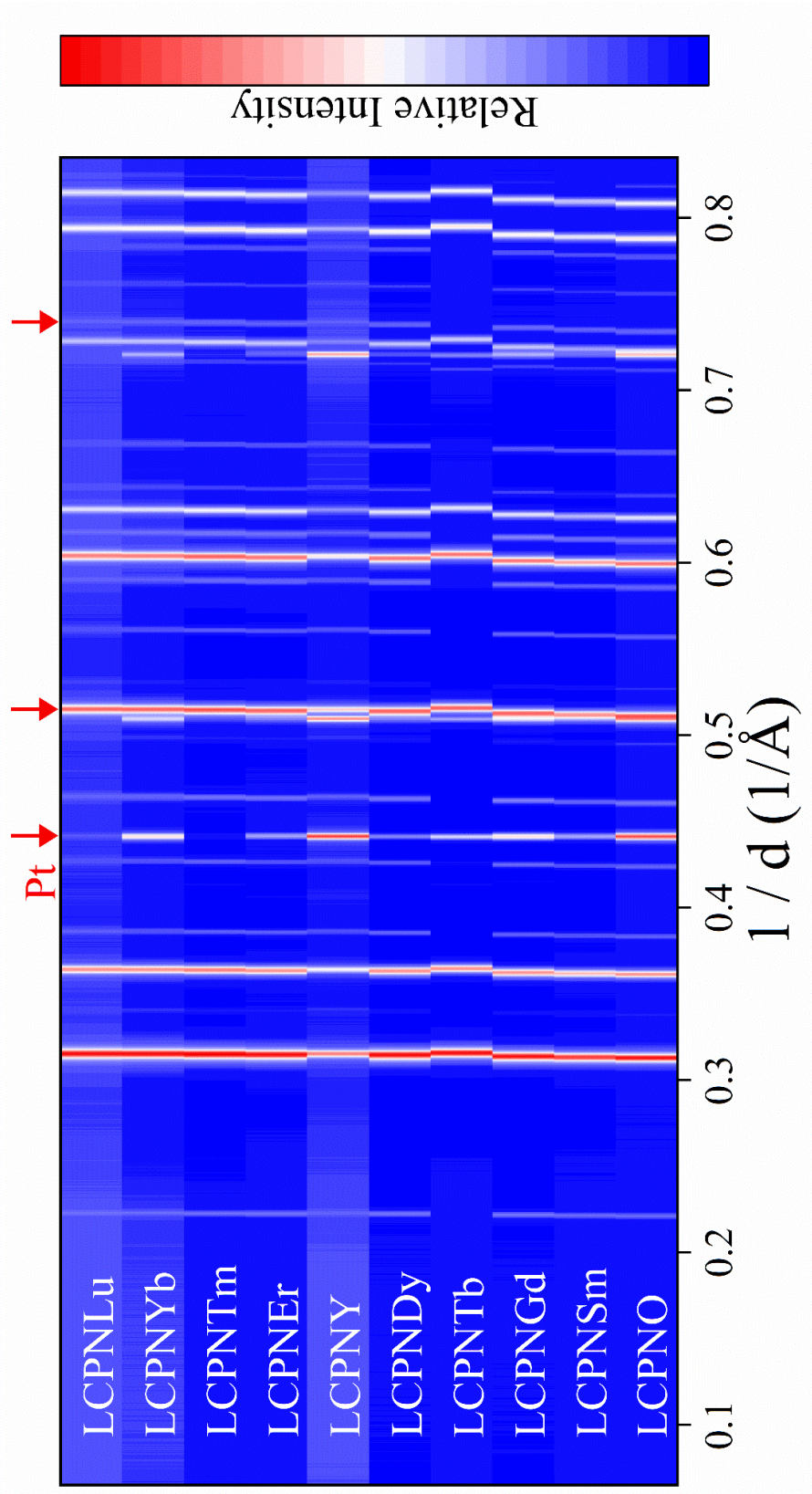


Figure 35. Intensity maps of crystallized LCPN samples

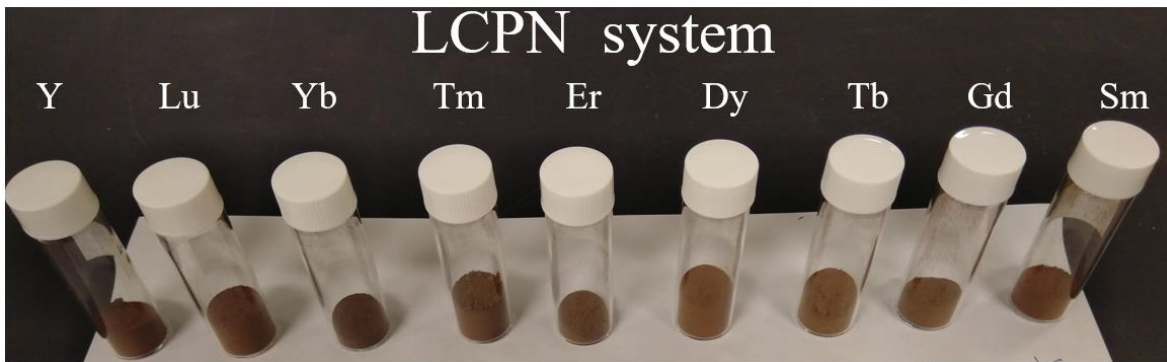


Figure 36. The colors of crystallized powder samples in the LCPN system

The detail information of each HELO was listed in Table 13. The size of LCPNTb was doubled since the tilted fluorite was interpreted to exist as a combination of 8 fluorite structures and oxygen vacancies. The lattice parameters linearly decreased as smaller cations were added into the structure, except for LCPNTb, which was classified in a different type of crystal structure. The lattice parameters are plotted in Figure 37 as a function of the size mismatch,  $\delta$ . In the LCPN system, the tilted fluorite structure remained stable as a single-phase, solid solution, up to the maximum value of designed mismatch parameter 5.81.

Table 13. Room-temperature structures of LCPN candidates and phase identification references

Chemistry	Abbreviation	Structure	Space Group	Pearson Symbol	Lattice Parameter
$(\text{La}_{0.5}\text{Ce}_{0.5}\text{Pr}_{0.5}\text{Nd}_{0.5})\text{O}_{3.5}$	LCPNO	Fluorite			11.0661
$(\text{La}_{0.4}\text{Ce}_{0.4}\text{Pr}_{0.4}\text{Nd}_{0.4}\text{Sm}_{0.4})\text{O}_{3.5}$	LCPNSm	(Tilted)	$Ia\bar{3}$	cI88	11.0410
$(\text{La}_{0.4}\text{Ce}_{0.4}\text{Pr}_{0.4}\text{Nd}_{0.4}\text{Gd}_{0.4})\text{O}_{3.5}$	LCPNGd				11.0277
$(\text{La}_{0.4}\text{Ce}_{0.4}\text{Pr}_{0.4}\text{Nd}_{0.4}\text{Tb}_{0.4})\text{O}_4$	LCPNTb	Fluorite	$Fm\bar{3}m$	cF12	10.9553 <sup>1</sup>
$(\text{La}_{0.4}\text{Ce}_{0.4}\text{Pr}_{0.4}\text{Nd}_{0.4}\text{Dy}_{0.4})\text{O}_{3.5}$	LCPNDy				11.0015
$(\text{La}_{0.4}\text{Ce}_{0.4}\text{Pr}_{0.4}\text{Nd}_{0.4}\text{Y}_{0.4})\text{O}_{3.5}$	LCPNY				10.9891
$(\text{La}_{0.4}\text{Ce}_{0.4}\text{Pr}_{0.4}\text{Nd}_{0.4}\text{Er}_{0.4})\text{O}_{3.5}$	LCPNEr	Fluorite	$Ia\bar{3}$	cI88	10.9784
$(\text{La}_{0.4}\text{Ce}_{0.4}\text{Pr}_{0.4}\text{Nd}_{0.4}\text{Tm}_{0.4})\text{O}_{3.5}$	LCPNTm	(Tilted)			10.9729
$(\text{La}_{0.4}\text{Ce}_{0.4}\text{Pr}_{0.4}\text{Nd}_{0.4}\text{Yb}_{0.4})\text{O}_{3.5}$	LCPNYb				10.9672
$(\text{La}_{0.4}\text{Ce}_{0.4}\text{Pr}_{0.4}\text{Nd}_{0.4}\text{Lu}_{0.4})\text{O}_{3.5}$	LCPNLu				10.9676

Database Structures	PDF#	Structure	Space Group	Pearson Symbol	Lattice Parameter	Prototype Structure
CeNdO <sub>3.5</sub>	04-013-6624 [92]	Fluorite (Tilted)	$Ia\bar{3}$	cI88	11.000	Ce <sub>0.4</sub> Gd <sub>0.6</sub> O <sub>1.7</sub>
CeO <sub>2</sub>	04-015-0301 [166]	Fluorite	$Fm\bar{3}m$	cF12	5.266	CaF <sub>2</sub>

<sup>1</sup>The lattice parameter was doubled for comparison

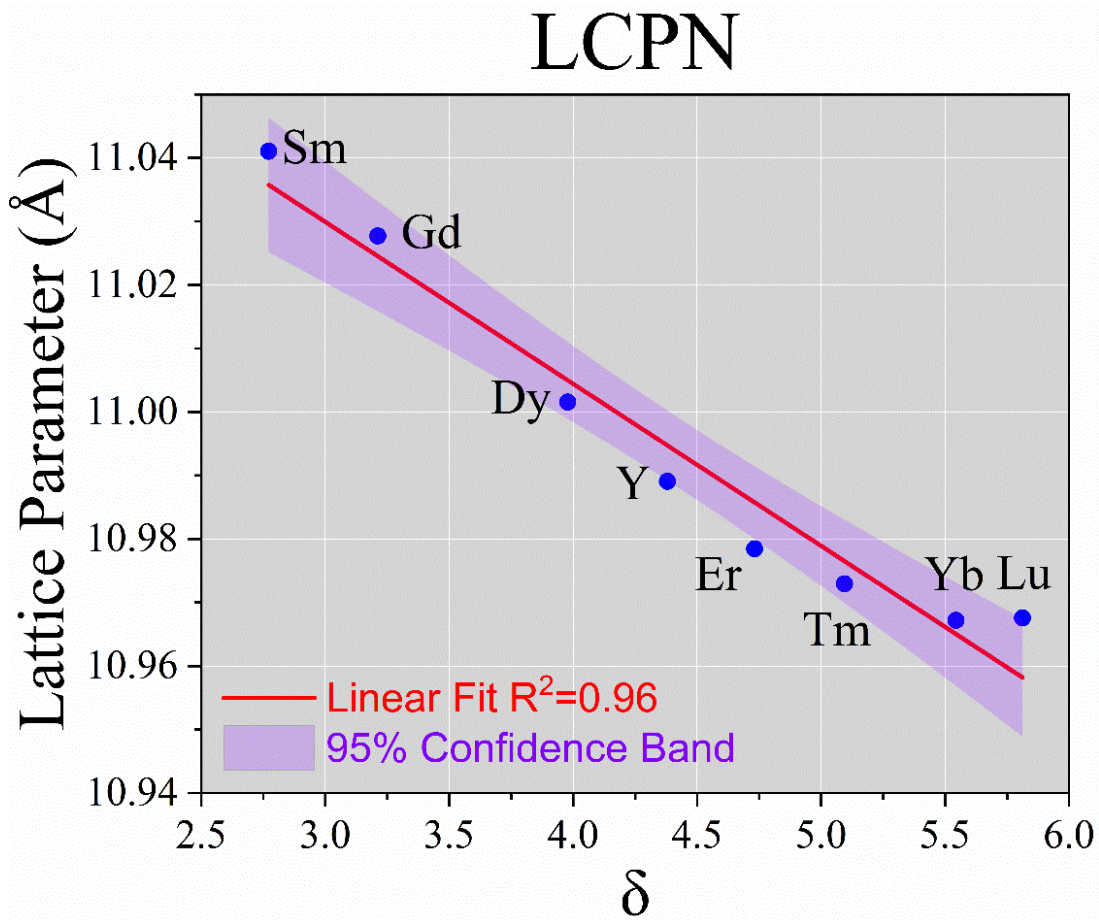


Figure 37. The size mismatch ( $\delta$ ) as a function of the lattice parameter in the LCPN system obtained via X-ray diffraction patterns. The lattice parameters of HELOs decreased as the smaller fifth cations (larger  $\delta$ ) were added to the structure.

### 5.3. Homogeneity of High-Entropy Lanthanide Oxide Systems

The single-phase HELOs were prepared by Kuo-Pin Tseng through a 10-stage cascade Multi Orifice Uniform Deposition Impactor, and further examined by TEM, carried out by Dr. Qun Yang at the ShanghaiTech University, Shanghai, China. For the LYTECe sample, TEM diffraction patterns were taken from multiple crystals, with comparisons to corresponding simulated patterns. The simulated patterns were generated through the crystallographic information file (CIF) obtained from the Rietveld refinement of synchrotron sourced XRD measurements. Figure 38 presents four

LYTECe diffraction patterns, where the results perfectly matched with the simulated pattern, having agreement to the lattice parameters at room temperature. Some of the crystals exhibited tiny superlattice peaks. No fluorite diffraction peaks were observed in the LYTECe sample.

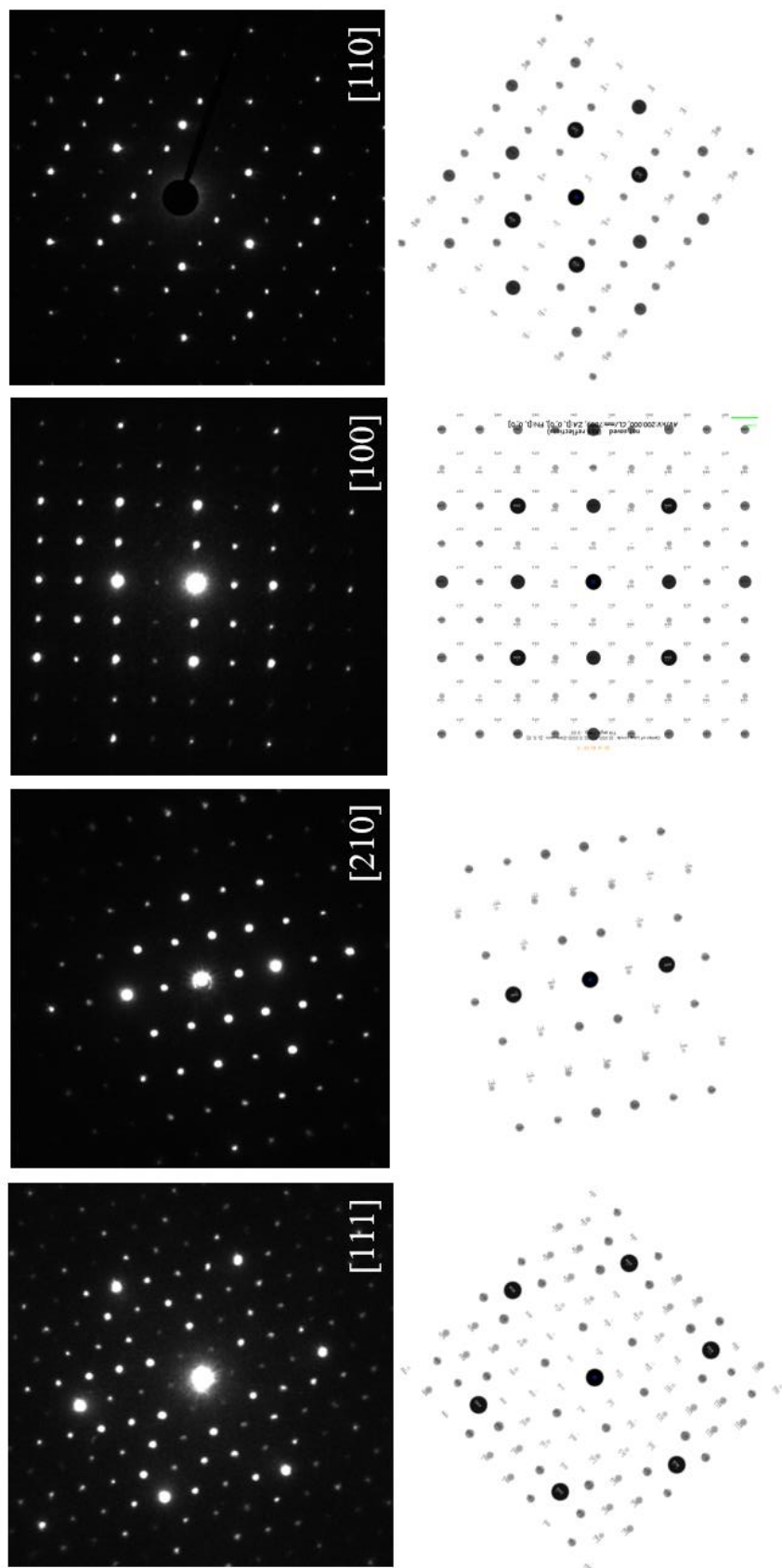


Figure 38. TEM diffraction of the LYTECe sample. The selected area electron diffraction (SAED) patterns were taken down different zone axes in different crystals. The measured SAD patterns matched with corresponding simulated patterns based on crystallographic information files (CIF) generated by XRD Rietveld refinement.

In the LCPN system, the STEM-EDS mapping (Figure 39) demonstrated the homogeneity of cations in the HELO sample with the largest size mismatch-LCPN<sub>Lu</sub>. No observable segregation or aggregation of any particular cation was found. Furthermore, by superimposing the ion positions, as constructed by the CIF file, to the EDS maps, both cations and oxygen locations fitted adequately to the experimental results.

The EDS results, listed in Table 14, confirmed that the single-phase HELOs were close to equimolar mixing among the five constituent cations. Except for the candidates containing yttrium, all five cations exhibited atomic composition in a range of  $20 \pm 1\%$ . The deficiency of yttrium cation was found in both LYTE and LCPN system. This result could be attributed to the quality of the nitrate precursor. Despite the deficiency of yttrium, both LYTEY and LCPNY still existed as single-phase, solid solutions in the synthesized powder samples. In an ideal equimolar mixing situation, the bixbyite structure in LYTEY and tilted fluorite structure in LCPNY would have lower values of Gibbs free energy.

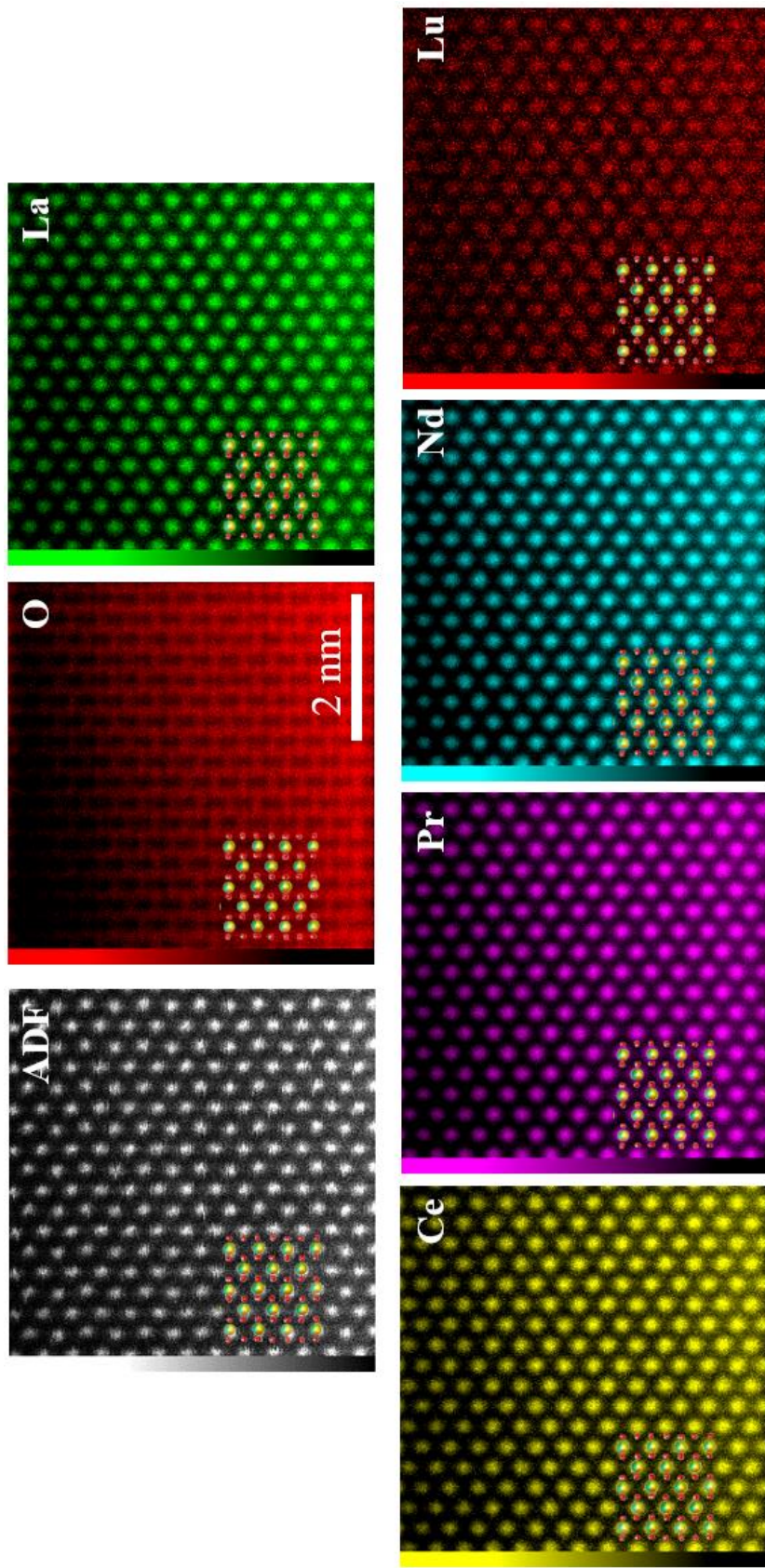


Figure 39. HAADF, ADF images, and atomic resolution elemental mappings were taken from the  $\langle 110 \rangle$  direction of LCPNLu. It is seen that five constituent cations were homogeneously distributed in the elemental maps. The anion/cation positions, obtained via the CIF file generated by XRD results, perfectly matched with the TEM microscopy maps.



Table 14. The atomic percentage of each cation in the LYTE and LCPN systems

LYTE system					
Ln <sup>I</sup>	Lu	Yb	Tm	Er	Ln <sup>I</sup>
Y	22%	22%	21%	20%	15%
Dy	20%	20%	20%	19%	21%
Tb	20%	20%	21%	19%	20%
Gd	20%	20%	21%	19%	20%
Sm	20%	19%	21%	20%	19%
Nd	21%	20%	20%	20%	19%
Pr	20%	20%	21%	20%	19%
Ce	21%	21%	20%	19%	19%
LCPN system					
Ln <sup>II</sup>	La	Ce	Pr	Nd	Ln <sup>II</sup>
Sm	20%	20%	20%	20%	20%
Gd	20%	21%	19%	21%	19%
Tb	20%	21%	19%	21%	19%
Dy	20%	21%	19%	21%	19%
Y	21%	21%	19%	22%	17%
Er	20%	21%	18%	21%	20%
Tm	20%	21%	19%	20%	20%
Yb	21%	20%	19%	20%	20%
Lu	20%	20%	19%	20%	21%

#### 5.4. Conclusions

The candidates in both LYTE and LCPN systems, except for LYTELa, were crystallized as single-phase HELOs. The HELO samples in the LYTE systems exhibited the C-type cubic bixbyite structure, which was the stable structure of base cation sesquioxides (Lu, Yb, Tm, Er) at ambient conditions. For the LCPN system, both tilted fluorite and CeO<sub>2</sub>-type fluorite structures were observed. The tilted fluorite structure was naturally seen in the sample with a mixture of trivalent and tetravalent states. This result agreed with the preferred tetravalent nature of the two base

cations: cerium and praseodymium. The high-temperature behavior of these candidates will be introduced in the next chapter. The detailed analysis of the effect from key parameters, size mismatch, and valence configurations, is proposed in CHAPTER 7:.

# CHAPTER 6: STRUCTURAL STABILITY AND TRANSFORMATIONS IN MULTI-COMPONENT OXIDES BELOW 2000°C

High-temperature behaviors of the synthesized powder samples were examined by in-situ heating XRD. From room temperature to about 1800°C, the oxides experienced homogeneous heat treatments in the quadrupole lamp furnace. The temperatures of a tested sample mounted in a sapphire capillary were determined by the lattice parameters of the platinum standard.[145] In the conical nozzle levitator, the top surface of a vertically rotated spherical sample was exposed to the CO<sub>2</sub> laser, which had the ability to control the heating environment from 800°C to 2000°C. The sample temperatures were acquired through the pyrometer.

## 6.1. Phase Evolution and Lattice Parameters of the LYTE System

In the LYTE system, most of the candidates had a stable structure from room temperature to ~1800°C, similar to the GTDHEO sample (Figure 19).[52, 169] Figure 40 to Figure 49 present the high-temperature XRD patterns as well as the Rietveld refinement results. Some tiny diffraction peaks were observed in the temperature region 1300-1700°C. These impurities exhibited diffraction intensities similar to the background and could not be identified. Furthermore, these unknown diffraction peaks disappeared as the temperature increased. The cerium cation in the LYTECe sample separated from the HELO structure and formed a CeO<sub>2</sub> fluorite structure under heat treatment. The evolution of this phase segregation will be discussed in the next paragraph. The coexistence of cubic-bixbyite and perovskite structures in LYTELa remained in the XRD results from room temperature to 1800°C, showing that the LYTELa sample did not become a

single-phase solid solution under higher thermal energy. The structural evolution above 1800°C in the LYTE system was examined in the conical nozzle levitator apparatus.

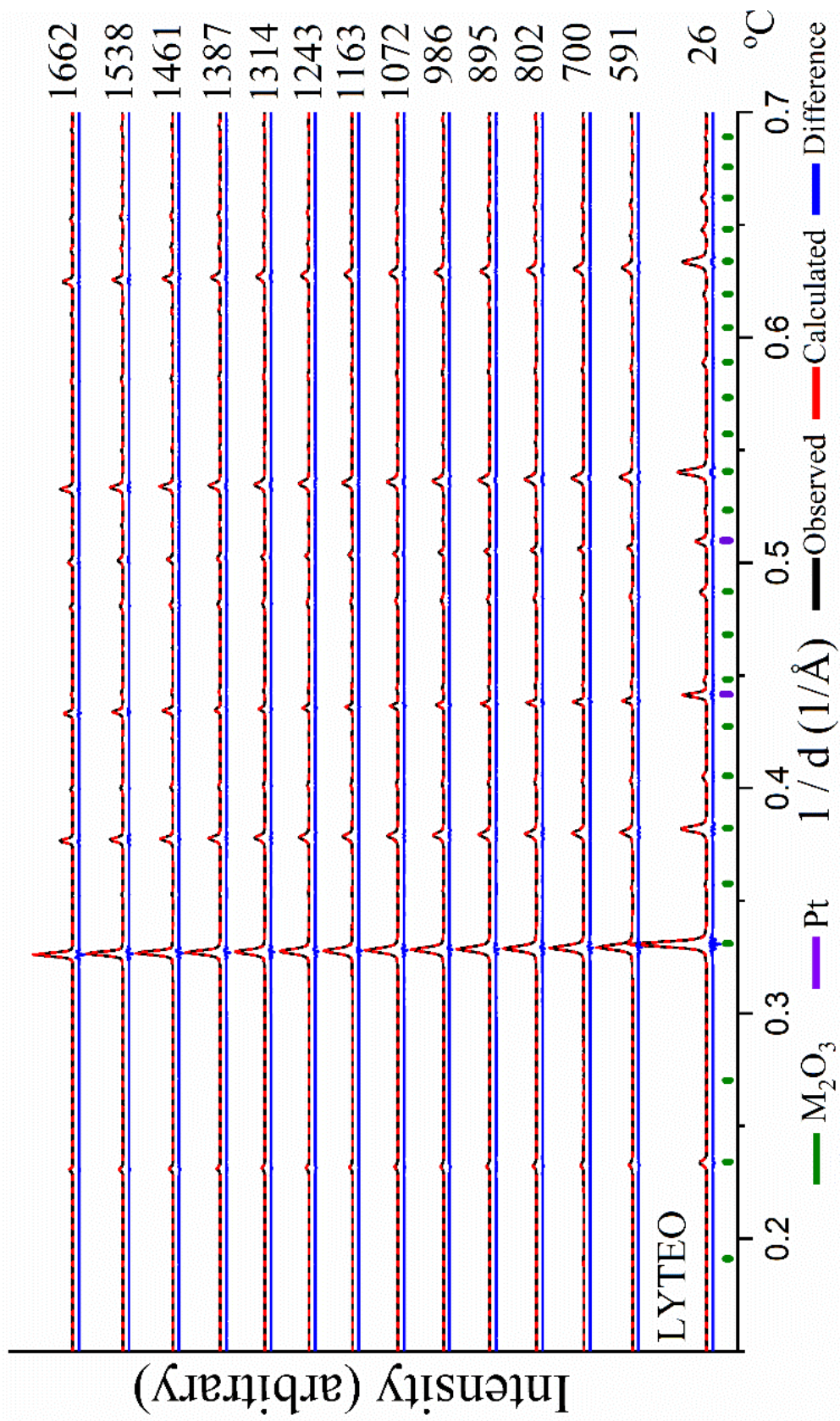


Figure 40. Rietveld refinement of the LYTEO powder

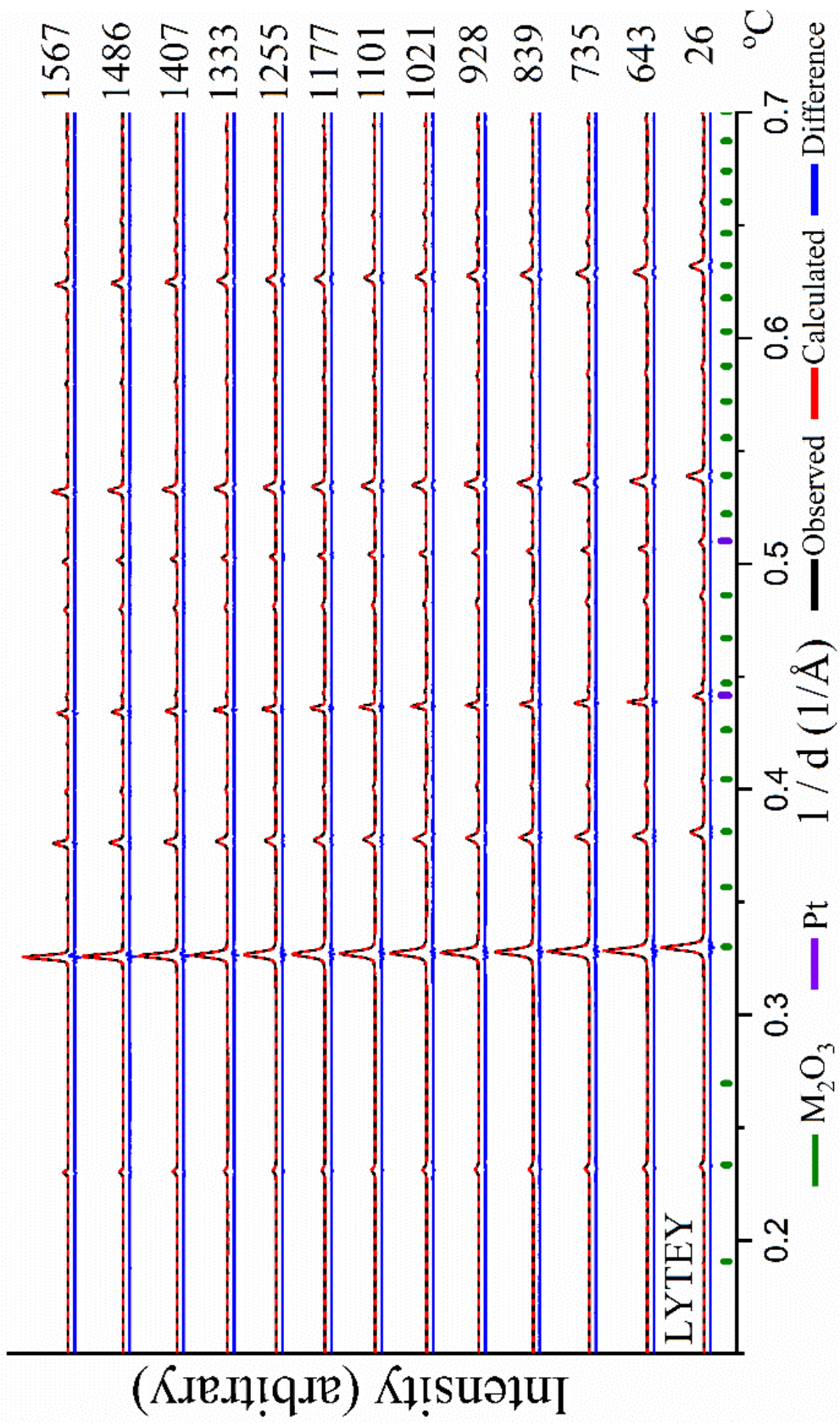


Figure 41. Rietveld refinement of the LYTEY powder

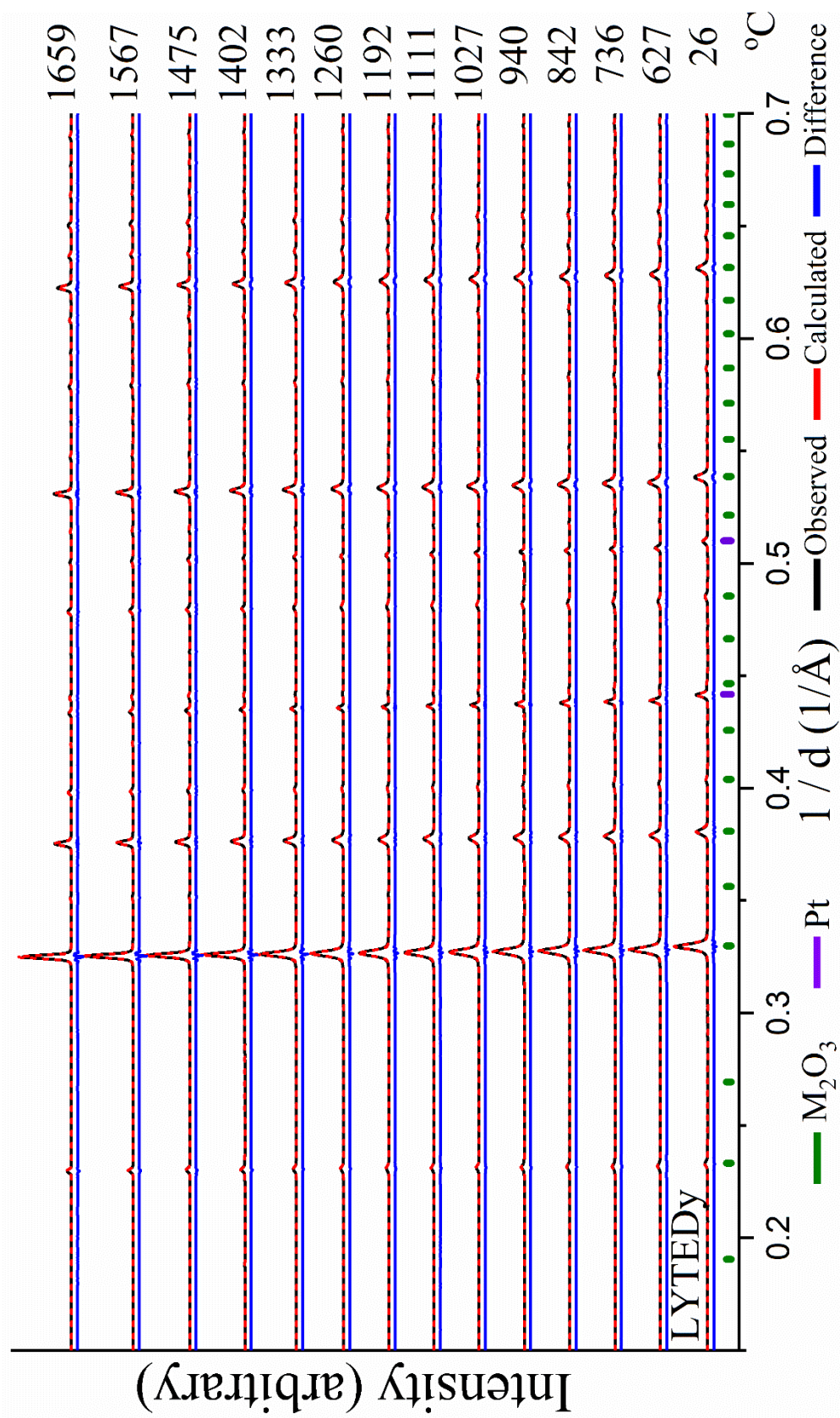


Figure 42. Rietveld refinement of the LYTEDy powder

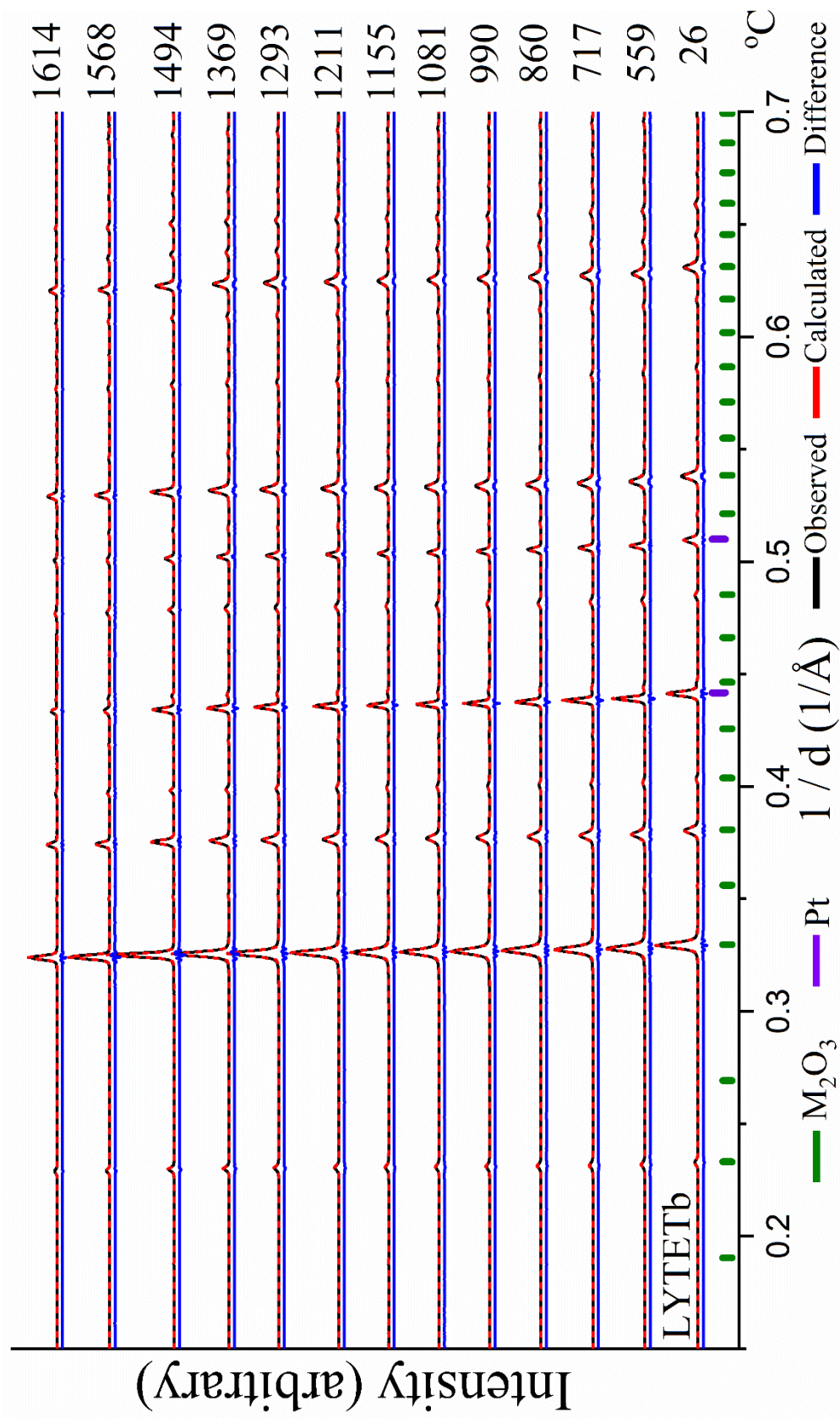


Figure 43. Rietveld refinement of the LYTETb powder



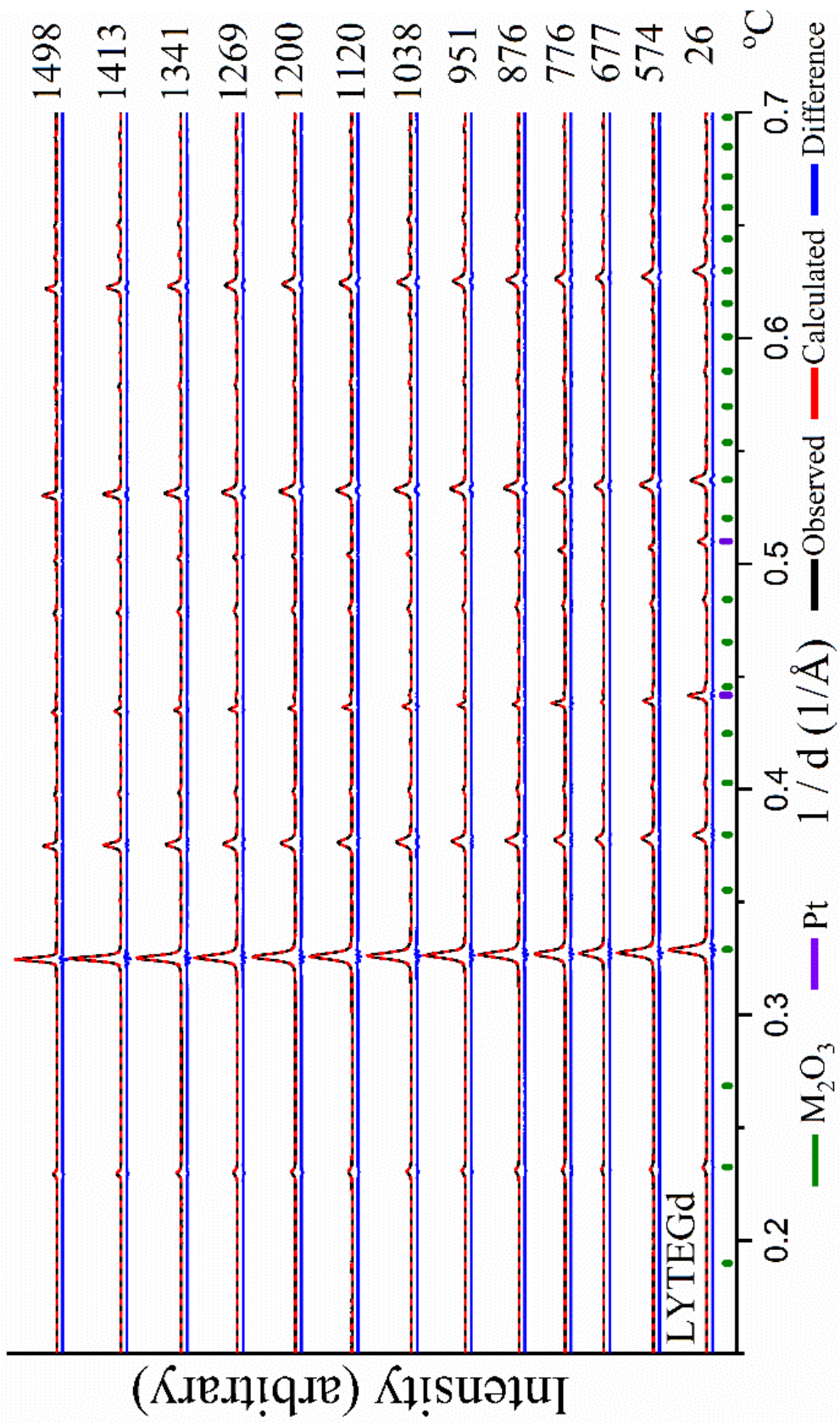


Figure 44. Rietveld refinement of the LYTEGd powder

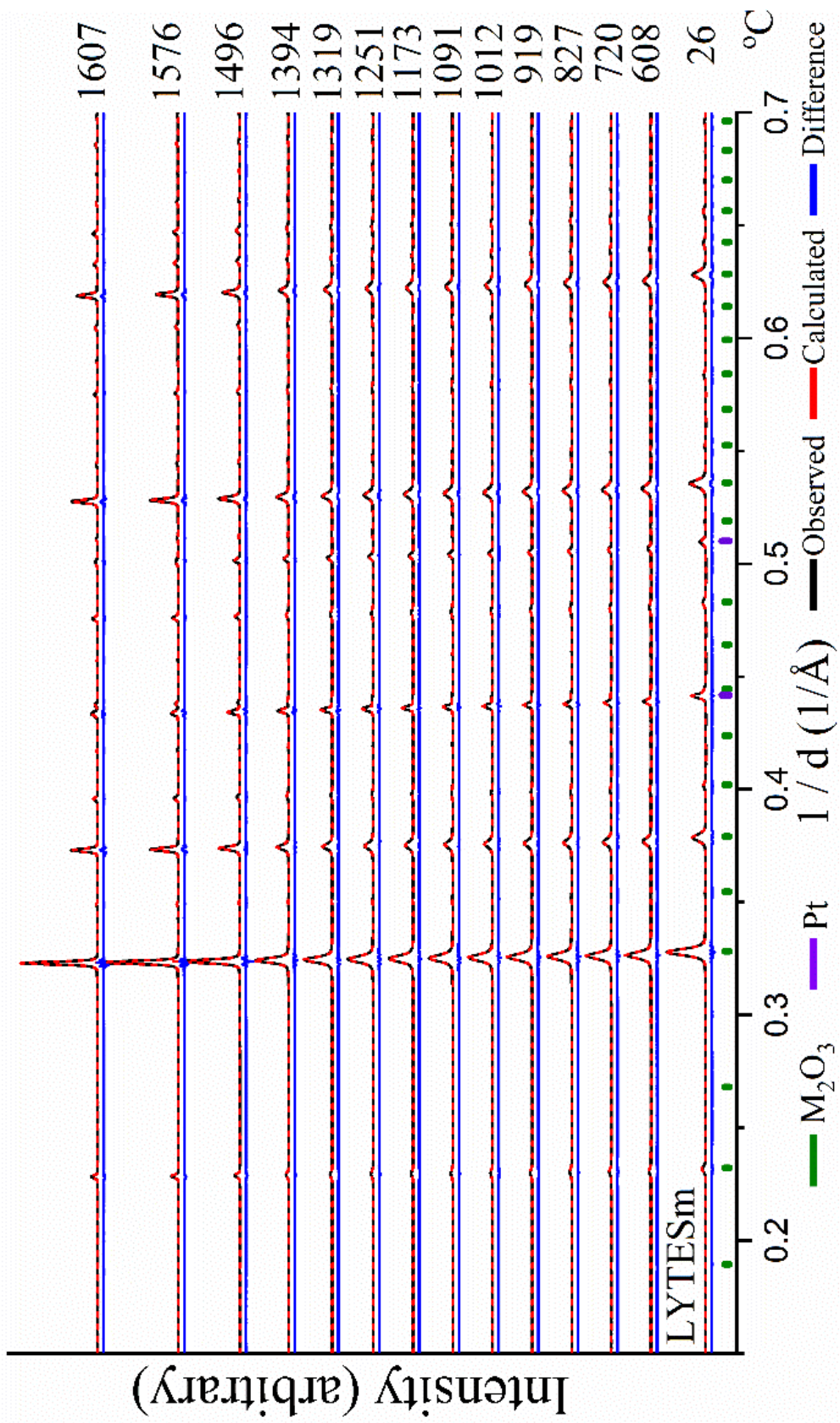


Figure 45. Rietveld refinement of the LYTESm powder

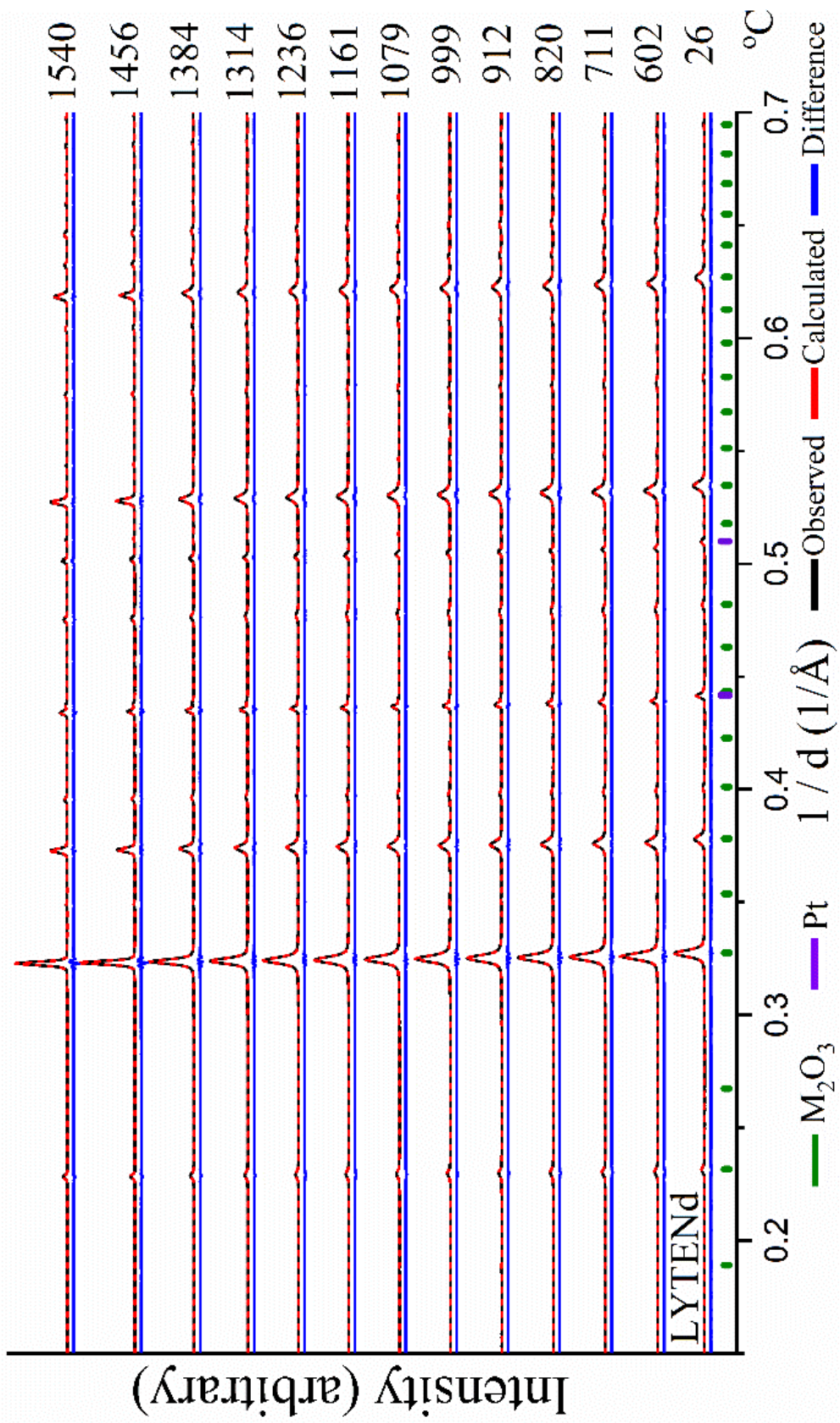


Figure 46. Rietveld refinement of the LYTEND powder

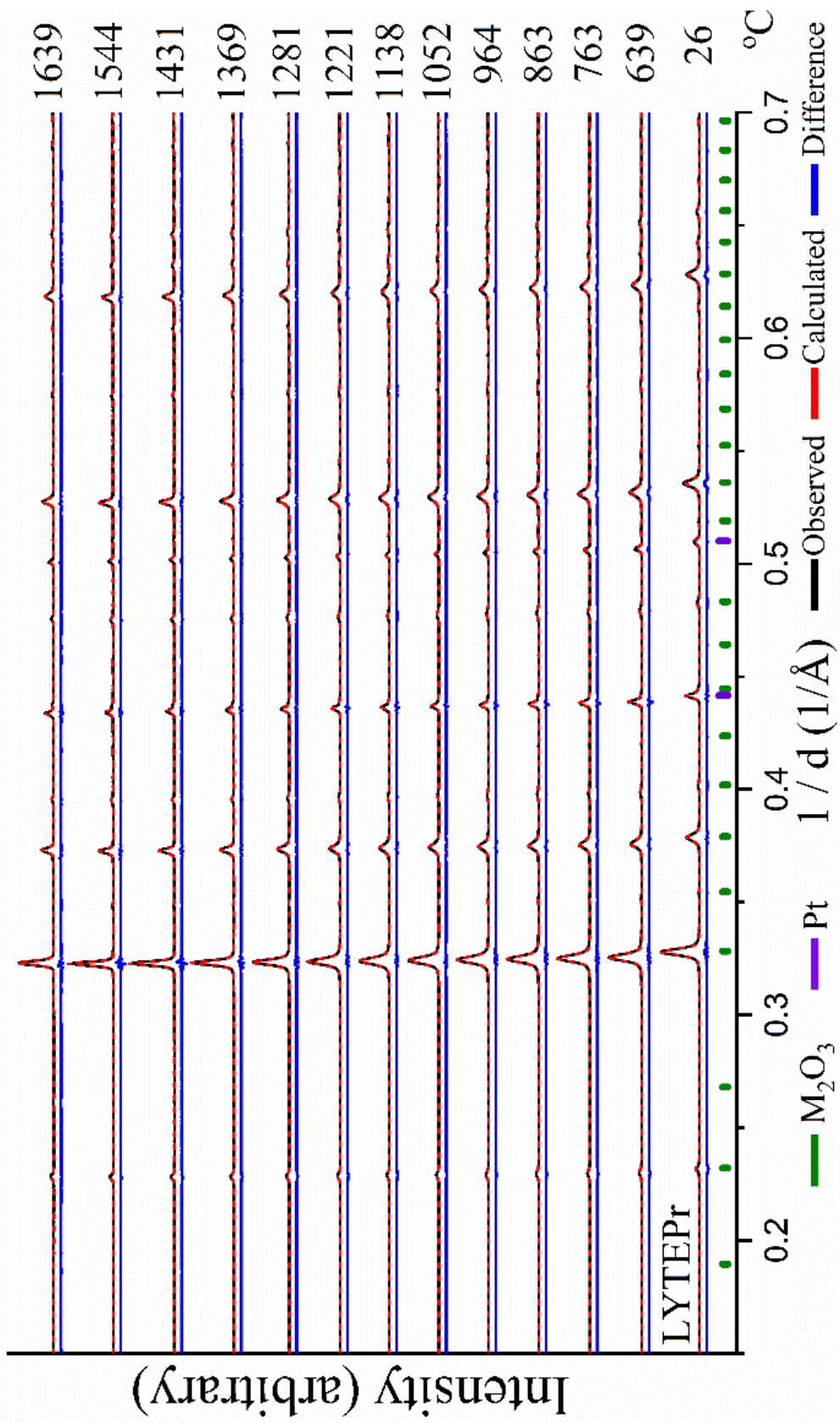


Figure 47. Rietveld refinement of the LYTEPr powder

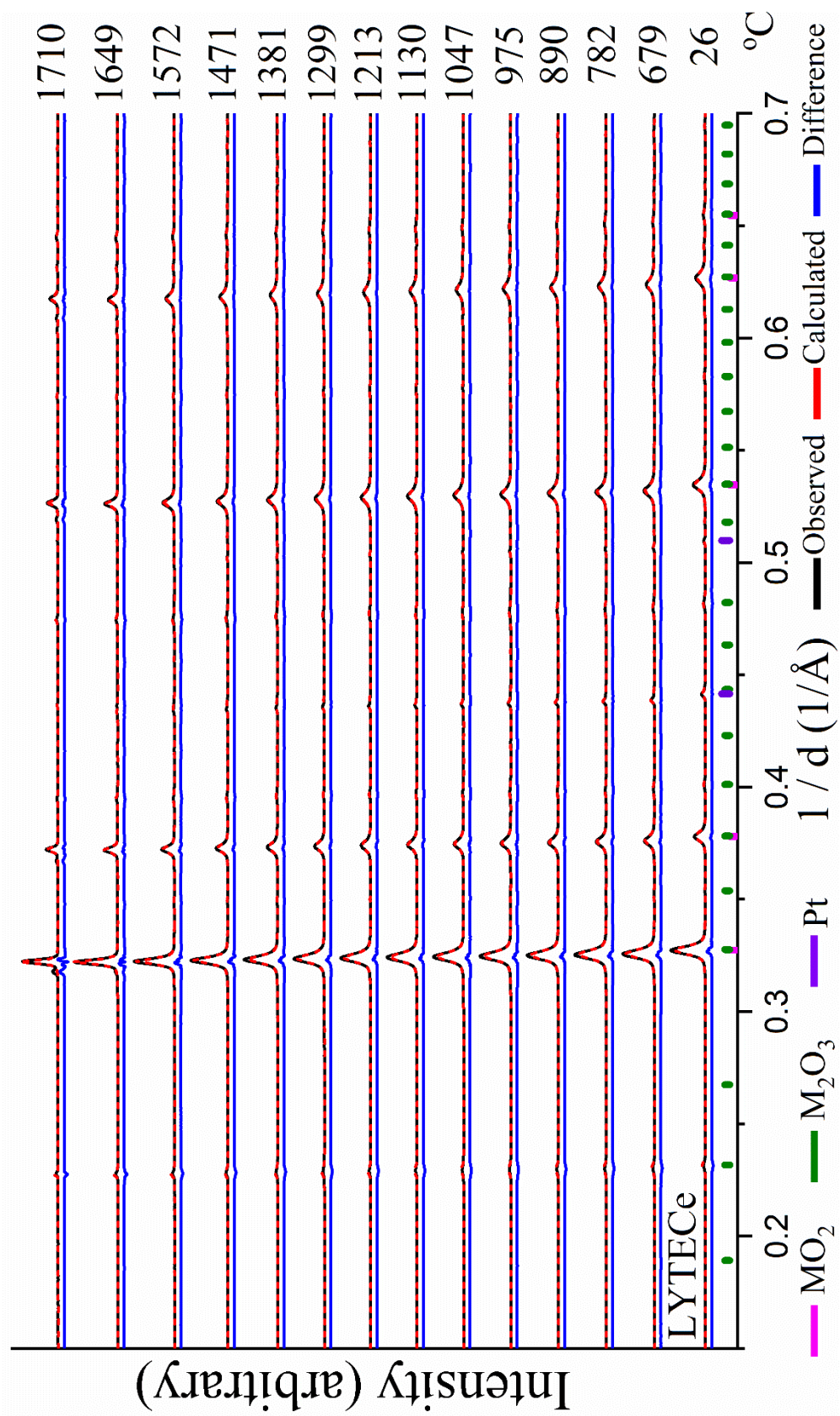


Figure 48. Rietveld refinement of the LYTECe powder

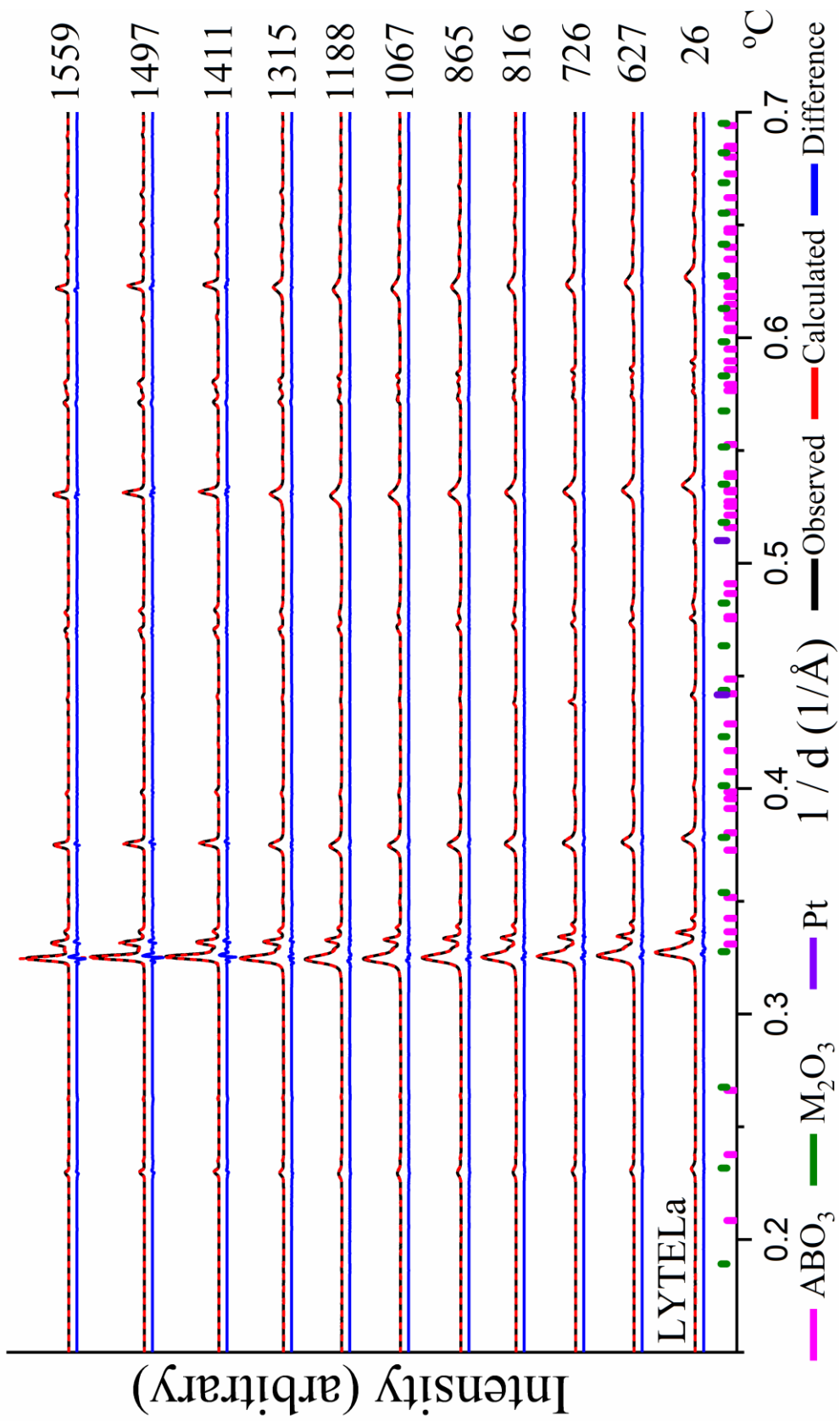


Figure 49. Rietveld refinement of the LYTELa powder

The XRD patterns obtained from the conical nozzle levitator apparatus are presented in Figure 50 and Figure 51. During the experiments, the spherical samples would change their morphology and became unstable above the levitator, especially after structural transitions or melting processes. This issue limited the highest temperatures performed on our candidate materials. Above 1800°C, most of the HELOs in the LYTE system remained stable as a single-phase bixbyite structure until melting. However, some secondary phases were found in other samples under extreme temperature conditions (~2000°C). A small portion of the hexagonal phase existed before melting in LYTESm and LYTENd samples. This structure was similar to the A-type  $\text{La}_2\text{O}_3$  structure.[170] Considering the mono-cation sesquioxides in LYTESm, none of them were naturally present in this hexagonal structure. It is possible that the observed structure was H-type tilted hexagonal, which had a similar arrangement to the A-type structure.[171] In LYTEGd, the origin bixbyite structure partially transformed into the X-type, tilted cubic structure.[172] All the formations of secondary phases were close to the melting temperature. Based on the previous observations in the HEO,  $(\text{Co}_{0.2}\text{Cu}_{0.2}\text{Mg}_{0.2}\text{Ni}_{0.2}\text{Zn}_{0.2})\text{O}$ , described in Section 8.1, the oxide might have partially melted and then evaporated in the air.

There was an exciting transition behavior found in LYTECe, as presented in Figure 52. At temperatures reached higher than 1300°C, the  $\text{CeO}_2$  fluorite structure became distinguishable from the bixbyite structure in the diffraction patterns due to the difference in thermal expansions of these two structures. The segregation of cerium could occur below 1300°C. However, the transition temperature was hard to establish by XRD measurement due to the overlap of diffraction peaks between the fluorite and bixbyite structures.[93, 97, 173] This binary structure persisted until the temperature reached 2200°C.

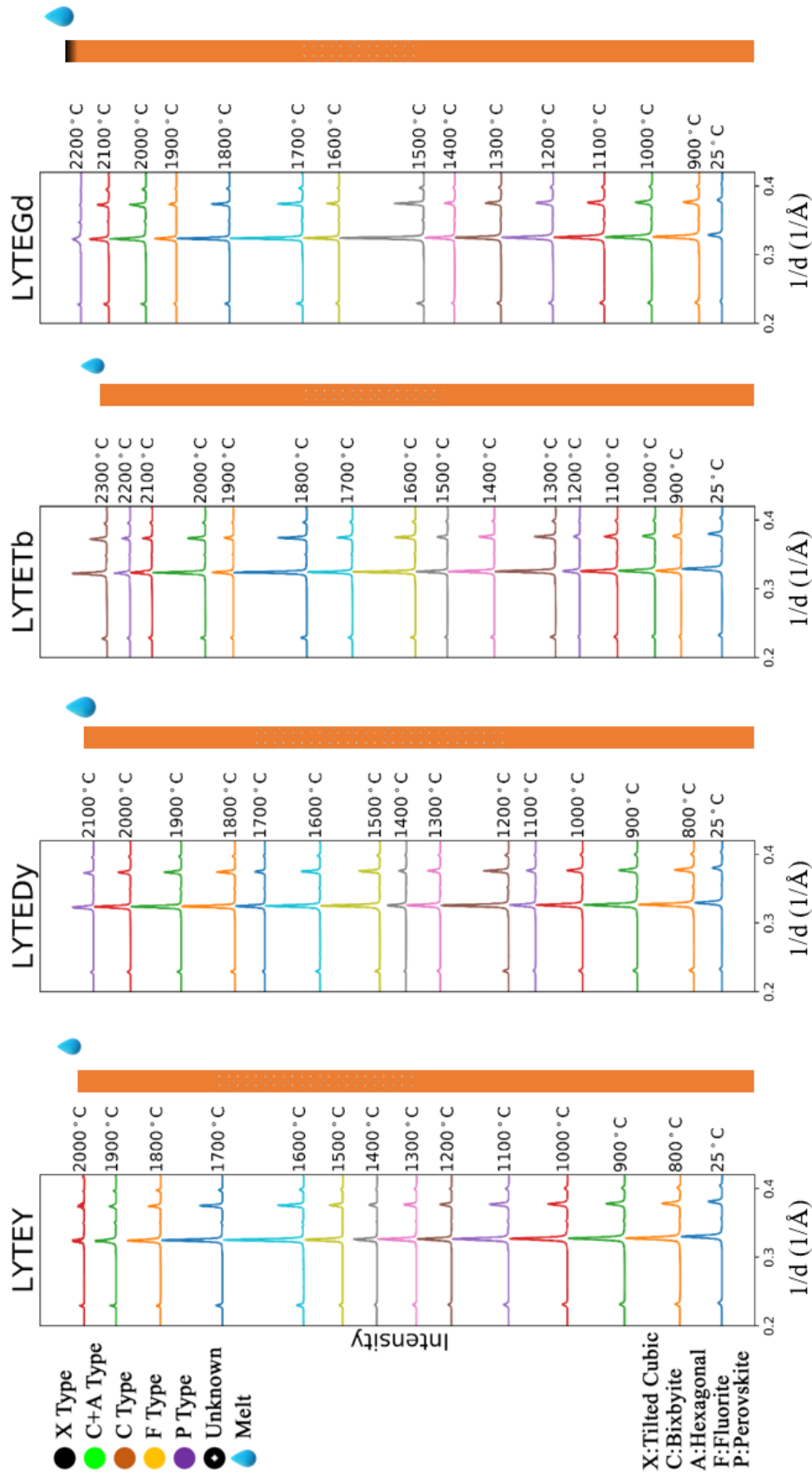


Figure 50. XRD patterns of LYTE candidates (LYTEY-LYTEGd) obtained with the conical nozzle levitator. The droplet symbol indicates melting during the in-situ experiment.



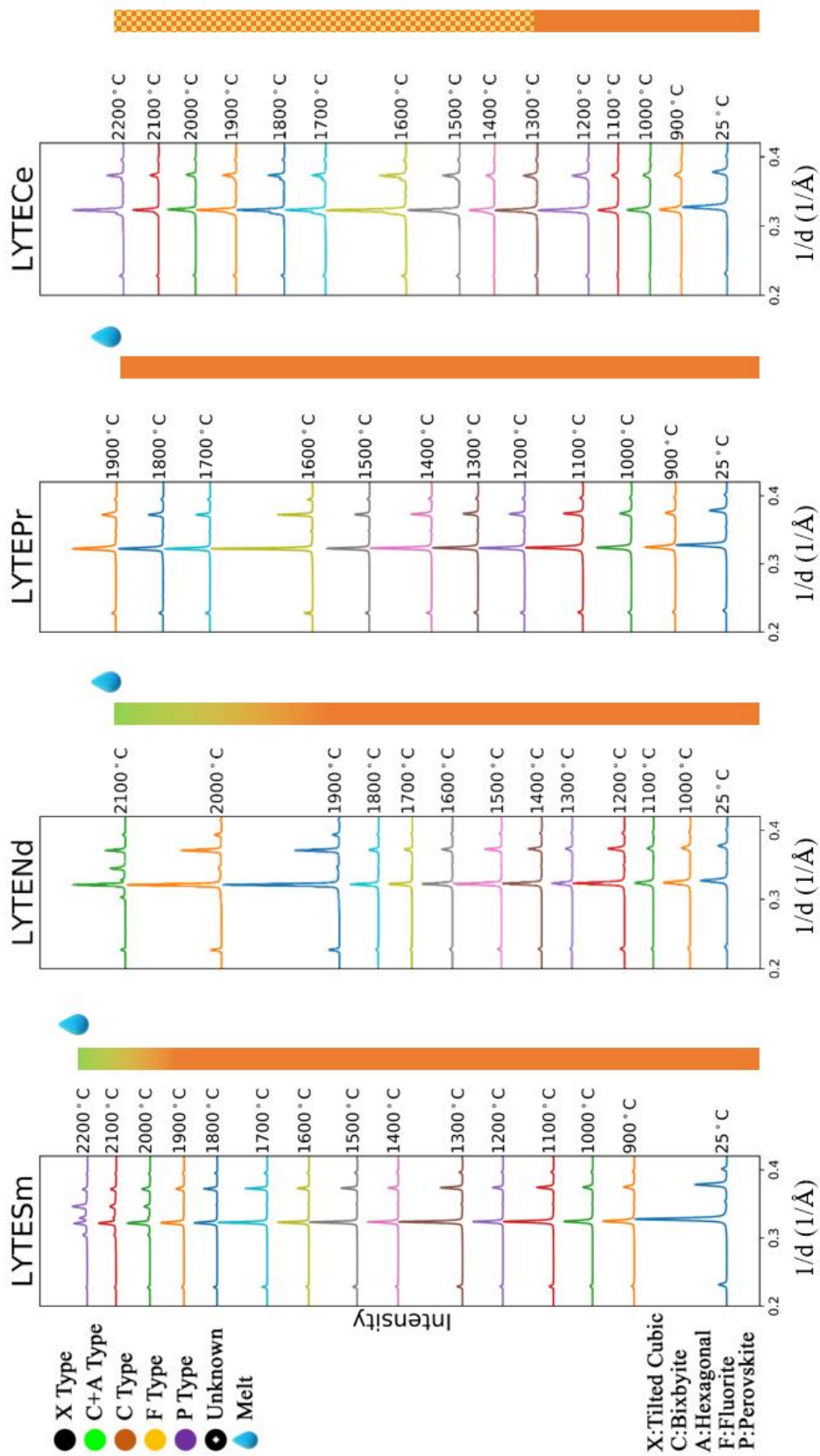


Figure 51. XRD patterns of LYTE candidates (LYTESm-LYTECe) obtained with the conical nozzle levitator. The droplet symbol indicates melting during the in-situ experiment.

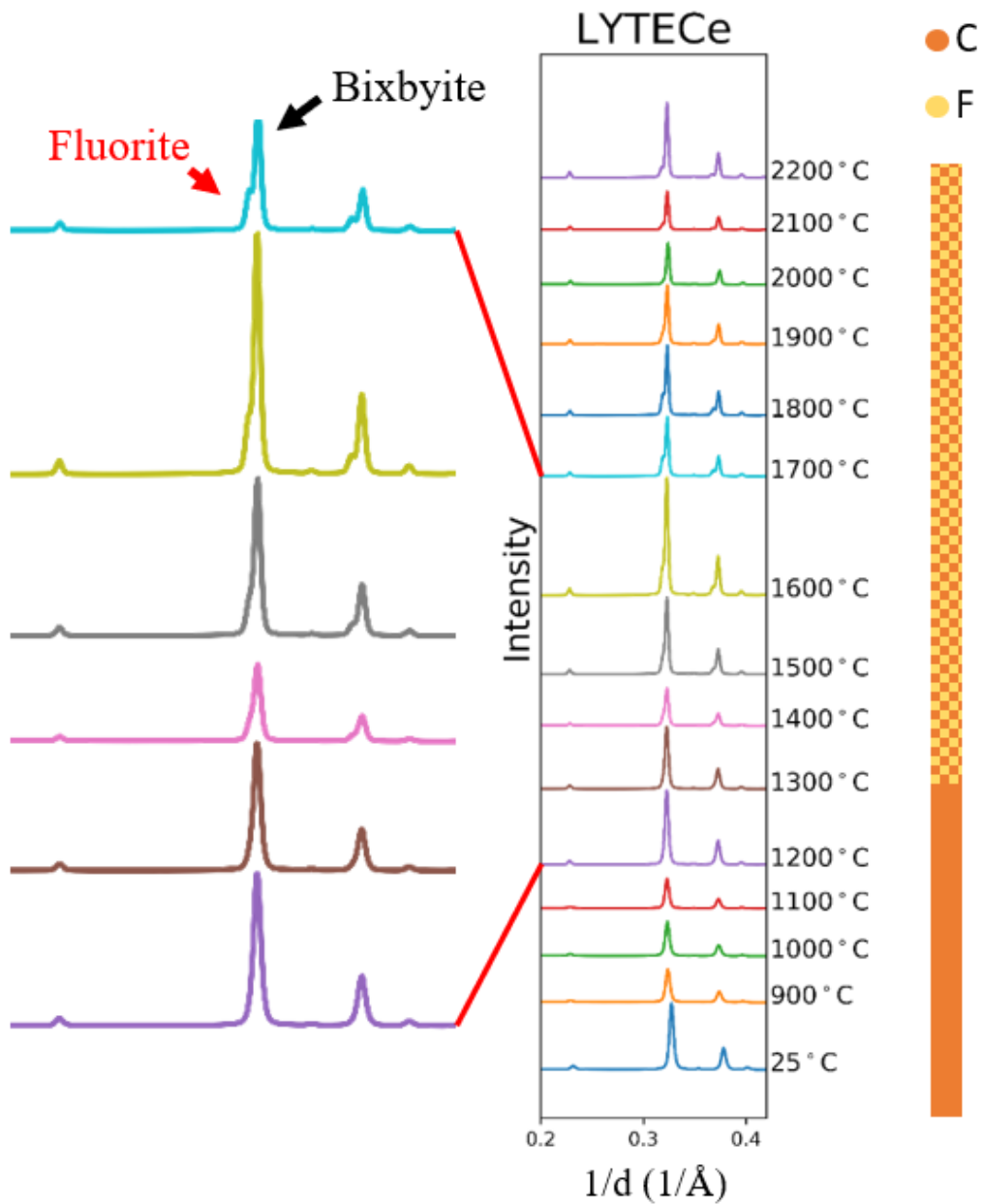


Figure 52. The zoomed-in view of XRD patterns obtained from the LYTECe sample. The  $\text{CeO}_2$  having the fluorite structure became distinguishable from the bixbyite structure above 1300°C.

## 6.2. Phase Evolution and Lattice Parameters of the LCPN System

The closely related phase transformations, up to 1800°C, were collected and analyzed in the LCPN system, and are presented in Figure 53 to Figure 62. All the crystallized HELOs could maintain their single-phase crystal structures at room temperature. This tilted fluorite structure, with Pearson symbol cI88, is denoted as the D-type phase in the following discussion. However, complicated phase transformations were detected when the temperature rose above 1400°C. The following is the phase transformation process for most of the candidates in the LCPN system. Firstly, a small portion (<10 mole %) of A-type hexagonal structure became observable. Next, the D-type phase experienced a complete structural transformation to the CeO<sub>2</sub> type fluorite (denoted as F-type), accompanied by the increasing amount of A-type phase as well as tiny, unknown diffraction peaks. These insignificant, unidentifiable, diffraction peaks disappeared at the completion of transformation between D-type to F-type, which could be easily inspected in the evolution of diffraction from the D-type (211) plane, at  $Q(1/d) \sim 0.22$ . These unknown diffraction peaks could be contributions from the intermediates during D-type to F-type formations. The F-type structure had some identical diffractions to the D-type structure. As a result, the F-type structure could have been present when the D-type diffraction peaks were unobservable in the XRD spectrum. Meanwhile, this transformation has also been observed in one of the reported HELO samples.[50] Two HELO samples prepared by the quenching process from 1150°C,  $(\text{Ce}_{0.2}\text{La}_{0.2}\text{Pr}_{0.2}\text{Sm}_{0.2}\text{Y}_{0.2})\text{O}_{2-x}$  and  $(\text{Ce}_{0.167}\text{Gd}_{0.167}\text{La}_{0.167}\text{Pr}_{0.167}\text{Sm}_{0.167}\text{Y}_{0.167})\text{O}_{2-x}$ , occurred in F-type phases, whereas the structure became D-type after the air-cooling process. The existence of hexagonal structures and tiny unknown diffraction peaks was not mentioned by Djenadic et al.[50] Based on their characterization methods and presented diffraction patterns, the insignificant intermediate phases might not be distinguished from the background generated by Cu-based laboratory XRD.

The transition temperatures obtained by XRD patterns are listed in Table 15. During the in-situ heating experiments, the reversibility of any transitions involved in the samples was tested by slowly decreasing temperatures through 200-300°C, at 50°C intervals, below the transition temperatures. The amount of the A-type phase would slightly decrease as the temperature decreased. However, the single-phase D-type structure coexisted with a small amount of impurities after cooling. In other words, the existence of an A-type structure could be non-reversible. On the other hand, the transition between the D-type and F-type structures was reversible. Above 1500°C, a minuscule amount of X-type tilted cubic phase appeared in the diffraction patterns, followed by a decline in the A-type phase. This transition was similar to the high-temperature behavior of mono-cation sesquioxides discussed previously in Figure 6, where the H-type tilted hexagonal transferred to X-type tilted cubic above 2000°C. Nevertheless, the existence of X-phase was not totally reversible. After cooling back to room temperature, some B-type monoclinic structure was observed in the diffraction patterns. According to the phase diagram in lanthanide sesquioxides, the B-type phase could be transformed from either H-type or X-type sesquioxides. Further experiments were designed to understand the phase stability in the LCPN system, as proposed in Section 6.3.

The structural transformations involved in the LCPN<sub>Lu</sub> sample were similar to other candidates in the LCPN system. However, the perovskite structure was observed at around 1448°C. The amount of this phase slightly increased as the temperature reached 1622°C. Then the composition started to decline at higher temperatures. The sample reacted with the sapphire capillary as the temperature reached 1727°C. The reversibility of this special phase transformation is described in the next Section 6.3.

LCPN<sub>Tb</sub> was the only candidate in the LCPN system which exhibited the F-type, instead of the D-type structure, at ambient conditions. Above 790°C, the diffraction peaks from the D-type

phase started to grow as the temperature increased. This was the first discovery in a reversible transformation between two single-phase HEOs. As the temperature increased, the LCPNTb sample followed a similar structural transformation route to the other HEOs in the LCPN system. Surprisingly, after the F-type to D-type transition at around 790°C, the latter phase transformed to the prior F-type structure above 1626°C, accompanying the coexistence of H-type and X-type phases. After the cooling process in the quadrupole lamp furnace, tiny secondary phase(s) remained in the oxide powder.

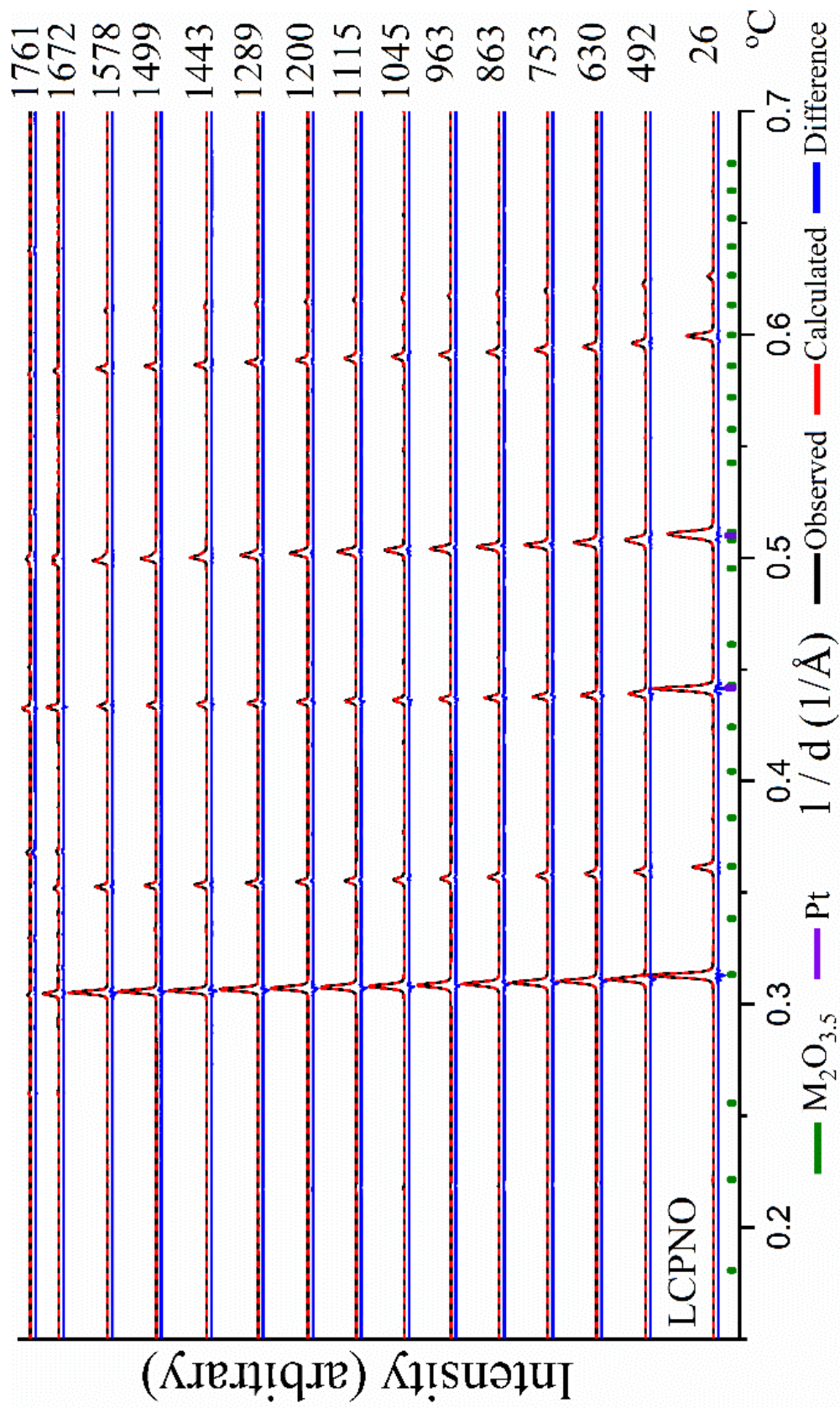


Figure 53. Rietveld refinement of the LCPNO powder

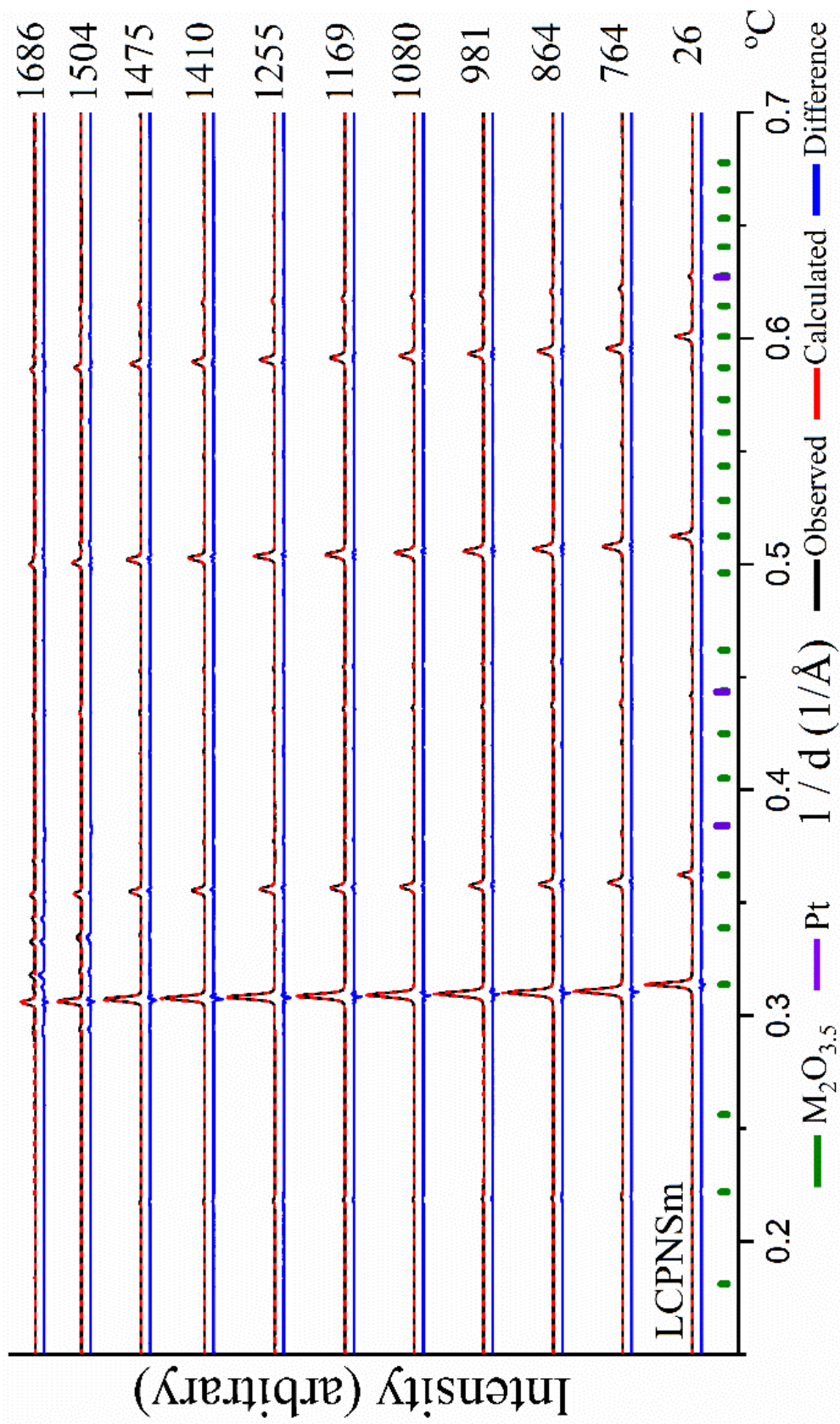


Figure 54. Rietveld refinement of the LCPNSm powder

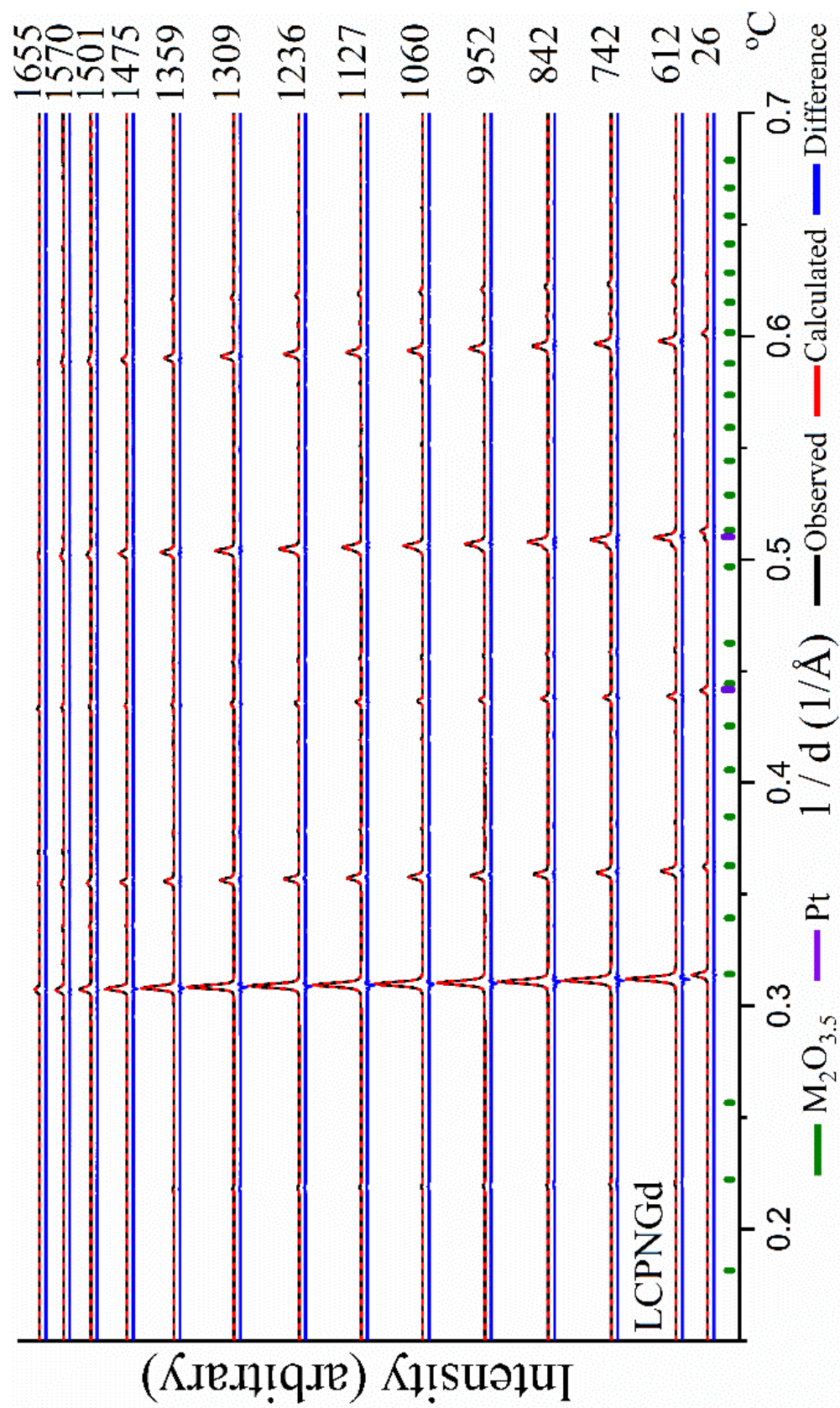


Figure 55. Rietveld refinement of the LCPNGd powder



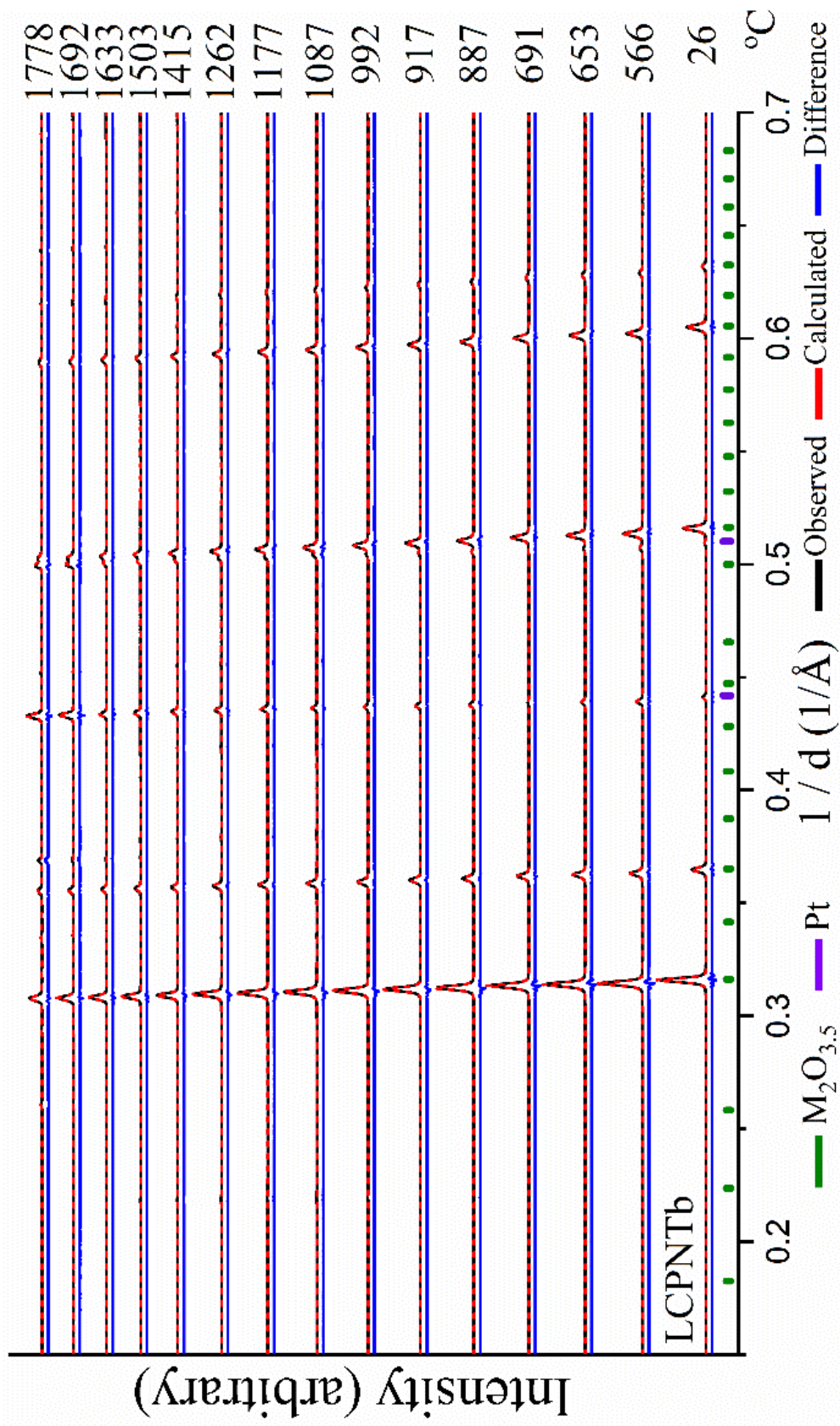


Figure 56. Rietveld refinement of the LCPNTb powder

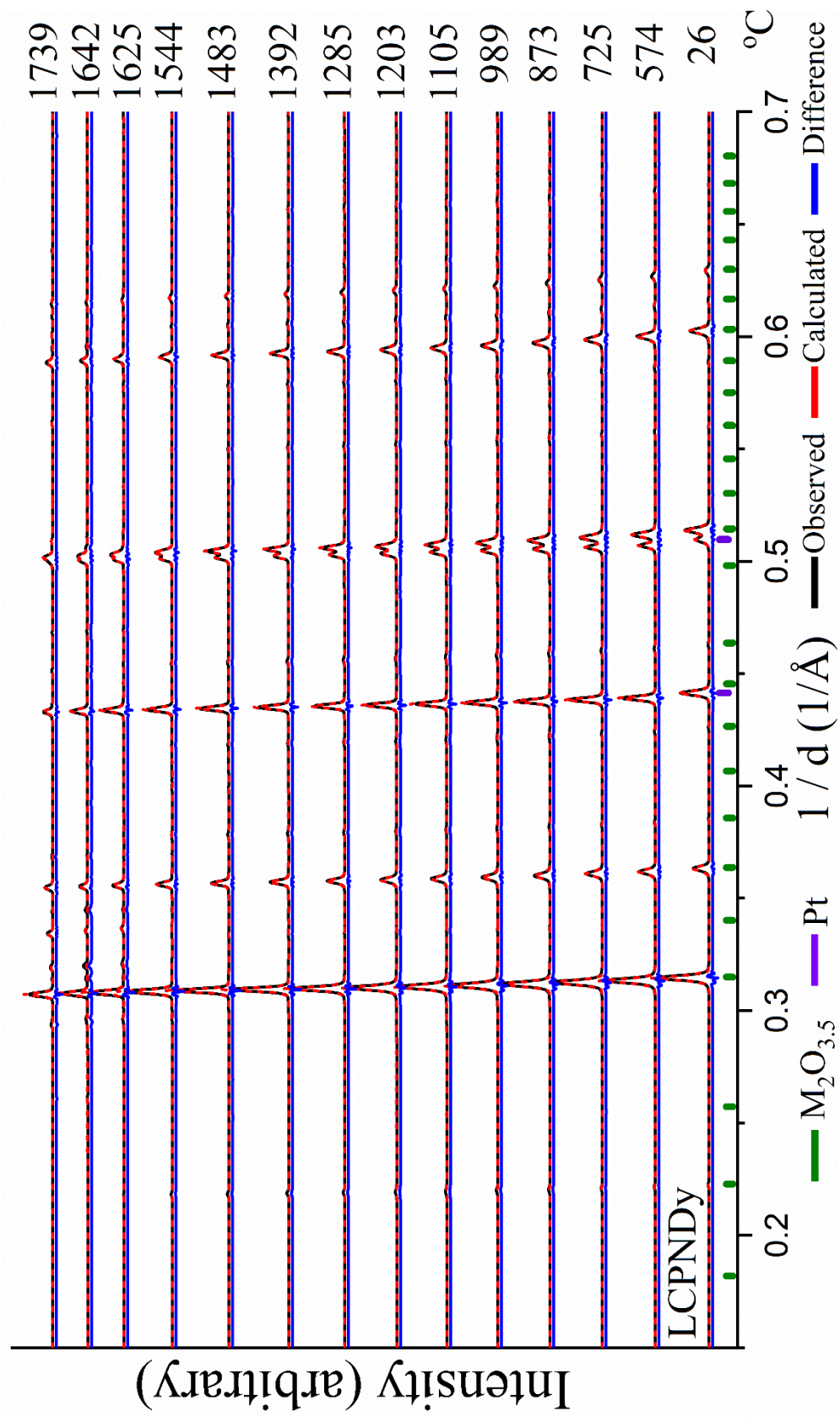


Figure 57. Rietveld refinement of the LCPNDy powder

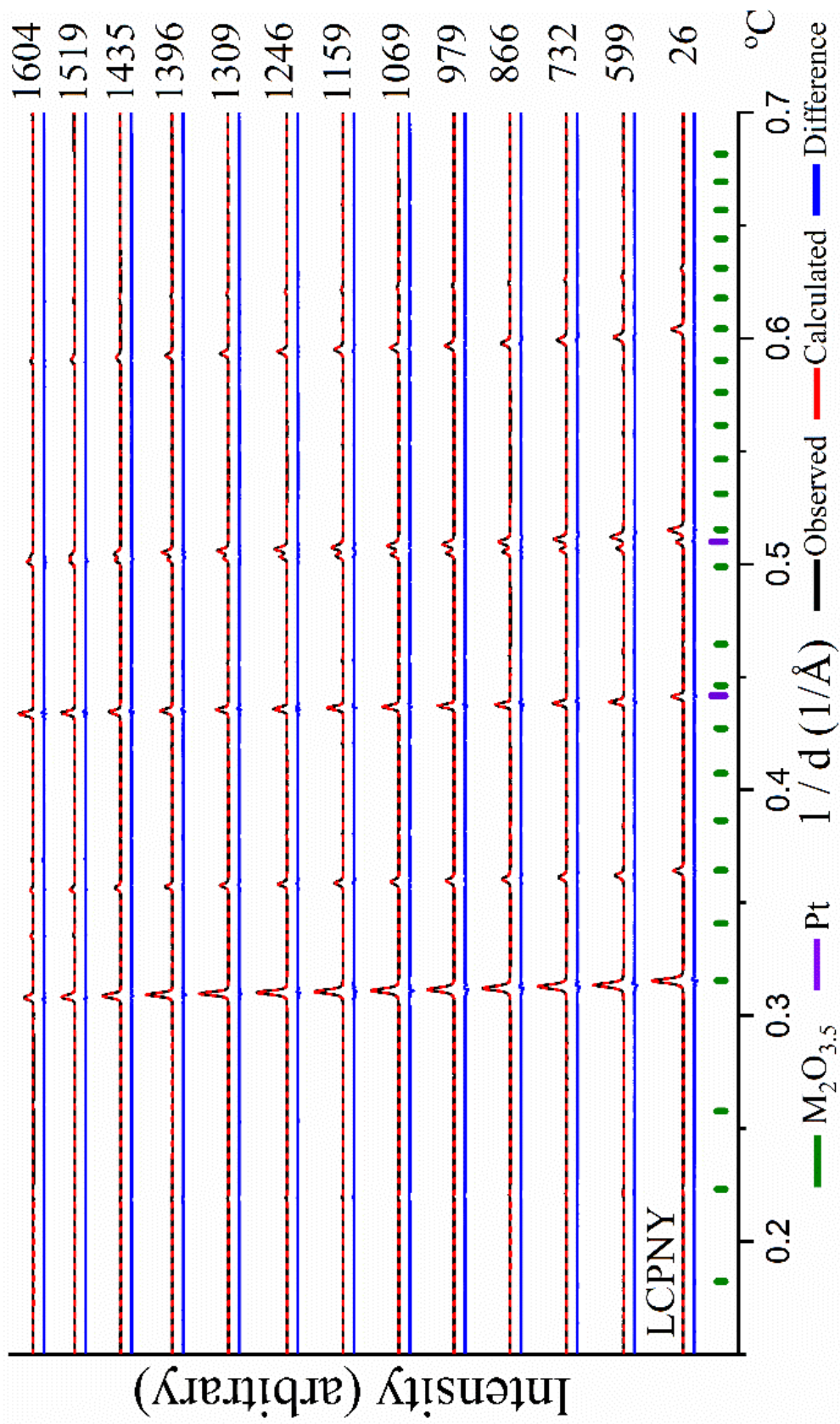


Figure 58. Rietveld refinement of the LCPNY powder

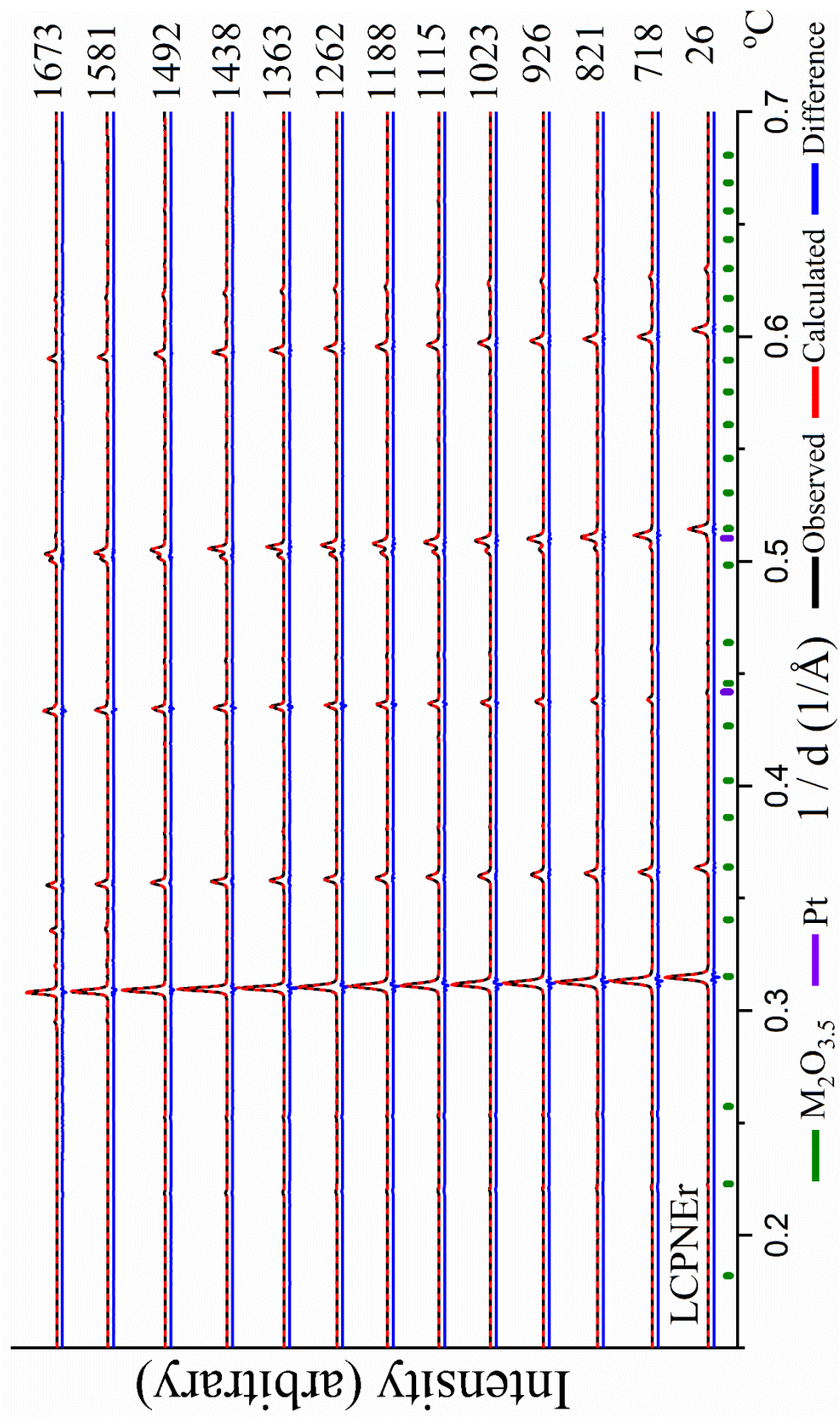


Figure 59. Rietveld refinement of the LCPNEr powder

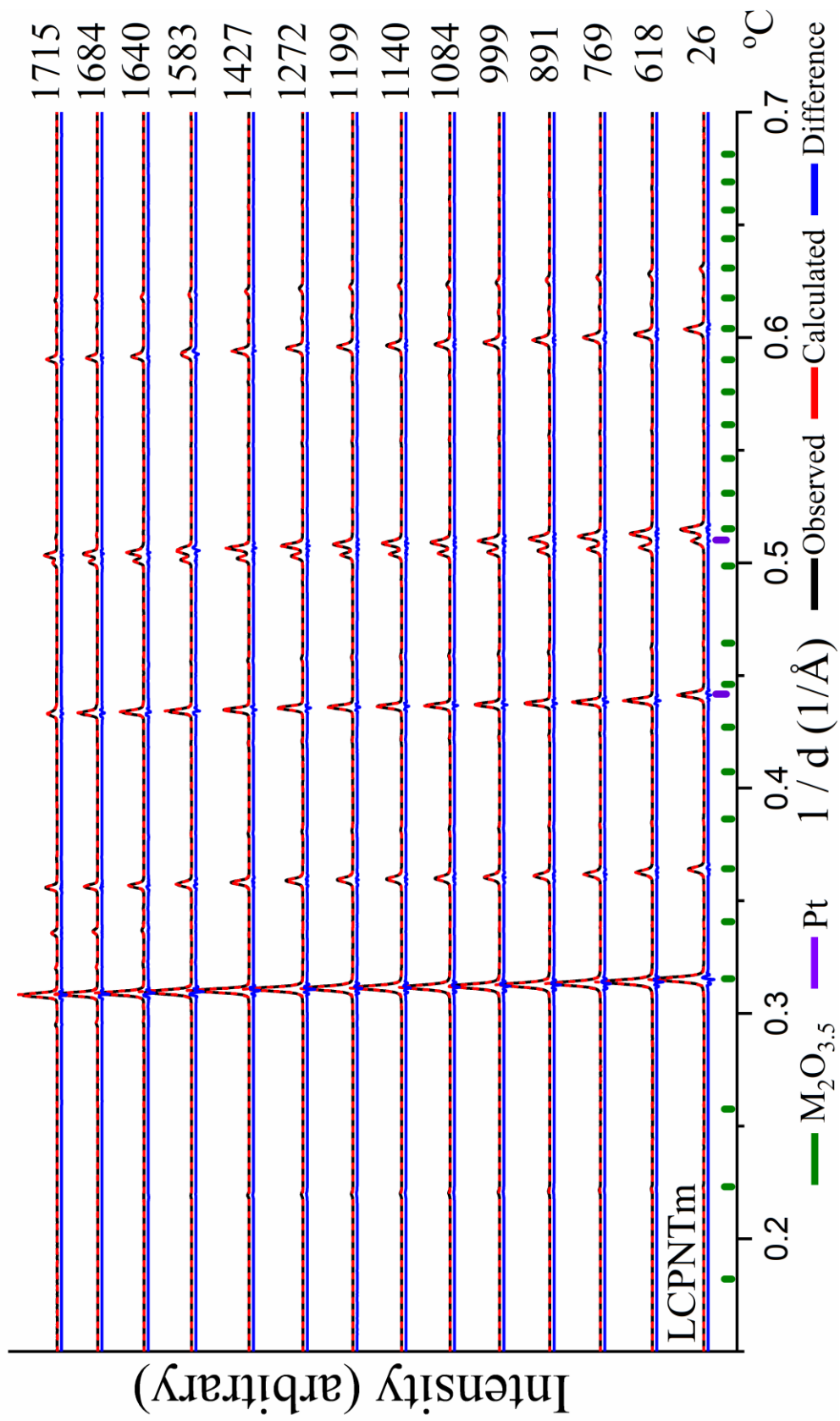


Figure 60. Rietveld refinement of the LCPNTm powder

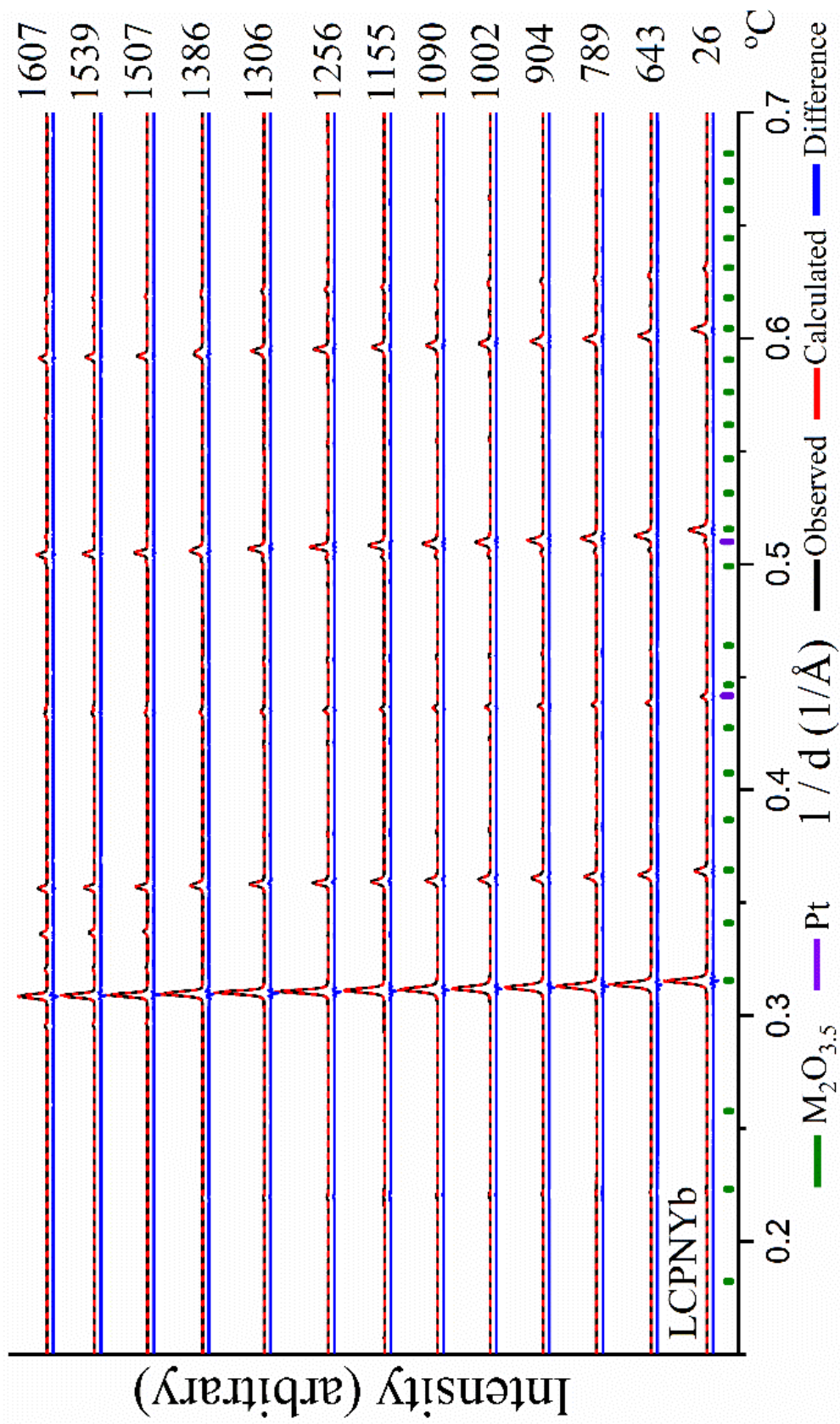


Figure 61. Rietveld refinement of the LCPNYb powder

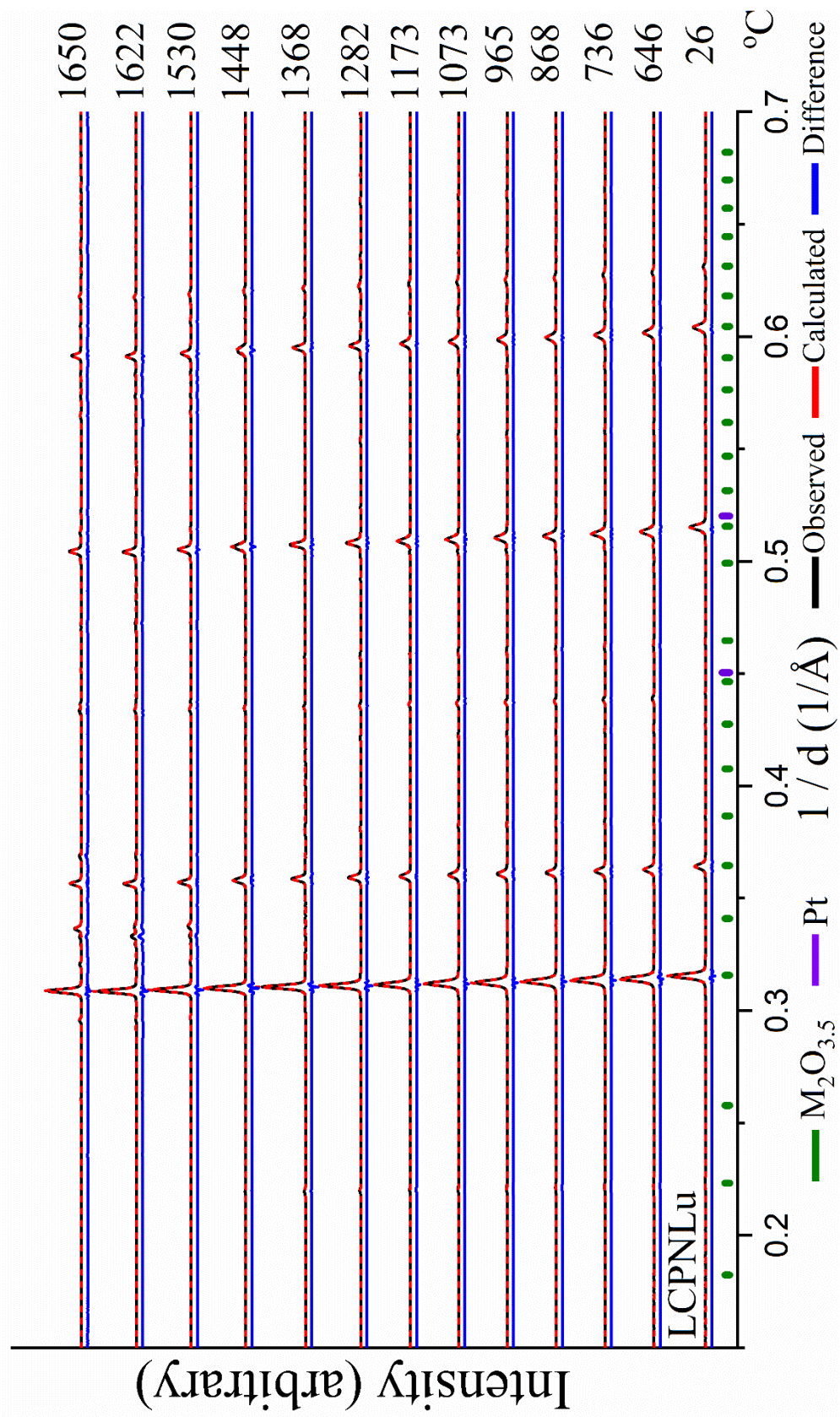


Figure 62. Rietveld refinement of the LCPN Lu powder

Table 15. Transition temperatures identified by the in-situ heating X-ray diffractions

	Transformation		Formation of secondary phases		
	D ↔ F	D ↔ F*	A-type	X-type	Perovskite
LCPNSm	-	1486 °C	1486 °C	-	-
LCPNGd	-	1655 °C	1475 °C	1570 °C	-
LCPNTb	790 °C	1626 °C	1568 °C	1626 °C	-
LCPNDy	-	1642 °C	1544 °C	1642 °C	-
LCPNY	-	1604 °C	1519 °C	1604 °C	-
LCPNEr	-	1673 °C	1581 °C	-	-
LCPNTm	-	1684 °C	1583 °C	1715 °C	-
LCPNYb	-	1507 °C	1507 °C	1607 °C	-
LCPNLu	-	1530 °C	1448 °C	1650 °C	1448 °C

	Database Structures	PDF#	Structure	Space Group	Pearson Symbol	Prototype Structure
D-type	CeNdO <sub>3.5</sub>	04-013-6624 [92]	Fluorite (Tilted)	<i>Ia</i> $\bar{3}$	cI88	Ce <sub>0.4</sub> Gd <sub>0.6</sub> O <sub>1.7</sub>
F-type	CeO <sub>2</sub>	04-015-0301 [166]	Fluorite	<i>Fm</i> $\bar{3}m$	cF12	CaF <sub>2</sub>
A-type	La <sub>2</sub> O <sub>3</sub>	01-071-5408 [170]	Hexagonal	<i>P</i> $\bar{3}m1$	cI5	La <sub>2</sub> O <sub>3</sub>
X-type	Nd <sub>2</sub> O <sub>3</sub>	04-007-2358 [172]	Cubic	<i>Im</i> $\bar{3}m$	hP5	Nd <sub>2</sub> O <sub>3</sub>
B-type	Nd <sub>2</sub> O <sub>3</sub>	00-028-0671 [174]	Monoclinic	<i>P</i> <sub>2</sub> /m	mP30	Ho <sub>2</sub> S <sub>3</sub>

\*The transition temperatures from D-type to F-type was identified by the total depletion of the D-type phase.

Under the extreme condition of >2000 °C, the X-type tilted cubic structure was found in some of the partially melted samples (Figure 63 and Figure 64). Based on the phase diagrams of monocation sesquioxides in Figure 6, the existence of the X-type phase could be transformed from the H-type structure. In this case, based on the hypothesis that the X-type phase was solely transformed from H-type phase, the F-type structure melted in the presence of the X-type phase, which



remained stable up to around 2300°C in the mono-cation sesquioxides. During the in-situ heating experiments in the conical nozzle levitator, the spherical beads deformed during transformations between D-type and F-type structures. Once the sample became dome shape or near-planar in shape, the power of the laser beam could melt the middle of the tested samples. In this case, the amorphous diffractions from a melt sample were not observable from a donut-shape sample. At below 2000°C, the transitions of HELOs in the LCPN system followed the trend observed in the quadrupole lamp furnace, which had higher precision with respect to sample temperature, as extrapolated from the thermal expansion of the platinum standard.

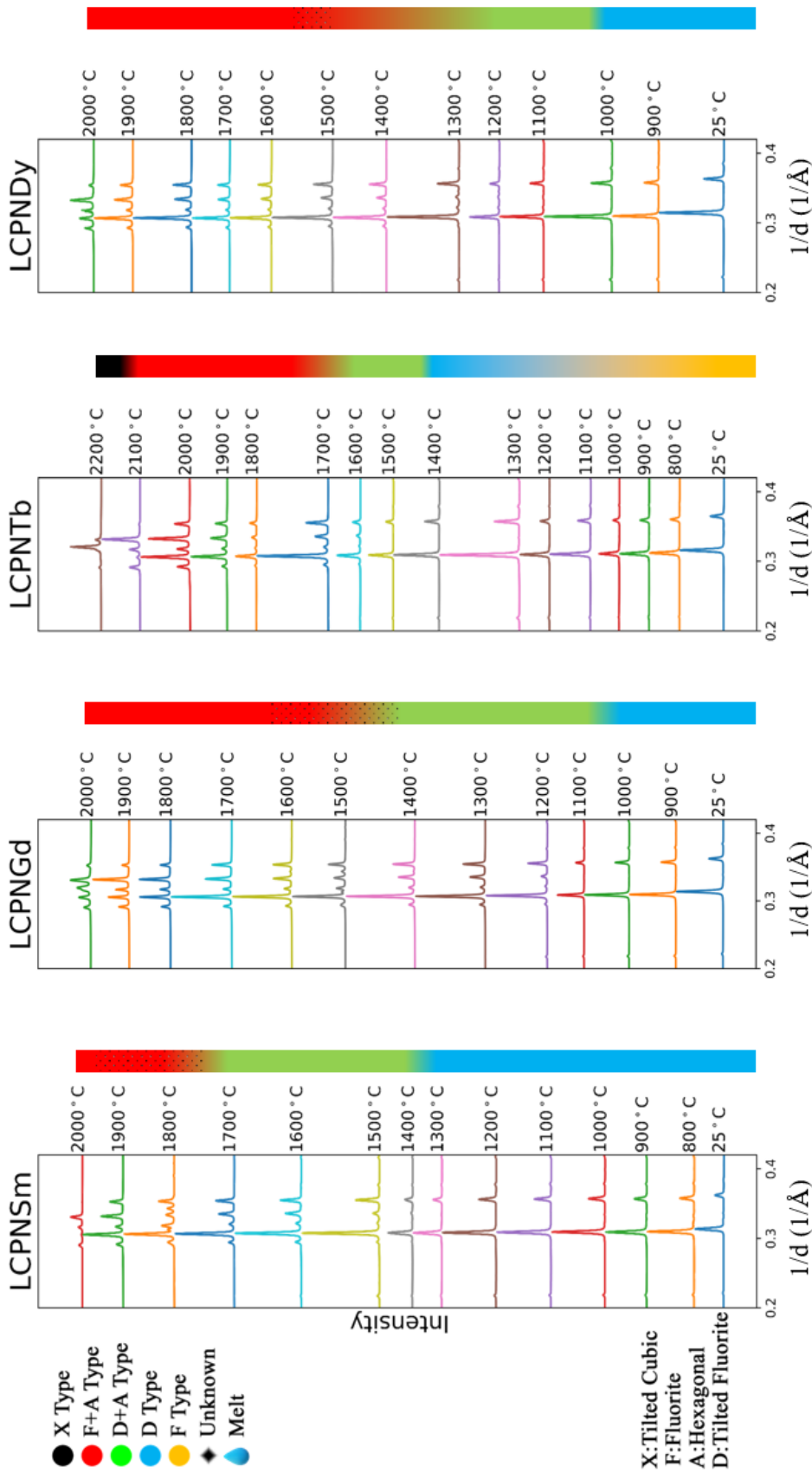


Figure 63. XRD patterns of LCPN candidates (LCPNSm-LCPNDy) obtained in the conical nozzle levitator. The droplet symbol indicates melting during the in-situ experiment.

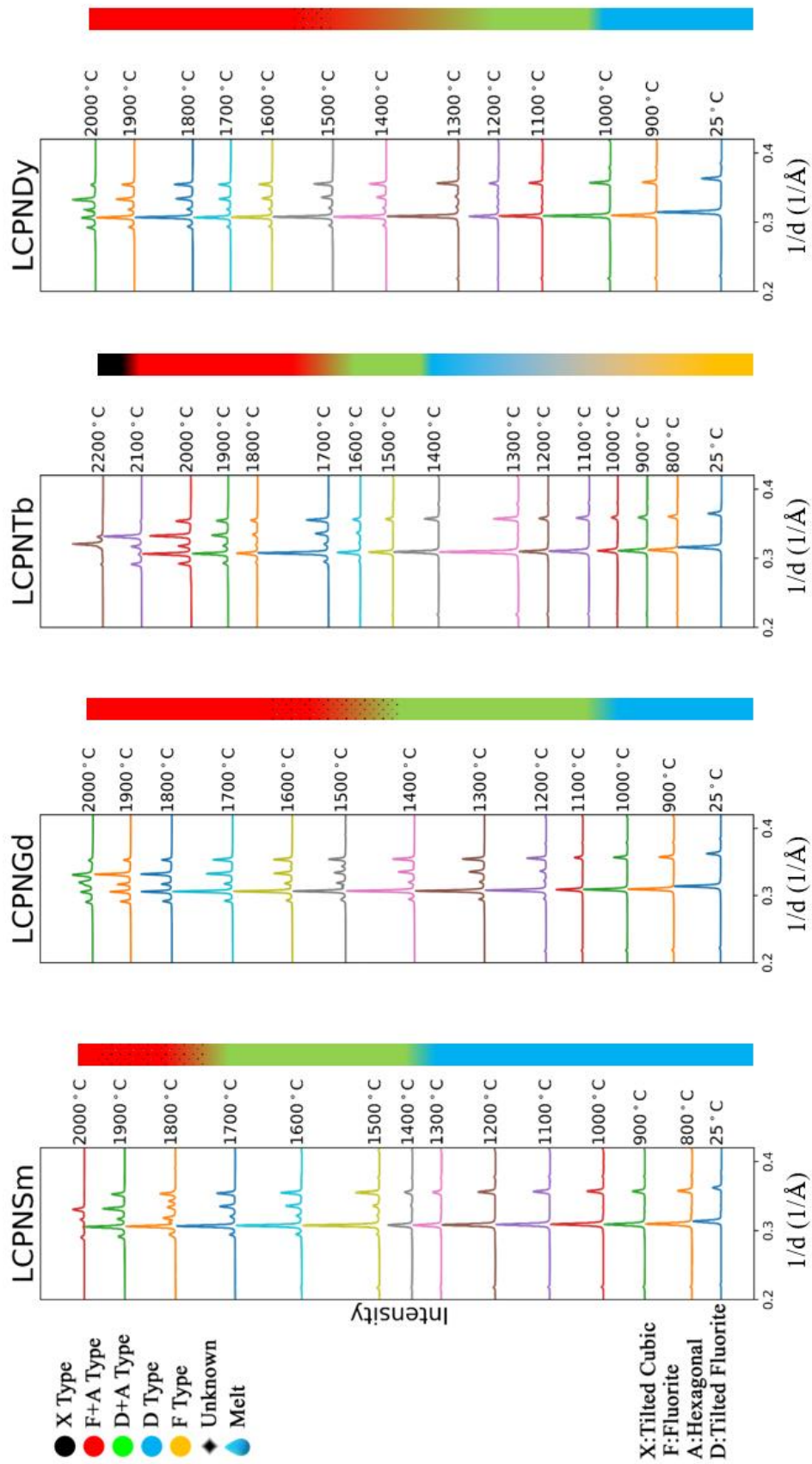


Figure 64. XRD patterns of LCPN candidates (LCPNY-LCPNLU) obtained in the conical nozzle levitator. The droplet symbol indicates melting during the in-situ experiment.

### 6.3. The Hypothesis of Stability with respect to LCPN Phase Transformations

A complex series of phase transformations was observed in the LCPN system. During both in-situ heating, synchrotron XRD experiments in the quadrupole lamp furnace and conical nozzle levitator, some secondary phases (A-type, B-type, or H-type structures occurring in mono-cation sesquioxides) remained after the cooling process. However, the cooling rates from these in-situ experimental experiments were fast, compared to the air-cooling rates in a conventional furnace. In the situation where if the cooling transformations required a longer time for H-type and X-type phases to revert back to D-type and F-type structures, respectively, this reversibility might not be observable in the in-situ experiments. In order to determine the phase stability of these HELOs, another heat treatment process was applied to some of the crystallized powder samples in the LCPN system. Firstly, the samples were heated in a conventional furnace at 5°C/min up to 1500°C, and annealed for 4 hours, and then cooled down at the same rate to 1100°C, the temperature which is about 300°C below the H-type and X-type transitions, for 10 hours, followed by the conventional air-cooling process to room temperature.

The XRD patterns of the LCPNEr samples obtained from three different heat treatments are presented in Figure 65. The as-synthesized (1150°C 2hours, 5°C/min) LCPNEr sample had a single-phase D-type structure (where the diffraction peaks are denoted as orange lines). The coexistence of D-type, B-type (monoclinic), and A-type structures was discovered from the sample after relatively fast cooling down from 1673°C via the quadrupole lamp furnace. The last sample was the one designed to study the stability of the phase transformations. After 10 hours annealing at the temperature below the H-type and X-type transformations, there were still insignificant impurities in the diffraction patterns. The specific phase(s) of those impurities could not be identified due to their low intensities. Compared to the rapidly cooled samples collected by in-situ experiments, the annealing process was able to determine whether the high-temperature secondary

phase(s) could be retained. This transformation was observed in most of the candidates in LCPN system.

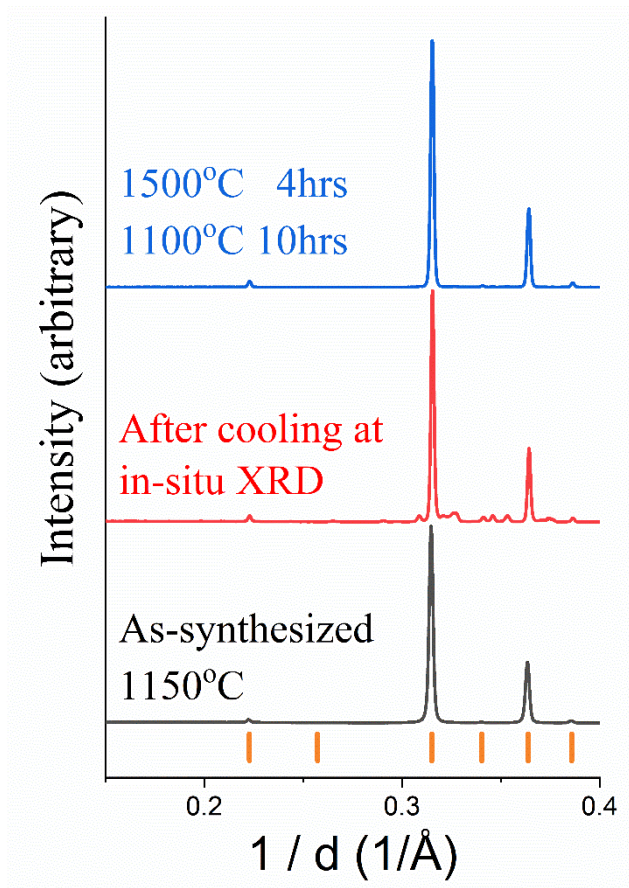


Figure 65. XRD patterns of LCPNER under three different heat treatments. The orange lines indicate the D-type phase. Secondary phases were found in the powder sample after fast-cooling from 1673°C by in-situ measurements. The annealed sample had approximately identical phase to the single-phase HELO synthesized at 1150°C.

A hypothesis was made for the phase transformation behaviors of most of the LCPN candidates. Under ambient conditions, these HELO samples exhibited a single-phase D-type cubic structure. As the temperature increased, structural transformations became involved in these samples. The transformation routes are sketched in Figure 66. In the first case, oxygen vacancies

were the only variance between the transformation of D-type and F-type structures. The chemistry of cations remained the same in both structures. This reversible transformation as a function of temperature could be achieved in a short time (~mins). On the other hand, when a portion of cations precipitated from a HELO structure, the A-type phase of hexagonal structure could be seen in the diffraction patterns. This structure could possibly experience similar high-temperature transformation trends as H-type sesquioxides of the middle lanthanide cations ( $\text{Sm}_2\text{O}_3$ - $\text{Dy}_2\text{O}_3$ ). X-type tilted cubic structures and B-type monoclinic structures were observed in our in-situ experiments under extreme environments ( $2000^\circ\text{C}$ ) and after cooling back to room temperature, respectively. According to the results obtained from the annealing experiments, these impurities could transform back to a HELO structure after the annealing process. In these slow, reversible transformations, the precipitated cations homogeneously merged back to the HELO structures, which could be a hypothesis why hours of annealing were required to re-obtain HELOs with insignificant impurities. By increasing the annealing time, it is possible to complete this reversible transformation.

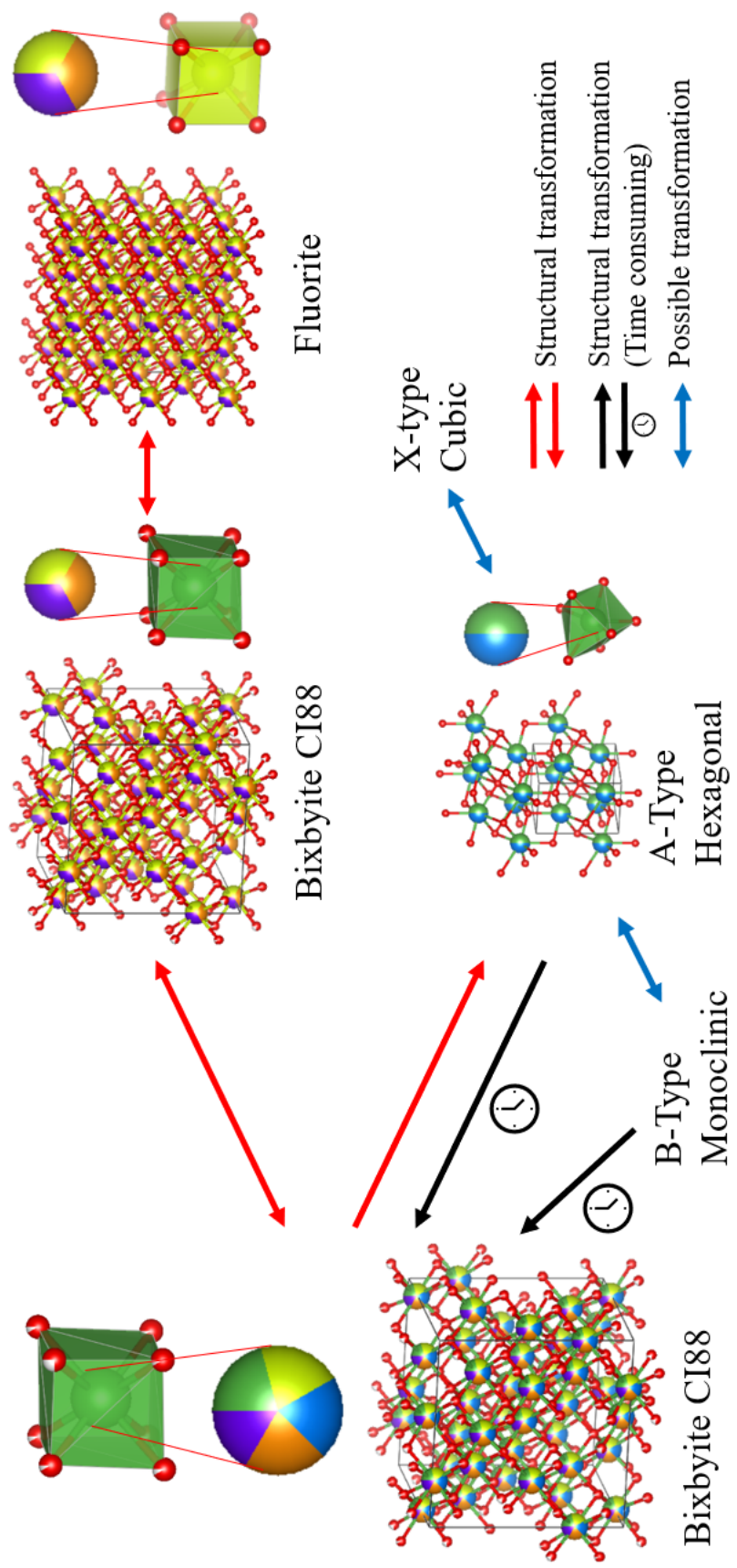


Figure 66. Possible routes for phase transformations involved in most of the LCPN candidates

LCPNTb exhibited an F-type fluorite structure under ambient conditions. As the temperature increased, the fluorite structure transformed into a D-type bixbyite structure, followed by the similar transformations mentioned in the last paragraph. The rapid, reversible, transformations between D-type and F-type structures provided evidence that HEOs could experience phase transformation as a function of temperature. In Figure 67, the annealed LCPNTb exhibited an almost identical single-phase F-type fluorite structure. The orange lines indicate the diffraction peaks from the F-type phase. By including this additional transformation route, the phase transformation behaviors of LCPNTb is summarized in Figure 68.

A unique phase was found in the LCPN Lu sample during the in-situ heating experiments. The perovskite phase was found in the diffraction pattern at 1448°C. Interestingly, the perovskite structure remained in the powder sample after 10 hours annealing at 1100°C, as presented in Figure 67. This additional phase, composed of at least one large cation and one small cation (lutetium in this case), could have required a longer time to transform back to the D-type structure. While this may be true, these two structures could also be thermodynamically stable under ambient conditions. In this case, preparing a precursor with cations homogeneously mixing may be a critical process in the HEOs formation.



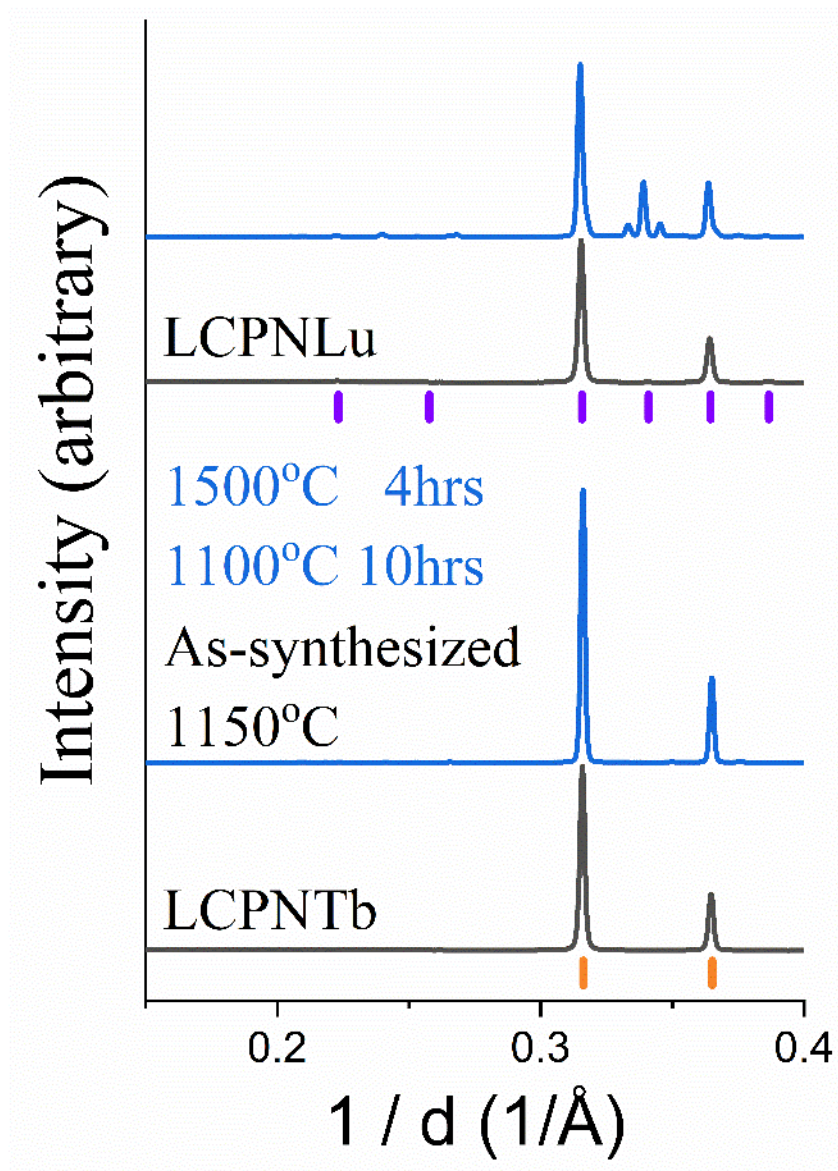


Figure 67. XRD patterns of LCPNLu and LCPNTb samples. The orange and purple lines were diffraction peaks from F-type and D-type structures, respectively. LCPNTb exhibited approximately identical patterns in the annealed sample (blue) and single-phase sample (black). A coexistence of perovskite structure and D-type structure were observed in the annealed LCPNLu sample.

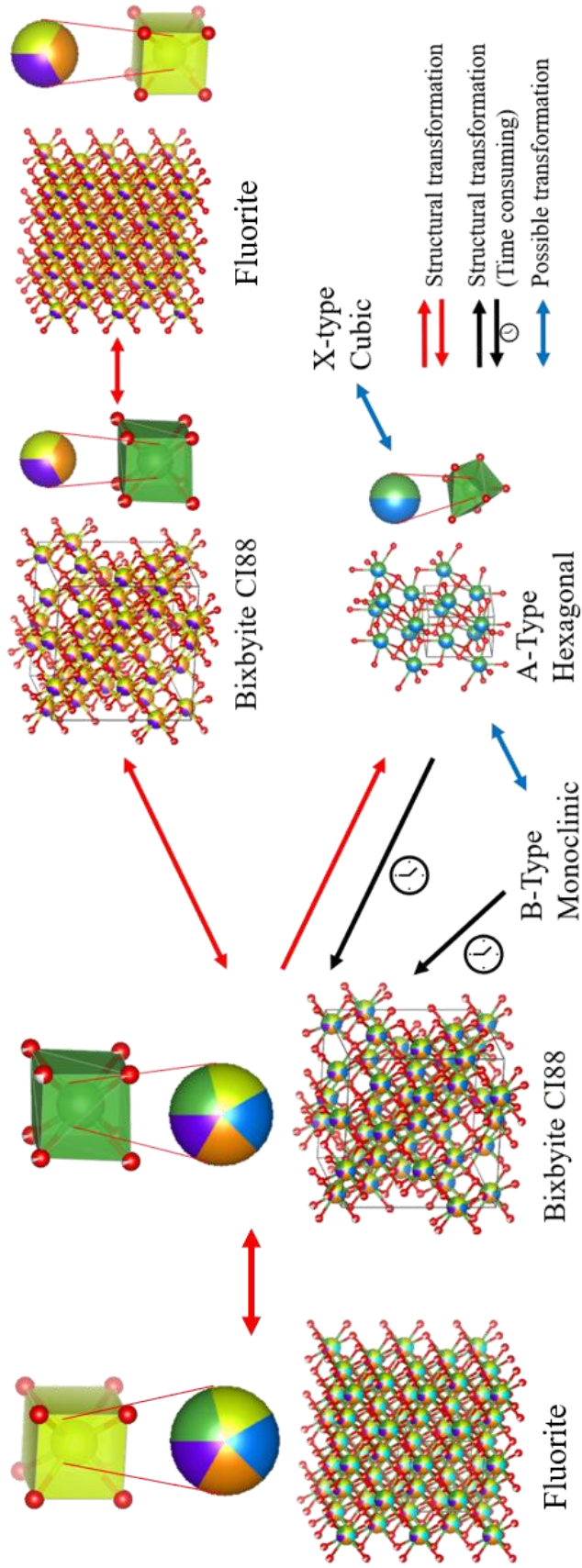


Figure 68. Possible routes for phase transformations involved in the LCPNTb sample. The rapid, reversible transformation between F-type fluorite and D-type bixbyite structures occurred at  $\sim 790^{\circ}\text{C}$ , followed by similar high-temperature behavior observed in other LCPN candidates.

#### 6.4. Thermal Expansions of Single-Phase High-Entropy Lanthanide Oxides

In the previous Sections, the outcomes from the in-situ heating experiments at synchrotron-sourced X-ray facilities revealed possible structural transformations and thermal stabilities among the LYTE and LCPN systems. Furthermore, the merit of the quadrupole lamp furnace was that it was able to obtain the precise evolution of thermal expansions, where the actual sample temperature could be obtained from a platinum standard.[147, 175] Here, the thermal expansion behaviors of our candidate materials could be analyzed through the evolution of lattice parameters. Only single-phase HELOs were discussed in this section since the composition shifted as secondary phases existed. In the LYTE system, all candidates became single-phase HELOs except LYTELa. Secondary phases were merely found in the seven out of nine samples in this system. Above 1300°C, the diffraction from the CeO<sub>2</sub> fluorite structure became evident in the XRD patterns. The evolutions of HELOs are presented in Figure 69. The trends between the lattice parameters of the bixbyite structure and temperature were fitted via second-order polynomial curves (  $y = a + bT + cT^2$  ). The detail information, including the lattice parameters corresponding to the sample temperatures, and each coefficient in the polynomial curves, are listed in Table 16 and Table 17, respectively.

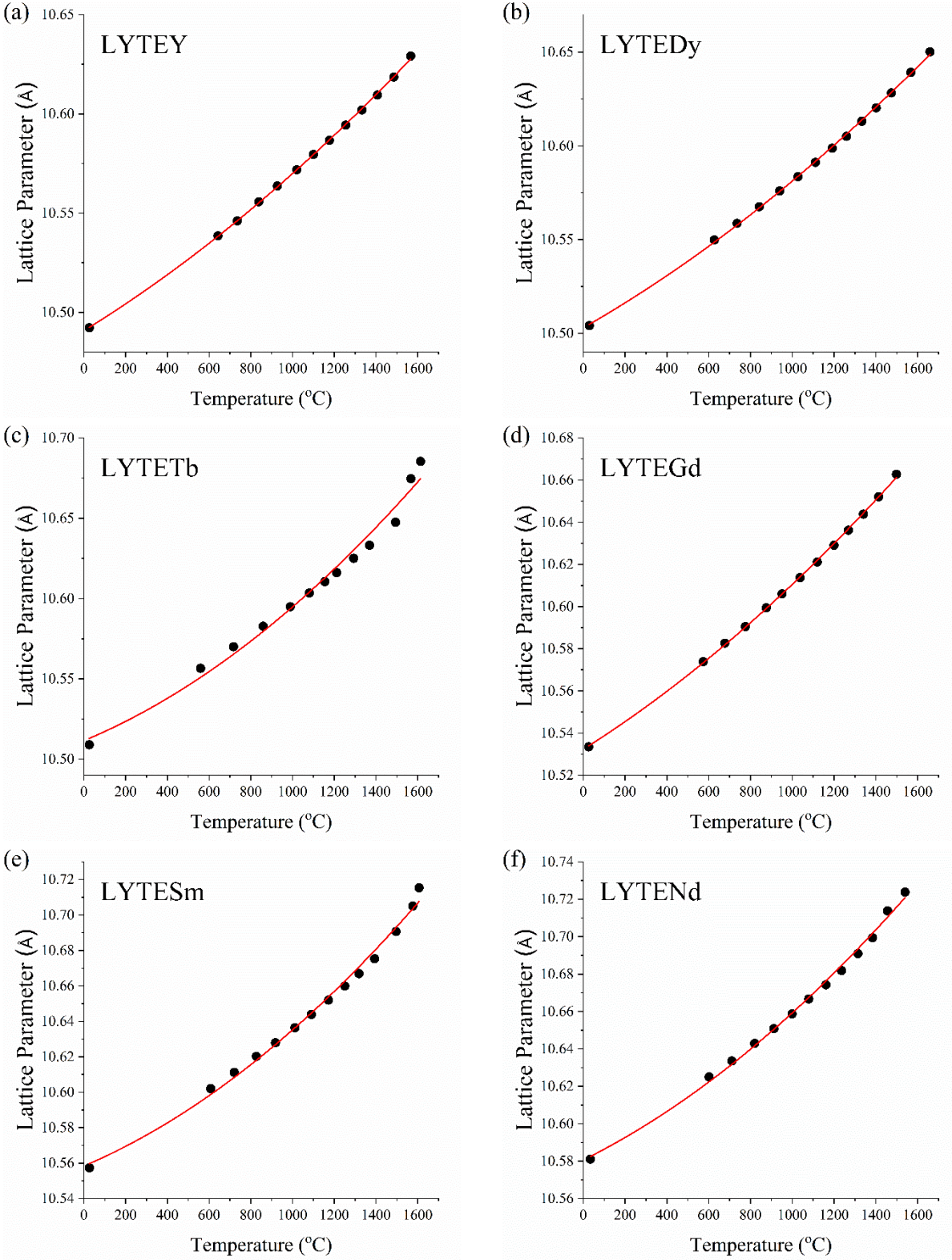


Figure 69. The evolution of lattice parameters of LYTE HELOs obtained in-situ in the quadrupole lamp furnace

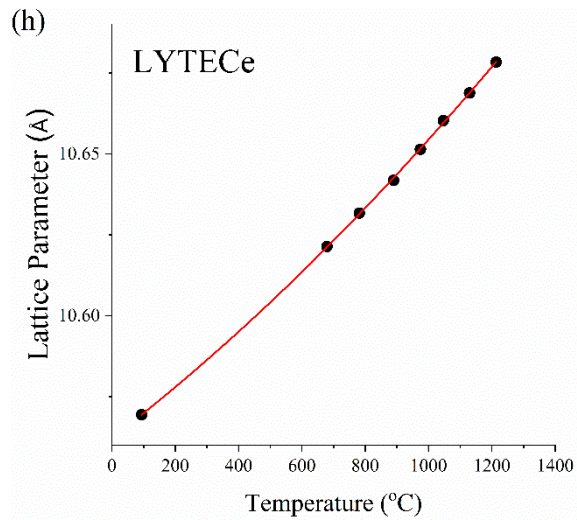
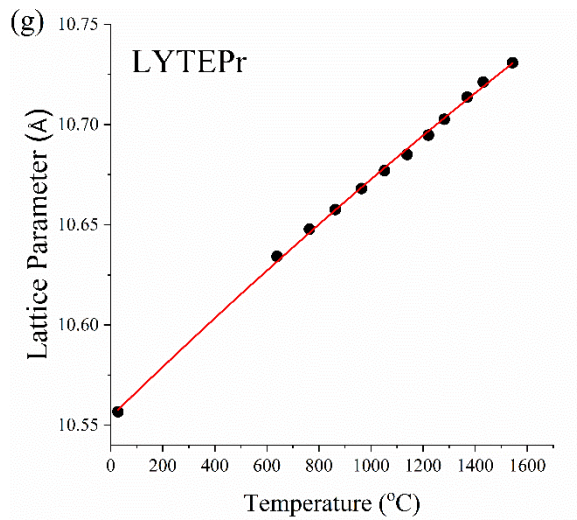


Figure 69 (continued). The evolution of lattice parameters in LYTE HELOs obtained in-situ in the quadrupole lamp furnace

Table 16. Lattice parameters (a) of cubic-bixbyite structures in LYTE HELOs corresponding to temperature (T)

LYTEY		LYTEDy		LYTETb	
T (°C)	a (Å)	T (°C)	a (Å)	T (°C)	a (Å)
26	10.49223(3)	26	10.50405(5)	26	10.50899(2)
643	10.53857(12)	627	10.54978(3)	559	10.55655(7)
735	10.54611(3)	736	10.55866(9)	717	10.57004(9)
839	10.55572(9)	842	10.56755(6)	860	10.58276(11)
928	10.5637(10)	940	10.57596(6)	990	10.59492(8)
1021	10.57188(7)	1027	10.58357(5)	1081	10.60342(8)
1101	10.57957(7)	1111	10.59119(4)	1155	10.61054(8)
1177	10.58666(6)	1192	10.59872(4)	1211	10.61610(2)
1255	10.59433(13)	1260	10.60507(4)	1293	10.62506(7)
1333	10.60202(10)	1333	10.61313(12)	1369	10.63313(4)
1407	10.6095(11)	1402	10.62027(10)	1494	10.64748(4)
1486	10.61858(13)	1475	10.62825(12)	1568	10.67457(7)
1567	10.62914(14)	1567	10.63919(2)	1614	10.68535(4)
		1659	10.65014(1)		

LYTEGd		LYTESm		LYTEND	
T (°C)	a (Å)	T (°C)	a (Å)	T (°C)	a (Å)
26	10.53349(8)	26	10.55735(10)	26	10.58106(8)
574	10.57384(4)	608	10.60204(4)	602	10.62501(1)
677	10.58263(4)	720	10.61118(1)	711	10.63359(2)
776	10.59050(2)	827	10.62020(6)	820	10.64292(2)
876	10.59939(2)	919	10.62794(7)	912	10.65082(7)
951	10.60606(6)	1012	10.63641(8)	999	10.65874(4)
1038	10.61373(1)	1091	10.64389(1)	1079	10.66672(1)
1120	10.62114(8)	1173	10.65196(11)	1161	10.67428(3)
1200	10.62906(9)	1251	10.65994(10)	1236	10.68189(5)
1269	10.63620(5)	1319	10.66692(2)	1314	10.69096(12)
1341	10.64385(3)	1394	10.67531(9)	1384	10.69940(6)
1413	10.65207(1)	1496	10.69065(8)	1456	10.71377(6)
1498	10.66271(9)	1576	10.70501(1)	1540	10.72382(17)
		1607	10.71533(15)		

Table 16 (continued). Lattice parameters (a) of cubic-bixbyite structures in LYTE HELOs corresponding to temperature (T)

LYTEPr		LYTECe	
T (°C)	a (Å)	T (°C)	a (Å)
26	10.55668(2)	26	10.56941(1)
639	10.63424(12)	679	10.62136(5)
763	10.64780(8)	782	10.63169(2)
863	10.65757(5)	890	10.64179(11)
964	10.66802(5)	975	10.65138(12)
1052	10.67701(1)	1047	10.66024(2)
1138	10.68504(6)	1130	10.66876(5)
1221	10.69468(4)	1213	10.67832(6)
1281	10.70258(12)		
1369	10.71365(1)		
1431	10.72115(11)		
1544	10.73081(12)		

Table 17. Coefficients of the second-order polynomial fitting curves ( $y = a + bT + cT^2$ ) in LYTE HELOs

	a	b	c	R <sup>2</sup>
LYTEY	10.49075	6.47384 X 10 <sup>-5</sup>	1.44405 X 10 <sup>-8</sup>	99.97%
LYTEDy	10.50293	6.37192 X 10 <sup>-5</sup>	1.45689 X 10 <sup>-8</sup>	99.96%
LYTETb	10.51154	5.42225 X 10 <sup>-5</sup>	2.89887 X 10 <sup>-8</sup>	98.44%
LYTEGd	10.5323	6.2465 X 10 <sup>-5</sup>	1.5729 X 10 <sup>-8</sup>	99.96%
LYTESm	10.55836	5.02584 X 10 <sup>-5</sup>	2.65322 X 10 <sup>-8</sup>	99.39%
LYTENd	10.58061	5.55923 X 10 <sup>-5</sup>	2.30654 X 10 <sup>-8</sup>	99.69%
LYTEPr	10.55409	1.26377 X 10 <sup>-4</sup>	-7.82501 X 10 <sup>-9</sup>	99.87%
LYTECe	10.56218	7.54468 X 10 <sup>-5</sup>	1.67676 X 10 <sup>-8</sup>	99.98%

As mentioned in Section 4.2.1, the coefficients of thermal expansions were calculated by using equation {9}. The CTE in the LYTE system was derived from the first-order equation ( $y = a + bT$ ), whose results are listed in Table 18. The results are plotted in Figure 70, in increasing order of the smallest fifth cation (yttrium, Y) to the largest cation (cerium, Ce). All the samples

exhibited positive thermal expansion behavior with increasing temperatures, as seen in Figure 69. By comparing the CTE values among these candidates, there was no clear correlation between CTE and size mismatch in LYTE HELOs. Interestingly, the candidate LYTEPr had a different tendency from other LYTE HELOs. While the value of CTE increased as temperature increased in other LYTE HELOs, LYTEPr was the only candidate showing a negative slope in the CTE values listed in Table 18. From the experimental results mentioned in Section 6.1, the melting temperature of LYTEPr was around 1900°C. By extending the trends of CTEs, the thermal expansion behavior of LYTEPr would remain at a positive value until it reached its melting point.

Table 18. The detail values of the coefficients of thermal expansion ( $y = a + bT$ ) in LYTE HELOs

	a	b
LYTEY	$6.170128 \times 10^{-4}$	$2.752608 \times 10^{-7}$
LYTEDy	$6.066153 \times 10^{-4}$	$2.773957 \times 10^{-7}$
LYTETb	$5.159631 \times 10^{-4}$	$5.516934 \times 10^{-7}$
LYTEGd	$5.930135 \times 10^{-4}$	$2.986476 \times 10^{-7}$
LYTESm	$4.760511 \times 10^{-4}$	$5.026297 \times 10^{-7}$
LYTENd	$5.253942 \times 10^{-4}$	$4.359751 \times 10^{-7}$
LYTEPr	$1.197129 \times 10^{-3}$	$-1.48248 \times 10^{-9}$
LYTECe	$7.138223 \times 10^{-4}$	$3.172855 \times 10^{-7}$



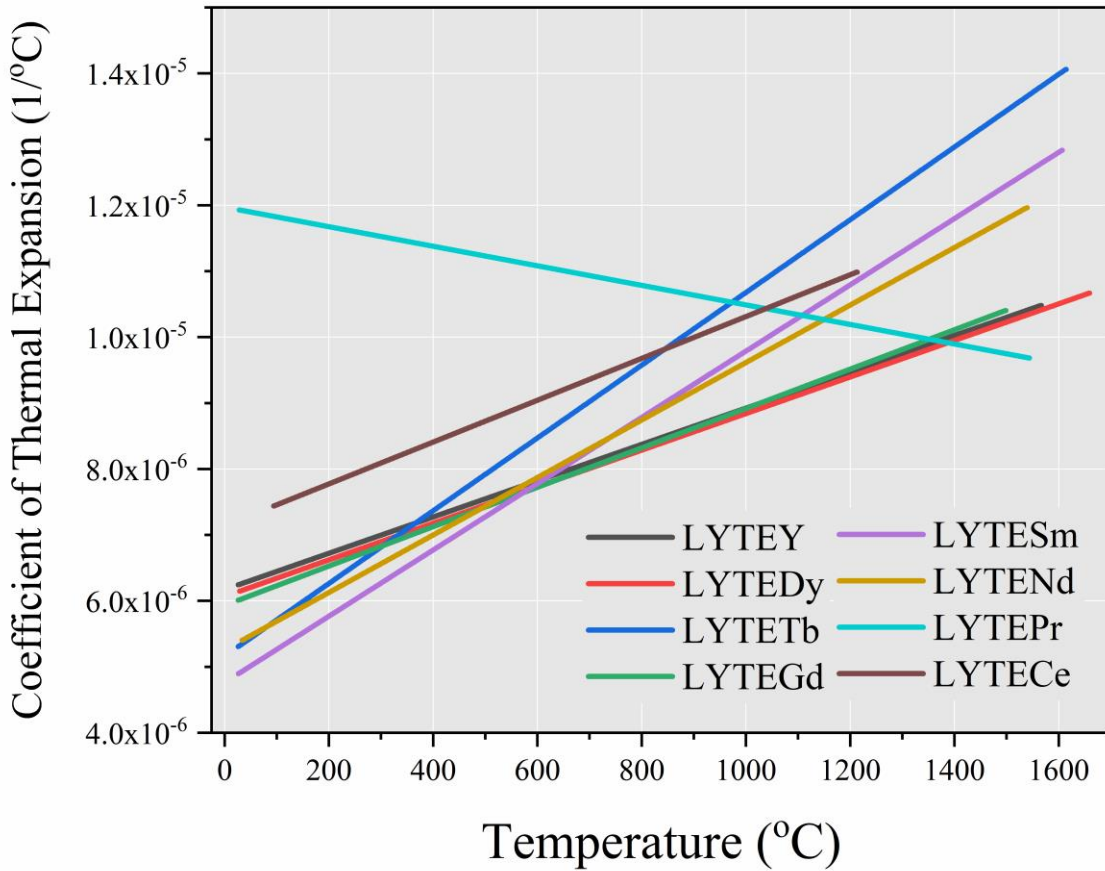


Figure 70. Evolution of the coefficients of thermal expansion among the LYTE systems. All candidates exhibited positive thermal expansions in their cubic structures.

In the LCPN system, the candidates experienced phase transformations at high temperatures. The A-type hexagonal structure existed when the temperature reached above 1500°C. In this case, a portion of cations was precipitated out from the HELO and formed secondary phase(s), leading to the composition changes in the original HELO. The lattice parameters chosen for the CTE analysis came from single-phase HELOs. The LCPNTb sample experienced a phase transformation between the two single-phase structures of F-type fluorite and D-type tilted fluorite. The thermal expansion behavior of these two structures could be analyzed separately. The evolution between lattice parameters at different temperatures is presented in Figure 71. The trends

were fitted by second-order polynomial equations. Detailed lattice parameters and coefficients of corresponding polynomial equations are listed in Table 19 and Table 20, respectively.

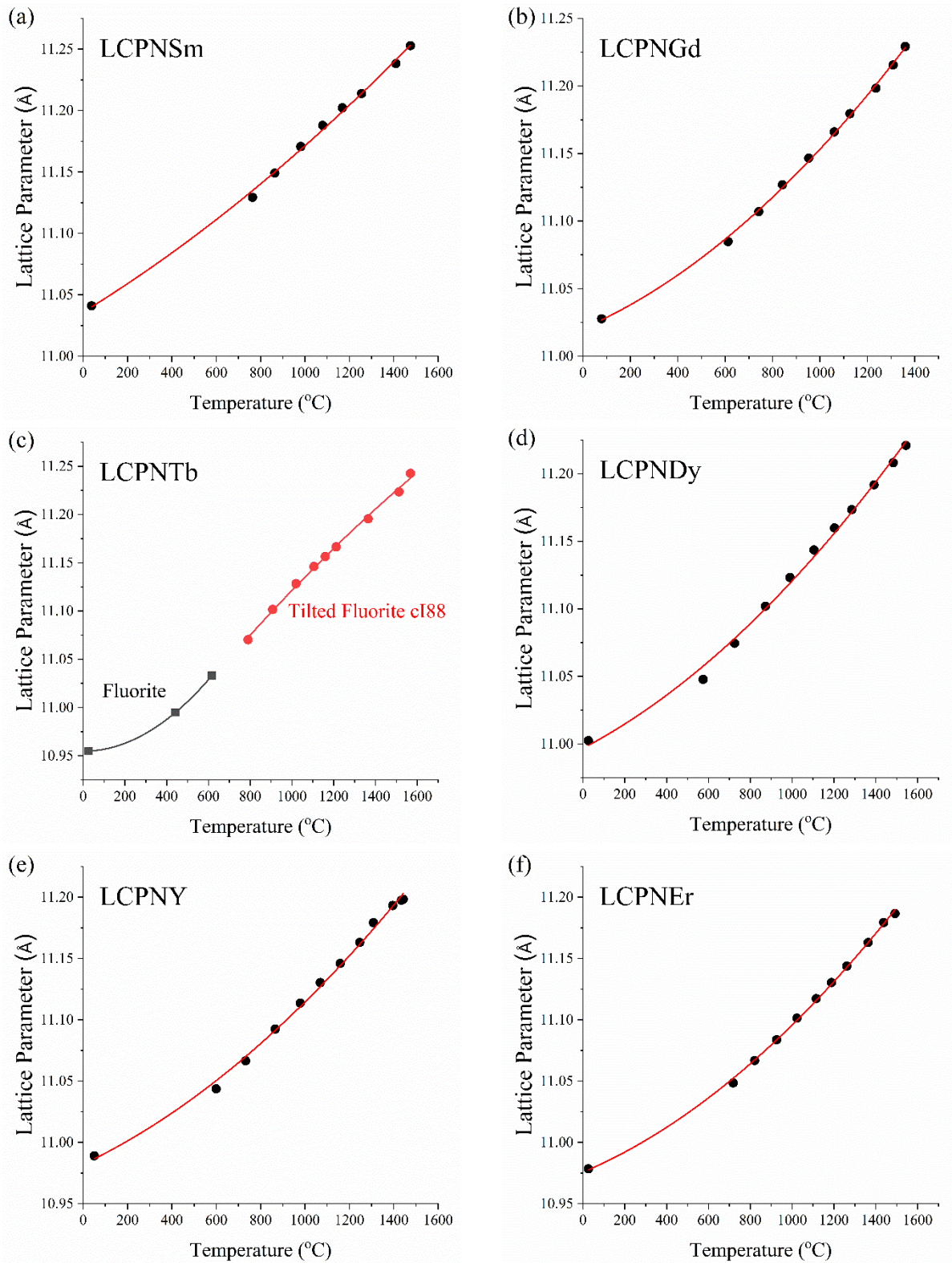


Figure 71. The evolution of lattice parameters in LCPN HELOs obtained in-situ in the quadrupole lamp furnace

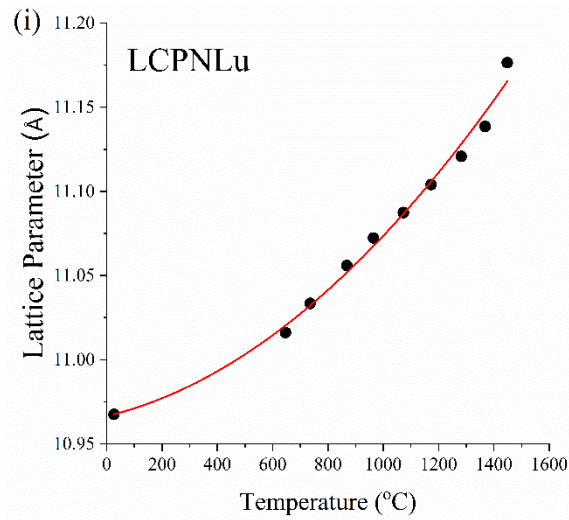
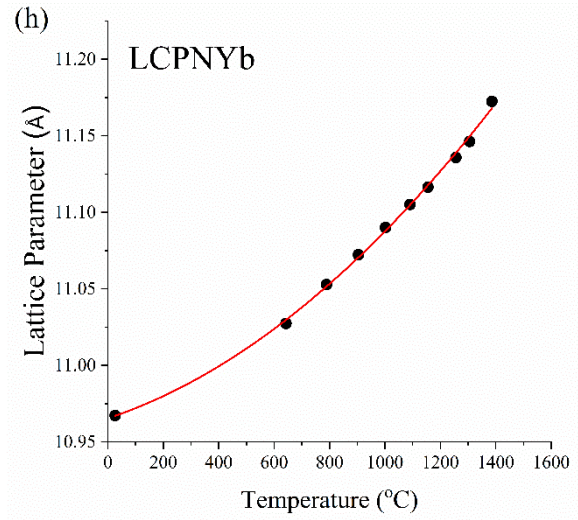
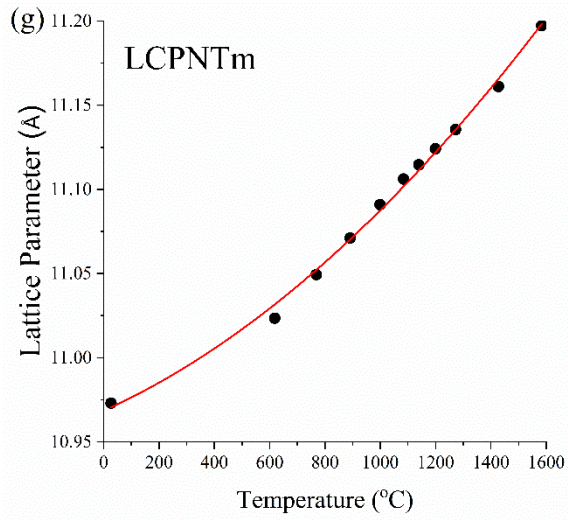


Figure 71 (continued). The evolution of lattice parameters in LCPN HELOs obtained in-situ in the quadrupole lamp furnace

Table 19. Cubic lattice parameters (a) of single-phase structures in LCPN HELOs corresponding to temperature (T)

LCPNSm		LCPNGd		LCPNTb	
T (°C)	a (Å)	T (°C)	a (Å)	T (°C)	a (Å)
26	11.04103(13)	26	11.02770(8)	26	10.95533(12)
764	11.12935(12)	612	11.08481(4)	442	10.99483(11)
864	11.14915(7)	742	11.10704(3)	616	11.03288(2)
981	11.17069(8)	842	11.12695(3)	790	11.07024(12)
1080	11.18791(8)	952	11.14662(7)	908	11.10156(6)
1169	11.20224(7)	1060	11.16605(3)	1020	11.12835(6)
1255	11.21384(12)	1127	11.17955(14)	1105	11.14611(4)
1410	11.23826(14)	1236	11.19839(8)	1159	11.15635(4)
1475	11.25285(3)	1309	11.21560(3)	1212	11.16644(9)
		1359	11.22927(13)	1365	11.19548(10)
				1513	11.22344(5)
				1568	11.24255(5)

LCPNDy		LCPNY		LCPNEr	
T (°C)	a (Å)	T (°C)	a (Å)	T (°C)	a (Å)
26	11.00154(8)	26	10.98907(9)	26	10.97844(5)
574	11.04776(12)	599	11.04365(6)	718	11.04849(7)
725	11.07446(9)	732	11.06664(12)	821	11.06684(9)
873	11.10195(8)	866	11.09249(7)	926	11.08377(3)
989	11.12322(10)	979	11.11365(10)	1023	11.10140(8)
1105	11.14354(13)	1069	11.13033(11)	1115	11.11729(8)
1203	11.15985(13)	1159	11.14599(10)	1188	11.13038(9)
1285	11.17335(3)	1247	11.16312(9)	1262	11.14381(9)
1392	11.19174(9)	1309	11.17923(3)	1363	11.16306(8)
1483	11.20809(5)	1396	11.19318(9)	1438	11.17932(3)
1544	11.22094(5)	1435	11.1975(7)	1492	11.18668(4)
		1443	11.19825(13)		

Table 19 (continued). Lattice parameters (a) of single-phase structures in LCPN HELOs corresponding to temperature (T)

LCPNTm		LCPNYb		LCPNLu	
T (°C)	a (Å)	T (°C)	a (Å)	T (°C)	a (Å)
26	10.97293(5)	26	10.96719(7)	26	10.96756(3)
618	11.02349(4)	643	11.02739(7)	646	11.01609(8)
769	11.04938(8)	789	11.05278(1)	736	11.03339(6)
891	11.07115(5)	904	11.07238(9)	868	11.05599(8)
999	11.09095(13)	1002	11.09009(11)	965	11.07232(9)
1084	11.10614(9)	1090	11.10513(12)	1073	11.08745(4)
1140	11.11461(11)	1155	11.11641(14)	1173	11.10405(4)
1199	11.12406(11)	1256	11.13583(11)	1282	11.12079(6)
1272	11.13553(9)	1306	11.14630(4)	1368	11.13852(1)
1427	11.16105(9)	1386	11.17242(3)	1448	11.17641(13)
1583	11.19718(11)				

Table 20. Coefficient of the second-order polynomial fitting curves ( $y = a + bT + cT^2$ ) in LCPN HELOs

	a	b	c	R <sup>2</sup>
LCPNSm	11.03594	1.10711 X 10 <sup>-4</sup>	2.47452 X 10 <sup>-8</sup>	99.79%
LCPNGd	11.02052	7.64532 X 10 <sup>-5</sup>	5.62781 X 10 <sup>-8</sup>	99.89%
LCPNTb_Fluorite	10.9547	-1.21837 X 10 <sup>-7</sup>	2.05959 X 10 <sup>-7</sup>	100.00%
LCPNTb_cI88	10.86219	2.93666 X 10 <sup>-4</sup>	-3.45485 X 10 <sup>-8</sup>	99.73%
LCPNDy	10.99679	8.13642 X 10 <sup>-5</sup>	4.25268 X 10 <sup>-8</sup>	99.58%
LCPNY	10.9822	8.57691 X 10 <sup>-5</sup>	4.66015 X 10 <sup>-8</sup>	99.70%
LCPNEr	10.97573	7.24084 X 10 <sup>-5</sup>	4.76468 X 10 <sup>-8</sup>	99.91%
LCPNTm	10.96852	7.4559 X 10 <sup>-5</sup>	4.45332 X 10 <sup>-8</sup>	99.63%
LCPNYb	10.96546	6.00586 X 10 <sup>-5</sup>	6.20912 X 10 <sup>-8</sup>	99.83%
LCPNLu	10.96654	3.95866 X 10 <sup>-5</sup>	6.74843 X 10 <sup>-8</sup>	99.10%

The evolution of CTE in LCPN system, except for LCPNTb, is plotted in Figure 72. All of them indicated positive thermal expansion behavior. The CTE values as a function of temperature were calculated using Equation {9}. The detailed CTE equations are listed in Table 21. There was

no significant correlation in thermal expansion properties among the designed candidate materials. In LCPNTb, the gradients of the CTEs significantly changed with the structural transformation from fluorite to D-type tilted fluorite (Figure 73). Below 600°C, the CTEs increased with increasing temperatures in the CeO<sub>2</sub>-type fluorite structures. However, after the structure become a tilted fluorite structure (with Pearson symbol cI88), the CTE trends had a negative slope up to around 1550°C. This outcome confirmed that the phase transformations involved in LCPNTb affected its behavior with regard to thermal expansion. The CTE data reported in this research will be helpful for further research on these HELO samples and future materials design.

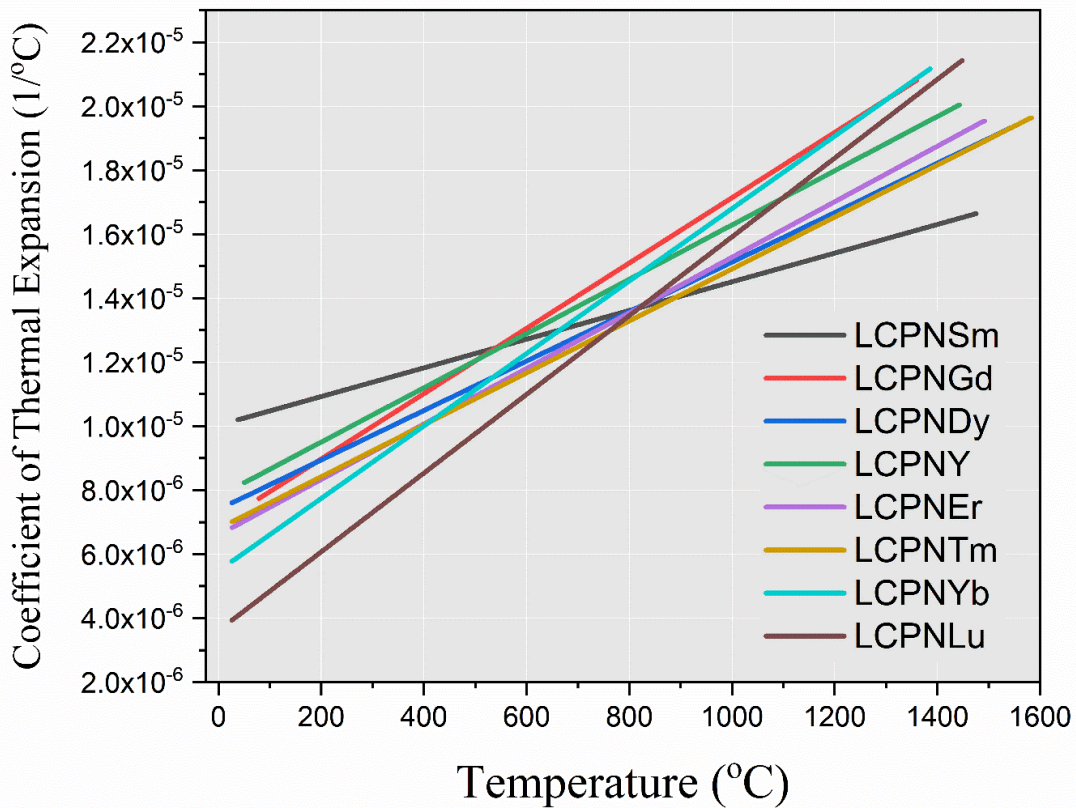


Figure 72. The evolution of the coefficients of thermal expansion among the LCPN system (except for LCPNTb). All candidates exhibited positive thermal expansions in their cubic structures.

Table 21. The detailed equations for the coefficients of thermal expansion ( $y = a + bT$ ) in LCPN HELOs

	a	b
LCPNSm	$1.00272348 \times 10^{-3}$	$4.48240789 \times 10^{-7}$
LCPNGd	$6.93283278 \times 10^{-4}$	$1.02066795 \times 10^{-8}$
LCPNTb_Fluorite	$-1.1121753 \times 10^{-3}$	$3.76014689 \times 10^{-8}$
LCPNTb_cI88	$2.68069688 \times 10^{-6}$	$-6.3074415 \times 10^{-7}$
LCPNDy	$7.39509346 \times 10^{-3}$	$7.73041855 \times 10^{-7}$
LCPNY	$7.80494619 \times 10^{-4}$	$8.48142745 \times 10^{-7}$
LCPNEr	$6.59550902 \times 10^{-4}$	$8.68006748 \times 10^{-7}$
LCPNTm	$6.79476898 \times 10^{-4}$	$8.11686868 \times 10^{-7}$
LCPNYb	$5.47620676 \times 10^{-4}$	$1.13230828 \times 10^{-8}$
LCPNLu	$3.60942634 \times 10^{-4}$	$1.23061647 \times 10^{-8}$

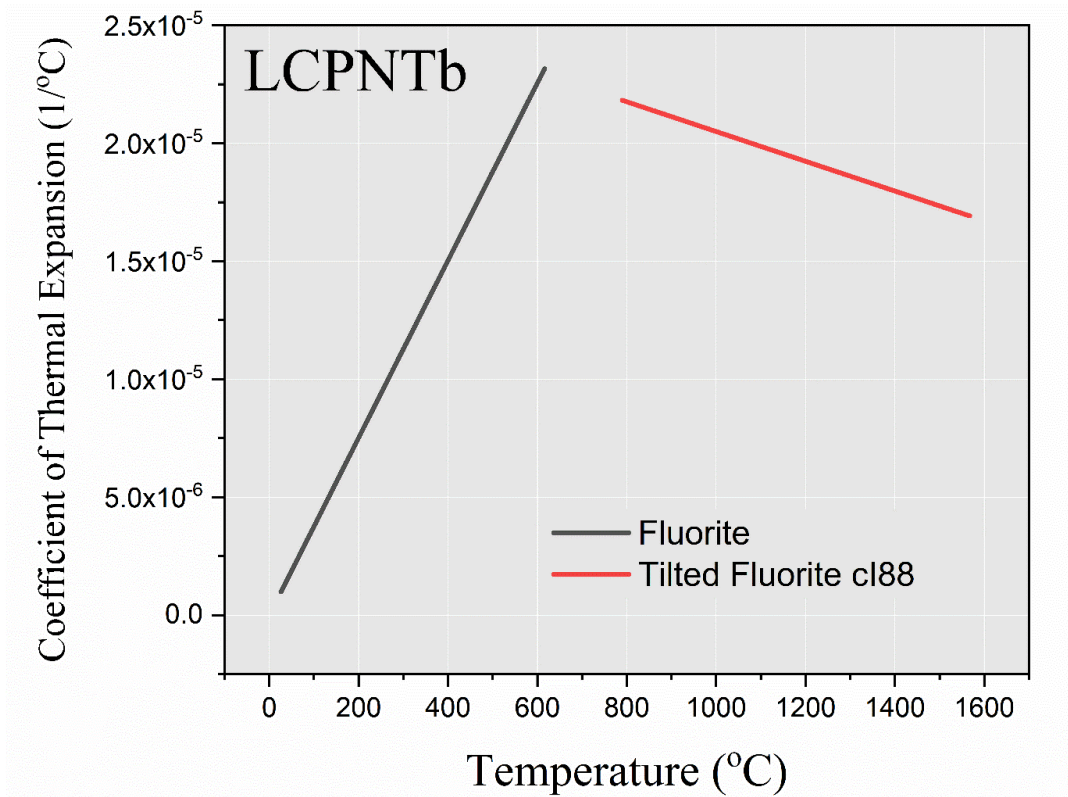


Figure 73. The evolution of thermal expansion coefficients in LCPNTb. The tendency changed after the phase transformation from the F-type fluorite structure to the D-type tilted fluorite structure.



## CHAPTER 7: KEY PARAMETERS OF THE SINGLE-PHASE HIGH-ENTROPY LANTHANIDE OXIDES

Size mismatch and valence configurations were the key parameters in designing our candidate materials. In this chapter, the effect of these two factors are introduced. Furthermore, additional HELO samples were synthesized and analyzed for stability research. These parameters were found to have a critical influence on single-phase formation and structural stability from room temperature to 2000°C.

### 7.1. Size Mismatch ( $\delta$ ) of Constituent Lanthanide Cations

In this research, 20 samples, containing equimolar cations, were designed having different size mismatches ( $\delta$ ) and valence configurations. According to XRD analyses, 18 of the 20 samples became single-phase HELOs under ambient conditions. The size mismatches of all the designed samples are listed in Table 22. In the LYTE system, initially, all cations were considered to be in the trivalent states in a C-type bixbyite structure. In this case, the size mismatch increased as the larger fifth cation was added to the system, from the smallest cation yttrium to the largest cation lanthanum. However, after analyzing the relationship between  $\delta$  values and the lattice parameters of the crystal structure (shown in Figure 33), it is seen that cerium and praseodymium cations have a preference for the tetravalent state, instead of the trivalent state. In the ceramic field, the radius of a cation depends on its oxidation state and coordination number. The value of  $\delta$  significantly decreased after the modified calculation was applied to LYTECe and LYTEPr candidate materials. Despite the fact that these two samples had lower  $\delta$  values from the initially designed composition, the LCPNLa sample provided an example of failure to form single-phase HELO. The coexistence of perovskite and C-type structures in the LYTELa sample provided the evidence that secondary

phase(s) could exist in a solid solution as the cation size mismatch reached 7.0273. This system demonstrated the tolerance of larger cations being merged in a HELO structure. In contrast, the LCPN system provided the example for adding a smaller cation into a system that could be up to  $\delta=5.8124$ . All the designed candidates turned out to form single-phase solid solutions after air-cooling to room temperature.

Table 22. Configurational entropy and size mismatches ( $\delta$ ) of synthesized candidates

Chemistry	Abbreviation	Structure	$\Delta S_{conf}/R$	$\delta \times 100$
(Gd <sub>0.4</sub> Tb <sub>0.4</sub> Dy <sub>0.4</sub> Ho <sub>0.4</sub> Er <sub>0.4</sub> )O <sub>3</sub>	GTDHEO	Bixbyite cI80	0.644	1.8324
(Lu <sub>0.5</sub> Yb <sub>0.5</sub> Tm <sub>0.5</sub> Er <sub>0.5</sub> )O <sub>3</sub>	LYTEO		0.555	1.2714
(Lu <sub>0.4</sub> Yb <sub>0.4</sub> Tm <sub>0.4</sub> Er <sub>0.4</sub> Y <sub>0.4</sub> )O <sub>3</sub>	LYTEY			1.6113
(Lu <sub>0.4</sub> Yb <sub>0.4</sub> Tm <sub>0.4</sub> Er <sub>0.4</sub> Dy <sub>0.4</sub> )O <sub>3</sub>	LYTEDy			2.0308
(Lu <sub>0.4</sub> Yb <sub>0.4</sub> Tm <sub>0.4</sub> Er <sub>0.4</sub> Tb <sub>0.4</sub> )O <sub>3</sub>	LYTETb			2.4551
(Lu <sub>0.4</sub> Yb <sub>0.4</sub> Tm <sub>0.4</sub> Er <sub>0.4</sub> Gd <sub>0.4</sub> )O <sub>3</sub>	LYTEGd			3.0635
(Lu <sub>0.4</sub> Yb <sub>0.4</sub> Tm <sub>0.4</sub> Er <sub>0.4</sub> Sm <sub>0.4</sub> )O <sub>3</sub>	LYTESm	Bixbyite cI80	0.644	3.8988
(Lu <sub>0.4</sub> Yb <sub>0.4</sub> Tm <sub>0.4</sub> Er <sub>0.4</sub> Nd <sub>0.4</sub> )O <sub>3</sub>	LYTEND			4.9563
(Lu <sub>0.4</sub> Yb <sub>0.4</sub> Tm <sub>0.4</sub> Er <sub>0.4</sub> Pr <sub>0.4</sub> )O <sub>3</sub>	LYTEPr			5.2530
				3.9831*
(Lu <sub>0.4</sub> Yb <sub>0.4</sub> Tm <sub>0.4</sub> Er <sub>0.4</sub> Ce <sub>0.4</sub> )O <sub>3</sub>	LYTECe			6.0997
				4.4056*
(Lu, Yb, Tm, Er, La)O <sub>x</sub>	LYTELa	Bixbyite cI80	<0.64	7.0273 <sup>#</sup>
		Perovskite		NA
(La <sub>0.5</sub> Ce <sub>0.5</sub> Pr <sub>0.5</sub> Nd <sub>0.5</sub> )O <sub>3.5</sub>	LCPNO		0.504	2.8029
(La <sub>0.4</sub> Ce <sub>0.4</sub> Pr <sub>0.4</sub> Nd <sub>0.4</sub> Sm <sub>0.4</sub> )O <sub>3.5</sub>	LCPNSm	Bixbyite cI88	0.585	2.7723
(La <sub>0.4</sub> Ce <sub>0.4</sub> Pr <sub>0.4</sub> Nd <sub>0.4</sub> Gd <sub>0.4</sub> )O <sub>3.5</sub>	LCPNGd			3.2118
(La <sub>0.4</sub> Ce <sub>0.4</sub> Pr <sub>0.4</sub> Nd <sub>0.4</sub> Tb <sub>0.4</sub> )O <sub>4</sub>	LCPNTb	Fluorite	0.536	5.0952
(La <sub>0.4</sub> Ce <sub>0.4</sub> Pr <sub>0.4</sub> Nd <sub>0.4</sub> Dy <sub>0.4</sub> )O <sub>3.5</sub>	LCPNDy			3.9783
(La <sub>0.4</sub> Ce <sub>0.4</sub> Pr <sub>0.4</sub> Nd <sub>0.4</sub> Y <sub>0.4</sub> )O <sub>3.5</sub>	LCPNY			4.3803
(La <sub>0.4</sub> Ce <sub>0.4</sub> Pr <sub>0.4</sub> Nd <sub>0.4</sub> Er <sub>0.4</sub> )O <sub>3.5</sub>	LCPNER			4.7317
(La <sub>0.4</sub> Ce <sub>0.4</sub> Pr <sub>0.4</sub> Nd <sub>0.4</sub> Tm <sub>0.4</sub> )O <sub>3.5</sub>	LCPNTm	Bixbyite cI88	0.585	5.0952
(La <sub>0.4</sub> Ce <sub>0.4</sub> Pr <sub>0.4</sub> Nd <sub>0.4</sub> Yb <sub>0.4</sub> )O <sub>3.5</sub>	LCPNYb			5.5446
(La <sub>0.4</sub> Ce <sub>0.4</sub> Pr <sub>0.4</sub> Nd <sub>0.4</sub> Lu <sub>0.4</sub> )O <sub>3.5</sub>	LCPNLu			5.8124
(La, Ce, Pr, Nd, Ag)O <sub>x</sub>	LCPNAg	-	<0.58	14.42727 <sup>#</sup>

\*Ce and Pr were in tetravalent states and in 8-fold coordination

<sup>#</sup>Calculated for candidates in a single-phase HELO bixbyite (cI80 or cI88) structure

R: gas constant 8.314 J/mol·K

Figure 74 summarizes all the reported HEOs (listed in Table 1), and the candidate materials synthesized in this research (Table 22), as a function of configurational entropy and size mismatch

( $\delta$ ). First of all, in the HEOs system, the contribution from configurational entropy is not significant compared to the atomic arrangements in HEAs. So far, successfully synthesized HEOs existed in a  $\delta$  range up to about 7. An exception was the HEOs in the yttria stabilized zirconia prototype. In this special doped structure, the  $ZrO_2$  high-temperature phase transformation behaviors could be constrained via doping with the large yttrium cation ( $Y_{VI}^{3+}$  at the zirconium cation ( $Zr_{VII}^{4+}$ , 0.78Å) polyhedral sites. According to the Kröger-Vink equation, each oxygen vacancy was created by two aliovalent dopants. This doping mechanism could either achieve charge balance or create space for larger cations. In the HEOs study, most of the literature references only reported the HEOs, which were successfully synthesized. As a result, only two candidates which failed in HELO formation were included, denoted by a blue “X” in Figure 74. In the situation when they were homogeneously mixing in a single crystal, they both exceeded the value of 7.0 in size mismatch. In conclusion, in a binary oxide prototype, the difference in cation radii among multi-components has a critical effect on the formation of single-phase HEOs.

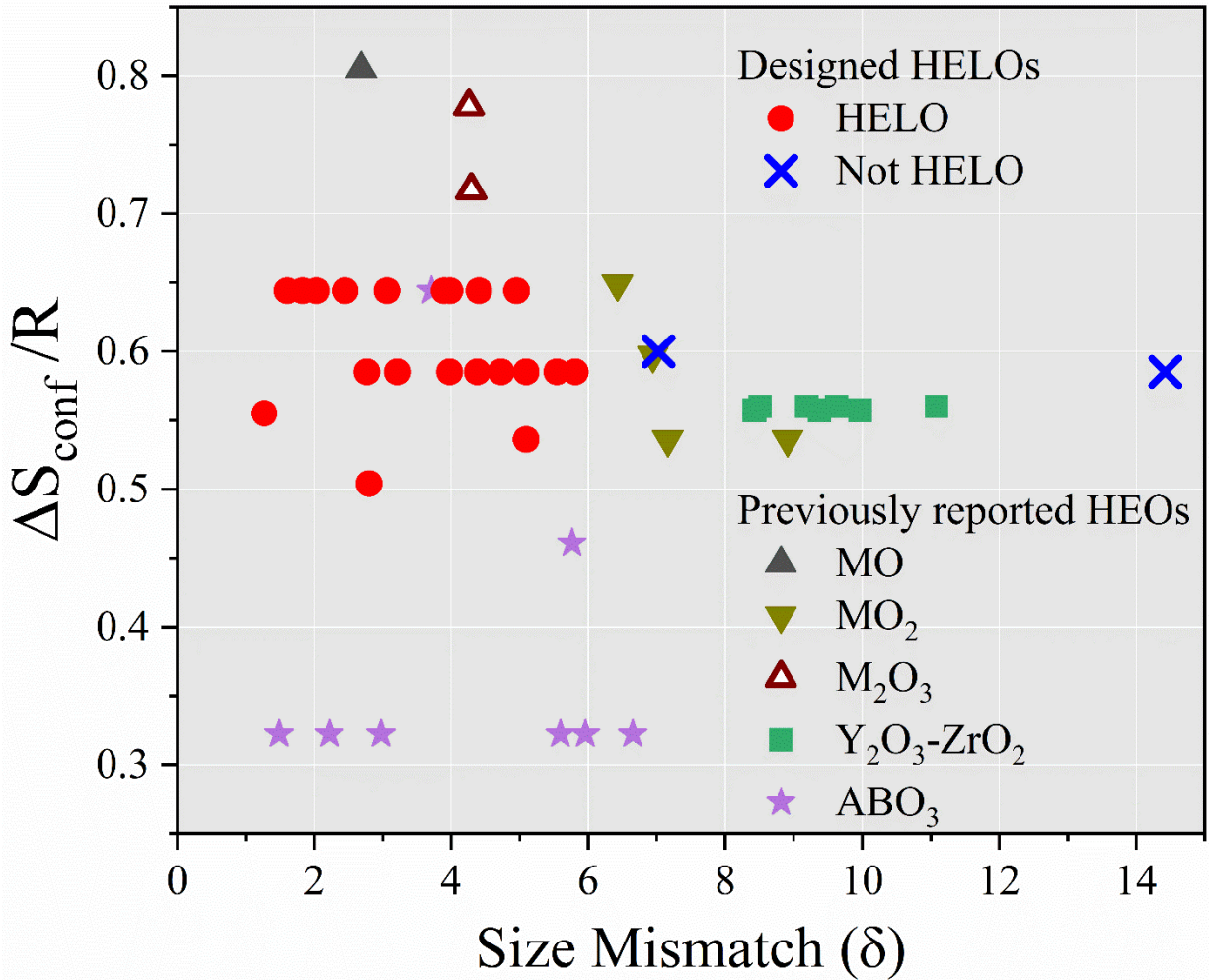


Figure 74. Summary of high-entropy oxides (HEOs) as a function of configurational entropy and size mismatch ( $\delta$ ). In this research, most of the designed high-entropy lanthanide oxides became a single-phase solid solution (red circle), while two of them formed secondary phases (blue “X” cross). The contribution from configurational entropy was not significant, due to the cation-anion arrangements in ceramics. For most of the single-phase HEOs, the threshold of  $\delta$  was determined to be around 7.0. R: gas constant 8.314 J/mol·K

In the LYTE system, all designed candidates became single-phase HELOs, except for LYTELa. The  $\text{LaTmO}_3$ -like perovskite structure was found in this sample as a secondary phase. An attempt was made to alter the composition in lanthanum, which could lower both the configurational entropy and change the value of size mismatch. In these  $(\text{LuYbTmEr})_{1-x}\text{La}_x\text{O}_y$

compositions, lanthanum lay in a range  $x=0.059$  to  $0.5$ , which covered the larger and smaller ranges of the equimolar mixing condition ( $x=0.2$ ). The XRD results are presented in Figure 75. Obviously, the amount of perovskite structure was dominated by the composition of lanthanum in the sample. When the lanthanum reached 50% among all of the constituent cations, the  $\text{La}_2\text{O}_3$  hexagonal phase, within  $P\bar{3}m1$  space group, existed in the sample. This hexagonal structure was naturally stable for a binary lanthanum oxide under ambient conditions. When a small amount of lanthanum was present (6% among cations) in the system, the highest peaks from the perovskite structure were still observable in the diffraction pattern. In conclusion, the difference in cation size mismatch had a significant effect on the formation of single-phase HEOs. Altering the composition of extraordinary cations might decrease the value of the size mismatch, but it had limited contribution to eliminating secondary phase(s).

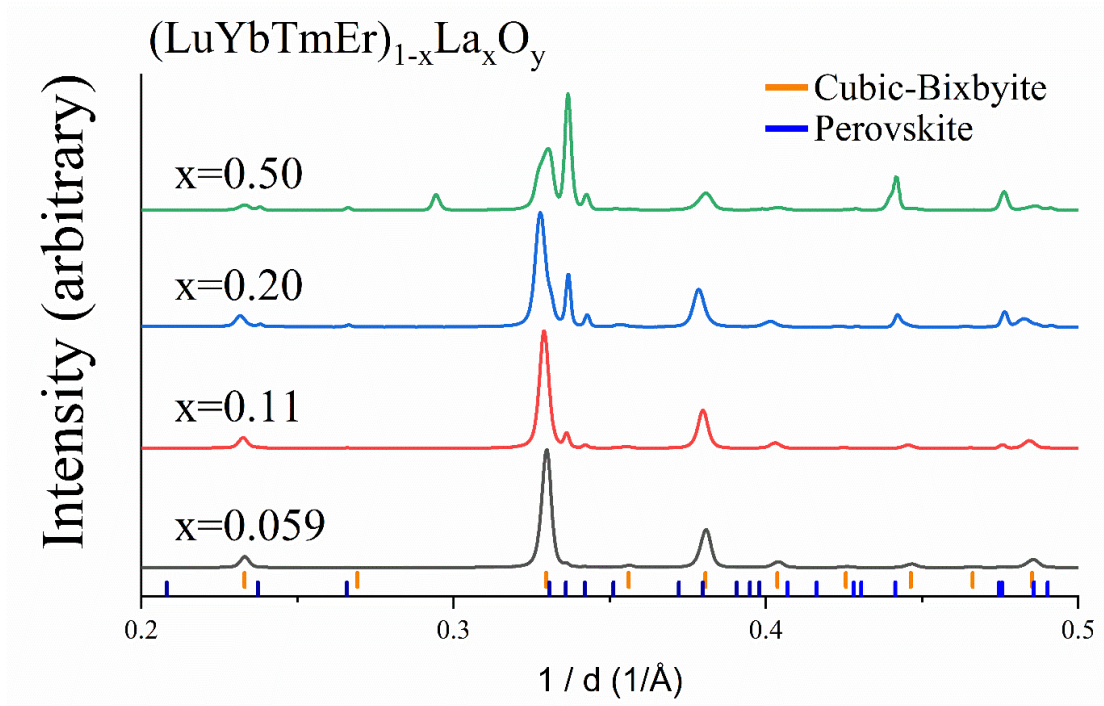


Figure 75. XRD patterns obtained from different levels of lanthanum contained in the LYTELa candidates. The amount of secondary phase(s) was dominated by the lanthanum content.

## 7.2. Valence Configurations and High-Temperature Stability

All the HELO candidates exhibited cubic structures after the crystallization processes. Three different cubic structures were observed in the LCPN and LYTE systems. By comparing the prototype structures, the constituent cations had different combinations of valence states. The C-type cubic-bixbyite structure ( $M_2O_3$ , Pearson symbol cI80) is the common structure for middle and heavy binary lanthanide sesquioxides ( $Sm_2O_3$ - $Lu_2O_3$ ). In this structure, all cations are in the trivalent states. This phase was found in the LYTE system, where the constituent cations were dominated by cations in their trivalent states. On the other hand, the D-type tilted fluorite structure, the so-called bixbyite structure ( $M_2O_{3.5}$ , Pearson symbol cI88), was found in most of the LCPN candidate materials. This structure was derived from the  $CeNdO_{3.5}$  prototype, with both trivalent and tetravalent cations present in the crystal structure. In the LCPN system, at least 40 mol% of

cations (Ce, Pr) had a preference for tetravalent configurations. These outcomes agreed with the initial design of the two systems. In the LCPNTb sample, the structure behaved as fluorite structure ( $\text{MO}_2$ ), with 60 mol% tetravalence-preferred cations present. As a result, the crystal structures of HEOs could possibly be modified through the preferred valence states of its constituent cations. The compositions of tetravalent cations presented in HELO candidates are organized in Table 23.



Table 23. The molecular composition (mol %) of tetravalent cations (Bold, Red) among constituent cations

	Gd	Tb	Dy	Ho	Er	Total M <sup>4+</sup>
GTDHEO	20%	<b>20%</b>	20%	20%	20%	20%
	Lu	Yb	Tm	Er	Ln <sup>II</sup>	
LYTEY	20%	20%	20%	20%	20%	0%
LYTEDy	20%	20%	20%	20%	20%	0%
LYTETb	20%	20%	20%	20%	<b>20%</b>	20%
LYTEGd	20%	20%	20%	20%	20%	0%
LYTESm	20%	20%	20%	20%	20%	0%
LYTENd	20%	20%	20%	20%	20%	0%
LYTEPr	20%	20%	20%	20%	<b>20%</b>	20%
LYTECe	20%	20%	20%	20%	<b>20%</b>	20%
	La	Ce	Pr	Nd	Ln <sup>II</sup>	
LCPNSm	20%	<b>20%</b>	<b>20%</b>	20%	20%	40%
LCPNGd	20%	<b>20%</b>	<b>20%</b>	20%	20%	40%
LCPNTb	20%	<b>20%</b>	<b>20%</b>	20%	<b>20%</b>	60%
LCPNDy	20%	<b>20%</b>	<b>20%</b>	20%	20%	40%
LCPNY	20%	<b>20%</b>	<b>20%</b>	20%	20%	40%
LCPNEr	20%	<b>20%</b>	<b>20%</b>	20%	20%	40%
LCPNTm	20%	<b>20%</b>	<b>20%</b>	20%	20%	40%
LCPNYb	20%	<b>20%</b>	<b>20%</b>	20%	20%	40%
LCPNLu	20%	<b>20%</b>	<b>20%</b>	20%	20%	40%
(LCPN) <sub>1-x</sub> Tb <sub>x</sub> O <sub>y</sub>						
X = 0.059	23.53%	<b>23.53%</b>	<b>23.53%</b>	23.53%	<b>5.88%</b>	52.94%
0.11	22.22%	<b>22.22%</b>	<b>22.22%</b>	22.22%	<b>11.11%</b>	55.56%
0.5	12.50%	<b>12.50%</b>	<b>12.50%</b>	12.50%	<b>50%</b>	75%

In order to study the final HELO structures affected by the number of preferred valence states of constituent cations, different levels of terbium were added to the LCPNTb sample, with other cations balanced in equimolar ratios. LCPNTb was the only sample exhibiting the fluorite phase, instead of the tilted fluorite structure found in other LCPN candidates. In the LCPN system, there were at least 40 mol% cations inherently stable in tetravalent states. Inclusion of terbium into the

LCPN sample did increase the overall preference for the tetravalent configuration. In the LCPNTb sample containing equimolar mixing of cations, a total of 60 mol% (40%+20%) tetravalent cations was found in the powder. In Figure 76, the intensity of XRD peaks was plotted on a log scale for better differentiation between fluorite and tilted fluorite phases. The fluorite structure corresponded to the range of constituent tetravalent cations from 56 mol% to 75 mol% (11 mol%-50 mol% Tb). However, the structure became the D-type tilted fluorite phase as the level of tetravalent cations decreased to 53 mol%. In Table 23, it is seen that only 6 mol% of tetravalent cations were contributed by the terbium. The results provided evidence that the final structures of HELO samples could be modified by the valence configurations of the intrinsic cations.

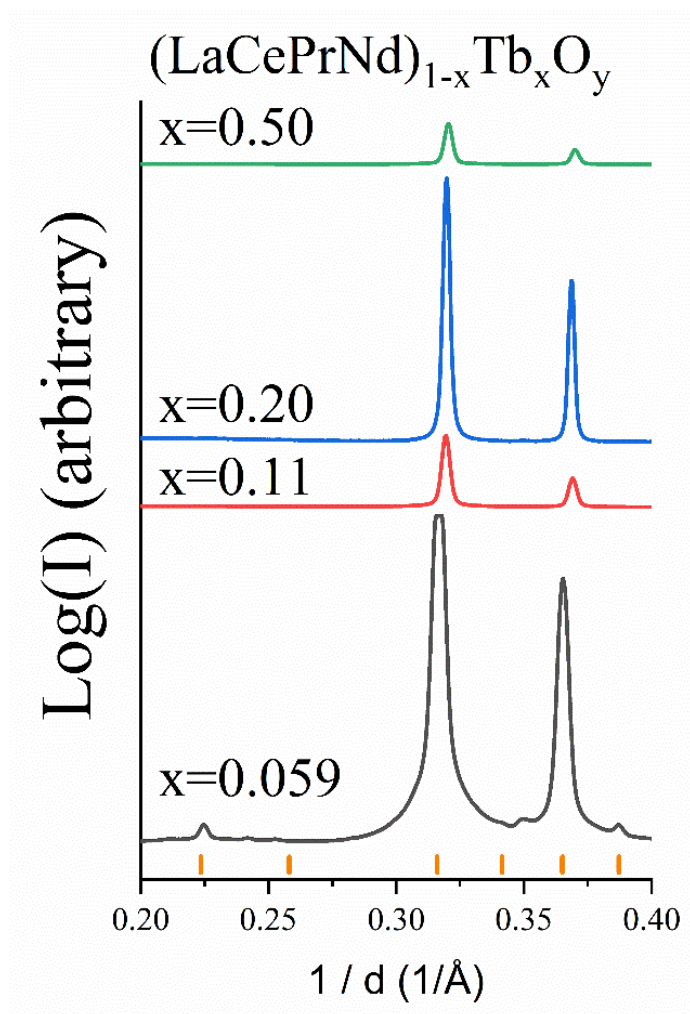


Figure 76. XRD patterns obtained from LCPNTb candidate materials having varying terbium compositions. The structure remained fluorite within the composition of 11 mol% terbium involved in the cations. The bixbyite structure showed up with a further decrease ( $x=0.059$ ) of terbium cations. The diffraction intensity was expressed as a log scale for better differentiation between these two structures.

By including all the HELOs synthesized in this research, the relationships between the final crystal structure and valence configurations of constituent cations are plotted in Figure 77. The structure changed from cubic-bixbyite, as found in LYTE candidates, to a tilted fluorite structure, in most of the candidate materials in the LCPN samples. In the LYTE system, the maximum

possible content of tetravalent cations was 20 mol%, under the circumstances when the fifth cations (Ce, Pr, Tb) preferring tetravalent states were added. The crystal structure became tilted fluorite and fluorite as the levels of tetravalent cations reached 40 mol% and 60 mol %, respectively. In the previous experiments containing various amounts of terbium concentration in the LCPNTb sample, the result provided evidence that the final HELOs could be modified by the composition of constituent cations having different valence preferences. Those results lead to the conclusion that the crystal structures of HELOs can be adjusted by the competition between cations with trivalent and tetravalent configurations.

Moreover, as the relative ratio of oxidation states in crystal structure is varied, the resulting high-temperature behavior could also be affected. In the LYTE system, the candidates remained stable in the C-type bixbyite structure from room-temperature up to 2000°C. However, with the amount of non-trivalent cations reached 40 mol% (the LCPN system), multiple phase transformations became involved during heat treatments. As temperature increased, a portion of the constituent cations became thermodynamically unstable and precipitated out from the high-entropy arrangements. These results demonstrate that the structural stability could be lowered with a higher level of mixture between cations having different preferences in oxidation states. Even so, addition research into high-temperature HEOs is required in order to clarify the relationship between mixed valence states of constituent cations and the occurrence of high-temperature phase transformations. Based on this concept, the choice of cations having the same valence state will ensure structural stability at high temperatures in refractory applications.

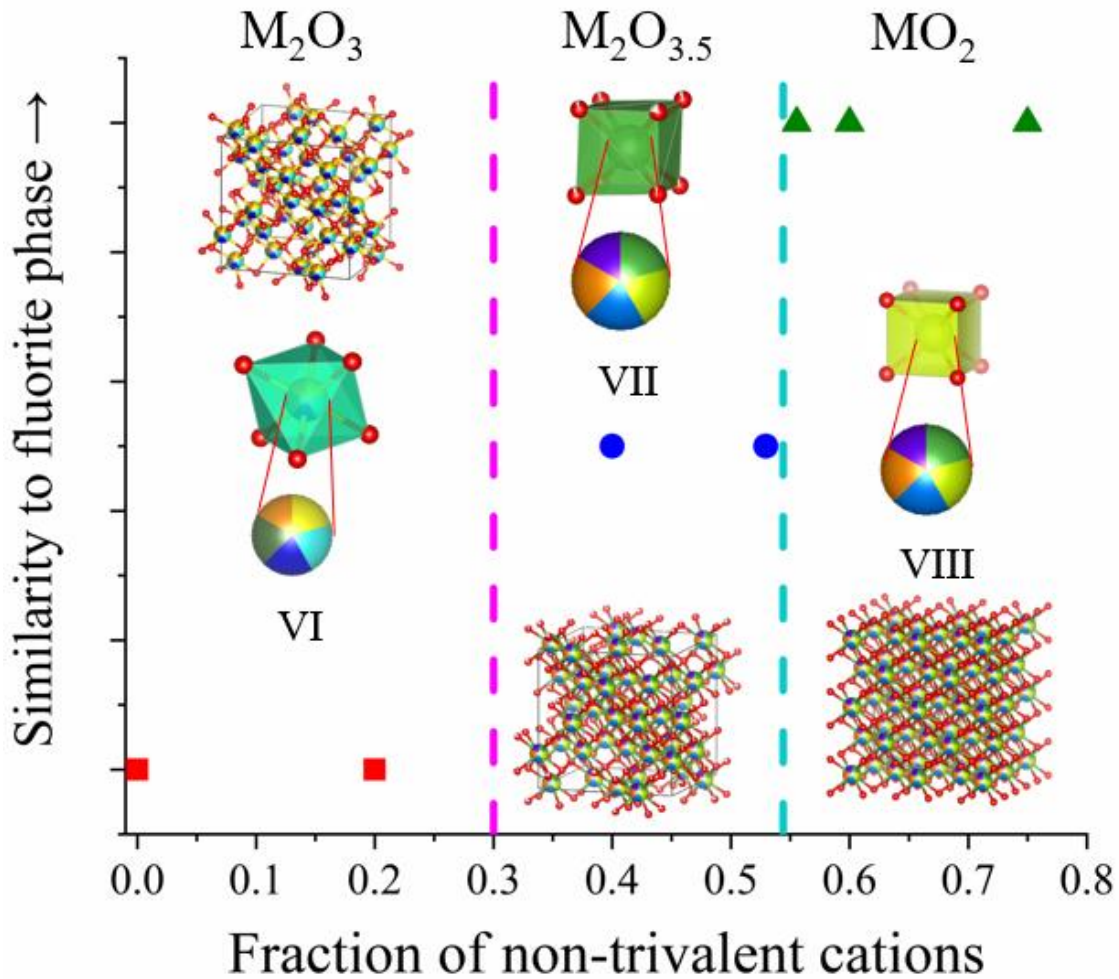


Figure 77. The relationship between the valence states and the final crystal structures. In the LYTE system, the maximum non-trivalent cations came from one constituent cation (20 mol%). As the non-trivalent cation (Ce, Pr, Tb) content in HELOs increases, the structure can be modified from C-type bixbyite ( $M_2O_3$ ), tilted fluorite ( $M_2O_{3.5}$ ) to fluorite ( $MO_2$ ) structures.

### 7.3. Mixing Enthalpy and Mixing Entropy

According to the “high-entropy effect” in high-entropy materials, a single-phase solid solution is stabilized by a large value of configurational mixing entropy. In Sections 3.1 and 7.1, the values of configurational mixing entropy in high-entropy oxides have been calculated. Compared to the high-entropy alloys containing five equimolar components ( $\Delta S_{conf} = 1.61R$ ), the values of configurational mixing entropy in up-to-date synthesized HEOs are relatively small

( $\Delta S_{conf} \leq 0.80R$ ). In this case, whether the single-phase HEOs is stabilized by configurational mixing entropy should be re-evaluated. Three circumstances are involved in the competition between mixing entropy and mixing enthalpy. If the value of mixing enthalpy is negative in an HEO system, the free energy of mixing naturally becomes negative. Under the situation when an HEO has a positive value in mixing enthalpy, the combination of configurational mixing entropy and temperature could possibly lead to lower the free energy of mixing in single-phase formation. However, the single-phase HEO formation might not be accessible when an extremely high formation temperature is required, such as 3000°C. By considering such situations, the HEOs could be stabilized by mixing entropy when the enthalpy value is positive, and the formation temperature is accessible.

The values of configurational mixing entropy in the reported HEOs are listed in Table 1 and Table 22, calculated through Equation {5}. On the other hand, in order to calculate the mixing enthalpy, building a crystal structure with randomly distributed constituent cations is required. In high-entropy oxides, multiple unit cells should be required to mimic a structure with a homogeneous cation arrangement. In this case, density functional theory might not be an ideal method for covering the whole range of a structure.

As an example, Anand et al. [176] evaluated the competition between mixing enthalpy and mixing entropy in the high-entropy oxide,  $(Mg_{0.2}Co_{0.2}Ni_{0.2}Cu_{0.2}Zn_{0.2})O$ , as well as other HEOs with similar compositions. Using the genetic algorithm strategy, multiple microstates containing 1,000 cations and 1,000 oxygen anions were constructed. An order parameter was used to examine the potential segregation of the cations in each microstate. From different chemistry stoichiometries, the total number of configurations successfully generated from their constituent cations were different. For example, the total number of configurations decreased from 23,536 to 351 by replacing magnesium with calcium in the  $(Mg_{0.2}Co_{0.2}Ni_{0.2}Cu_{0.2}Zn_{0.2})O$  composition. In

other words, only 351 microstates were successfully constructed without cation segregation in  $(\text{Ca}_{0.2}\text{Co}_{0.2}\text{Ni}_{0.2}\text{Cu}_{0.2}\text{Zn}_{0.2})\text{O}$ . By taking the average value of all the microstates, the statistical mixing enthalpy in a high-entropy oxide could thus be obtained.

However, there are obstacles to calculating the mixing enthalpy in the LYTE and LCPN systems using the genetic algorithm strategy. First, the crystal structures having enormous oxygen vacancies could collapse in the relaxation process. Moreover, the lattice parameters of the unit cells obtained from X-ray diffraction (listed in Table 11 and Table 12) are more than twice that of the rocksalt structure ( $a=4.2\text{\AA}$ ). The size of a microstate needs to increase significantly to resemble a structure with a homogeneous cation arrangement. In the rocksalt sample, a microstate containing 1000 cations and 1000 anions can represent 200 unit cells. On the other hand, the same size of a microstate can accommodate only 31 unit cells in C-type cubic bixbyite structure. The microstate size has a critical effect on the total number of configurations in a high-entropy oxide. To construct a structure of a high-entropy oxide through the genetic algorithm strategy, a larger number of configurations is preferred to acquire a reliable value of the mixing enthalpy. In this research, due to the lack of computational resources, the quantitative values of mixing enthalpy among our candidates were not calculated.

Despite the fact that calculating the mixing enthalpy of a high-entropy oxide is challenging, two factors can be applied to qualitatively compare the mixing enthalpy among our candidates. First, the mixing entropy of a high-entropy oxide could increase when any constituent mono-cation oxide exhibits different crystal structures to the high-entropy oxide. In the LYTE HEOs, the C-type bixbyite structure is naturally stable in the base mono-cation oxide ( $\text{Er}_2\text{O}_3\text{-Lu}_2\text{O}_3$ ). For lanthanide cations having a different sesquioxide structure ( $\text{La}_2\text{O}_3\text{-Nd}_2\text{O}_3$ ) or preferred valence states (Ce, Pr, and Tb), the transformation from their naturally stable structure to the high-entropy oxide could cause a penalty in mixing enthalpy. The influence of the enthalpy penalty could

possibly overcome the entropy contribution. In the previous study on  $(\text{Mg}_{0.2}\text{Co}_{0.2}\text{Ni}_{0.2}\text{Cu}_{0.2}\text{Zn}_{0.2})\text{O}$ , copper and zinc are not naturally stable in a rocksalt structure.[176] The simulation results presented that the formation temperature would decrease in a four-component system by removing either copper or zinc. The configurational entropy decreases as the number of components decrease from five to four. Normally, higher formation temperatures would be required if the changes in mixing enthalpy could be neglected. However, in this case, the contribution of enthalpy by removing either copper or zinc, which are not naturally stable in the rocksalt structure, overcomes the influence of mixing entropy, leading to lowering the formation temperature. In LCPN HEOs, the final crystal structures exist either in tilted fluorite or fluorite structures, which are not the naturally stable phases of constituent mono-cation oxides. The base cations ( $\text{La}_2\text{O}_3$ - $\text{Nd}_2\text{O}_3$ ) are stable in the A-type hexagonal structure as sesquioxides. Cerium and praseodymium prefer to exist in a tetravalent state than in a trivalent state. By comparing the enthalpy between LYTE and LCPN system, we can expect that the average mixing enthalpy in the LCPN system is higher than that in the LYTE system. Furthermore, as the temperature increases, the constituent mono-cation oxides could experience structural transformations, which changes the enthalpy. The formation enthalpy, transition enthalpy, and standard entropy values are listed in Table 24. These two factors, (1) structural difference between final HEO and room-temperature stable phase of constituent mono-cation oxides, and (2) possible high-temperature structural transformations, would increase mixing enthalpy in a HEO sample.



Table 24. Formation enthalpy ( $\Delta H_{f(298K)}^o$ , kJ/mol), transition enthalpy ( $\Delta H_{trs}^o$ , kJ/mol), and standard entropy (J/mol·K) in mono-cation lanthanide oxides [62]

Oxides	$\Delta H_{f(298K)}^o$	$\Delta H_{trs}^o$ (→B Type)	$\Delta H_{trs}^o$ (→A Type)	$\Delta H_{trs}^o$ (→H Type)	$\Delta S_{(298K)}^o$
La <sub>2</sub> O <sub>3</sub>	-1791.6 ± 5			23±5	127.3 ± 0.84
CeO <sub>2</sub>	-1090.4 ± 1				69.3 ± 0.07
Ce <sub>2</sub> O <sub>3</sub>	-1799.8 ± 1.8			28±8	148.1 ± 0.4
Pr <sub>6</sub> O <sub>11</sub>	-944.6 ± 2.5				79.2 ± 2.0
Pr <sub>2</sub> O <sub>3</sub>	-1809.9 ± 3			28±8	152.7 ± 0.3
Nd <sub>2</sub> O <sub>3</sub>	-1806.9 ± 3			29±8	158.7 ± 1.0
Sm <sub>2</sub> O <sub>3</sub>	-1826.8 ± 4.8	6±3	7±3	32±8	150.6 ± 0.3
Gd <sub>2</sub> O <sub>3</sub>	-1819.7 ± 3.6	9±2	6.3±3.3	34.7±3.3	150.6 ± 0.2
Tb <sub>7</sub> O <sub>12</sub>	-963.8 ± 5				
Tb <sub>11</sub> O <sub>20</sub>	-957.8 ± 5				
Tb <sub>2</sub> O <sub>3</sub>	-1865.2 ± 6	12±4		55±8	159.2 ± 3.0
Dy <sub>2</sub> O <sub>3</sub>	-1863.4 ± 5	14±5		55±8	149.8 ± 0.15
Ho <sub>2</sub> O <sub>3</sub>	-1883.3 ± 8.2	16±5		57±8	156.4 ± 0.15
Er <sub>2</sub> O <sub>3</sub>	-1900.1 ± 6.5			25±5	153.1 ± 0.15
Tm <sub>2</sub> O <sub>3</sub>	-1889.3 ± 5.7			26±5	139.7 ± 0.4
Yb <sub>2</sub> O <sub>3</sub>	-1814.5 ± 6			27±5	133.1 ± 0.3
Lu <sub>2</sub> O <sub>3</sub>	-1877.0 ± 7.7				110.0 ± 0.13

The detailed structural information and transformation temperatures were introduced in Section 2.4.

The second factor that could possibly increase mixing enthalpy is due to the size mismatch among constituent cations. According to the simulation results, the formation temperature increases from 476°C to 2992°C by replacing magnesium with calcium in the high-entropy oxide (Mg<sub>0.2</sub>Co<sub>0.2</sub>Ni<sub>0.2</sub>Cu<sub>0.2</sub>Zn<sub>0.2</sub>)O.[176] Due to the notable difference in cation radii, substituting magnesium (0.72Å) with calcium (1.00Å) would increase the size mismatch parameter ( $\delta$ ) from 2.69 to 14.24. Large distortion generated from the polyhedral sites containing calcium in the rocksalt structure causes a considerable increase in mixing enthalpy, leading to non-reachable formation temperature (exceeding the boiling point of most of the constituent mono-cation oxides).

In this research, the distortion among polyhedral sites in a single-phase structure increases with the addition of a larger or smaller fifth cation in the LYTE or LCPN system, respectively. As mentioned in Section 7.1, exceeding the threshold of size mismatch ( $>7$ ) would cause the failure of formation of a single-phase, high-entropy oxide. From the thermodynamic perspective, larger distortion involved in a structure would cause a penalty in mixing enthalpy, leading to possible segregation of constituent cations.

In conclusion, the stabilization of an HEO is determined by the competition between mixing enthalpy and mixing entropy. The calculation of configurational mixing entropy has been introduced in Section 3.1. Contributions from both the cations and anions should be considered in the entropy calculation. Due to the homogeneous arrangement of cations in high-entropy oxides, building an ideal model is challenging, especially when oxygen vacancies and high-temperature transformations involved. At ambient conditions, the difference between stable structures of a mono-cation oxide and single-phase HEO, and an increase in cation size mismatch could cause penalties in the mixing enthalpy. If mixing enthalpy has either a negative or small positive value, the free energy could possibly be negative at room temperature. In this case, the HEO structure is naturally stable without a quenching process. As the value of mixing enthalpy becomes larger, the formation temperature of HEO would also increase. In this case, the free energy might reach zero by the contribution from temperature and mixing entropy. If the positive mixing enthalpy dominates ( $\Delta H_{mix} \gg \Delta S_{mix}$ ), the single-phase HEO might not be stable at ambient conditions. In order to fully understand the contribution of mixing entropy in “high-entropy oxides,” further investigations on both experimental results and simulation improvements would be required.

## CHAPTER 8: MINOR PROJECT

### 8.1. High-Temperature Behavior of $(\text{Mg}_{0.2}\text{Co}_{0.2}\text{Ni}_{0.2}\text{Cu}_{0.2}\text{Zn}_{0.2})\text{O}$

Prior to the design of the HELO systems, an attempt was made to reproduce the HEO,  $(\text{Mg}_{0.2}\text{Co}_{0.2}\text{Ni}_{0.2}\text{Cu}_{0.2}\text{Zn}_{0.2})\text{O}$  (MCCZN), reported by Rost et al. in 2015.[7] The HEO was successfully synthesized via the polymeric steric entrapment method from nitrate precursors. The next step was to study the high-temperature behavior of MCCZN in the conical nozzle levitator at the APS beamline 6ID-D. As shown in the diffraction patterns from room temperature to 2200°C (Figure 78), no secondary phase were observed in the experiment. After cooling back to room temperature, the sample remained in its rocksalt structure. However, even the CO<sub>2</sub> laser was able to create an environment with temperatures up to 3000°C, such that the sample bead deformed at temperature >2000°C. Figure 79 presented the evolution of sample morphology in a temperature range 2000°C to 2100°C. A portion of the tested bead evaporated under exposure to the CO<sub>2</sub> laser. The donut-like shaped sample had a hole in the middle, corresponding to the direction of the heating source. The initial hypothesis was that the MCCZN sample might reach its melting point, whose value has not yet been determined according to the literature. After testing different beads with a careful increase in temperature, the tested sample still became volatile instead of remaining in a melted state as the temperature reached above 2000°C. In this case, the in-situ heating experiment was forced to stop.

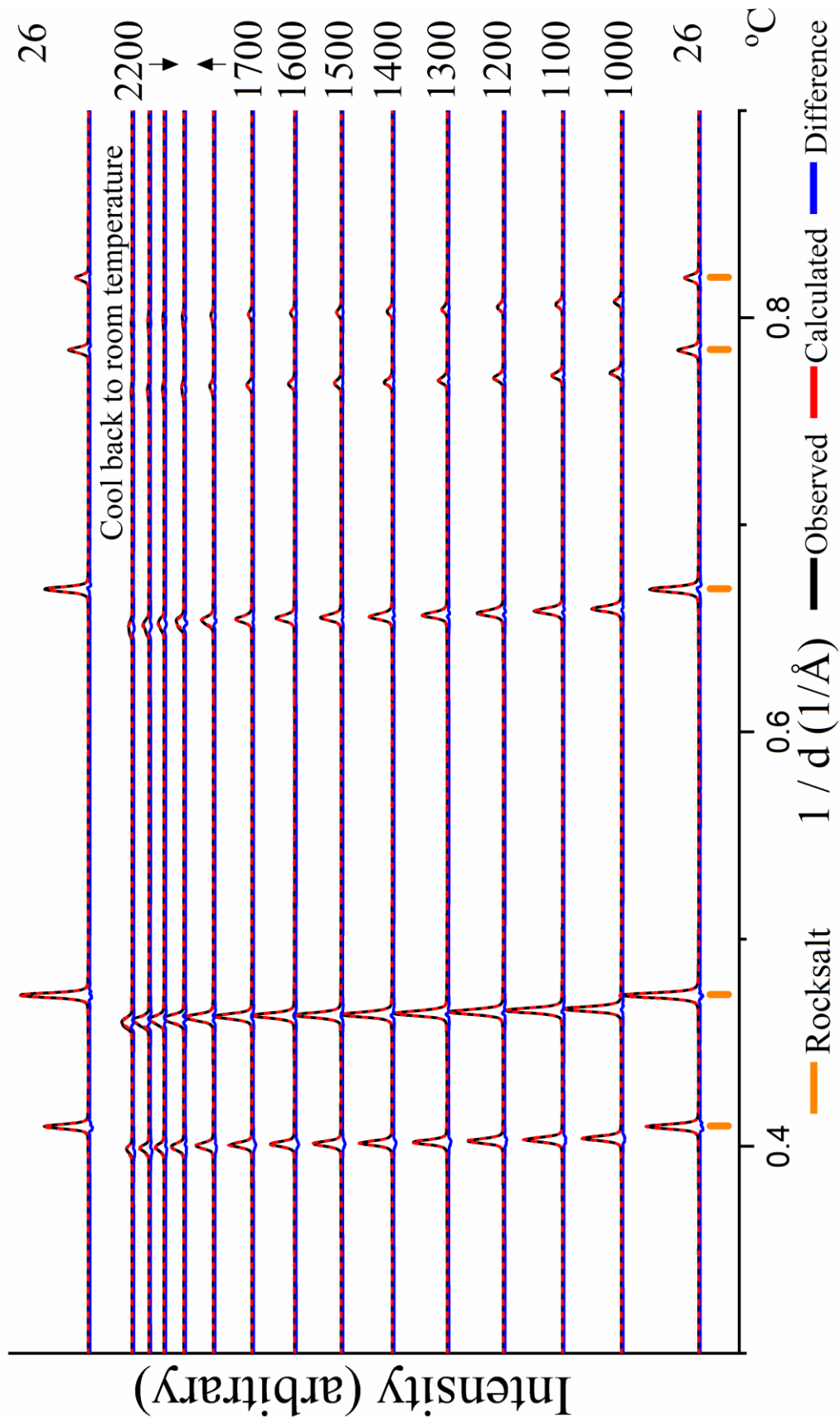


Figure 78. Rietveld refinement of the MCCZN sample, obtained by the conical nozzle levitator

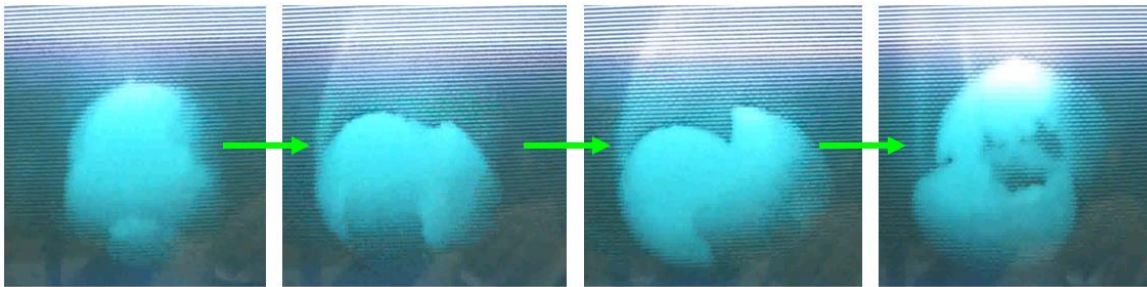


Figure 79. The MCCZN sample became volatile as the temperature reached above 2000°C, under the exposure to the CO<sub>2</sub> laser.

The tested bead lost significant mass during the in-situ experiments. In order to understand if there was any variation in composition, the deformed beads were examined by SEM-EDS. The SEM/EDS results are presented in Figure 80. The remaining composition was determined to be primarily magnesium and oxygen. The other components must therefore have been volatile and left the HEO structure above 2000°C. The melting temperatures of binary oxides of constituent cations are listed in Table 25. It is worth noting that MgO was the only component of these five mono-cation oxides that had a melting point above 2000°C. In this case, the following hypothesis was made for choosing cations for future study of high-temperature behavior of HEOs: the binary oxides should have relatively high melting temperatures. The melting points of binary oxides in MCCZN and the lanthanide cations are listed in Table 25. All lanthanides and yttrium cations exhibited melting temperatures above 2100°C, which would be ideal candidates for a study of phase stability in high-temperature environments.

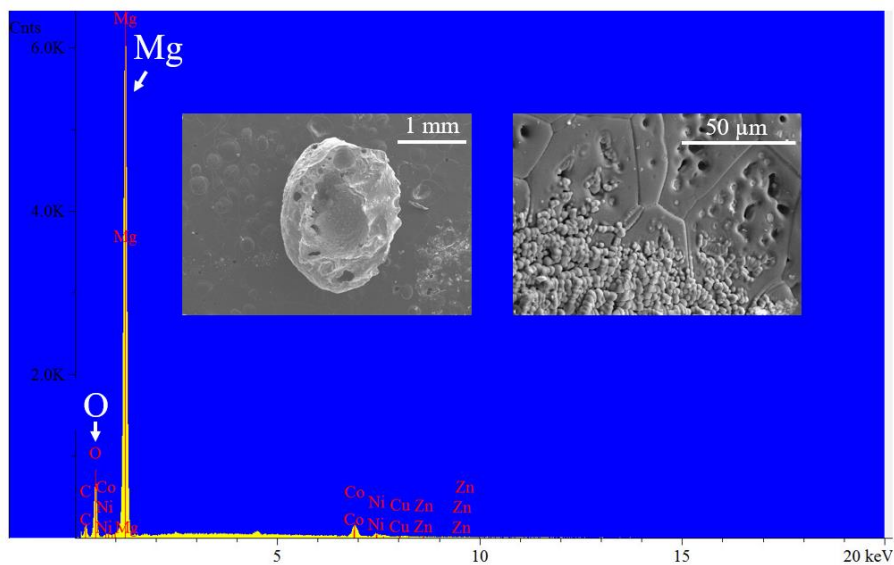


Figure 80. SEM/EDS analyses of the deformed MCCZN bead after heat treatment at  $>2000^{\circ}\text{C}$ . The remnant phase was dominated by the presence of magnesium and oxygen.

Table 25. Melting points of binary oxides [146]

MCCZN system		Candidates in this research	
Oxides	Melting Point ( $^{\circ}\text{C}$ )	Oxides	Melting Point ( $^{\circ}\text{C}$ )
MgO	2852	$\text{La}_2\text{O}_3$	2304
ZnO	1975	$\text{Ce}_2\text{O}_3$	2250
NiO	1955	$\text{CeO}_2$	2480
CoO	1933	$\text{Pr}_2\text{O}_3$	2183
CuO	1326	$\text{Nd}_2\text{O}_3$	2233
		$\text{Sm}_2\text{O}_3$	2335
		$\text{Eu}_2\text{O}_3$	2350
		$\text{Gd}_2\text{O}_3$	2425
		$\text{Tb}_4\text{O}_7$	2303
		$\text{Dy}_2\text{O}_3$	2408
		$\text{Y}_2\text{O}_3$	2439
		$\text{Ho}_2\text{O}_3$	2415
		$\text{Er}_2\text{O}_3$	2418
		$\text{Tm}_2\text{O}_3$	2341
		$\text{Yb}_2\text{O}_3$	2355
		$\text{Lu}_2\text{O}_3$	2490

## CHAPTER 9: CONCLUSIONS

Three multicomponent oxide systems, including 20 candidate materials, were synthesized by the organic steric entrapment, which had no history of a prior crystalline structure. This is in contrast to the conventional synthesis method involving solid state diffusion of crystalline precursor components. The polymeric steric entrapment method had the advantage of homogeneously mixing cations in liquid precursor solutions and forming homogeneous amorphous solid mixtures. This research focused on the study of the chemical selection rules for the formation of high-entropy oxides (HEOs).

Lanthanides were chosen as cations in this research due to their physical behavior, such as large range of cation radii, a variety of preferred oxidation states, and high melting points. Based on observations in the single-phase, high-entropy lanthanide oxide (HELO),  $(\text{Gd}_{0.4}\text{Tb}_{0.4}\text{Dy}_{0.4}\text{Ho}_{0.4}\text{Er}_{0.4})\text{O}_3$ , the terbium cation, which exhibited a mixture of trivalent and tetravalent states, could be constrained in a C-type  $\text{M}_2\text{O}_3$  cubic-bixbyite structure.

The other two systems, LYTE and LCPN, were designed based on their differences in size mismatch and oxidation states. In the prior case, four of the smallest cations (Lu, Yb, Tm, Er) were fixed and a further cation was added to create a powder sample containing five cations. On the other hand, the design for the LCPN system was based on selecting the four largest cations (La, Ce, Pr, Nd) as the base. Furthermore, despite the fact that most of the lanthanide cations were thermodynamically stable in their trivalent state under ambient conditions, cerium, praseodymium, and terbium exhibited a preference for the tetravalent state. The LYTE system demonstrated a minimum effect from mixing cations with different valence configurations, while the LCPN system was based on a mixture of cations which preferred trivalent and tetravalent states. The crystal structures in the LYTE and LCPN systems were measured by in-situ heating X-ray

diffraction, from room temperature to 2000°C. Phase transformations and stability were examined in these 19 candidate materials. Their thermal expansions behaviors were measured by in situ high temperature synchrotron diffraction and analyzed in 3D, resulting in a unique second order polynomial function to describe the thermal expansion in 3D.

The results observed in this research demonstrated that size mismatch in cations had a critical effect on the formation of HELOs. In the LYTE system, a secondary phase within the perovskite structure was found in the LYTELa sample, which had the largest value ( $\delta=7.03$ ) of size mismatch. By altering the composition of lanthanum, the existence of secondary phase(s) could not be eliminated. In the future design of HEOs, choosing cations having a large size mismatch would fail to form a single-phase solid solution.

The second selection parameter was the preferred valence states among the constituent cations. Despite the fact that cation radii could vary with oxidation states and coordination numbers, the effect of preferred valence configurations had a minor contribution to single-phase formation. However, by altering the number of cations containing different oxidation states, the final crystal structure could possibly shift to a prototype composed of a major preferred valence state. The levels of trivalent preferring cations among constituent cations in LYTEDy, LYTETb, LCPNDy, and LCPNTb compositions were 100 mol %, 80 mol %, 60 mol %, and 40 mol %, respectively. As the preferred valence configurations varied, the final structures changed from C-type cubic bixbyite ( $M_2O_3$ ), to tilted fluorite ( $M_2O_{3.5}$ ), and then to fluorite ( $MO_2$ ). In the LCPNTb sample, the crystal structure could be modified between tilted fluorite and fluorite structures by altering the content of terbium. These results provided evidence that the final structures of HEOs could be dominated by the preferred valence states of the intrinsic cations. In addition, mixing cations with different preferred oxidation states in a HEO could decrease their structural stability under high temperature heat treatments.



Even though the materials studied in this research were called “high-entropy oxides,” the contribution from entropy was not significant. Considering that the mixing entropy contribution comes from both cations and anions in ceramics, the existence by anions significantly decreased the configurational entropy in HEOs. Moreover, multiple cations occupying only one of the polyhedral sites could further decrease the configurational entropy, such as in the case of the high-entropy perovskite  $\text{Ba}(\text{Zr}_{0.2}\text{Sn}_{0.2}\text{Ti}_{0.2}\text{Hf}_{0.2}\text{Ce}_{0.2})\text{O}_3$ .

In this research, altering the composition of the fifth cation in both LYTE and LCPN systems decreased their configurational entropies. However, the changes in entropy made less of a contribution to their final structures, compared to size mismatch and preferred valence states. Even though the significance of configurational entropy might be negligible in “high-entropy oxides,” the occupation of one polyhedral site with at least five cations can still impart local strength throughout the structures. The lattice distortion, sluggish diffusion, and cocktail effects still have contributions to HEOs.

In conclusion, this research provided an initial study of chemical selection rules for the future design of a single-phase HEO. Two parameters, (1) size mismatch, and (2) preferred valence states should be taken into account in choosing cations for the formation of single-phase HEOs with desired crystal structures. The size mismatch parameter has a critical effect on single-phase formation, while the preferred valence states affects the final structure and thermal stability. As an initial study in this novel ceramic field, further study would be required to understand other possible parameters in single-phase formation of HEOs.

## CHAPTER 10: SUGGESTIONS FOR FUTURE RESEARCH

Based on a short research history of high-entropy oxides, the investigation of several unknown questions would be required to fully understand the complicated correlation between cations and oxygen anions in different crystal structures. The cation radii change with different valence states and coordination geometry. Different coordination geometries in oxide structures might exhibit different strain tolerances among constituent cations. Cations existing in different valence states in a HEO structure could produce oxygen vacancies. The following paragraphs provide a hypothesis for future research in HEOs.

The radius of a cation is determined by its valence state and coordination geometry. In this research, initially, the radii of lanthanide cations were based on the condition of trivalent oxidation state and 6-fold coordination. All the single-phase HEOs in the LYTE system became a C-type bixbyite structure constructed by octahedra. In LCPN HEOs, the constituent cations were either located in 7-fold coordination, in a tilted fluorite structure, or in 8-fold coordination, in a fluorite structure. Based on the coordination geometry, the cation site surrounded by 8 oxygen anions is larger than the site surrounded by 6 oxygen anions. Different coordination geometries could exhibit different tolerances in cation size mismatch. In addition, the existence of oxygen vacancies could possibly increase the tolerance of specific polyhedral sites.

From the perspective of thermodynamics, an ideal model in building a high-entropy structure having a homogeneous cation distribution is required to evaluate the competition between mixing enthalpy and mixing entropy. According to the experimental results and thermodynamic calculations, oxides containing different numbers of components (3-5) could exhibit the same crystal structure.[50, 176] In this research, the candidate composed of four base lanthanide cations exhibited identical crystal structures to most of the five-component oxides. As mentioned in

Section 3.1, the contribution from configurational mixing entropy in HEOs is significantly lower than in the HEAs system. The difference between the constituent mono-cation oxide structures and final HEO structure, as well as lattice distortion produced by cation size mismatch cause a penalty in the mixing enthalpy. Whether the final crystal structures of HEOs are stabilized by configurational mixing entropy is controversial. In addition, the effects of HEOs on their physico-chemical properties are still unclear. In the development of this novel oxide field, the chemical selection rules proposed in this research provide a threshold of single-phase formation and guidelines in final possible transformations in a final HEO structure.

## REFERENCES

1. Cantor B, Chang ITH, Knight P, Vincent AJB. Microstructural development in equiatomic multicomponent alloys. *Materials Science and Engineering: A*. 2004;375-377:213-8.
2. Yeh JW, Chen SK, Lin SJ, Gan JY, Chin TS, Shun TT, Tsau CH, Chang SY. Nanostructured high-entropy alloys with multiple principal elements: Novel alloy design concepts and outcomes. *Advanced Engineering Materials*. 2004;6(5):299-303.
3. Gao MC, Yeh J-W, Liaw PK, Zhang Y. *High-Entropy Alloys: Fundamentals and Applications*: Springer; 2016.
4. Jien-Wei Y. Recent progress in high entropy alloys. *Annales de Chimie Science des Materiaux (Paris)*. 2006;31(6):633-48.
5. Tsai M-H, Yeh J-W. High-entropy alloys: A critical review. *Materials Research Letters*. 2014;2(3):107-23.
6. Tsai M-H. Physical properties of high entropy alloys. *Entropy*. 2013;15(12):5338-45.
7. Rost CM, Sachet E, Borman T, Moballegh A, Dickey EC, Hou D, Jones JL, Curtarolo S, Maria J-P. Entropy-stabilized oxides. *Nature Communications*. 2015;6.
8. Bérardan D, Franger S, Dragoe D, Meena AK, Dragoe N. Colossal dielectric constant in high entropy oxides. *Physica Status Solidi (RRL)-Rapid Research Letters*. 2016;10(4):328-33.
9. Gild J, Samiee M, Braun JL, Harrington T, Vega H, Hopkins PE, Vecchio K, Luo J. High-entropy fluorite oxides. *Journal of the European Ceramic Society*. 2018;38(10):3578-84.
10. Hong W, Chen F, Shen Q, Han YH, Fahrenholtz WG, Zhang L. Microstructural evolution and mechanical properties of (Mg,Co,Ni,Cu,Zn)O high-entropy ceramics. *Journal of the American Ceramic Society*. 2019;102(4):2228-37.
11. Meisenheimer PB, Kratochvil TJ, Heron JT. Giant enhancement of exchange coupling in entropy-stabilized oxide heterostructures. *Scientific Reports*. 2017;7(1):13344.
12. Sarkar A, Loho C, Velasco L, Thomas T, Bhattacharya SS, Hahn H, Djenadic R. Multicomponent equiatomic rare earth oxides with a narrow band gap and associated praseodymium multivalency. *Dalton Transactions*. 2017;46(36):12167-76.
13. Zhou J, Zhang J, Zhang F, Niu B, Lei L, Wang W. High-entropy carbide: A novel class of multicomponent ceramics. *Ceramics International*. 2018;44(17):22014-8.
14. Gild J, Zhang Y, Harrington T, Jiang S, Hu T, Quinn MC, Mellor WM, Zhou N, Vecchio K, Luo J. High-entropy metal diborides: A new class of high-entropy materials and a new type of ultrahigh temperature ceramics. *Scientific Reports*. 2016;6.

15. Jin T, Sang X, Unocic RR, Kinch RT, Liu X, Hu J, Liu H, Dai S. Mechanochemical-assisted synthesis of high-entropy metal nitride via a soft urea strategy. *Advanced Materials*. 2018;30(23):1707512.
16. Shen W, Tsai M, Tsai K, Juan C, Tsai C, Yeh J, Chang Y. Superior oxidation resistance of  $(Al_{0.34}Cr_{0.22}Nb_{0.11}Si_{0.11}Ti_{0.22})_{50}N_{50}$  high-entropy nitride. *Journal of The Electrochemical Society*. 2013;160(11):C531-C5.
17. Zhang R-Z, Gucci F, Zhu H, Chen K, Reece MJ. Data-driven design of ecofriendly thermoelectric high-entropy sulfides. *Inorganic Chemistry*. 2018;57(20):13027-33.
18. Wang T, Chen H, Yang Z, Liang J, Dai S. High-entropy perovskite fluorides: A new platform for oxygen evolution catalysis. *Journal of the American Chemical Society*. 2020.
19. Murty BS, Yeh J-W, Ranganathan S, Bhattacharjee P. *High-Entropy Alloys*: Elsevier; 2019.
20. Miracle DB, Senkov ON. A critical review of high entropy alloys and related concepts. *Acta Materialia*. 2017;122:448-511.
21. Huang PK, Yeh JW, Shun TT, Chen SK. Multi-principal-element alloys with improved oxidation and wear resistance for thermal spray coating. *Advanced Engineering Materials*. 2004;6(1-2):74-8.
22. Senkov O, Miller J, Miracle D, Woodward C. Accelerated exploration of multi-principal element alloys with solid solution phases. *Nature Communications*. 2015;6(1):1-10.
23. Gorsse S, Miracle DB, Senkov ON. Mapping the world of complex concentrated alloys. *Acta Materialia*. 2017;135:177-87.
24. Jain A, Ong SP, Hautier G, Chen W, Richards WD, Dacek S, Cholia S, Gunter D, Skinner D, Ceder G, Persson KA. Commentary: The Materials Project: A materials genome approach to accelerating materials innovation. *APL Materials*. 2013;1(1):011002.
25. Guo S, Hu Q, Ng C, Liu CT. More than entropy in high-entropy alloys: Forming solid solutions or amorphous phase. *Intermetallics*. 2013;41:96-103.
26. Wang X, Zhang Y, Qiao Y, Chen G. Novel microstructure and properties of multicomponent  $CoCrCuFeNiTi_x$  alloys. *Intermetallics*. 2007;15(3):357-62.
27. Liu W, Lu Z, He J, Luan J, Wang Z, Liu B, Liu Y, Chen M, Liu C. Ductile  $CoCrFeNiMo_x$  high entropy alloys strengthened by hard intermetallic phases. *Acta Materialia*. 2016;116:332-42.
28. Zhang Y, Zhou YJ, Lin JP, Chen GL, Liaw PK. Solid-solution phase formation rules for multi-component alloys. *Advanced Engineering Materials*. 2008;10(6):534-8.
29. Steurer W. Single-phase high-entropy alloys—A critical update. *Materials Characterization*. 2020:110179.

30. Qin G, Chen R, Liaw PK, Gao Y, Wang L, Su Y, Ding H, Guo J, Li X. An as-cast high-entropy alloy with remarkable mechanical properties strengthened by nanometer precipitates. *Nanoscale*. 2020.
31. Sarkar A, Djenadic R, Usharani NJ, Sanghvi KP, Chakravadhanula VS, Gandhi AS, Hahn H, Bhattacharya SS. Nanocrystalline multicomponent entropy stabilised transition metal oxides. *Journal of the European Ceramic Society*. 2017;37(2):747-54.
32. Sarkar A, Djenadic R, Wang D, Hein C, Kautenburger R, Clemens O, Hahn H. Rare earth and transition metal based entropy stabilised perovskite type oxides. *Journal of the European Ceramic Society*. 2018;38(5):2318-27.
33. Sarkar A, Wang Q, Schiele A, Chellali MR, Bhattacharya SS, Wang D, Brezesinski T, Hahn H, Velasco L, Breitung B. High-entropy oxides: Fundamental aspects and electrochemical properties. *Advanced Materials*. 2019;31(26):1806236.
34. Zhang Y, Zuo T, Cheng Y, Liaw PK. High-entropy alloys with high saturation magnetization, electrical resistivity, and malleability. *Scientific Reports*. 2013;3:1455.
35. Shao Y-T, Yuan R, Hu Y, Yang Q, Zuo J-M. The paracrystalline nature of lattice distortion in a high entropy alloy. *arXiv preprint arXiv:190304082*. 2019.
36. Dong W, Zhou Z, Zhang M, Ma Y, Yu P, Liaw PK, Li G. Applications of high-pressure technology for high-entropy alloys: A review. *Metals*. 2019;9(8):867.
37. Yeh J-W. Alloy design strategies and future trends in high-entropy alloys. *JOM*. 2013;65(12):1759-71.
38. Ranganathan S. Alloyed pleasures: Multimetalllic cocktails. *Current Science*. 2003;85(5):1404-6.
39. Pogrebnjak A, Bagdasaryan AAe, Yakushchenko I, Beresnev VM. The structure and properties of high-entropy alloys and nitride coatings based on them. *Russian Chemical Reviews*. 2014;83(11):1027.
40. Tang Z, Gao MC, Diao H, Yang T, Liu J, Zuo T, Zhang Y, Lu Z, Cheng Y, Zhang Y. Aluminum alloying effects on lattice types, microstructures, and mechanical behavior of high-entropy alloys systems. *JOM*. 2013;65(12):1848-58.
41. Chen H, Fu J, Zhang P, Peng H, Abney CW, Jie K, Liu X, Chi M, Dai S. Entropy-stabilized metal oxide solid solutions as CO oxidation catalysts with high-temperature stability. *Journal of Materials Chemistry A*. 2018;6(24):11129-33.
42. Chen H, Lin W, Zhang Z, Jie K, Mullins DR, Sang X, Yang S-Z, Jafta CJ, Bridges CA, Hu X. Mechanochemical synthesis of high entropy oxide materials under ambient conditions: Dispersion of catalysts via entropy maximization. *ACS Materials Letters*. 2019;1(1):83-8.

43. Guo S. Phase selection rules for cast high entropy alloys: An overview. *Materials Science and Technology*. 2015;31(10):1223-30.
44. Sheng G, Liu CT. Phase stability in high entropy alloys: Formation of solid-solution phase or amorphous phase. *Progress in Natural Science: Materials International*. 2011;21(6):433-46.
45. Fang S, Xiao X, Xia L, Li W, Dong Y. Relationship between the widths of supercooled liquid regions and bond parameters of Mg-based bulk metallic glasses. *Journal of Non-Crystalline Solids*. 2003;321(1-2):120-5.
46. Guo S, Ng C, Lu J, Liu CT. Effect of valence electron concentration on stability of fcc or bcc phase in high entropy alloys. *Journal of Applied Physics*. 2011;109(10):103505.
47. Otto F, Yang Y, Bei H, George EP. Relative effects of enthalpy and entropy on the phase stability of equiatomic high-entropy alloys. *Acta Materialia*. 2013;61(7):2628-38.
48. Dąbrowa J, Stygar M, Mikuła A, Knapik A, Mroczka K, Tejchman W, Danielewski M, Martin M. Synthesis and microstructure of the (Co,Cr,Fe,Mn,Ni)<sub>3</sub>O<sub>4</sub> high entropy oxide characterized by spinel structure. *Materials Letters*. 2018;216:32-6.
49. Shannon RD. Revised effective ionic radii and systematic studies of interatomic distances in halides and chalcogenides. *Acta Crystallographica Section A: Crystal Physics, Diffraction, Theoretical and General Crystallography*. 1976;32(5):751-67.
50. Djenadic R, Sarkar A, Clemens O, Loho C, Botros M, Chakravadhanula VS, Kübel C, Bhattacharya SS, Gandhi AS, Hahn H. Multicomponent equiatomic rare earth oxides. *Materials Research Letters*. 2017;5(2):102-9.
51. Chen K, Pei X, Tang L, Cheng H, Li Z, Li C, Zhang X, An L. A five-component entropy-stabilized fluorite oxide. *Journal of the European Ceramic Society*. 2018;38(11):4161-4.
52. Tseng KP, Yang Q, McCormack SJ, Kriven WM. High-entropy, phase-constrained, lanthanide sesquioxide. *Journal of the American Ceramic Society*. 2020;103(1):569-76.
53. Jiang S, Hu T, Gild J, Zhou N, Nie J, Qin M, Harrington T, Vecchio K, Luo J. A new class of high-entropy perovskite oxides. *Scripta Materialia*. 2018;142:116-20.
54. Mao A, Xiang H-Z, Zhang Z-G, Kuramoto K, Zhang H, Jia Y. A new class of spinel high-entropy oxides with controllable magnetic properties. *Journal of Magnetism and Magnetic Materials*. 2020;497:165884.
55. Mao A, Zhang Z-G, Zhang H, Ran S. A novel six-component spinel-structure high-entropy oxide with ferrimagnetic property. *Journal of Magnetism and Magnetic Materials*. 2020:166594.

56. Chen H, Qiu N, Wu B, Yang Z, Sun S, Wang Y. A new spinel high-entropy oxide ( $\text{Mg}_{0.2}\text{Ti}_{0.2}\text{Zn}_{0.2}\text{Cu}_{0.2}\text{Fe}_{0.2}$ ) $_3\text{O}_4$  with fast reaction kinetics and excellent stability as an anode material for lithium ion batteries. *RSC Advances*. 2020;10(16):9736-44.
57. Zhang J, Zhang X, Li Y, Du Q, Liu X, Qi X. High-entropy oxides  $10\text{La}_2\text{O}_3$ - $20\text{TiO}_2$ - $10\text{Nb}_2\text{O}_5$ - $20\text{WO}_3$ - $20\text{ZrO}_2$  amorphous spheres prepared by containerless solidification. *Materials Letters*. 2019;244:167-70.
58. Zinkevich M. Thermodynamics of rare earth sesquioxides. *Progress in Materials Science*. 2007;52(4):597-647.
59. Zhang Y, Jung I-H. Critical evaluation of thermodynamic properties of rare earth sesquioxides (RE = La, Ce, Pr, Nd, Pm, Sm, Eu, Gd, Tb, Dy, Ho, Er, Tm, Yb, Lu, Sc and Y). *Calphad*. 2017;58:169-203.
60. Adachi G-y, Imanaka N. The binary rare earth oxides. *Chemical Reviews*. 1998;98(4):1479-514.
61. Zinkevich M, Djurovic D, Aldinger F. Thermodynamic modelling of the cerium–oxygen system. *Solid State Ionics*. 2006;177(11-12):989-1001.
62. Konings RJ, Beneš O, Kovács A, Manara D, Sedmidubský D, Gorokhov L, Iorish VS, Yungman V, Shenyavskaya E, Osina E. The thermodynamic properties of the f-elements and their compounds. Part 2. The lanthanide and actinide oxides. *Journal of Physical and Chemical Reference Data*. 2014;43(1):013101.
63. Navrotsky A, Lee W, Mielewczyk-Gryn A, Ushakov SV, Anderko A, Wu H, Riman RE. Thermodynamics of solid phases containing rare earth oxides. *The Journal of Chemical Thermodynamics*. 2015;88:126-41.
64. Kittiratanawasin L, Smith R, Uberuaga BP, Sickafus KE. Radiation damage and evolution of radiation-induced defects in  $\text{Er}_2\text{O}_3$  bixbyite. *Journal of Physics: Condensed Matter*. 2009;21(11):115403.
65. Haire R, Eyring L. Comparisons of the Binary Oxides. *Handbook on the Physics and Chemistry of Rare Earths*. 18: Elsevier; 1994. p. 413-505.
66. Eyring L. The Binary Rare Earth Oxides. *Handbook on the Physics and Chemistry of Rare Earths*. 3: Elsevier; 1979.
67. Petit L, Svane A, Szotek Z, Temmerman WM. First-principles study of rare-earth oxides. *Physical Review B*. 2005;72(20):205118.
68. Konings RJ, Beneš O. The thermodynamic properties of the f-elements and their compounds. I. The lanthanide and actinide metals. *Journal of Physical and Chemical Reference Data*. 2010;39(4):043102.



69. Bevan D, Summerville E. Mixed rare earth oxides. Handbook on the Physics and Chemistry of Rare Earths. 1979;3:401-524.
70. Caro P.  $OM_4$  Tetrahedra linkages and the cationic group  $(M^{n+})_n$  in rare earth oxides and oxyalts. Journal of the Less Common Metals. 1968;16(4):367-77.
71. Hill R. The specific heats of  $Tb_2O_3$  and  $Tb_4O_7$  between 0.5 and 22K. Journal of Physics C: Solid State Physics. 1986;19(5):673.
72. Vratny F. Reflectance spectra of terbium oxides in the range  $Tb_2O_3$  to  $Tb_4O_7$ . The Journal of Chemical Physics. 1961;34(4):1377-9.
73. Lonappan D, Chandra Shekar NV, Sahu PC, Kumar J, Paul R, Paul P. Unusually large structural stability of terbium oxide phase under high pressure. Journal of Alloys and Compounds. 2010;490(1-2):47-9.
74. Zhang J, Von Dreele R, Eyring L. The structures of  $Tb_7O_{12}$  and  $Tb_{11}O_{20}$ . Journal of Solid State Chemistry. 1993;104(1):21-32.
75. Baran S, Duraj R, Hoser A, Penc B, Szytuła A. Crystal structure and magnetic properties of  $Tb_{11}O_{20}$ . Acta Physica Polonica, A. 2013;123(1).
76. Balabanov SS, Permin DA, Rostokina EY, Egorov SV, Sorokin AA, Kuznetsov DD. Synthesis and structural characterization of ultrafine terbium oxide powders. Ceramics International. 2017;43(18):16569-74.
77. Jero R, Kriven WM. High Temperature Transformation Toughening of Magnesia by Terbia. Science and Technology of Zirconia V: CPC Press; 1993. p. 190-7.
78. Holland-Moritz E. Coexistence of valence fluctuating and stable Pr ions in  $Pr_6O_{11}$ . Zeitschrift für Physik B Condensed Matter. 1992;89(3):285-8.
79. Hyde B, Garver E, Kuntz U, Eyring L. Kinetic studies on reactions of praseodymium oxides in an oxygen atmosphere:  $PrO_{1.83} + O_2 \rightleftharpoons PrO_2$ . The Journal of Physical Chemistry. 1965;69(5):1667-75.
80. Treu BL, Fahrenholtz W, O'Keefe M. Thermal decomposition behavior of praseodymium oxides, hydroxides, and carbonates. Inorganic Materials. 2011;47(9):974.
81. Eyring L, Gschneidner KA, Lander GH. Handbook on the Physics and Chemistry of Rare Earths: Elsevier; 2002.
82. Binnemans K, Görlner-Walrand C. On the color of the trivalent lanthanide ions. Chemical Physics Letters. 1995;235(3-4):163-74.
83. Fursikov P, Abdusalyamova M, Makhmudov F, Shairmardanov E, Kovalev I, Kovalev DY, Morgunov R, Koplak O, Volodin A, Khodos I. Structural features and magnetic behavior of nanocrystalline powders of terbium oxide prepared by the thermal decomposition of terbium acetate in air. Journal of Alloys and Compounds. 2016;657:163-73.

84. Bünzli JCG. Lanthanides. Kirk-Othmer Encyclopedia of Chemical Technology: John Wiley & Sons; 2013.
85. Inaba H, Tagawa H. Ceria-based solid electrolytes. *Solid State Ionics*. 1996;83(1-2):1-16.
86. Zhu B, Mat MD. Studies on dual phase ceria-based composites in electrochemistry. *International Journal of Electrochemical Science*. 2006;1(8):383-402.
87. Arunkumar P, Meena M, Babu KS. A review on cerium oxide-based electrolytes for ITSOFC. *Nanomaterials and Energy*. 2012;1(5):288-305.
88. Stambouli AB, Traversa E. Solid oxide fuel cells (SOFCs): A review of an environmentally clean and efficient source of energy. *Renewable and Sustainable Energy Reviews*. 2002;6(5):433-55.
89. Nishino H, Matsunaga N, Kakinuma K, Yamamura H, Nomura K. Crystal Structure and Electrical Conductivity of Pyrochlore-type Composition Systems,  $A_2B_2O_7$ . *Journal of the Ceramic Society of Japan*. 2004;112:S738-S41.
90. Yamamura H, Takeda S, Kakinuma K. Dielectric relaxations in the  $Ce_{1-x}Nd_xO_{2-\delta}$  system. *Solid State Ionics*. 2007;178(15-18):1059-64.
91. Grover V, Achary SN, Tyagi AK. Structural analysis of excess-anion C-type rare earth oxide: A case study with  $Gd_{1-x}Ce_xO_{1.5+x/2}$  ( $x= 0.20$  and  $0.40$ ). *Journal of Applied Crystallography*. 2003;36(4):1082-4.
92. Chakraborty KR, Krishna P, Chavan S, Tyagi A. A neutron diffraction study on ceria-neodia solid solutions. *Powder Diffraction*. 2006;21(1):36-9.
93. Hagiwara T, Kyo Z, Manabe A, Yamamura H, Nomura K. Formation of C-type rare earth structures in the  $Ce_{1-x}Nd_xO_{2-\delta}$  system: A factor in the decrease in oxide-ion conductivity. *Journal of the Ceramic Society of Japan*. 2009;117(1372):1306-10.
94. Mori T, Buchanan R, Ou DR, Ye F, Kobayashi T, Kim J-D, Zou J, Drennan J. Design of nanostructured ceria-based solid electrolytes for development of IT-SOFC. *Journal of Solid State Electrochemistry*. 2008;12(7-8):841-9.
95. Wang Y, Kageyama H, Mori T, Yoshikawa H, Drennan J. Local structures around Y and Ce cations in 10 mol%  $Y_2O_3$  doped ceria ceramics by EXAFS spectroscopy. *Solid State Ionics*. 2006;177(19-25):1681-5.
96. Pearson WB. *A Handbook of Lattice Spacings and Structures of Metals and Alloys*. International Series of Monographs on Metal Physics and Physical Metallurgy. 4: Elsevier; 2013.
97. Chavan S, Tyagi A. Phase relations and lattice thermal expansion studies in the  $Ce_{0.50}RE_{0.50}O_{1.75}$  (RE= rare-earths). *Materials Science and Engineering: A*. 2005;404(1-2):57-63.

98. Artini C, Costa G, Carnasciali M, Masini R. Comparative study and properties of  $\text{RuSr}_2\text{Gd}_{1.4}\text{Ce}_{0.6}\text{Cu}_2\text{O}_{10-\delta}$  ruthenocuprate samples by different preparation methods. *Materials Science and Engineering: B*. 2012;177(1):112-6.
99. Spivakov A, Zakharov YN, Ter-Oganessian N, Lutokhin A, Panchenko E, Sakhnenko V. Interrelation of ferroelectricity and tilting in perovskites using the phase transitions in  $\text{PbZr}_{1-x}\text{Ti}_x\text{O}_3$  as an example. *Solid State Sciences*. 2015;40:105-10.
100. Kumar HP, Kumar SS, Venugopal M, Binila R, Nissamudeen K, Thomas J, Solomon S. Synthesis, characterization and photoluminescent properties of  $\text{BaZr}_x\text{Nd}_{1-x}\text{O}_3$  perovskites. *Journal of Alloys and Compounds*. 2015;629:173-7.
101. Doshi R, Alcock C, Gunasekaran N, Carberry J. Carbon monoxide and methane oxidation properties of oxide solid solution catalysts. *Journal of Catalysis*. 1993;140(2):557-63.
102. Artini C. Crystal chemistry, stability and properties of interlanthanide perovskites: A review. *Journal of the European Ceramic Society*. 2017;37(2):427-40.
103. Qi J, Guo X, Mielewczyk-Gryn A, Navrotsky A. Formation enthalpies of  $\text{LaLn}'\text{O}_3$  ( $\text{Ln}' = \text{Ho, Er, Tm and Yb}$ ) interlanthanide perovskites. *Journal of Solid State Chemistry*. 2015;227:150-4.
104. Ito K, Tezuka K, Hinatsu Y. Preparation, magnetic susceptibility, and specific heat on interlanthanide perovskites  $\text{ABO}_3$  ( $\text{A} = \text{La-Nd}$ ,  $\text{B} = \text{Dy-Lu}$ ). *Journal of Solid State Chemistry*. 2001;157(1):173-9.
105. Berndt U, Maier D, Keller C. New  $\text{A}^{\text{III}}\text{B}^{\text{III}}\text{O}_3$  interlanthanide perovskite compounds. *Journal of Solid State Chemistry*. 1975;13(1-2):131-5.
106. Kriven WM. Possible alternative transformation tougheners to zirconia: Crystallographic aspects. *Journal of the American Ceramic Society*. 1988;71(12):1021-30.
107. Heuer A, Hobbs L. *Advances in Ceramics: Science and Technology of Zirconia: The American Ceramic Society, Inc.*; 1981.
108. Gates-Rector S, Blanton T. The powder diffraction file: A quality materials characterization database. *Powder Diffraction*. 2019;34(4):352-60.
109. Paul R, Sen P, Das I. Effect of morphology on the magnetic properties of  $\text{Gd}_2\text{O}_3$  nanotubes. *Physica E: Low-Dimensional Systems and Nanostructures*. 2016;80:149-54.
110. Chen D-X, Skumryev V, Bozzo B. Calibration of ac and dc magnetometers with a  $\text{Dy}_2\text{O}_3$  standard. *Review of Scientific Instruments*. 2011;82(4):045112.
111. Mortazavi-Derazkola S, Zinatloo-Ajabshir S, Salavati-Niasari M. New facile preparation of  $\text{Ho}_2\text{O}_3$  nanostructured material with improved photocatalytic performance. *Journal of Materials Science: Materials in Electronics*. 2017;28(2):1914-24.

112. Yuan Y, Wu Y, Tong X, Zhang H, Wang H, Liu X, Ma L, Suo H, Lu Z. Rare-earth high-entropy alloys with giant magnetocaloric effect. *Acta Materialia*. 2017;125:481-9.
113. Fukuma K, Torii M. Absolute calibration of low-and high-field magnetic susceptibilities using rare earth oxides. *Geochemistry, Geophysics, Geosystems*. 2011;12(7).
114. Lide D. Magnetic susceptibility of the elements and inorganic compounds. *Handbook of Chemistry and Physics*. 2000:130-5.
115. Kennedy BJ, Avdeev M. The structure of C-type Gd<sub>2</sub>O<sub>3</sub>. A powder neutron diffraction study using enriched <sup>160</sup>Gd. *Australian Journal of Chemistry*. 2011;64(1):119-21.
116. Gülgün MA, Nguyen MH, Kriven WM. Polymerized organic-inorganic synthesis of mixed oxides. *Journal of the American Ceramic Society*. 1999;82(3):556-60.
117. Nguyen MH, Lee S-J, Kriven WM. Synthesis of oxide powders by way of a polymeric steric entrapment precursor route. *Journal of Materials Research*. 1999;14(8):3417-26.
118. Gülgün MAK, Waltraud M. A simple solution-polymerization route for oxide powder synthesis. *Ceramic Transactions*. 1995;62:57-66.
119. Lee S, Biegalski M, Kriven WM. Powder synthesis of barium titanate and barium orthotitanate via an ethylene glycol complex polymerization route. *Journal of Materials Research*. 1999;14(7):3001-6.
120. Gülgün MA, Kriven WM, Nguyen MH, inventors; US Patent Number 6,482,387, assignee. Processes for preparing mixed metal oxide powders 2002.
121. Jurkschat K, Sarin P, Siah L, Kriven W. In situ high temperature phase transformations in rare earth niobates. *Advances in X-ray Analysis*. 2004;47:357-62.
122. Lee S-J, Kriven WM. Synthesis and hydration study of portland cement components prepared by the organic steric entrapment method. *Materials and Structures*. 2005;38(1):87-92.
123. Kriven W, Rosczyk B. SOFC Powder Synthesis by the Organic Steric Entrapment Method. *Fuel Cell Technologies: State and Perspectives*: Springer; 2005. p. 381-94.
124. Gordon M, Bell J, Kriven W. Comparison of naturally and synthetically-derived potassium-based geopolymers. *Ceramic Transactions*. 2005;165:95-106.
125. Jia D, Kim D, Kriven WM. Sintering behavior of gehlenite. Part I: Self-forming, macro-/mesoporous gehlenite—pore-forming mechanism, microstructure, mechanical, and physical properties. *Journal of the American Ceramic Society*. 2007;90(6):1760-73.
126. Jia D, Kriven WM. Sintering behavior of gehlenite, part II. Microstructure and mechanical properties. *Journal of the American Ceramic Society*. 2007;90(9):2766-70.

127. Kim DK, Kriven WM. Processing and characterization of multiphase ceramic composites Part II: Triplex composites with a wide sintering temperature range. *Journal of the American Ceramic Society*. 2008;91(3):793-8.
128. Kim DK, Kriven WM. Processing and characterization of multiphase ceramic composites part I: Duplex composites formed in situ from solution. *Journal of the American Ceramic Society*. 2008;91(3):784-92.
129. Kim DK, Kriven WM. Processing and characterization of multiphase ceramic composites part III: strong, hard and tough, high temperature-stable quadruplex and quintuplex composites. *Journal of the American Ceramic Society*. 2008;91(3):799-805.
130. Jia D, Kim D, Kriven WM. Preparation of a Pore Self-Forming Macro-/Mesoporous Gehlenite Ceramic by the Organic Steric Entrapment (PVA) Technique. *Developments in Porous, Biological and Geopolymer Ceramics*. 28: Wiley; 2008. p. 67-75.
131. Jung C-H, Lee SJ, Kriven WM, Park J-Y, Ryu W-S. A polymer solution technique for the synthesis of nano-sized  $\text{Li}_2\text{TiO}_3$  ceramic breeder powders. *Journal of Nuclear Materials*. 2008;373(1-3):194-8.
132. Lee SJ, Kwak JY, Kriven WM. Effect of a polymer addition on the crystallite size and sinterability of hydroxyapatite prepared with CaO powder and phosphoric acid. *Journal of Ceramic Processing Research*. 2012;13(3):243-7.
133. Özer A, Kriven WM, Tür YK. The effect of 3 mol%  $\text{Y}_2\text{O}_3$  stabilized  $\text{ZrO}_2$  produced by a steric entrapment method on the mechanical and sintering properties of  $\text{Cr}_3\text{C}_2$  based cermets. *Materials Science and Engineering: A*. 2012;556:878-84.
134. García-Moreno O, Kriven WM, Moya JS, Torrecillas R. Alumina region of the lithium aluminosilicate system: A new window for temperature ultrastable materials design. *Journal of the American Ceramic Society*. 2013;96(7):2039-41.
135. Ubc R, Tolman K, Chan K, Lundy N, Letourneau S, Kriven WM. Effective size of vacancies in aliovalently doped  $\text{SrTiO}_3$  perovskites. *Journal of Alloys and Compounds*. 2013;575:239-45.
136. Letourneau S, Zhen Z, Owens J, Tolman K, Ubc R, Kriven WM. Lattice constant prediction of defective rare earth titanate perovskites. *Journal of Solid State Chemistry*. 2014;219:99-107.
137. Seymour KC, Kriven WM. Synthesis and thermal expansion of  $\beta$ -eucryptite powders produced by the inorganic-organic steric entrapment method. *Journal of the American Ceramic Society*. 2014;97(10):3087-91.

138. Tolman KR, Ubic R, Papac M, Seymour KC, McCormack SJ, Kriven WM, Kungl H. Structural effect of aliovalent doping in lead perovskites. *Journal of Solid State Chemistry*. 2015;225:359-67.
139. Ribero D, Kriven WM. Synthesis of LiFePO<sub>4</sub> powder by the organic–inorganic steric entrapment method. *Journal of Materials Research*. 2015;30(14):2133-43.
140. Ribero D, Seymour KC, Kriven WM. Synthesis of NaTi<sub>2</sub>(PO<sub>4</sub>)<sub>3</sub> by the inorganic–organic steric entrapment method and its thermal expansion behavior. *Journal of the American Ceramic Society*. 2016;99(11):3586-93.
141. Bagci C, Yang Q, Kriven WM. Formation of  $\alpha/\beta$ -Si<sub>3</sub>N<sub>4</sub> nanoparticles by carbothermal reduction and nitridation of geopolymers. *Journal of the American Ceramic Society*. 2019;102(11):6542-51.
142. Yang X, Zhang Y. Prediction of high-entropy stabilized solid-solution in multi-component alloys. *Materials Chemistry and Physics*. 2012;132(2):233-8.
143. Lee SJ, Benson EA, Kriven WM. Preparation of portland cement components by poly (vinyl alcohol) solution polymerization. *Journal of the American Ceramic Society*. 1999;82(8):2049-55.
144. Lee SJ, Kriven WM. Crystallization and densification of nano-size amorphous cordierite powder prepared by a PVA solution-polymerization route. *Journal of the American ceramic society*. 1998;81(10):2605-12.
145. Sarin P, Yoon W, Jurkschat K, Zschack P, Kriven WM. Quadrupole lamp furnace for high temperature (up to 2050 K) synchrotron powder X-ray diffraction studies in air in reflection geometry. *Review of Scientific Instruments*. 2006;77(9):093906.
146. Haynes WM. *CRC Handbook of Chemistry and Physics*: CRC Press; 2014.
147. Kok D, Yadav D, Sortino E, McCormack SJ, Tseng KP, Kriven WM, Raj R, Mecartney ML.  $\alpha$ -Alumina and spinel react into single-phase high-alumina spinel in < 3 seconds during flash sintering. *Journal of the American Ceramic Society*. 2019;102(2):644-53.
148. Ho CY, Taylor RE. *Thermal Expansion of Solids*: ASM International; 1998.
149. Touloukian YS. *Thermal expansion: Nonmetallic solids*. *Thermophysical Properties of Matter*. 1977;13:247-50.
150. Siah L, Kriven WM, Schneider J. In situ, high-temperature, synchrotron, powder diffraction studies of oxide systems in air, using a thermal-image furnace. *Measurement Science and Technology*. 2005;16(6):1291.
151. Weber J, Tamalonis A, Benmore C, Alderman O, Sendelbach S, Hebden A, Williamson M. Aerodynamic levitator for in situ X-ray structure measurements on high temperature and molten nuclear fuel materials. *Review of Scientific Instruments*. 2016;87(7):073902.

152. Santos CJE, Nelson AZ, Mendoza E, Ewoldt RH, Kriven WM. Design and fabrication of ceramic beads by the vibration method. *Journal of the European Ceramic Society*. 2015;35(13):3587-94.
153. McCormack SJ, Tseng KP, Weber RJ, Kapush D, Ushakov SV, Navrotsky A, Kriven WM. In-situ determination of the  $\text{HfO}_2\text{-Ta}_2\text{O}_5$ -temperature phase diagram up to 3000° C. *Journal of the American Ceramic Society*. 2019;102(8):4848-61.
154. McCormack SJ, Tamalonis A, Weber RJ, Kriven WM. Temperature gradients for thermophysical and thermochemical property measurements to 3000° C for an aerodynamically levitated spheroid. *Review of Scientific Instruments*. 2019;90(1):015109.
155. McCormack SJ, Weber RJ, Kriven WM. In-situ investigation of  $\text{Hf}_6\text{Ta}_2\text{O}_{17}$  anisotropic thermal expansion and topotactic, peritectic transformation. *Acta Materialia*. 2018;161:127-37.
156. Saiki A, Ishizawa N, Mizutani N, Kato M. Variation structurale des sesquioxydes de lanthanides C,  $\text{Yb}_2\text{O}_3$  et  $\text{Er}_2\text{O}_3$  en fonction de la température. *Journal of the Ceramic Society of Japan*. 1985;93(10):649-54.
157. Coelho AA. TOPAS and TOPAS-Academic: An optimization program integrating computer algebra and crystallographic objects written in C++. *Journal of Applied Crystallography*. 2018;51(1):210-8.
158. Rietveld HM. A profile refinement method for nuclear and magnetic structures. *Journal of Applied Crystallography*. 1969;2(2):65-71.
159. Stadelmann P. Java electron microscopy simulation (JEMS) software. Switzerland: CIME-EPFL, École Polytechnique Fédérale de Lausanne. 2006.
160. Toby BH. R factors in Rietveld analysis: How good is good enough? *Powder Diffraction*. 2006;21(1):67-70.
161. Touloukian YS. Thermal Expansion: Metallic Elements and Alloys. *Thermophysical Properties of Matter*. 12: IFI/Plenum; 1975.
162. Sarma D, Hegde M, Rao C. Study of surface oxidation of rare-earth metals by photoelectron spectroscopy. *Journal of the Chemical Society, Faraday Transactions 2: Molecular and Chemical Physics*. 1981;77(9):1509-20.
163. Dai H, Ng C, Au C.  $\text{SrCl}_2$ -promoted  $\text{REO}_x$  (RE= Ce, Pr, Tb) catalysts for the selective oxidation of ethane: A study on performance and defect structures for ethene formation. *Journal of Catalysis*. 2001;199(2):177-92.
164. Moulder JF, Stickle WF, Sobol PE, Bomben KD. *Handbook of X-ray Photoelectron Spectroscopy*: Perkin-Elmer Corporation; 1995. 230-2 p.

165. Belaya S, Bakovets V, Boronin A, Koshcheev S, Lobzareva M, Korolkov I, Stabnikov P. Terbium oxide films grown by chemical vapor deposition from terbium (III) dipivaloylmethanate. *Inorganic Materials*. 2014;50(4):379-86.
166. Xiao W, Tan D, Li Y, Liu J. The effects of high temperature on the high-pressure behavior of CeO<sub>2</sub>. *Journal of Physics: Condensed Matter*. 2007;19(42):425213.
167. Gallagher, McCarthy. Penn State University, University Park, PA, USA, ICDD Grant-in-Aid. 1973.
168. Kröger F, Vink H. Relations Between the Concentrations of Imperfections in Crystalline Solids. *Solid State Physics*. 3: Elsevier; 1956. p. 307-435.
169. Tseng KP, Yang Q, McCormack SJ, Kriven WM. High-entropy, phase-constrained, lanthanide sesquioxide. *Journal of the American Ceramic Society*. 2020;103(1):569-76.
170. Tomaszewski P. *Golden Book of Phase Transitions*: Wroclaw; 2002.
171. Foex M, Traverse J. Remarques sur les transformations cristallines presentees a haute temperature par les sesquioxydes de terres rares. *Revue Internationale des Hautes Temperatures et des Refractaires*. 1966;3(4):429-53.
172. Aldebert P, Traverse J. Etude par diffraction neutronique des structures de haute temperature de La<sub>2</sub>O<sub>3</sub> et Nd<sub>2</sub>O<sub>3</sub>. *Materials Research Bulletin*. 1979;14(3):303-23.
173. Horlait D, Claparede L, Clavier N, Szenknect S, Dacheux N, Ravaux J, Podor R. Stability and structural evolution of Ce<sup>IV</sup><sub>1-x</sub>Ln<sup>III</sup><sub>x</sub>O<sub>2-x/2</sub> solid solutions: A coupled  $\mu$ -Raman/XRD approach. *Inorganic Chemistry*. 2011;50(15):7150-61.
174. Shafer M, Roy R. Rare-earth polymorphism and phase equilibria in rare-earth oxide-water systems. *Journal of the American Ceramic Society*. 1959;42(11):563-70.
175. Seymour KC, Ribero D, McCormack SJ, Kriven WM. Relationship between the orthorhombic and hexagonal phases in Dy<sub>2</sub>TiO<sub>5</sub>. *Journal of the American Ceramic Society*. 2016;99(11):3739-44.
176. Anand G, Wynn AP, Handley CM, Freeman CL. Phase stability and distortion in high-entropy oxides. *Acta Materialia*. 2018;146:119-25.